

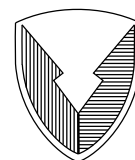
The AFDD International Dynamic Stall Workshop on Correlation of Dynamic Stall Models with 3-D Dynamic Stall Data

C. M. Tan and L. W. Carr

July 1996



National Aeronautics and
Space Administration



US Army
Aviation and Troop Command

The AFDD International Dynamic Stall Workshop on Correlation of Dynamic Stall Models with 3-D Dynamic Stall Data

C. M. Tan and L. W. Carr, *Aeroflightdynamics Directorate, U.S. Army Aviation and Troop Command, Ames Research Center, Moffett Field, California*

July 1996



National Aeronautics and
Space Administration

Ames Research Center
Moffett Field, CA 94035-1000



US Army
Aviation and Troop Command

Aeroflightdynamics Directorate
Moffett Field, CA 94035-1000

The AFDD International Dynamic Stall Workshop on Correlation of Dynamic Stall Models with 3-D Dynamic Stall Data

C. M. TAN AND L. W. CARR

*Aeroflightdynamics Directorate, U.S. Army Aviation and Troop Command
Ames Research Center, Moffett Field, CA 94035-1000*

Summary

A variety of empirical and computational fluid dynamics (CFD) two-dimensional (2-D) dynamic stall models were compared to recently obtained three-dimensional (3-D) dynamic stall data in a workshop on modeling of 3-D dynamic stall of an unswept, rectangular wing of aspect ratio 10. Dynamic stall test data both below and above the static stall angle of attack were supplied to the participants, along with a "blind" case where only the test conditions were supplied in advance, with results being compared to experimental data at the workshop itself. Detailed graphical comparisons are presented in the report, which also includes discussion of the methods and the results. The primary conclusion of the workshop was that the 3-D effects of dynamic stall on the oscillating wing studied in the workshop can be reasonably reproduced by existing semi-empirical models once 2-D dynamic stall data have been obtained. The participants also emphasized the need for improved quantification of 2-D dynamic stall.

Introduction

Dynamic-stall-induced pitching moments have limited the fatigue life of critical helicopter rotor components, and quantification of these loads has been a major factor in rotor-loads analysis. In the past, rotor-loads analysis has been primarily based on 2-D empirical dynamic-stall models, due to limitations on theory and computation of 3-D effects. However, improvements in modeling of rotor wakes have resulted in semi-empirical modeling techniques which address 3-D effects. In addition, advances in full Navier-Stokes equation modeling of unsteady 3-D flows have introduced the possibility of accurate calculation of this unsteady 3-D flow field, at least for dynamic stall of 3-D wings oscillating in pitch. Significant progress has been made in both modeling and measurement of 2-D dynamic stall on airfoils oscillating in angle of attack (refs. 1 and 2). Recent efforts at modeling 3-D effects have also shown some success, but the various researchers have often applied their models to different test cases; there has been little direct comparison between

models. The availability of a recent set of experimental results for a 3-D dynamic stall study (ref. 3) offered a unique opportunity to see how well 2-D models can reproduce 3-D characteristics, as well as to obtain a quantitative comparison between the various models. The U.S. Army Aeroflightdynamics Directorate (AFDD) therefore decided to host a workshop with invitations sent to the U.S. aerospace industry, academia, and government laboratories as well as to members of the European aerospace community. The participants were each supplied with test data for use in calibration and verification of their codes, and then were asked to calculate the loads for a set of conditions for which only nominal test conditions were supplied. The calculated results of each participant were then compared with the experimental data as well as with corresponding results from the other participants of the workshop. It was intended that such a workshop would lead to better understanding of the fundamentals of the dynamic stall phenomenon, and that the workshop would suggest directions for future research. In all, there were ten participants, of which seven contributed results for comparison to experiment. The AFDD International Dynamic Stall Workshop was held June 9–12, 1992, at the U.S. Army Aeroflightdynamics Directorate.

The authors would like to thank William Bousman, Francis Caradonna, William McCroskey, and Joon Lim for their assistance and valuable advice, and Myung Rhee for his assistance in preparing the graphics for this report.

Participants Who Entered Data for Comparison at the Workshop

T. Beddoes, Westland Helicopters, England
J. Costes, ONERA, France
R. Hixon, Georgia Institute of Technology
W. Johnson, Johnson Aeronautics
G. Leishman, University of Maryland
S. Srinivasan, Sterling Software
C. Tan, AFDD

Description of the Oscillating Wing Test Used as Reference

A review of dynamic stall literature shows there have been many 2-D dynamic stall experiments performed, covering a wide range of test conditions. However, with the exception of Lorber et al. (ref. 4), relatively little data is available that quantitatively documents the influence of 3-D flow, especially at high Reynolds number. Therefore, a special experiment was designed to produce 2-D and 3-D dynamic stall data using a simple wing planform. The test was performed on a 3-D rectangular semi-span wing with a NACA 0015 airfoil section. The test was performed in a 7- by 10-ft wind tunnel at Mach number of 0.3; no wall corrections were applied. Carefully controlled experiments were performed to isolate various aspects of the dynamic stall process.

The test focused on documentation of 2-D and 3-D dynamic stall in a nonrotating environment. Sufficient data were obtained to permit quantitative comparison between the experimental results and the various semi-empirical dynamic stall models that have been developed by industry, government, and university researchers; results from recent CFD techniques which directly compute the 3-D dynamic stall process were included in this comparison. Emphasis was placed on stall onset since it is one of the most difficult aspects of dynamic stall to accurately predict. Tests were performed over a wide range of mean angles of attack, varying from 4 to 17 degrees; oscillation amplitude was fixed at ± 2 , ± 4 , or ± 5 degrees. 2-D data were obtained through the use of an end-plate; 3-D data were then obtained using a square and a rounded wing-tip cap. One hundred instantaneous pressure transducers were distributed over the wing, with half concentrated at the tip, and half allocated to five additional span locations; the locations are shown in figure 1. For a detailed description of this experiment, as well as a comprehensive presentation and discussion of the test results, see reference 3.

Test Data Used in the 3-D Dynamic Stall Workshop

The test data used during the AFDD International Dynamic Stall Workshop are a small subset of the oscillating wing experimental data set described above. The subset supplied to the participants included cases with mean angles of attack of 11, 13, 15, and 17 degrees, each for reduced frequencies of 0.04, 0.1, and 0.14, at an oscillation amplitude of ± 4 degrees, and Mach number of 0.3. The experimental data for the 11-, 13-, and 17-degree cases were distributed to the workshop participants several months before the commencement of the

workshop. As noted above, it was decided to make the 15-degree data a “blind” test set for which experimental data would not be provided ahead of time in order to see how well the different analytical models would fare in the absence of actual experimental test data.

Each experimental data point resulted in integrated instantaneous aerodynamic loads at seven spanwise stations: 25.0, 47.5, 80.0, 90.0, 96.6, 98.6, and 99.5 percent of span. The data at each spanwise location included instantaneous values of lift, drag, and pitching moment integrated from instantaneous pressure distributions at 256 equally spaced time-intervals through the oscillation cycle. As noted above, experimental data were supplied to the participants for three mean angles, at each of three different oscillation frequencies. Angle-of-attack history and reduced frequency were the only information given concerning the blind case (the full data set is presented here for reference). Figures 2–11 present aerodynamic loads through the oscillation cycle for all the conditions studied in the workshop as described below. The workshop participants’ predictions will be presented later in this report.

Figures 2–4 (11-degree mean angle)– The lift and pitching-moment data for $\alpha = 11^\circ + 4^\circ \sin \omega t$, $k = 0.04$, are presented for 25 and 47.5 percent span locations in figure 2(a), for 80 and 90 percent span in figure 2(b), for 96.6 and 98.6 percent in figure 2(c), and for 99.5 percent span in figure 2(d). The drag coefficient through the oscillation cycle for the four stations where drag was measured is presented in figure 2(e) (note that all plots are scaled uniformly so that results obtained at various spanwise stations and/or test conditions can be directly compared). Based on the lift and pitching-moment behavior seen in figure 2(a), it is clear that for this angle of attack history, stall has been delayed beyond the static stall angle. Note the pitching-moment data; there is no negative spike in this data, even though pitching-moment stall is the first evidence that even light dynamic stall has occurred. Figures 3 and 4 present the results for $k = 0.10$ and 0.14; again, no stall is observed in the experimental data.

Figures 5–7 (13-degree mean angle)– Dynamic stall has occurred for the $\alpha = 13^\circ + 4^\circ \sin \omega t$, $k = 0.04$ case, as can be seen in figure 5. The sections of the wing which are far from the tip (fig. 5(a), 25 and 47.5 percent span) show clear evidence of lift loss as well as the appearance of an abrupt negative pitching-moment excursion that is associated with dynamic stall. However, the conditions nearer the wing tip are clearly different; figure 5(b) shows that neither the 80 nor 90 percent span station has experienced any stall. This is also true for 96.6, 98.6, and 99.5 percent span (figs. 5(c) and 5(d)). The drag data for 47.5 percent

span (fig. 5(e)) show the drag rise typical of dynamic stall; no stall appears at 96.6 or 98.6 percent, but a clear impact of the tip vortex is seen at 99.6 percent span.

The lift loss has been partially suppressed at $k = 0.10$, as can be seen in figure 6(a). Note that there is still a vestige of unsteady separation at both 25 and 47.5 percent span, as evidenced by the slight drop in pitching moment at the top of the cycle. The flow over the outer portion of the wing is fully attached, as can be seen in figures 6(b)–6(d); the drag curve at 47.5 percent span shows only a small perturbation from fully attached flow (fig. 6(e)).

The flow conditions for $k = 0.14$ are essentially those of a fully attached wing flow, as can be seen in figure 7. It is noteworthy the maximum angle of attack attained at this test condition is above the static stall angle for this airfoil, yet no stall has occurred during this test condition, due to the effects of high reduced frequency.

Figures 8–10 (15-degree mean angle)– Dynamic stall has clearly occurred at $\alpha = 15^\circ + 4^\circ \sin \omega t$, $k = 0.04$. This case, the first of the blind conditions, is presented in figure 8. The lift and pitching-moment curves for the inboard spanwise stations show the abrupt loss of lift, and the “figure eight on its side” pitching-moment curves that are typical of dynamic stall (fig. 8(a)). It is interesting that this dynamic stall behavior is completely absent at 80 percent span—3-D effects clearly have modified the flow at the stations near the tip (figs. 8(b)–8(d)). Again, the drag coefficient shows the dynamic stall type pattern at 47.5 percent span, but not at any other spanwise station (fig. 8(e)).

The $k = 0.10$ data show the influence that increase in frequency has on the dynamic stall process (fig. 9(a), 25 and 47.5 percent span). The loss in lift is delayed to the maximum angle of attack; the corresponding drop in pitching moment also occurs at this maximum α . The flow remains attached at 80 percent span and at all other stations out to the tip of the wing (figs. 9(b)–9(e)). The instantaneous drag at 47.5 percent span is the only data that shows the impact of dynamic stall for this condition (fig. 9(e)).

The effect of frequency is even more pronounced at $k = 0.14$, as can be seen in figure 10. Here, away from the wing tip, dynamic stall continues to occur, but the lift remains high even as the wing has pitched past the maximum angle and is moving to lower angle of attack (fig. 10(a)). This effect is also seen in the pitching moment, where the area inside the pitching-moment loop has increased dramatically, thus changing the aerodynamic damping magnitude, a parameter of major importance to rotor loads and stability. The flow nearer the tip

of the wing remains unstalled throughout the cycle, as can be seen in figures 10(b)–10(e); again, only the results at 47.5 percent span show any evidence of stall (fig. 10(e)).

Figures 11–13 (17-degree mean angle)– Airfoil stall occurs early in the oscillation cycle for $\alpha = 17^\circ + 4^\circ \sin \omega t$, $k = 0.04$, as can be seen in figure 11(a). For the first time, stall effects are evident at 80 percent span; even 90 percent span shows the presence of some separation (fig. 11(b)). The flow at 96.5, 98.6, and 99.6 percent remains attached (figs. 11(c)–11(e)). It is interesting to note that the pitching moment at 25 and 47.5 percent span show a gradual drop well before any loss in lift is observed. This is a characteristic associated with the movement of the dynamic stall vortex: while the dynamic stall vortex is on the airfoil, the lift remains high. However, the pitching moment progressively grows more negative as the dynamic stall vortex moves down the airfoil. When the dynamic stall vortex leaves the airfoil, the lift is abruptly lost, and the pitching moment gradually returns to zero. This pattern is observed throughout the $\alpha = 17^\circ$ mean-angle data.

At $k = 0.10$, dynamic stall has again been delayed to near the maximum angle of attack for 25 and 47.5 percent span (fig. 12(a)); this is shown both in the lift and in the pitching-moment coefficient behavior. No data are presented for lift at 80 percent span, due to a malfunction in data acquisition; however, the pitching-moment results show that some dynamic stall effects are still present at this spanwise location. No stall effects are observed in the lift or pitching-moment results at 96.6 or 98.6 percent span (fig. 12(c)), although there is a gradual decrease in pitching moment as the angle of attack increases. This decrease is more significant at 99.5 percent span (fig. 12(d)). The drag results show a gradual increase in drag associated with the onset of separation at 47.5 percent span (fig. 12(e)). Note that no separation effects are present at 96.6 or 98.6 percent span.

Figure 13 presents the highest mean-angle, highest frequency case supplied as part of the workshop. At this condition, the inboard stations on the wing experience strong stall effects, as can be seen in figure 13(a). It is again interesting to note that the pitching-moment results show a gradual decrease, while the lift results do not show any decrease until α_{\max} is reached. At 80 and 90 percent span (fig. 13(b)) little lift is lost, and the pitching-moment results show little change. The flow very near the tip (figs. 13(c)–13(d)) shows that this region of the wing has little flow separation as well. In figure 13(e), only the drag at 47.5 percent span shows any evidence of separation.

Dynamic Stall Models and Calculations

The participants at the AFDD International Dynamic Stall Workshop brought a wide range of dynamic stall air-load prediction techniques to the meeting. The methods can be separated into those that model the flow based on knowledge of the 2-D experimental dynamic stall data (the empirical or semi-empirical models) and those that compute the airfoil characteristics based on direct representation of the fluid flow behavior (the Navier-Stokes calculation techniques). In the discussion that follows, those techniques that use information from 2-D dynamic or static stall experiments are classified as dynamic stall “models,” and those that compute the load based on actual calculation of the flow will be classified as dynamic stall “calculations.”

There were five dynamic stall models represented at the workshop, identified for the purpose of the workshop as 2GCHAS, BEDDOES, JOHNSON, LEISHMAN, and ONERA. Two dynamic stall calculation techniques were presented: GATECH and SRINI. Each of the various techniques is briefly described below. These descriptions are intended only as general introductions to the methods; the reader is directed to the related references for additional details about each method.

2GCHAS– The 2GCHAS stall model (ref. 5) is a semi-empirical method that determines the aerodynamic response of the wing through the use of indicial response functions. The theory of the model used in 2GCHAS was developed by Leishman (derived from the original “Leishman/Beddoes” model of ref. 6). The indicial functions are time-dependent responses to a step change in angle of attack and are idealized into noncirculatory and circulatory parts. These response functions are written in terms of aerodynamic time (distance traveled in half chords) and Mach number. In addition, the circulatory component contains the Prandtl-Glauert compressibility correction. The coefficients of the exponential series are scaled with Mach number and are considered independent of airfoil shape. These coefficients have been determined through the inverse process of obtaining indicial response functions from the unsteady airloads of various airfoils in the frequency domain (ref. 5).

BEDDOES– This model is a semi-empirical method employing an indicial method by which a generalized response function developed from 2-D experimental dynamic stall results is used to represent the 3-D aerodynamic loading due to forcing functions. The 3-D effects of the time-varying trailed vorticity is incorporated by including a “near wake” model. For details of the indicial method adapted for rotor dynamic airloads, refer to references 7 and 8.

JOHNSON– Two models are considered in this technique. The “Boeing” model is a semi-empirical method that models both dynamic stall and radial flow effects. The lift, pitching-moment, and drag coefficients are calculated using static airfoil data obtained experimentally for the necessary angle of attack and Mach number range. These results are then modified using dynamic stall corrections obtained from oscillating airfoil tests, which are applied as corrections for angle of attack due to pitch rate (see ref. 9 for details). The “MIT Stall Method” is a semi-empirical method that bases its calculation of dynamic loading on experimental data, as detailed in reference 10. A dynamic stall angle is determined from experiments for a given airfoil, and the maximum lift and pitching moment due to dynamic stall overshoot is empirically calculated from experimental data. At the instant of stall, the loading is a function of pitch rate, chord length, and 2-D velocity.

LEISHMAN– The Leishman-Sikorsky model is similar to the stall model in 2GCHAS except for the addition of 3-D indicial functions for the induced velocity field to account for the unsteady trailed wake effects. In addition, the model also uses a 3-D aerodynamic center offset function which is determined from experimental data for finite wings combined with lifting surface theory. This model was recently developed by Leishman under contract from Sikorsky Aircraft and is considered proprietary information; hence, a written reference is not available at this time. However, information about the general concept used in this approach can be found in references 11–13.

ONERA– The ONERA model was developed from classical potential theory, with linear aerodynamics used for the calculation of downwash and aerodynamic forces. Extensions were made to include unsteadiness and nonlinear effects. It uses 2-D experimental results as a starting point for computing the loss of induced velocity due to stall. An extension to the 3-D case is made by assuming that the loss of induced velocity in the 3-D case is the same as the loss of induced velocity in the 2-D case. For details, refer to reference 14.

GATECH– The Georgia Institute of Technology Sankar/Hixon computations are performed using an unsteady, 3-D, noniterative Alternating Direction Implicit (ADI) Navier-Stokes solver. The Navier-Stokes equations are solved in the unsteady 3-D environment using an implicit/explicit hybrid scheme. In addition, a generalized minimal residual (GEMRES) method is used to lessen the computational time (ref. 15).

SRINI– The Srinivasan model uses an implicit Navier-Stokes numerical solution method. A modified version of the TURNS code which is capable of calculating the

aerodynamic and acoustic flow field in the rotor environment is used. The algebraic model of Baldwin-Lomax is used as the turbulence model. For details, refer to references 16 and 17.

It should be mentioned that those participants who employed Navier-Stokes methods were offered the option of “de-scoping” the task by attempting fewer cases because of the high computational costs involved in use of these codes. However, these participants were asked to run the blind case as a minimum set of results.

Discussion of Results

As mentioned above, many of the participants submitted results for virtually all of the supplied data cases, with the exception that the dynamic stall calculators limited themselves to the mid-frequency blind case. Since this resulted in a massive set of data, it was necessary to restrict the comparison set to be used as the topic for discussion during the workshop. Therefore, analysis and discussion during the workshop focused primarily on this single test condition:

$$\alpha = 15^\circ + 4^\circ \sin \omega t$$

$$k = 0.10$$

$$\text{Mach number} = 0.30$$

$$\text{Spanwise stations } 1, 2, 3, 4, \text{ and } 6 \text{ (25.0, 47.5, 80.0, 90.0, and 98.6 percent of span)}$$

The same approach is used in the present discussion: detailed comparison of the results for the various methods are restricted to the primary blind test condition noted above. Comparative data will also be presented for stations 5 and 7 (not available at the time of the workshop discussion) in order to fully map the performance of these methods at the benchmark condition. Note that these graphs are scaled such that the data fully fill the graphical image, thus allowing detailed comparison of the various methods with the experimental data. The reader is therefore cautioned to verify the vertical scales of the graphs before comparing results at differing spanwise stations. As noted earlier, the experimental data were plotted to a single scale in figures 2–13 so that direct comparisons between stations can be performed on a common reference basis.

Station 1 (25 percent span)– Figure 14(a) shows the result of both modeling and calculation of the lift coefficient at the 25 percent span location, for the blind case, $\alpha = 15^\circ + 4^\circ \sin \omega t$, $k = 0.10$. As can be seen in this figure, the dynamic stall modelers and calculators reproduce the experimental behavior with varying levels of success. On the upstroke, the lift curve slope is

captured accurately by BEDDOES and LEISHMAN, while 2GCHAS, JOHNSON, and ONERA present a higher slope than the experiment. The calculations by SRINI predict a lift value well above that of the experiment, and do not show the lift loss at the top of the cycle that is observed in the experiment. The calculations by GATECH capture the character of the flow at low angle, but predict full airfoil stall, whereas the experiment shows only a lift loss at the top of the cycle.

The representation of the lift behavior after maximum angle is less quantitative; however, it should be noted that the various models capture the essential characteristics of the lift hysteresis and reproduce the critical aspects of the lift history. The post-stall predictions by the two Navier-Stokes equation calculations miss significantly, and predict that the wing would either stall at 16 degrees (GATECH) or experience no stall at all (SRINI). It is appropriate at this point to address the apparent error on the part of the results computed through use of the Navier-Stokes equations. As noted earlier, the dynamic-stall *modelers* used 2-D experimental data as input to their techniques; therefore, the models were calibrated using the experimental data obtained for the airfoil under study, including information about the stall behavior of the airfoil. In contrast, the dynamic stall *calculators* were determining the airfoil performance directly, and the results demonstrate the difficulty that exists in quantitatively predicting the 2-D dynamic stall behavior of airfoils, as compared to the modeling of this behavior. When the results are viewed with this in mind, it is more understandable that the Navier-Stokes equation computations are less able to exactly represent the stall behavior of the inboard, essentially 2-D sections of the wing. On the other hand, as will be seen later, the Navier-Stokes *calculations* do capture the significant 3-D effects that appear very near the tip of the wing, an area where the dynamic stall *modeling* techniques are significantly less accurate.

The drag coefficient plots (fig. 14(b)) show the same trend as seen in the lift results. The curves produced by the modelers show a rise in drag in the range of maximum angle, while showing only the occurrence of light stall on the downstroke. In comparison, the two Navier-Stokes equation computations show either full separation or no separation at all. Note that no experimental data are shown in this figure. Drag data were not measured at this spanwise location; however, since many of the participants were able to model or compute drag, those results have been included in this report in order to place these data on record.

The pitching-moment coefficient results for Station 1 are presented in Figure 14(c). The maximum negative

pitching moment combined with the duration of large negative moments define the pitch link loads experienced by the helicopter. As can be seen in figure 14(c), the dynamic stall modelers represent this region with varying levels of success. Once more, most modelers come close to the experimental results, while the Navier-Stokes equation computations predict either fully separated or fully attached flow.

Station 2 (47.5 percent span)– Figure 15(a) presents the comparison for lift for the midspan location. As can be seen, the modelers represent the upstroke with reasonable accuracy, but are less consistent in quantitative comparison to experiment on the downstroke. However, these methods still capture the primary characteristics of the experimental data. Here, the GATECH calculations predict complete airfoil stall, whereas the experiment still shows essentially attached flow, but with a measurable loss of lift at the top of the cycle; the SRINI calculations capture this lift loss.

Figure 15(b) presents the corresponding drag comparison; the models again reproduce the experimental data with varying degrees of success; the Navier-Stokes solutions again either predict early stall or no stall at all. Figure 15(c) shows similar behavior of the pitching-moment comparisons.

Station 3 (80 percent span)– Figure 16(a), the comparison of lift results at 80% span location, shows significant variation among the various results. In particular, the experiment shows no lift loss at maximum angle of attack, while both models and calculations (with the exception of BEDDOES and ONERA) show a relatively large hysteresis in the lift curves. However, both BEDDOES and ONERA significantly overpredict the lift curve slope, and the maximum value of the lift coefficient. Drag is presented in figure 16(b); note that no drag values were measured at this spanwise location. The results for pitching moment, figure 16(c), show a relatively wide range of results. None of the methods quantitatively captured the character of the pitching-moment history, although several do show the figure-eight loop seen in the experimental data, although with varying degrees of accuracy.

Station 4 (90 percent span)– The various results for lift at this location are shown in figure 17(a). As can be seen, there are significant quantitative differences between the various results and between the results and the experimental data. Drag is again presented (fig. 17(b)) without experimental results, since no drag data were obtained at this spanwise location. The pitching-moment results (fig. 17(c)) show that most of the participants captured the character of the pitching moment; in particular, they reproduced the fact that the pitching moment has only one

loop in the hysteresis pattern (the two exceptions being 2GCHAS and GATECH).

Station 5 (96.6 percent span)– At station 5, all the participants were able to capture the lift coefficient behavior, which showed very little lift loss throughout the cycle of oscillation (fig. 18(a)). However, reproduction of the drag results is less uniform. In particular, LEISHMAN and ONERA predict a lower value for drag, as well as a lower slope for drag variation with angle of attack, than observed in the experiment (fig. 18(b)). However, the reader is cautioned to note the expanded scale of this plot. The pitching-moment results, presented in figure 18(c), show that none of the modelers capture the decrease in pitching moment as angle of attack increases; this pattern was only captured by the GATECH Navier-Stokes calculations; again note the expanded scale of the graph.

Station 6 (98.6 percent span)– This spanwise location, near the tip of the oscillating wing, shows essentially benign aerodynamic effects. The lift (fig. 19(a)) shows effectively no loss in lift throughout the cycle. The various modelers capture this behavior, as well as the hysteresis in lift that appears in the experimental results. The computation by GATECH shows a stronger hysteresis loop and predicts a higher net lift value.

The results for drag (fig. 19(b)) show that some of the models do quite well in representing the pressure drag in this region of the flow (note that the experiment only measured pressure drag; viscous drag was not determined). Again, the results of computation by GATECH is somewhat higher than the experimental data, while the ONERA and LEISHMAN model results are below the experimental curve. However, overall, the results are essentially representative of the experimental results.

The pitching moment (fig. 19(c)) shows significant differences. Here, the only technique to capture the character of the experiment is the Navier-Stokes calculation of GATECH; all of the models miss the change in pitching moment that appeared with increase in angle of attack. This result clearly shows the influence of the tip (most likely the tip vortex) on the flow, a fact that could only be captured by a technique that calculates the flow directly. However, it should be emphasized that the magnitude of the pitching moment is small at this spanwise location.

Station 7 (99.5 percent span)– This location, virtually at the tip of the oscillating wing, shows that the modelers do not accurately capture the strong three-dimensionality of the flow at this location (fig. 20(a)). Indeed, only the GATECH calculations come close to reproducing the character of the lift at this station. The results for drag are shown in figure 20(b); again, the GATECH calculations

are the only results which quantitatively capture the behavior of the experimental results. This same trend can be seen in the pitching-moment results, shown in figure 20(c). It should be emphasized that the flow in this region is dominated by the tip vortex, and such behavior can only be captured by Navier-Stokes calculations. It is worth noting that Navier-Stokes calculations are not a panacea—the SRINI results, also a Navier-Stokes calculation, do not fully capture this tip effect. These Navier-Stokes calculations were some of the first 3-D dynamic stall calculations performed using the Navier-Stokes equations, and show the difficulty associated with quantification of this very complex flow field.

Summary of Technical Discussions

A major purpose of the workshop was to bring together various experts on modeling and calculation of dynamic stall to permit detailed discussion of the result of comparing the output of these techniques to experimental data. The result of these discussions is summarized below:

Use of 2-D Experimental Data

The consensus was that semi-empirical models captured the essential 3-D aspects of 3-D dynamic stall experimental data while using 2-D airfoil data as input. It was concluded that the interaction of the unsteady wake with the local flow was modifying the dynamic stall environment by change of the effective angle of attack locally rather than by change of the dynamic stall physics. Thus, 2-D dynamic stall experiments will continue to form a critical part of the foundation for 3-D semi-empirical modeling of dynamic stall. In fact, the group concluded that major emphasis on 2-D dynamic stall prediction by Navier-Stokes calculation was more critical than calculation of 3-D effects using such calculation techniques.

Information Needed from 2-D Experimental Data

The consensus was that the critical missing information is in the area of 2-D dynamic stall behavior. In particular, it was recommended that quantification of Reynolds number and Mach number effects on stall onset in steady and unsteady flow regimes should be given more emphasis. The group concluded that once the 2-D dynamic stall data are available, the 3-D dynamic loads can be represented with sufficient accuracy using modeling techniques. However, at the present time, these 2-D data can only be obtained from experiment. Quantitative stall

calculation, both static and dynamic, remains a critical unsolved obstacle to effective dynamic stall load prediction.

Calculation

Again, the consensus was to place emphasis on 2-D dynamic stall behavior. There is a need for more accurate predictions of stall type. The ability to predict steady stall behavior (e.g., leading- or trailing-edge stall, progression of separation point as the angle of attack is increased, and Mach number effects on stall development) is critical to any plan to use calculation to replace experiment. Also, the ability to accurately determine the effect of unsteadiness on the stall type is of significant importance. The effect of unsteadiness on the position of the separation point during pitching motion of the airfoil would be of value to modelers, for instance, since the models depend on this information to prescribe the behavior of the airfoil during the stall process.

Semi-Empirical Modeling versus Calculation of Dynamic Stall

There were two groups of participants at the meeting—those who modeled the flow and those who calculated the flow. Discussion by the various members of the workshop group led to the conclusion that the targets of each of these groups are different, but complementary. For example, the models are directed toward simulation of aerodynamic effects, while Navier-Stokes solution representations are actually trying to compute the aerodynamic effects directly. Ultimately, calculation may be able to supply modelers with sufficiently accurate results that the modelers will not always be required to resort to experimental data to obtain the inputs for their techniques.

Future Challenges

The workshop comparisons were for an unswept, untapered wing at one Mach number. Semi-empirical models will require new data bases for representation of sweep, Mach number, Reynolds number, airfoil shape, mean angle, oscillation angle, etc.—each of which will require significant new experimental effort to acquire. It is possible that these effects may ultimately be calculated using Navier-Stokes equation solvers, with the results then used to calibrate the semi-empirical models that will continue to be used by helicopter designers. However, until these methods reach a high level of consistency and accuracy, they will not be routinely used in design.

Concluding Remarks

The AFDD International Dynamic Stall Workshop provided an excellent opportunity to assess the state of the art in dynamic stall modeling and calculation, and resulted in a unique “snapshot” of this field of endeavor. The various dynamic stall models did a reasonable job of reproducing the dynamic stall events that were observed experimentally. The dynamic stall calculations based on solution of the Navier-Stokes equations were not quantitatively correct, but offered the best representation of the 3-D effects that are present near the tip of the oscillating wing, and offer the possibility of reducing the dependence on experiment that presently is required for semi-empirical modeling of dynamic stall effects.

A significant result of the workshop is the discovery that semi-empirical models based on 2-D experimental results, combined with representation of the 3-D unsteady wake of the wing, did quite well in estimating the 3-D dynamic stall behavior observed in the experiment. This suggests that the presence of the wing tip and its associated vortex primarily resulted in changes in local angle of attack rather than changes in the physics of the dynamic stall process.

The workshop participants agreed that (1) the most critical need is to obtain better ways to determine 2-D dynamic stall information about airfoils of interest, and (2) the 3-D effects of the wing tip can be reasonably represented by inclusion of unsteady wake effects on the local angle of attack, at least for unswept, untwisted wings similar to those used for the benchmark experimental data set of this workshop.

References

1. Carr, L. W.: Progress in Analysis and Prediction of Dynamic Stall. *J. Aircraft*, vol. 25, no. 1, Jan. 1988, pp. 6–17.
2. Carr, L. W.; and McCroskey, W. J.: A Review of Recent Advances in Computational and Experimental Analysis of Dynamic Stall. IUTAM Symposium on Fluid Dynamics of High Angle of Attack, Tokyo, Japan, Sept. 13–17, 1992.
3. Piziali, R.: An Experimental Investigation of 2D and 3D Oscillating Wing Aerodynamics for a Range of Angle of Attack Including Stall. NASA TM-4632 and USAATCOM TR 94-A011, Sept. 1994.
4. Lorber, P.; Covino, A. F., Jr.; and Carta, F. O.: Dynamic Stall Experiments on a Swept Three-Dimensional Wing in Compressible Flow. AIAA Paper 91-1795, AIAA 22nd Fluid Dynamics, Plasma Dynamics, and Lasers Conference, Honolulu, Hawaii, June 24–26, 1991.
5. 2GCHAS Theory Manual, Vol. 2, Release 1.91, May 1991.
6. Leishman, J. G.; and Beddoes, T. S.: A Semi-Empirical Model for Dynamic Stall. *J. Amer. Heli. Soc.*, vol. 34, no. 3, July 1989, pp. 3–17.
7. Beddoes, T. S.: Two and Three Dimensional Indicial Methods for Rotor Dynamic Airloads. American Helicopter Society National Specialists Meeting, Arlington, Texas, Nov. 1989.
8. Beddoes, T. S.: A Near-Wake Dynamic Model. Proceedings of the AHS National Specialists Meeting on Aerodynamics and Acoustics, Feb. 1987.
9. Johnson, W.: Comparison of Three Methods for Calculation of Helicopter Rotor Blade Loading and Stresses Due to Stall. NASA TN D-7833, Nov. 1974.
10. Ham, N. D.; and Garelick, M. S.: Dynamic Stall Considerations in Helicopter Rotors. *J. Amer. Heli. Soc.*, vol. 13, no. 2, Apr. 1968.
11. Leishman, J. G.: A Two-Dimensional Model for Airfoil Unsteady Drag below Stall. *AIAA J. Aircraft*, vol. 25, no. 7, July 1988, pp. 665–666.
12. Leishman, J. G.; and Nguyen, K. Q.: State-Space Representation of Unsteady Airfoil Behavior. *AIAA J.*, vol. 28, no. 5, May 1990, pp. 836–844.
13. Leishman, J. G.: Indicial Lift Approximations for Two-Dimensional Subsonic Flow as Obtained from Oscillatory Measurements. *J. Aircraft*, vol. 30, no. 3, May–June 1993, pp. 340–351.
14. Costes, J. J.: Unsteady Three-Dimensional Stall on a Rectangular Wing. Twelfth European Rotorcraft Forum, Garmisch-Partenkirchen, Germany, Sept. 22–25, 1986.
15. Hixon, R.; Tsung, F.-L.; and Sankar, L. N.: A Comparison of Two Methods for Solving 3-D Unsteady Compressible Viscous Flows. AIAA Paper 93-0537, 31st Aerospace Sciences Meeting and Exhibit, Reno, Nev., Jan. 11–14, 1993.
16. Srinivasan, G. R.; and Ekaterinaris, J. A.: Dynamic Stall of an Oscillating Wing, Part 1: Evaluation of Turbulence Models. AIAA 11th Applied Aerodynamics Conference, Monterey, Calif., Aug. 1993.
17. Srinivasan, G. R.; and Baeder, J. D.: RNS: A Free-Wake Euler/Navier-Stokes Numerical Method for Helicopter Rotors. *AIAA J.*, vol. 31, no. 5, May 1993.

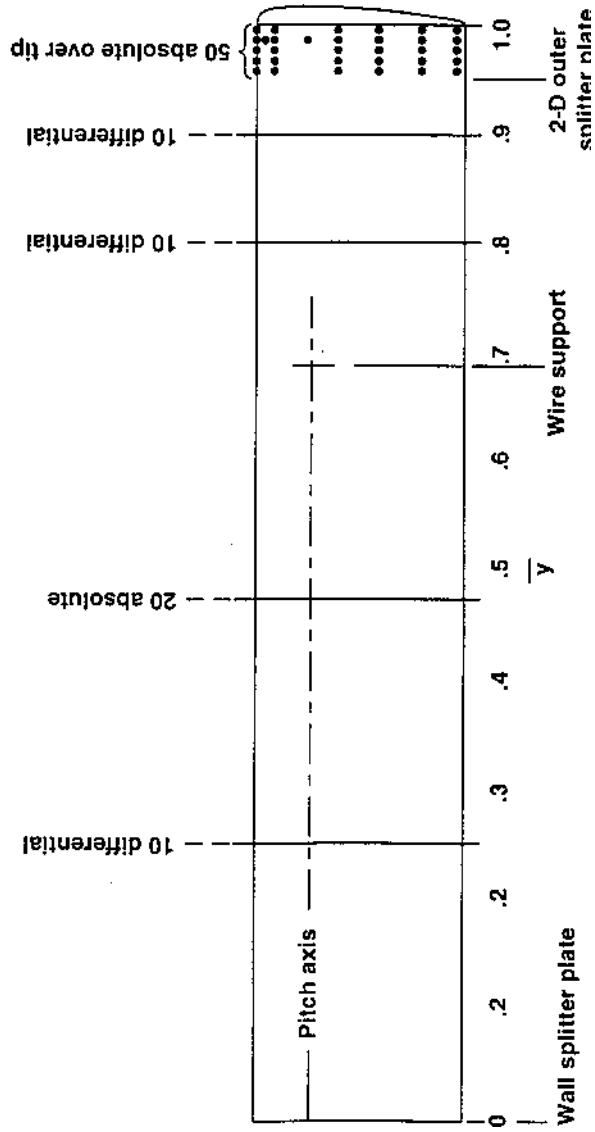
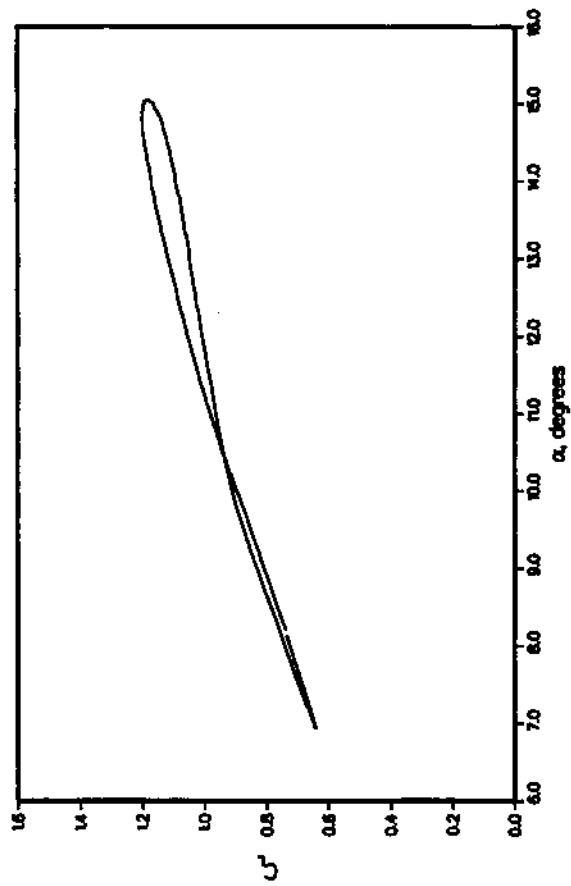


Figure 1. Diagram showing location of pressure transducers on 3-D wing used to obtain reference data (from ref. 3).

25% SPAN



47.5% SPAN

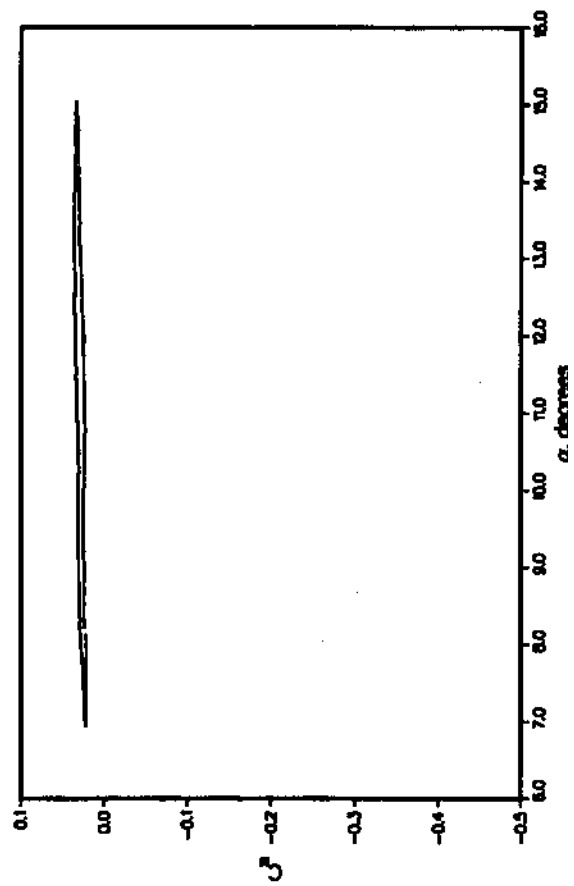
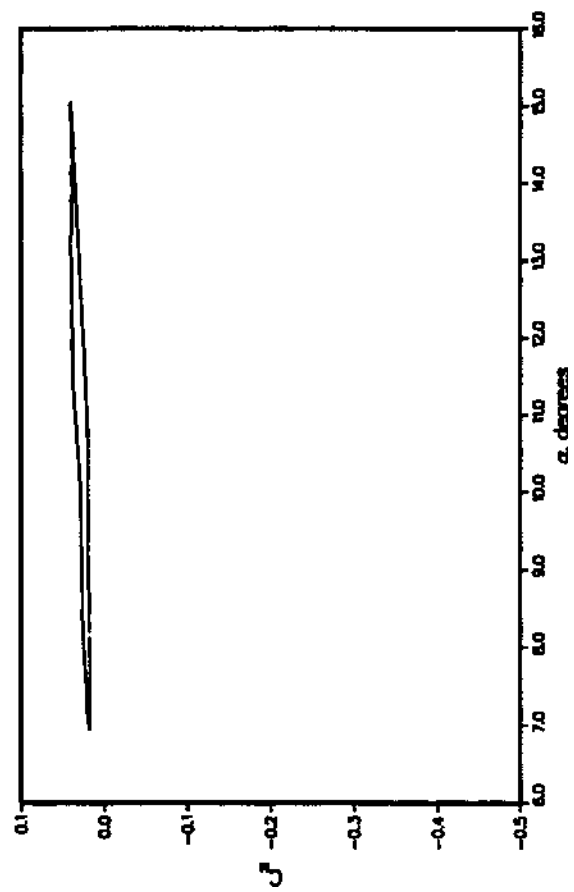
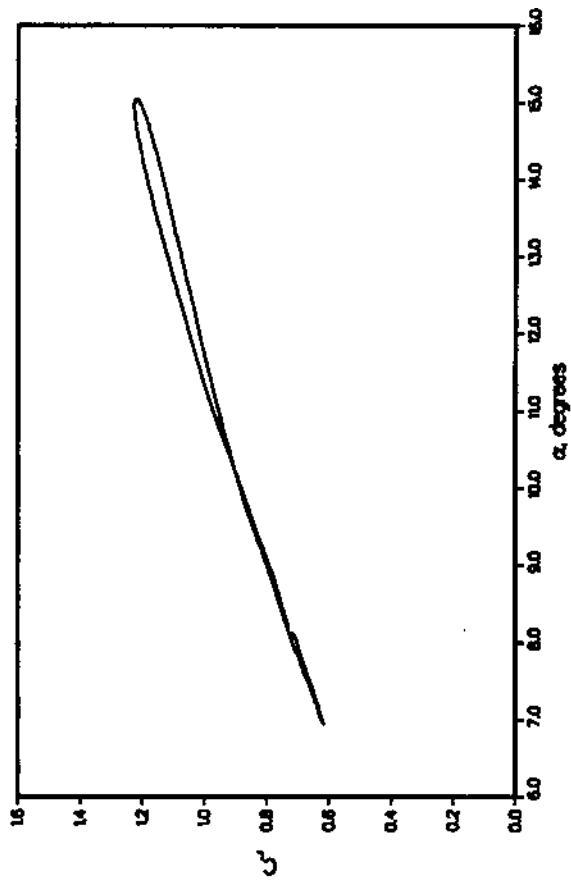
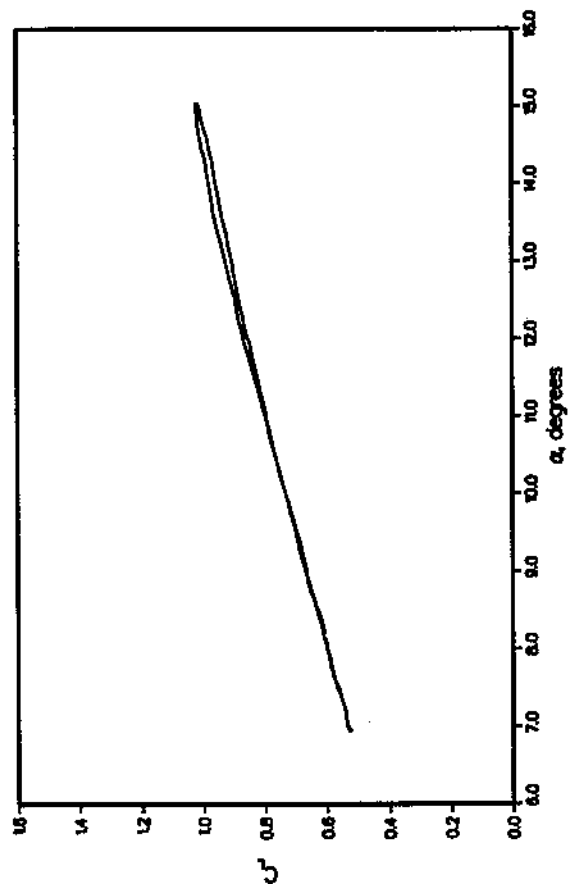


Figure 2(a). Lift and pitching-moment coefficients as a function of angle of attack, for 3-D wing experiencing dynamic stall at $M = 0.3$, $\alpha = 11^\circ + 4^\circ \sin \omega t$, $k = 0.04$ (from ref. 3).

80% SPAN



90% SPAN

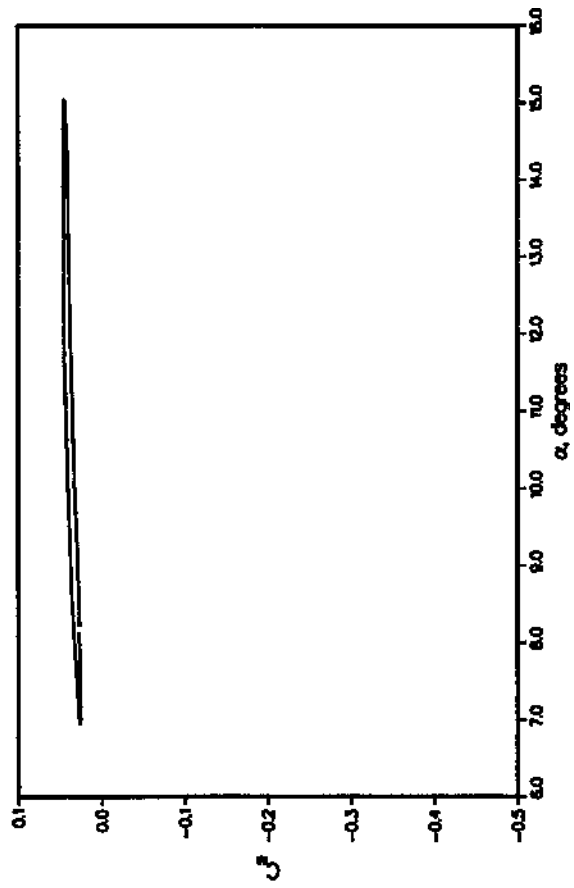
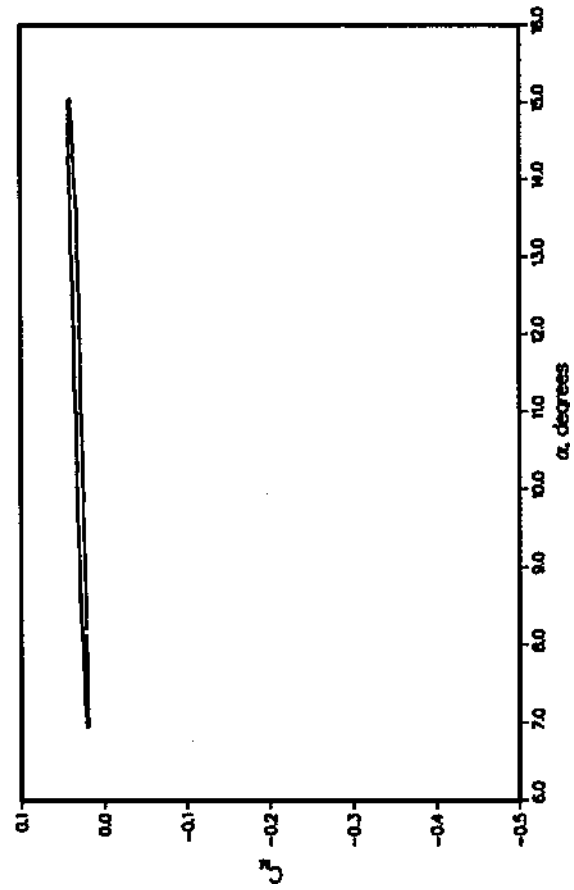
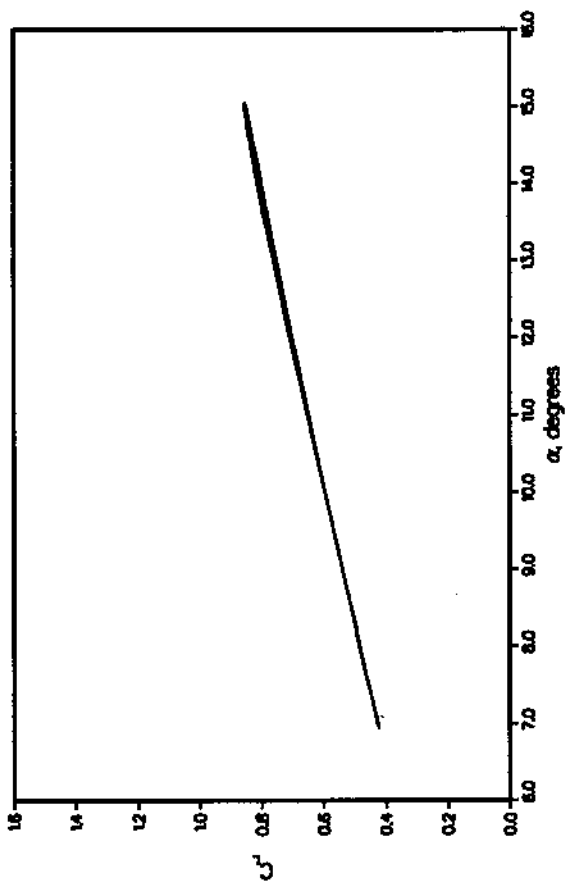
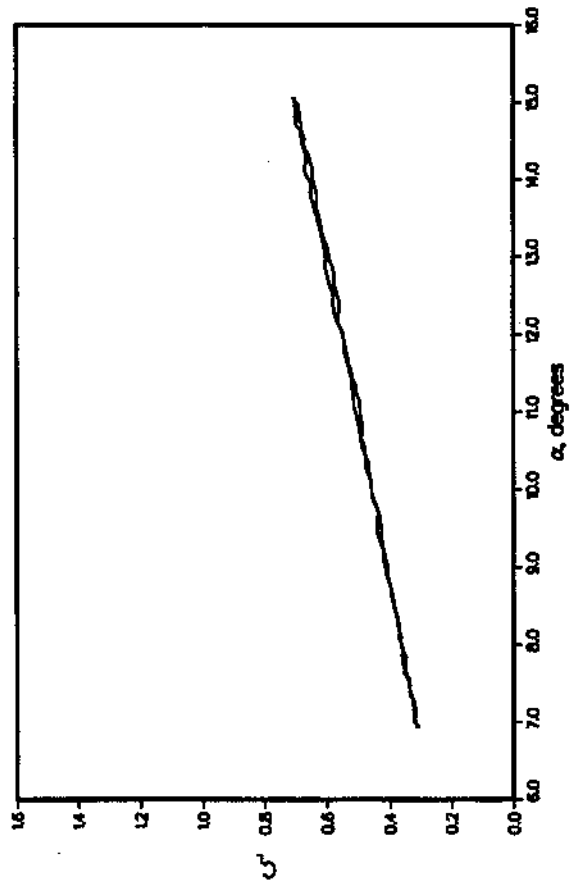


Figure 2(b). Lift and pitching-moment coefficients as a function of angle of attack, for 3-D wing experiencing dynamic stall at $M = 0.3$, $\alpha = 11^\circ + 4^\circ \sin \omega t$, $k = 0.04$ (from ref. 3).

96.6% SPAN



98.6% SPAN

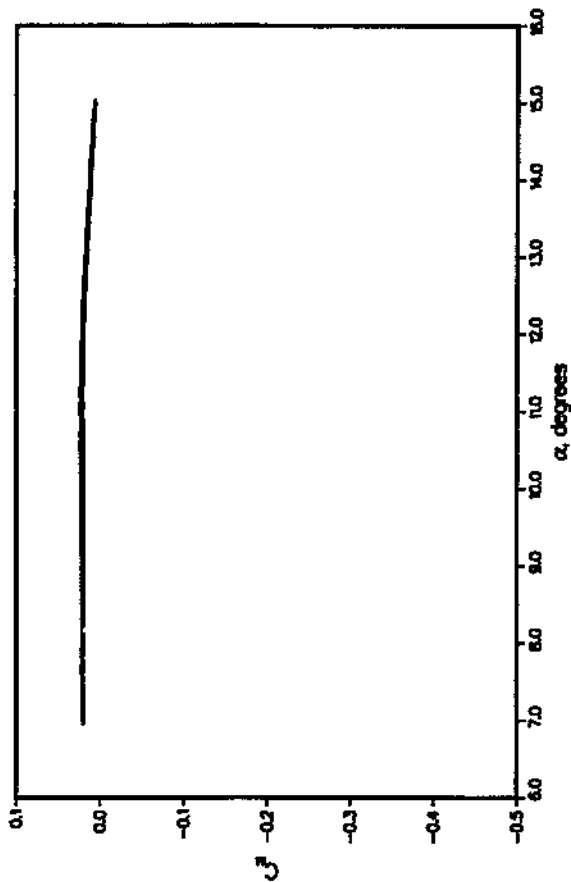
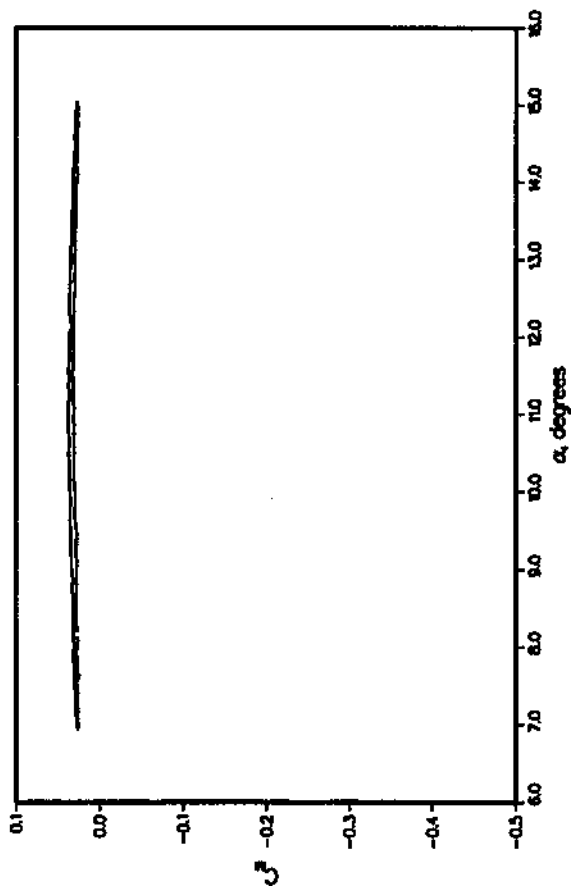
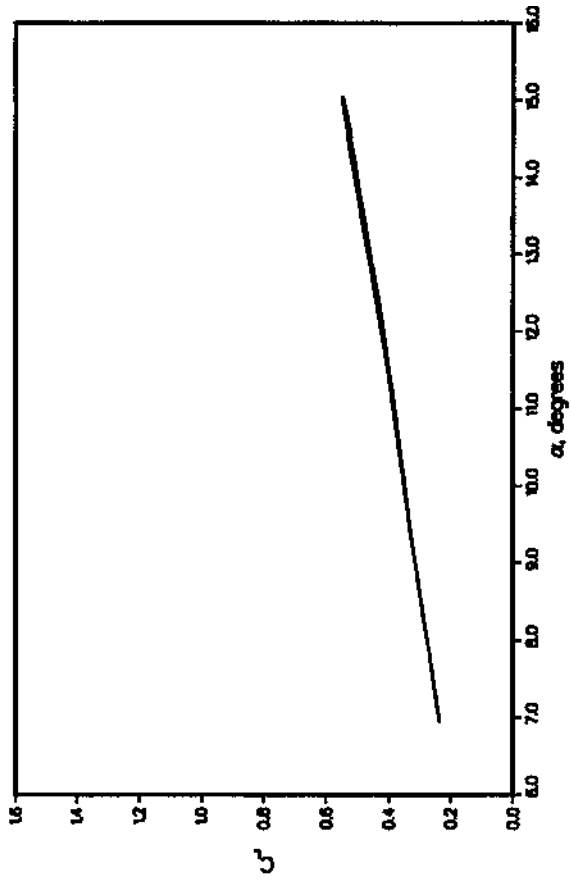


Figure 2(c). Lift and pitching-moment coefficients as a function of angle of attack, for 3-D wing experiencing dynamic stall at $M = 0.3$, $\alpha = 11^\circ + 4^\circ \sin \omega t$, $k = 0.04$ (from ref. 3).

99.5% SPAN

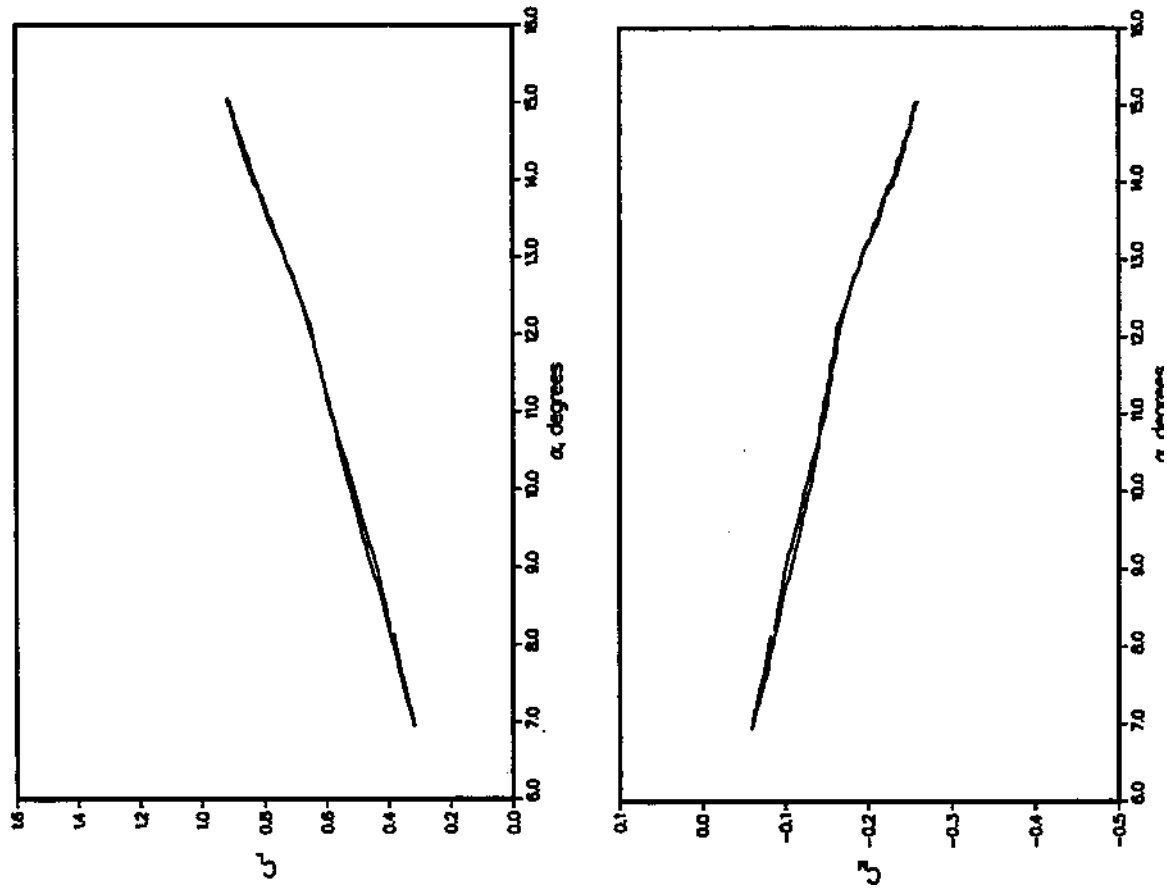
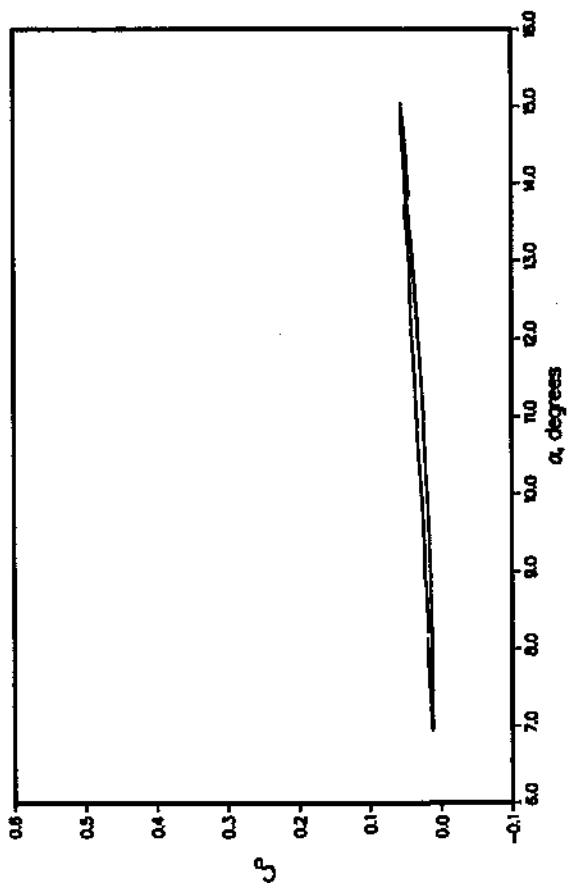
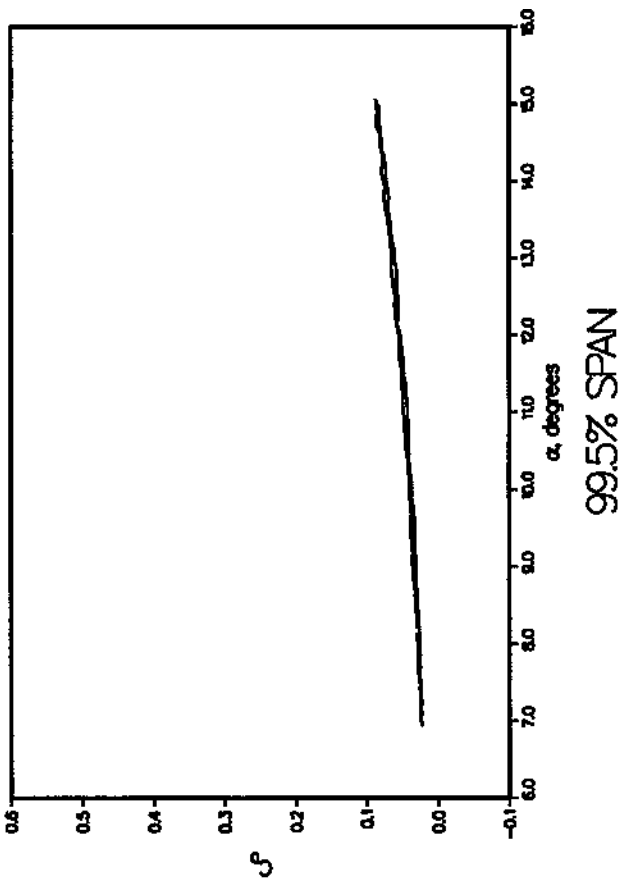


Figure 2(d). Lift and pitching-moment coefficients as a function of angle of attack, for 3-D wing experiencing dynamic stall at $M = 0.3$, $\alpha = 11^\circ + 4^\circ \sin \omega t$, $k = 0.04$ (from ref. 3).

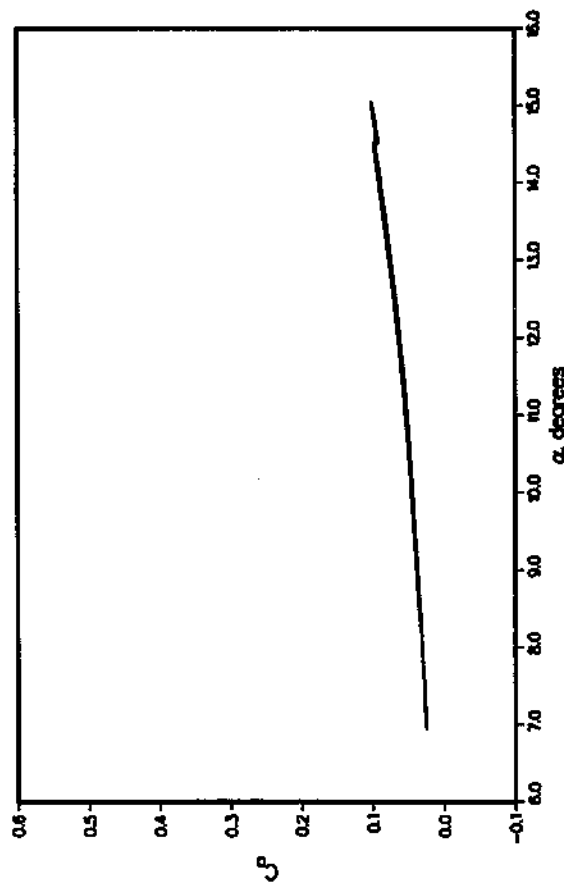
47.5% SPAN



96.6% SPAN



98.6% SPAN



99.5% SPAN

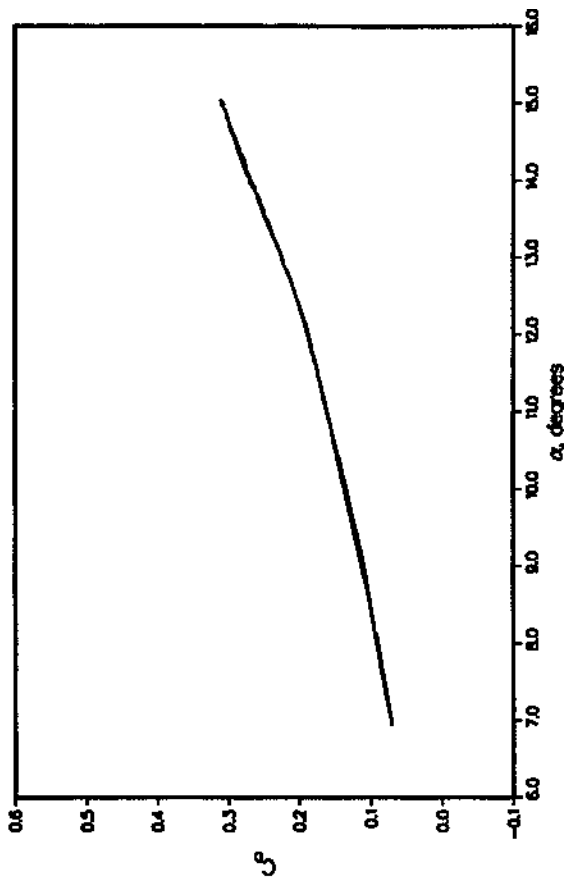
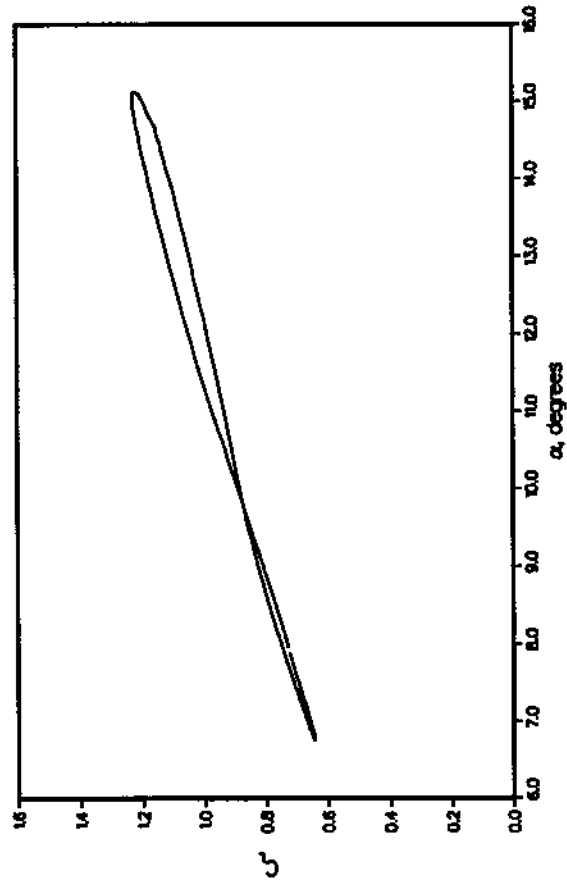


Figure 2(e). Drag coefficients as a function of angle of attack, for 3-D wing experiencing dynamic stall at $M = 0.3$, $\alpha = 11^\circ + 4^\circ \sin \omega t$, $k = 0.04$; drag at four spanwise stations (from ref. 3).

25% SPAN



47.5% SPAN

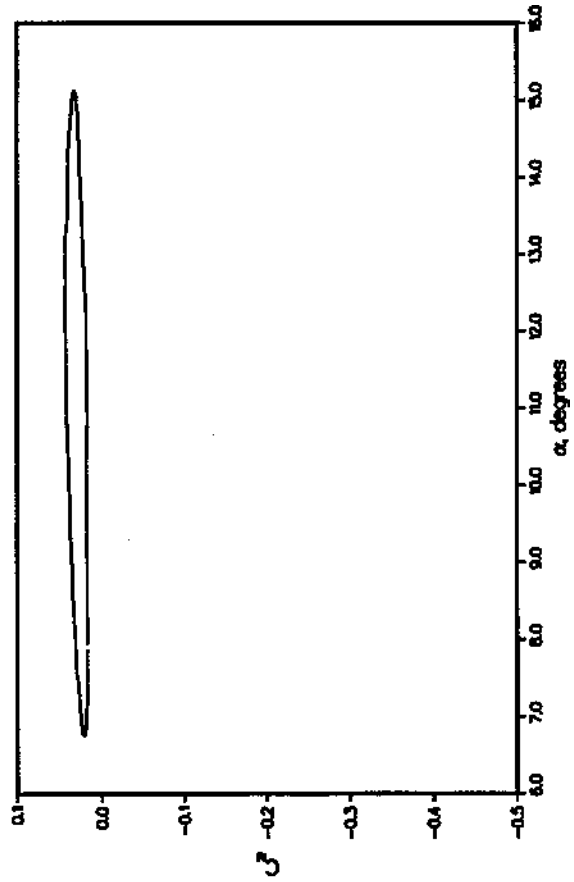
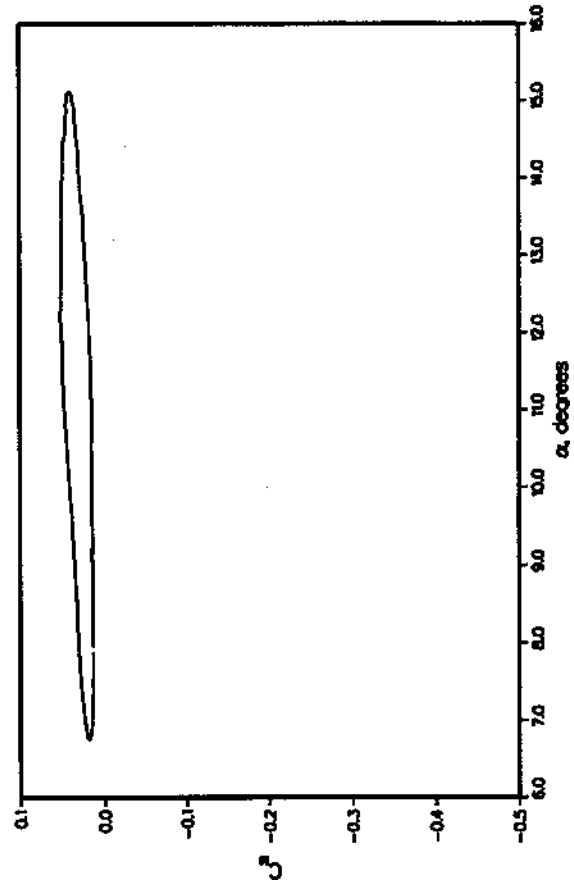
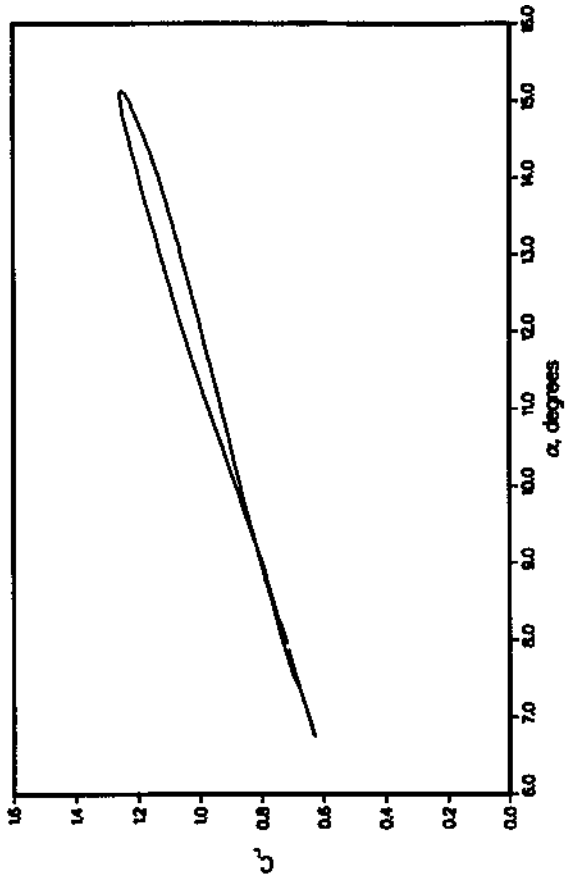
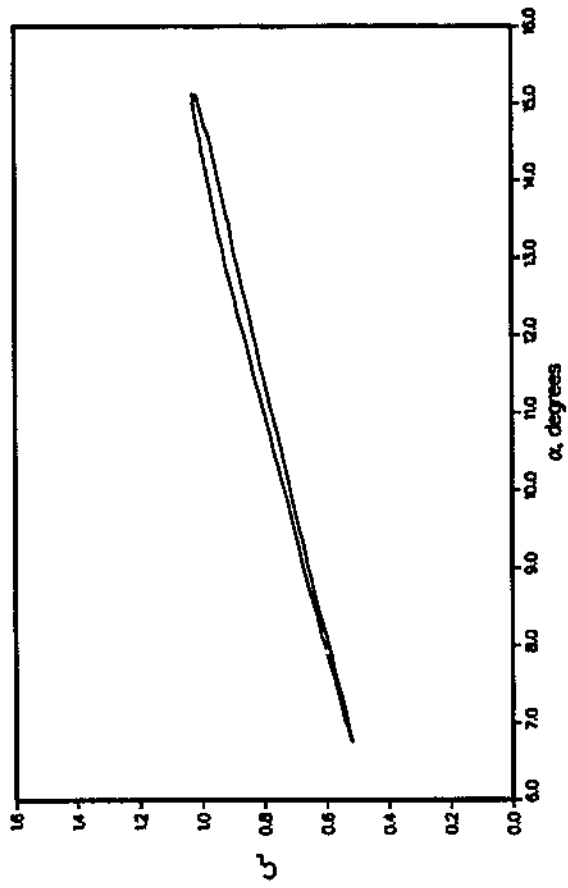


Figure 3(a). Lift and pitching-moment coefficients as a function of angle of attack, for 3-D wing experiencing dynamic stall at $M = 0.3$, $\alpha = 11^\circ + 4^\circ \sin \omega t$, $k = 0.10$ (from ref. 3).

80% SPAN



90% SPAN

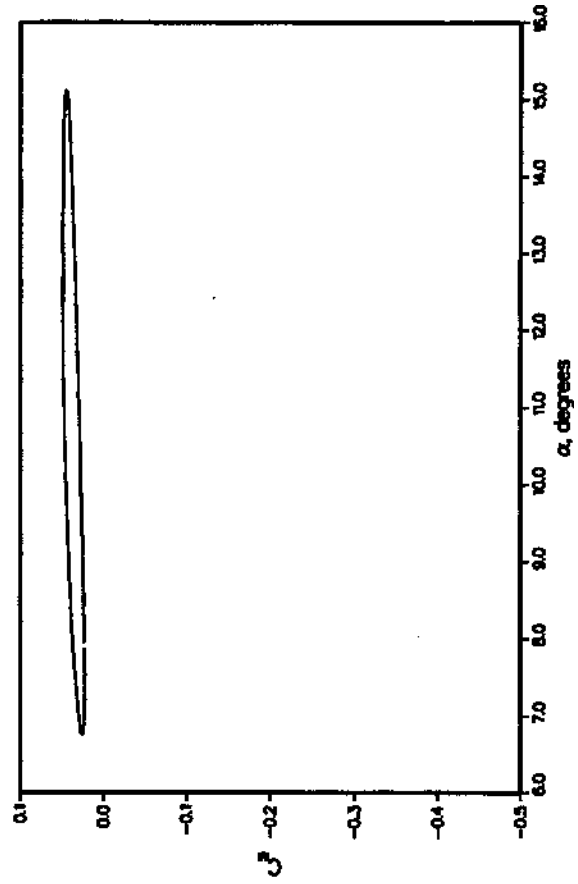
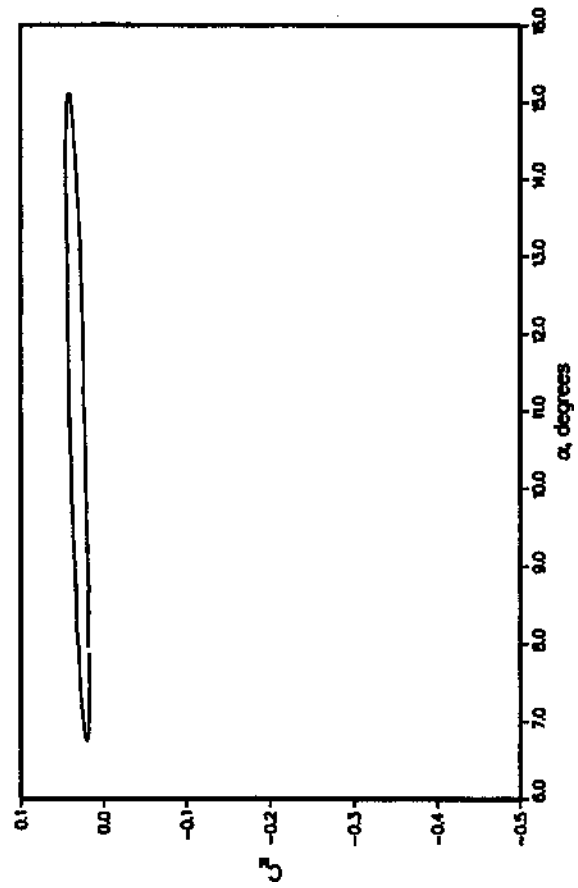
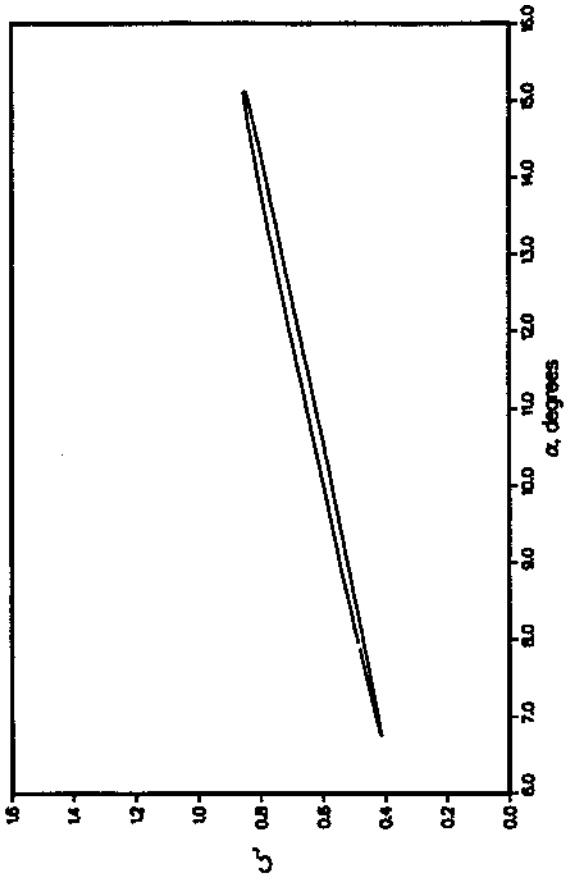
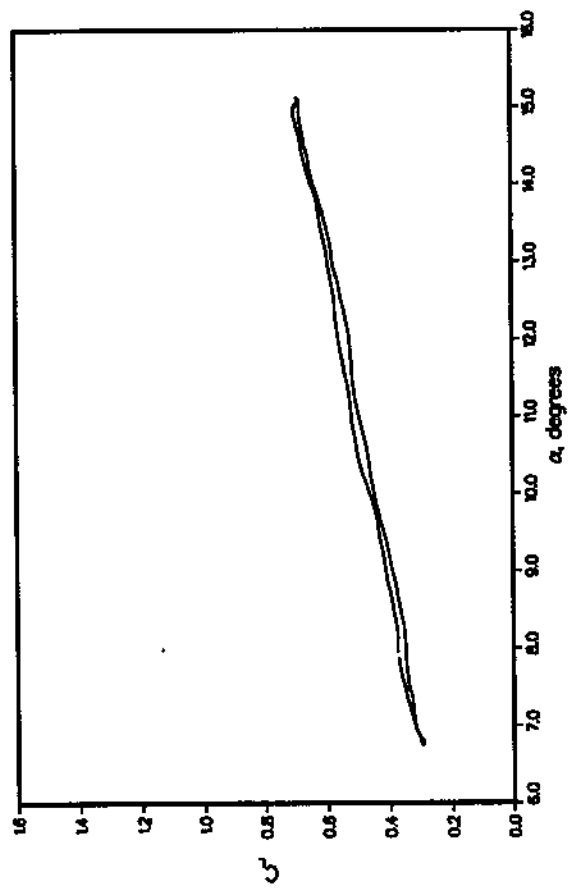


Figure 3(b). Lift and pitching-moment coefficients as a function of angle of attack, for 3-D wing experiencing dynamic stall at $M = 0.3$, $\alpha = 11^\circ + 4^\circ \sin \omega t$, $k = 0.10$ (from ref. 3).

96.6% SPAN



98.6% SPAN

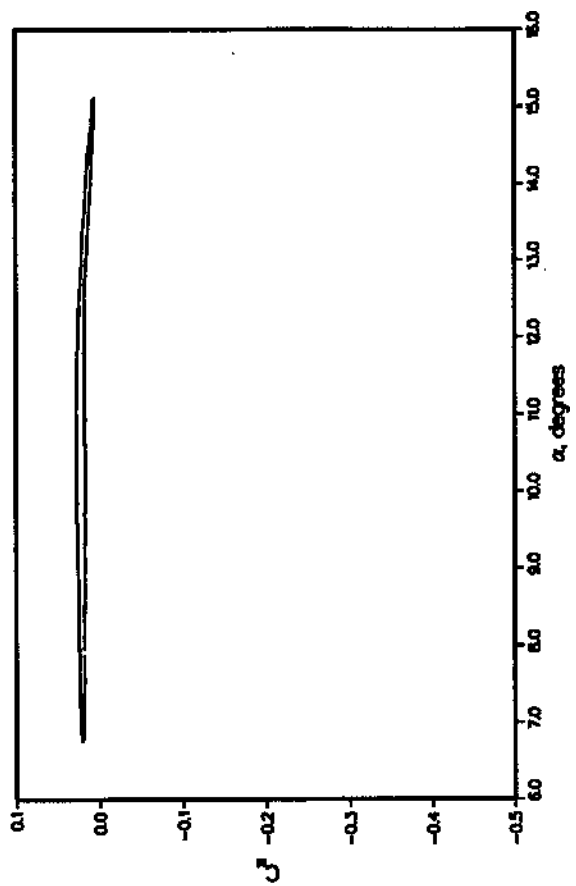
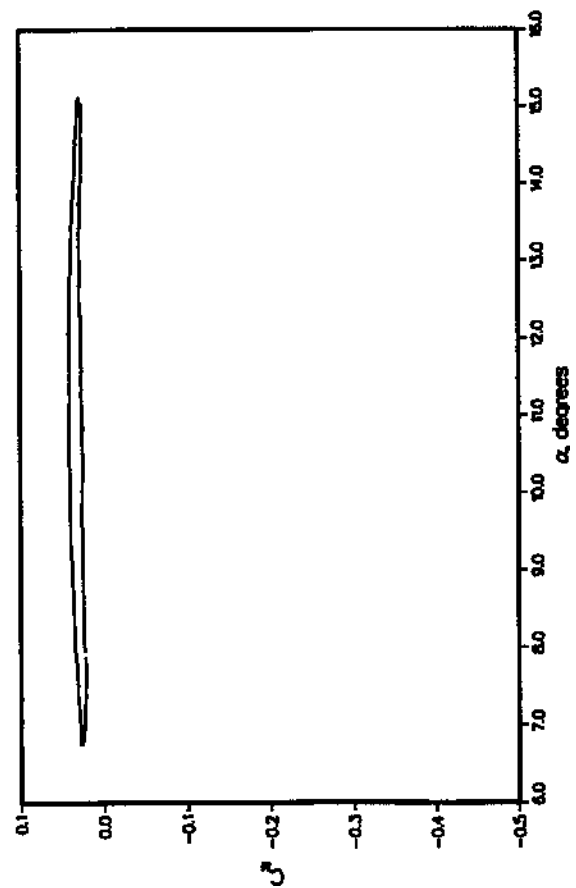
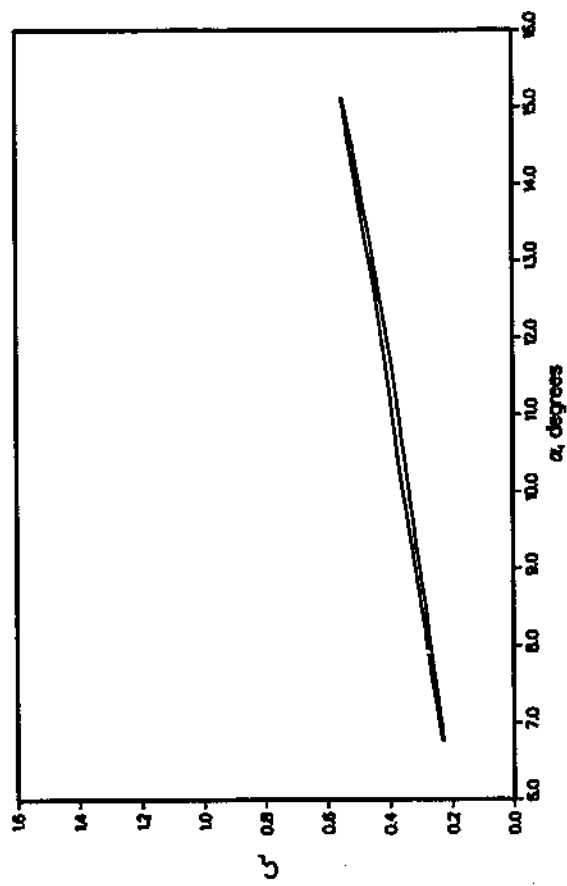


Figure 3(c). Lift and pitching-moment coefficients as a function of angle of attack, for 3-D wing experiencing dynamic stall at $M = 0.3$, $\alpha = 11^\circ + 4^\circ \sin \omega t$, $k = 0.10$ (from ref. 3).

99.5% SPAN

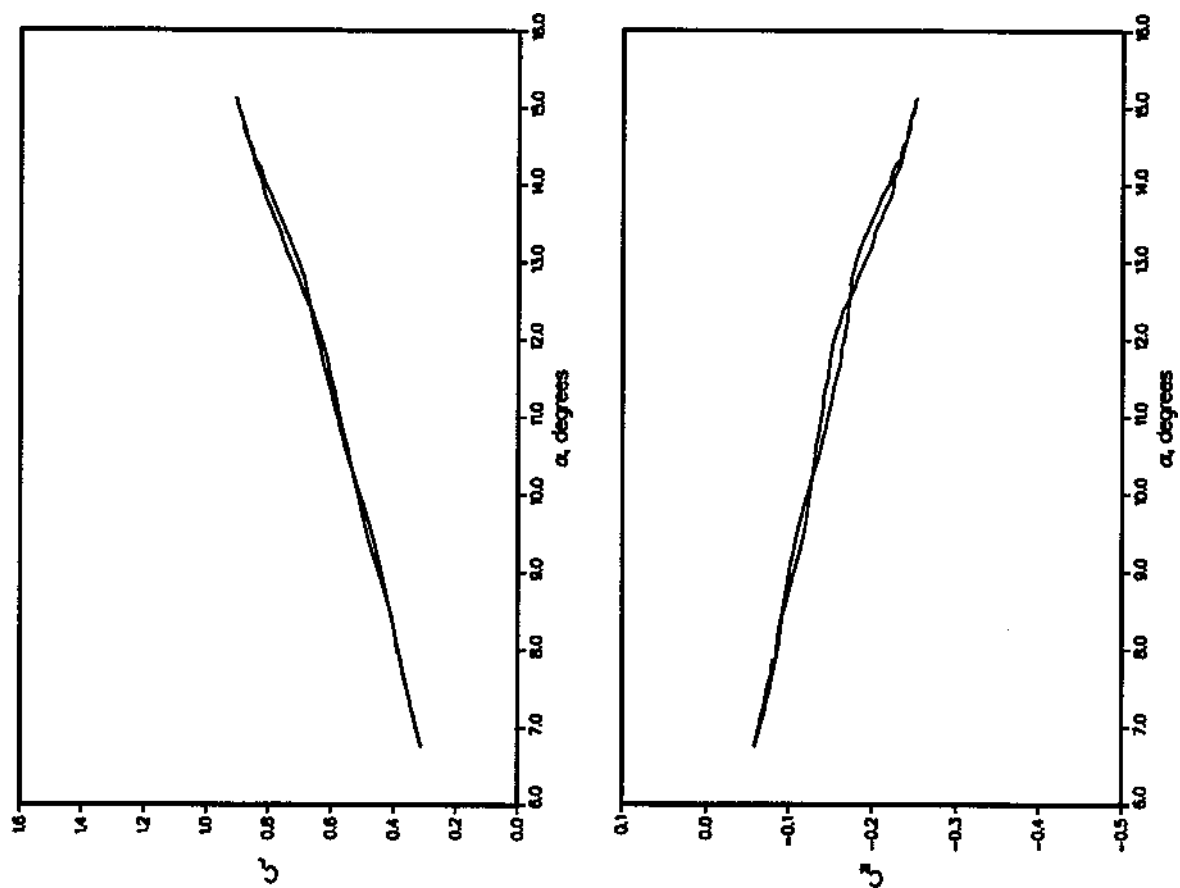
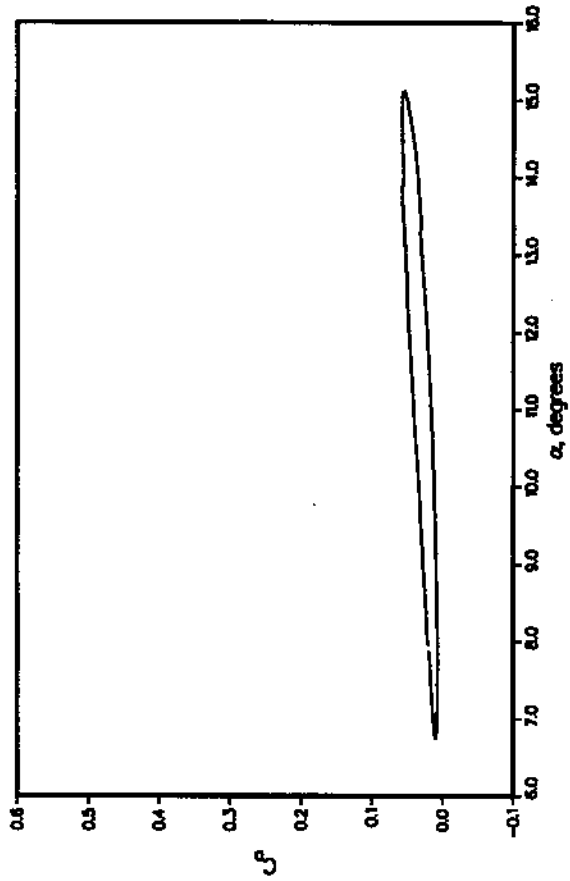
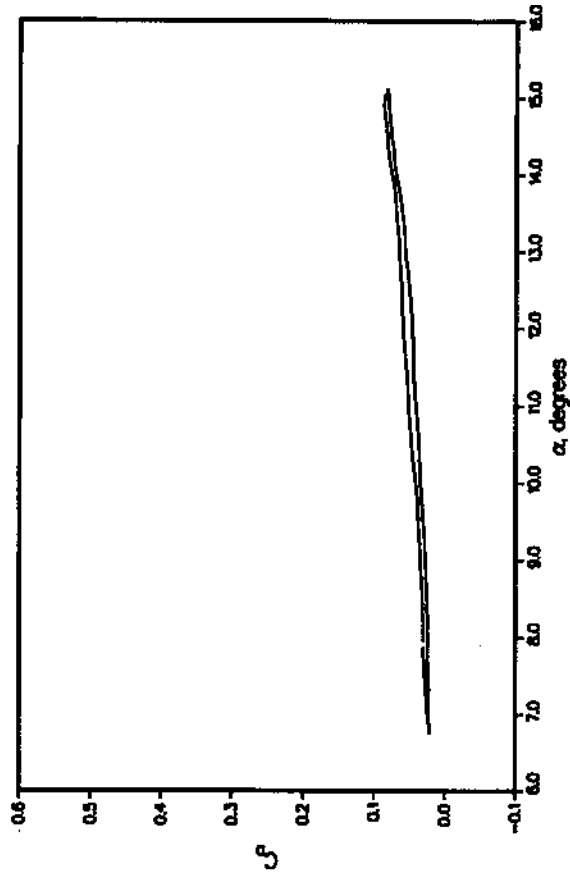


Figure 3(d). Lift and pitching-moment coefficients as a function of angle of attack, for 3-D wing experiencing dynamic stall at $M = 0.3$, $\alpha = 11^\circ + 4^\circ \sin \omega t$, $k = 0.10$ (from ref. 3).

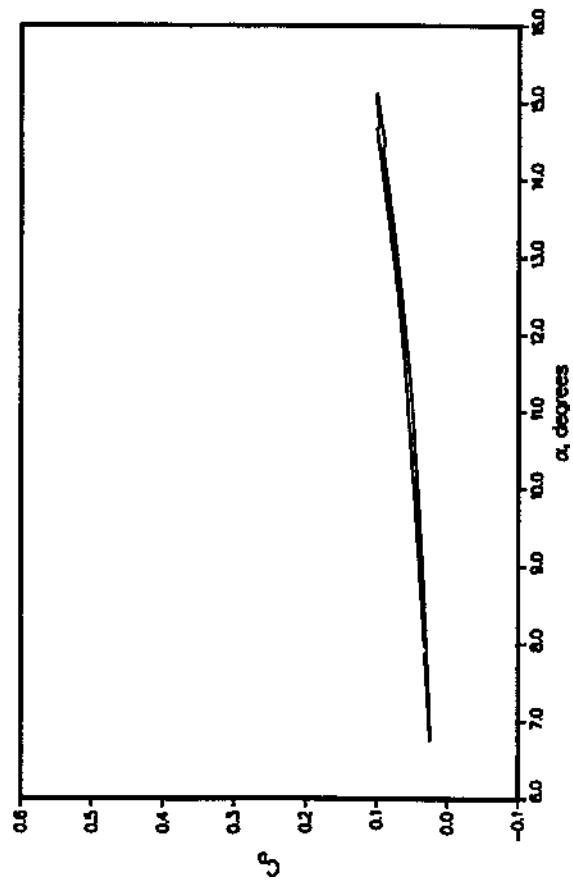
47.5% SPAN



96.6% SPAN



98.6% SPAN



99.5% SPAN

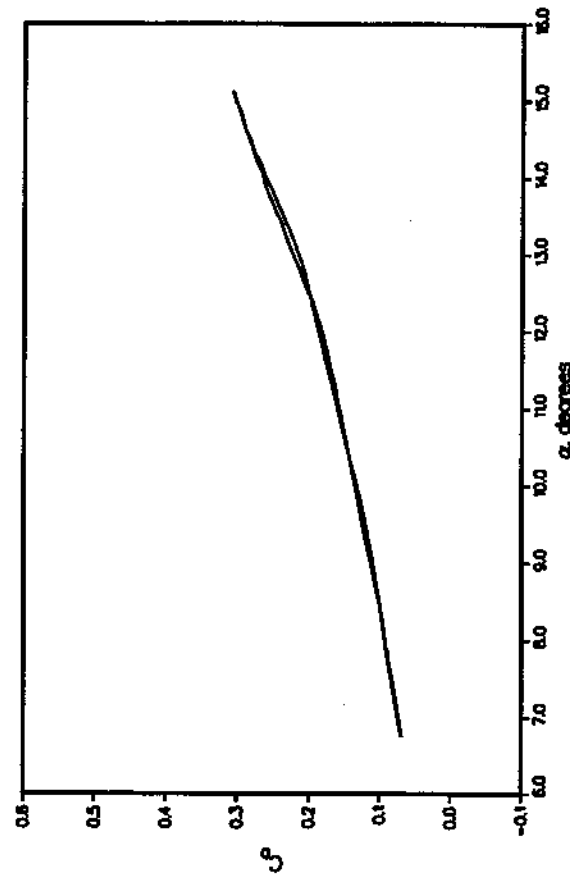
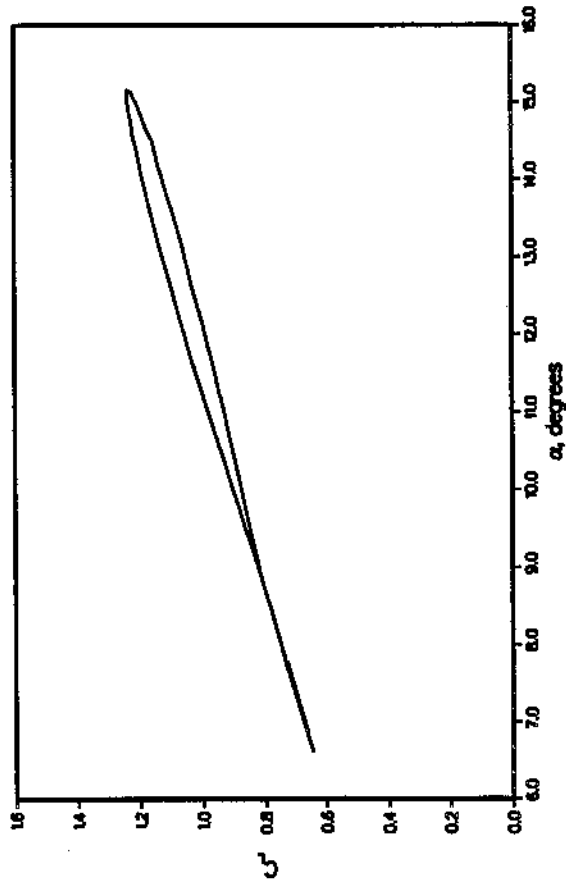


Figure 3(e). Drag coefficients as a function of angle of attack, for 3-D wing experiencing dynamic stall at $M = 0.3$, $\alpha = 11^\circ + 4^\circ \sin \omega t$, $k = 0.10$; drag at four spanwise stations (from ref. 3).

25% SPAN



47.5% SPAN

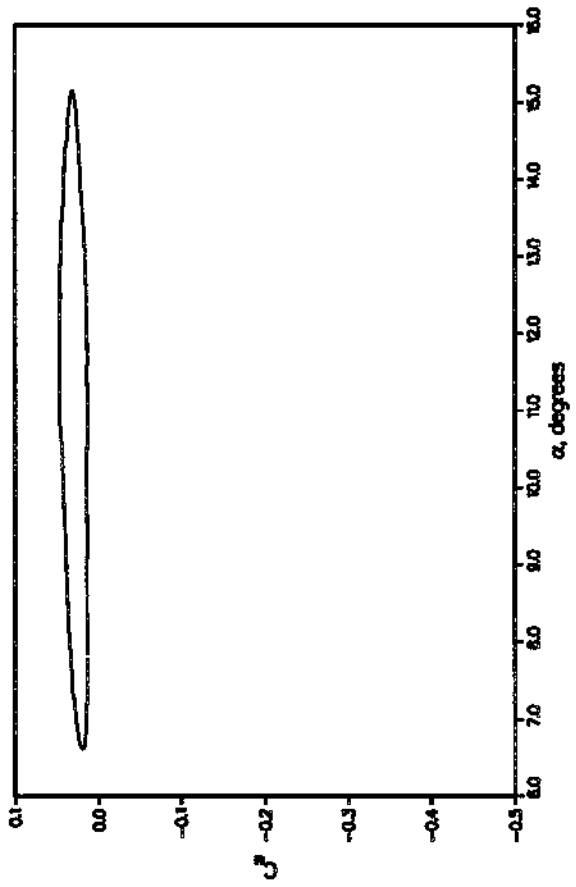
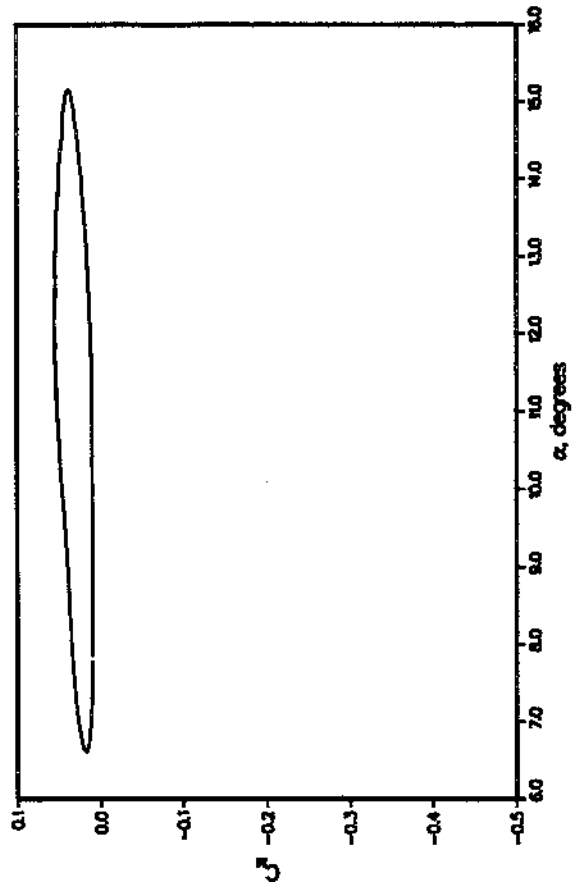
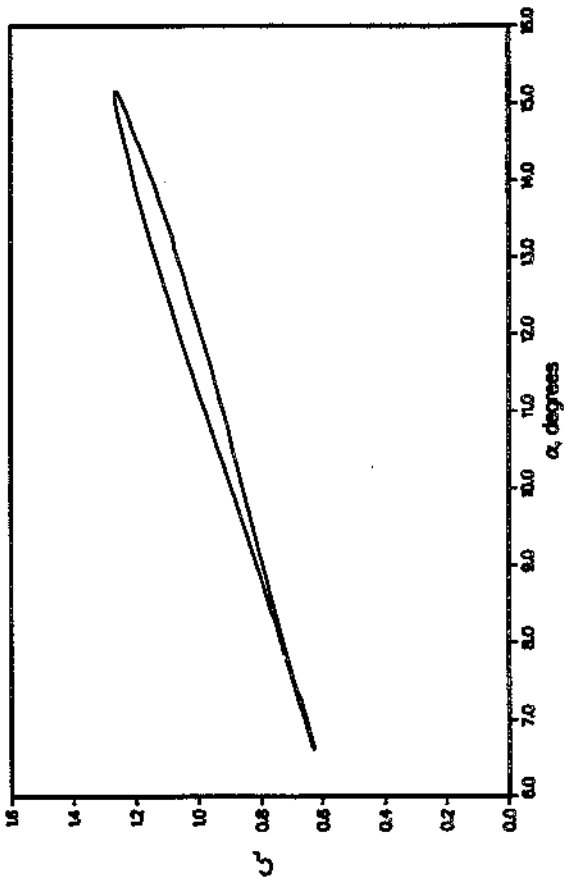
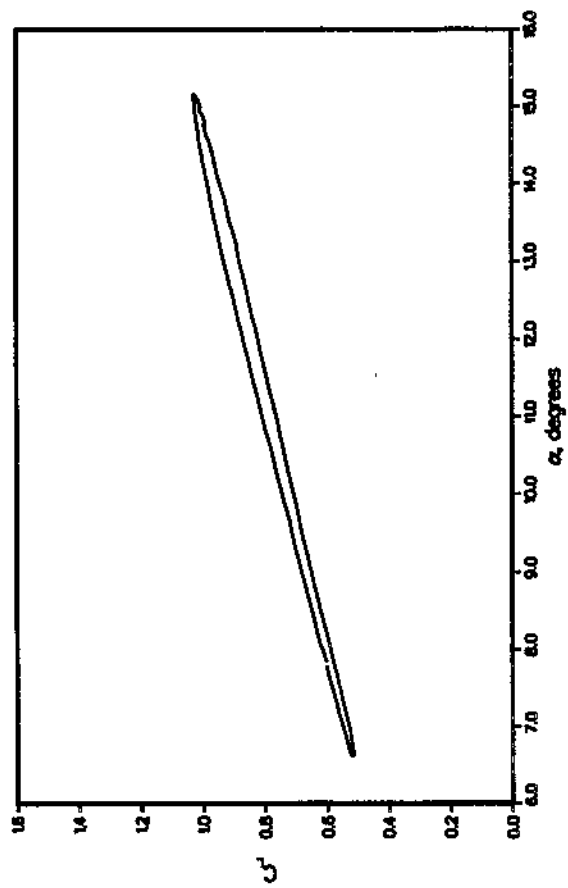


Figure 4(a). Lift and pitching-moment coefficients as a function of angle of attack, for 3-D wing experiencing dynamic stall at $M = 0.3$, $\alpha = 11^\circ + 4^\circ \sin \omega t$, $k = 0.14$ (from ref. 3).

80% SPAN



90% SPAN

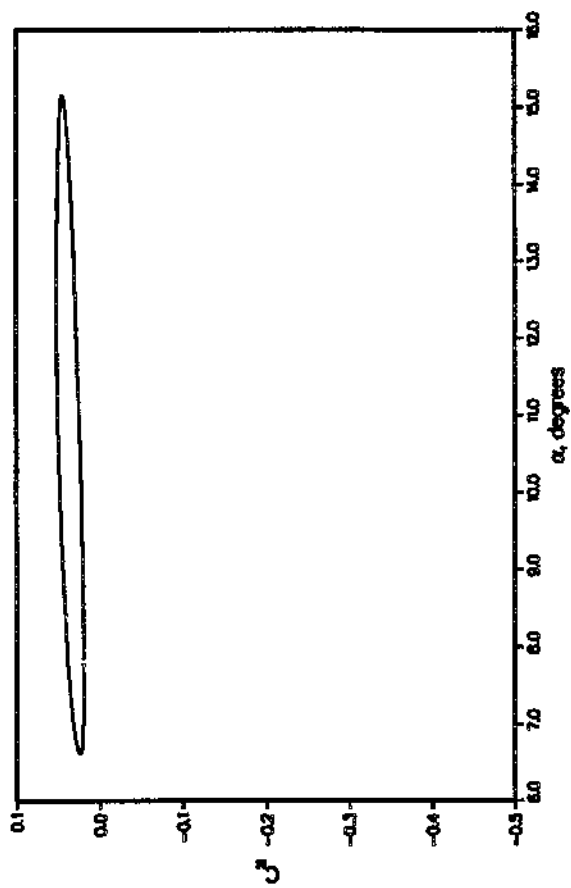
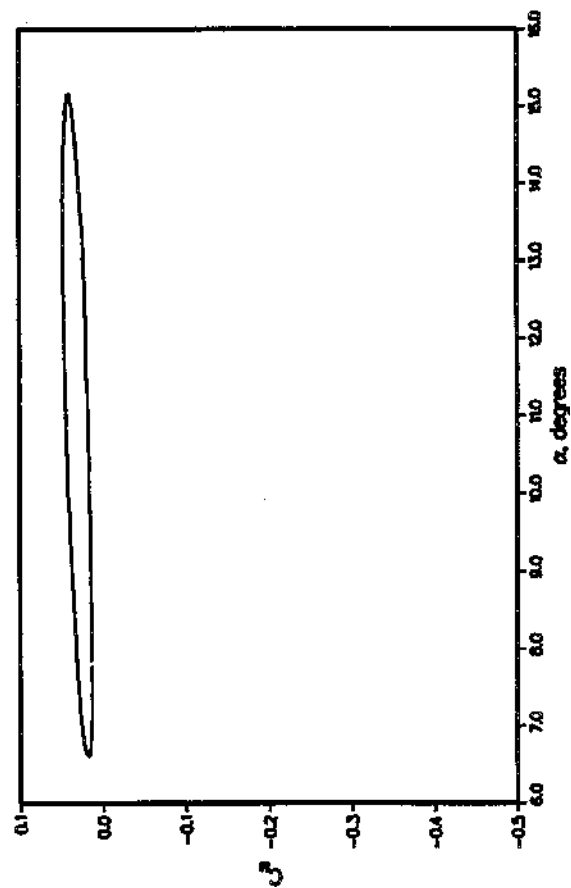
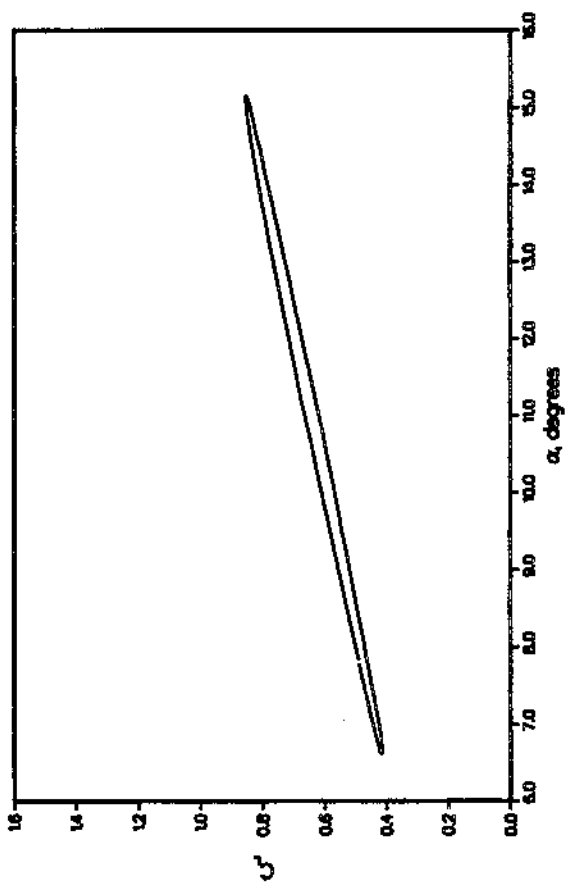
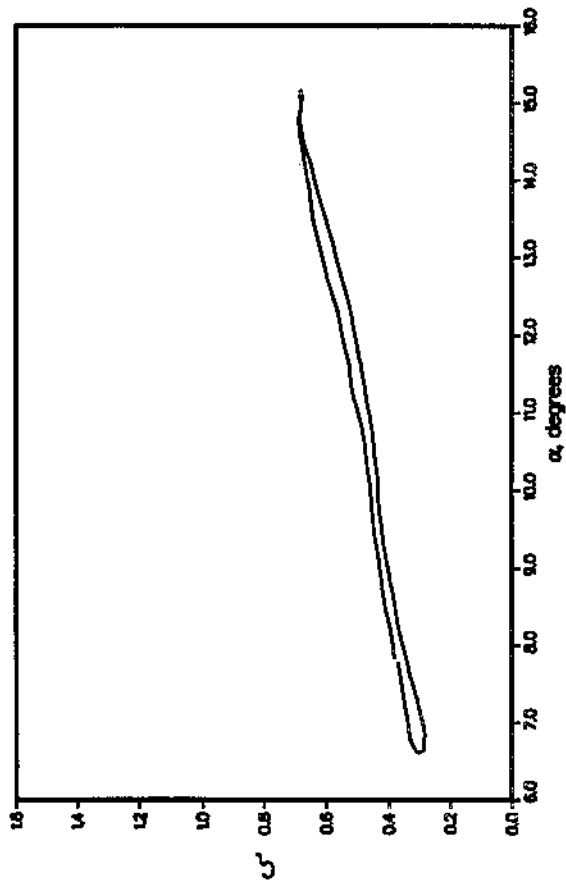


Figure 4(b). Lift and pitching-moment coefficients as a function of angle of attack, for 3-D wing experiencing dynamic stall at $M = 0.3$, $\alpha = 11^\circ + 4^\circ \sin \omega t$, $k = 0.14$ (from ref. 3).

96.6% SPAN



98.6% SPAN

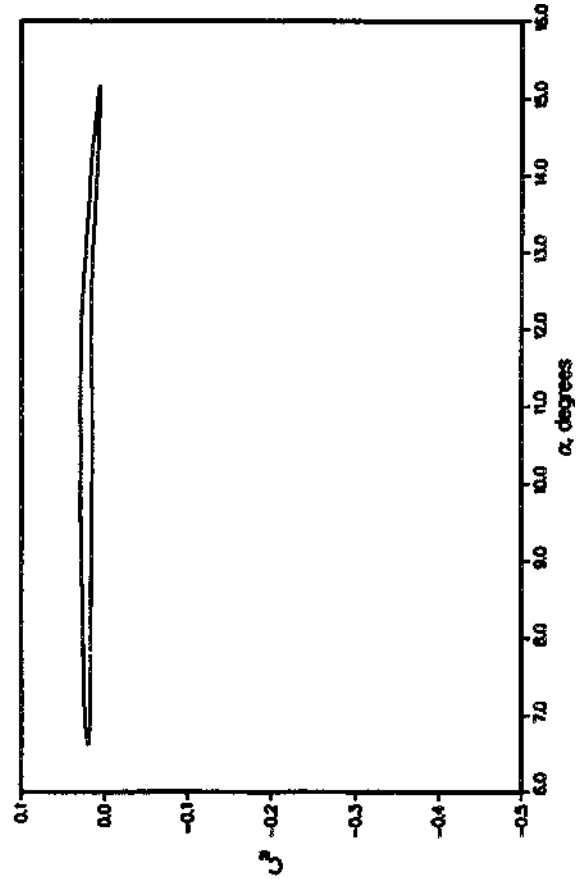
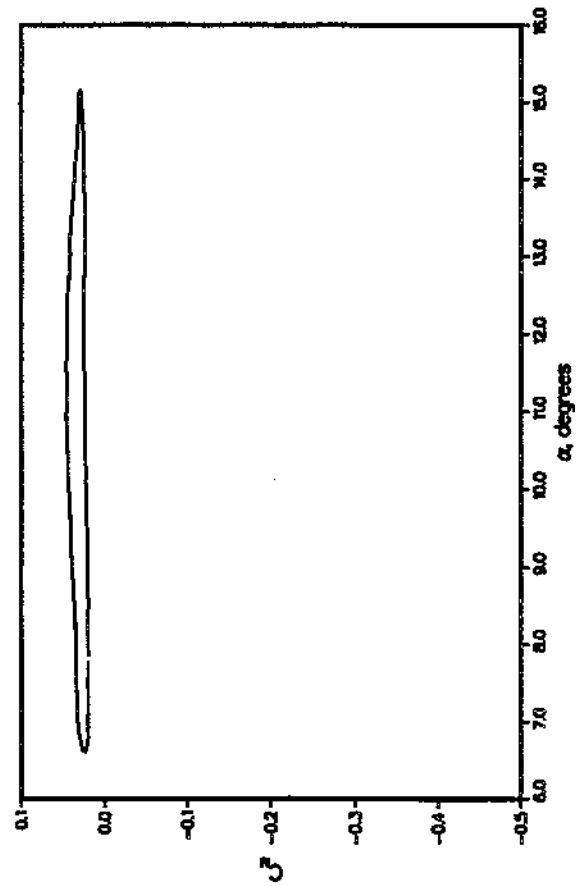
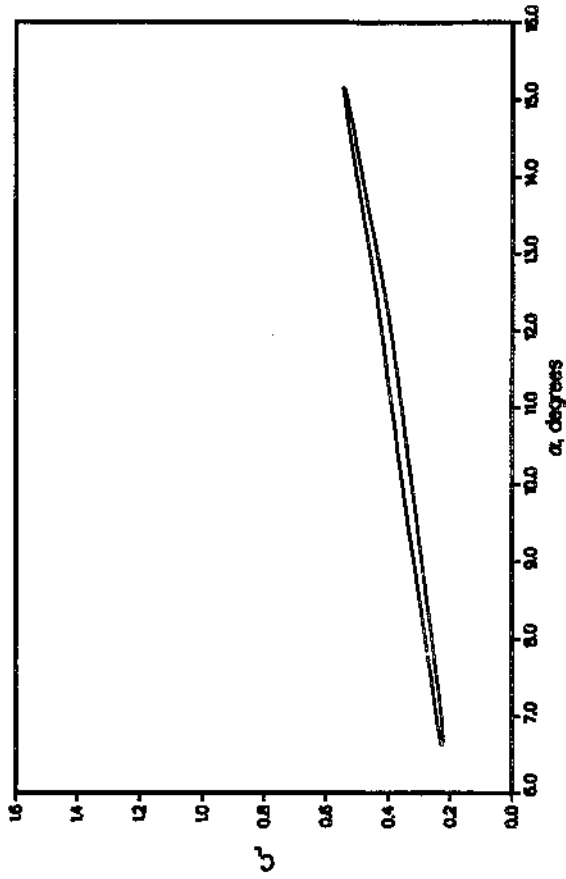


Figure 4(c). Lift and pitching-moment coefficients as a function of angle of attack, for 3-D wing experiencing dynamic stall at $M = 0.3$, $\alpha = 11^\circ + 4^\circ \sin \omega t$, $k = 0.14$ (from ref. 3).

99.5% SPAN

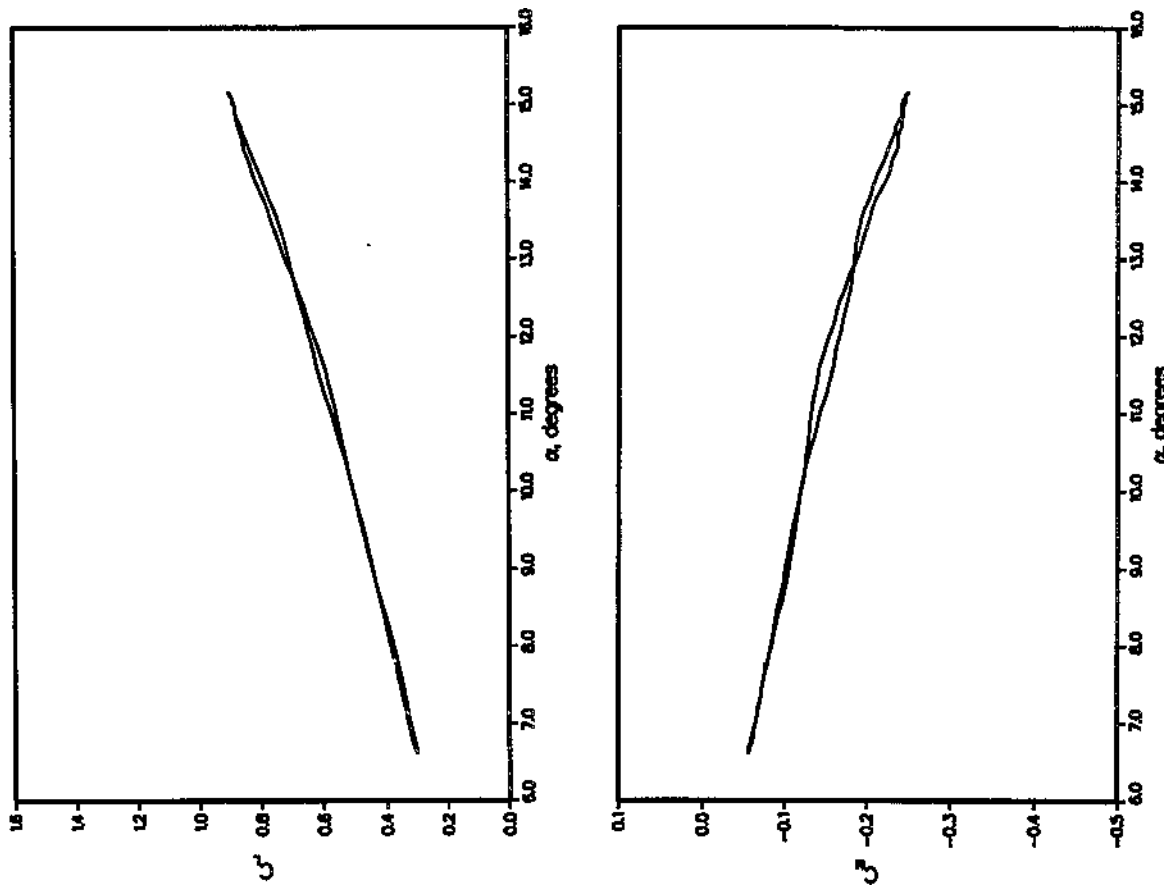
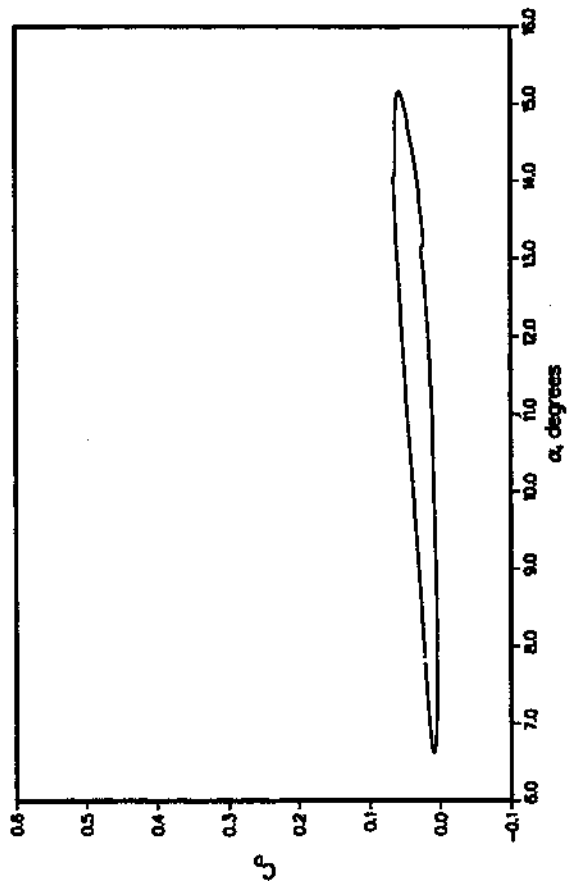
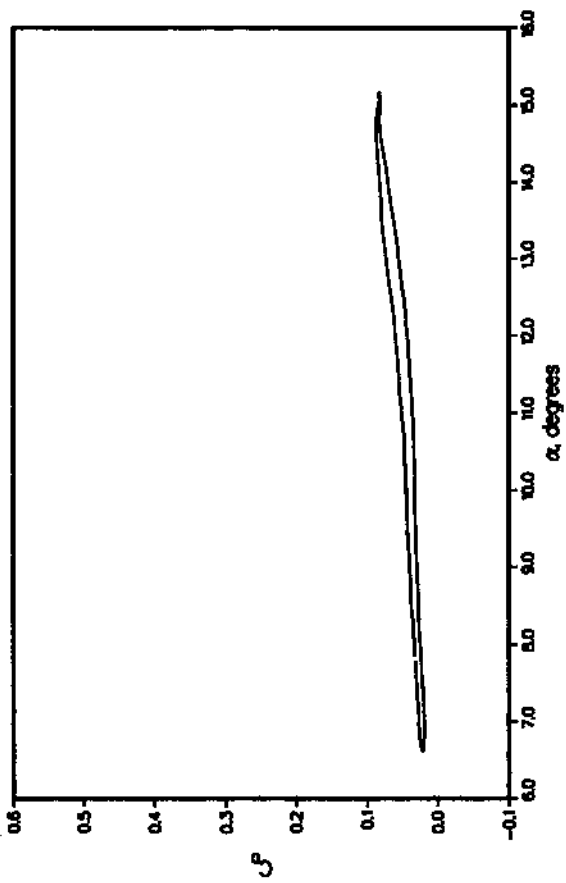


Figure 4(d). Lift and pitching-moment coefficients as a function of angle of attack, for 3-D wing experiencing dynamic stall at $M = 0.3$, $\alpha = 11^\circ + 4^\circ \sin \omega t$, $k = 0.14$ (from ref. 3).

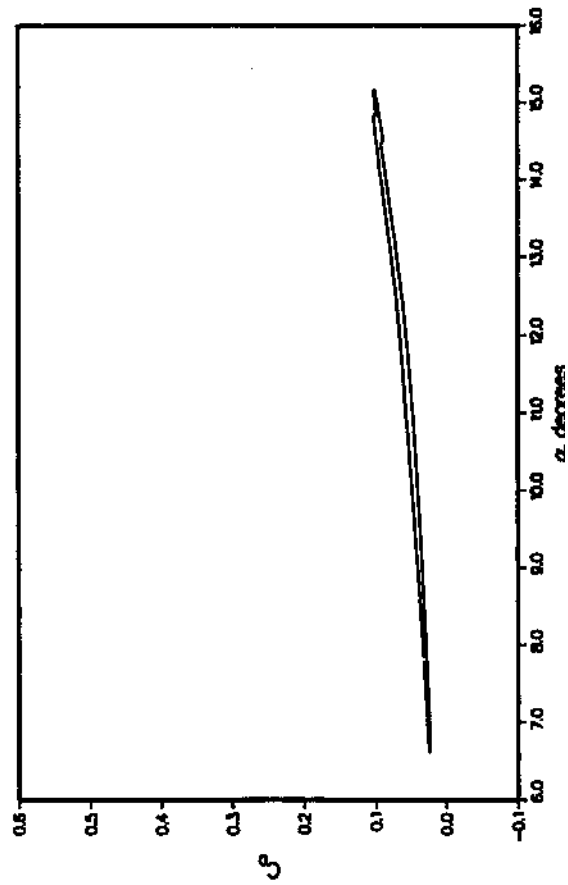
47.5% SPAN



96.6% SPAN



98.6% SPAN



99.5% SPAN

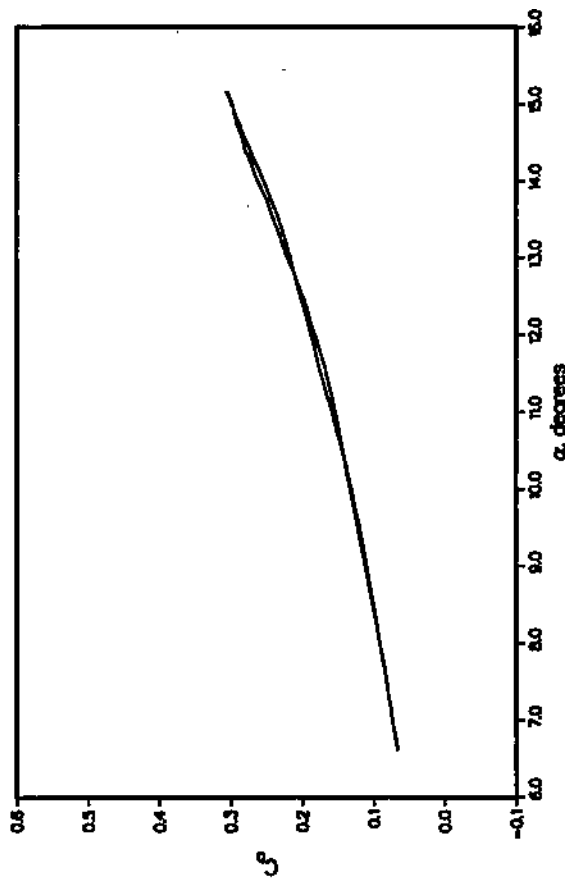
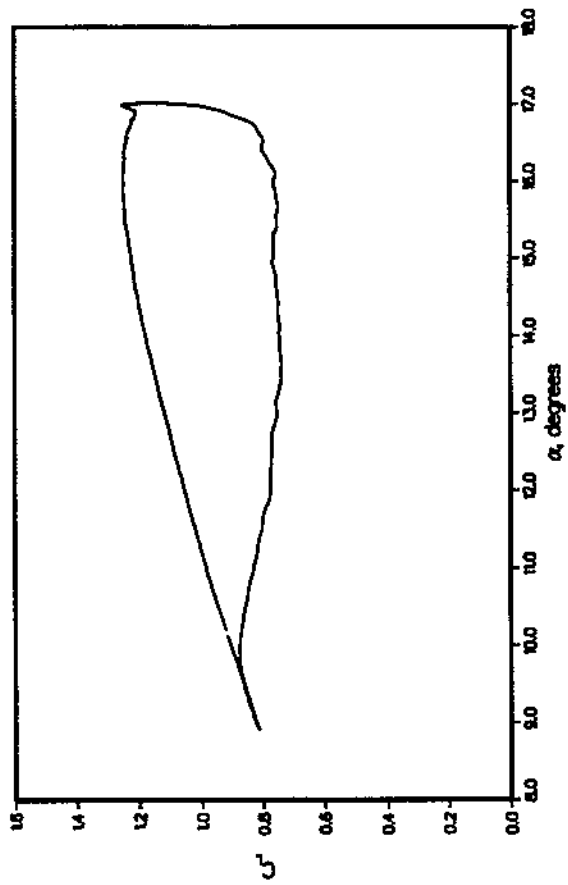


Figure 4(e). Drag coefficients as a function of angle of attack, for 3-D wing experiencing dynamic stall at $M = 0.3$, $\alpha = 11^\circ + 4^\circ \sin \omega t$, $k = 0.14$; drag at four spanwise stations (from ref. 3).

25% SPAN



47.5% SPAN

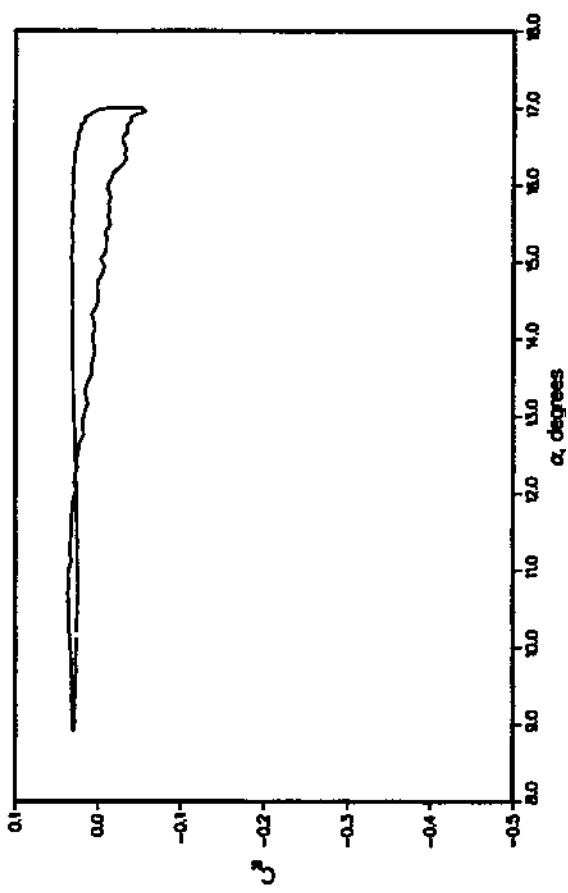
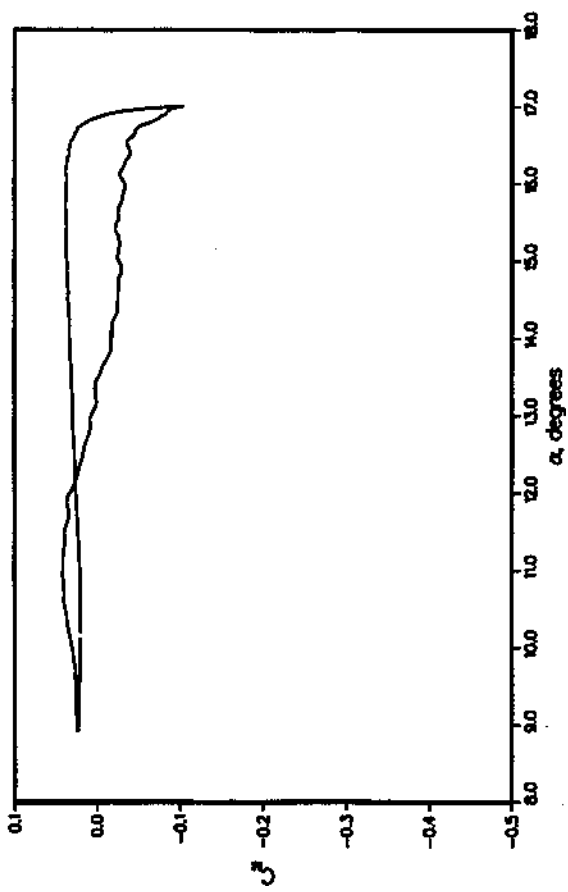
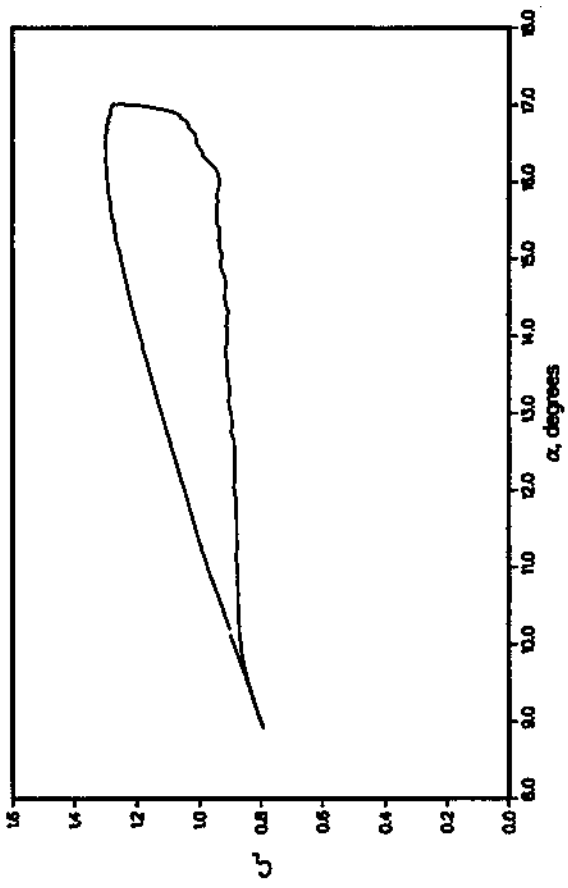
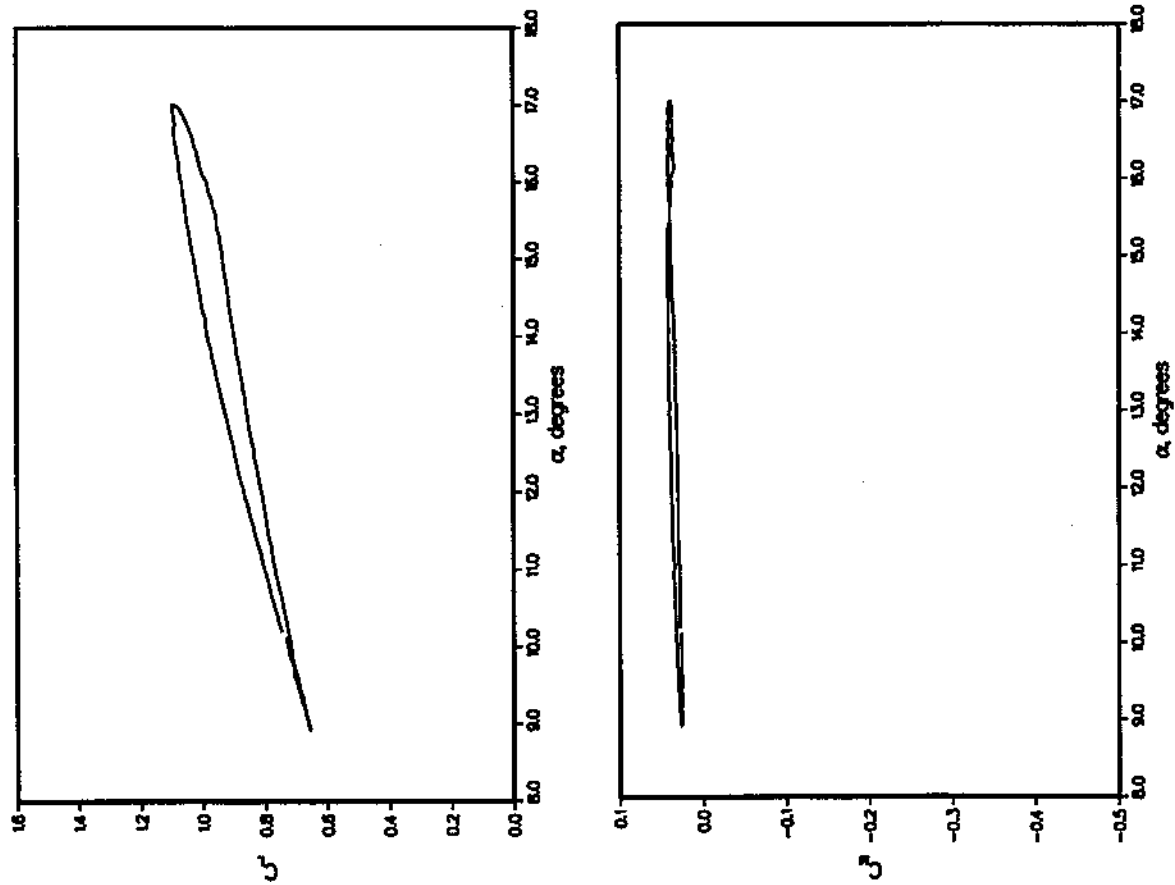


Figure 5(a). Lift and pitching-moment coefficients as a function of angle of attack, for 3-D wing experiencing dynamic stall at $M = 0.3$, $\alpha = 13^\circ + 4^\circ \sin \omega t$, $k = 0.04$ (from ref. 3).

80% SPAN



90% SPAN

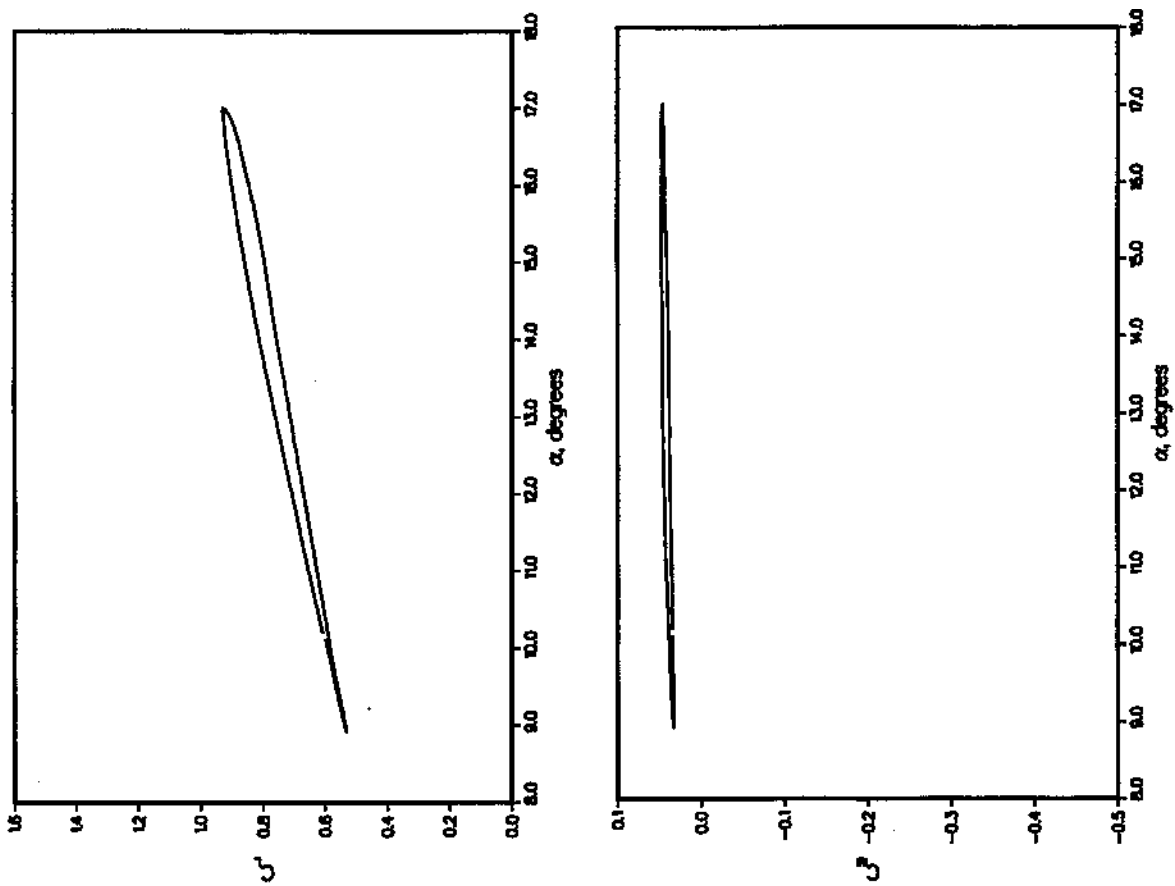
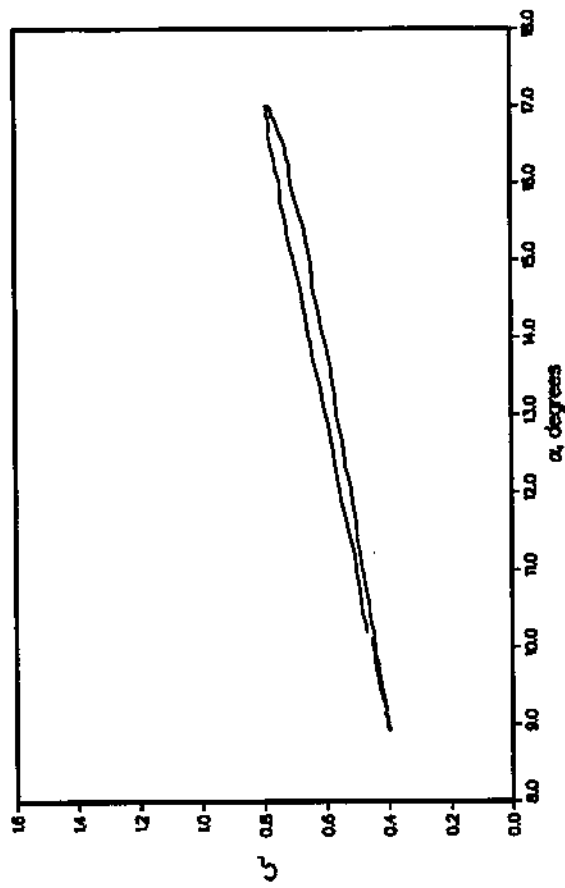


Figure 5(b). Lift and pitching-moment coefficients as a function of angle of attack, for 3-D wing experiencing dynamic stall at $M = 0.3$, $\alpha = 13^\circ + 4^\circ \sin \omega t$, $k = 0.04$ (from ref. 3).

96.6% SPAN



98.6% SPAN

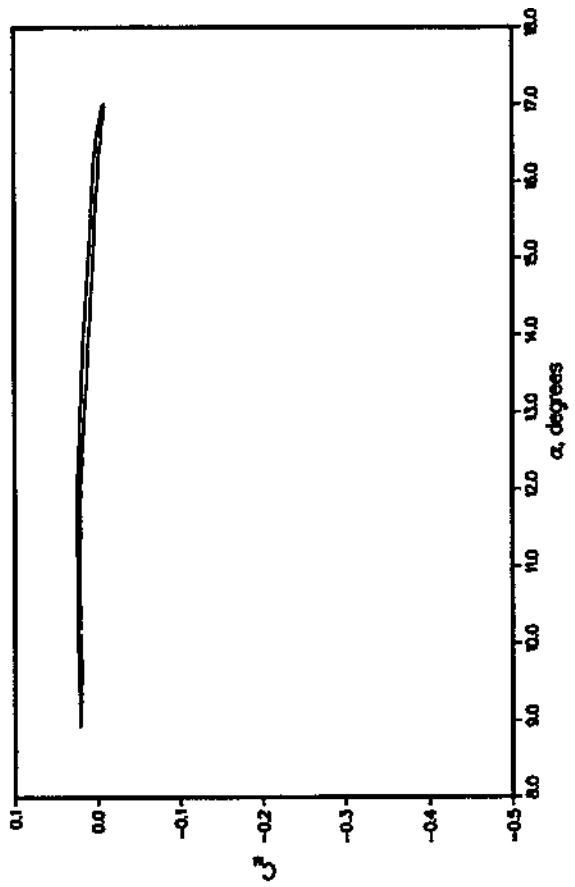
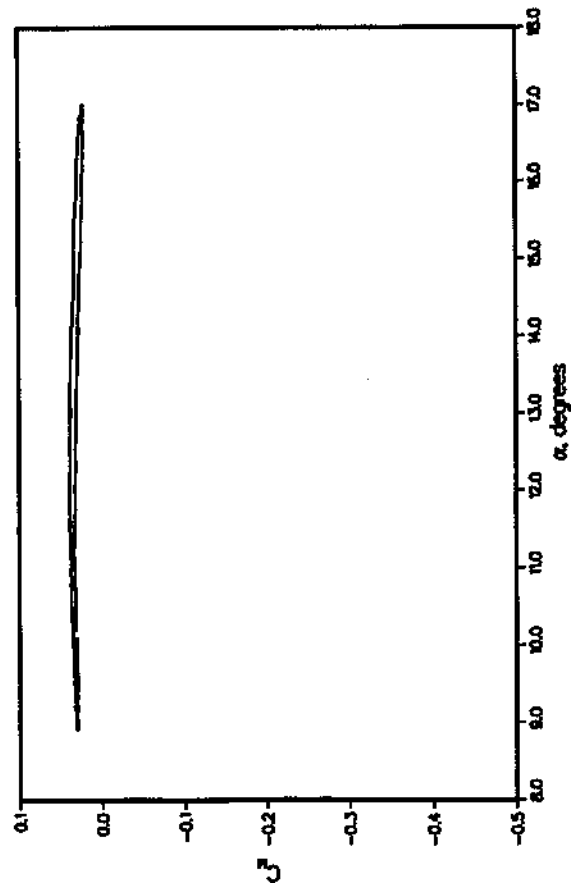
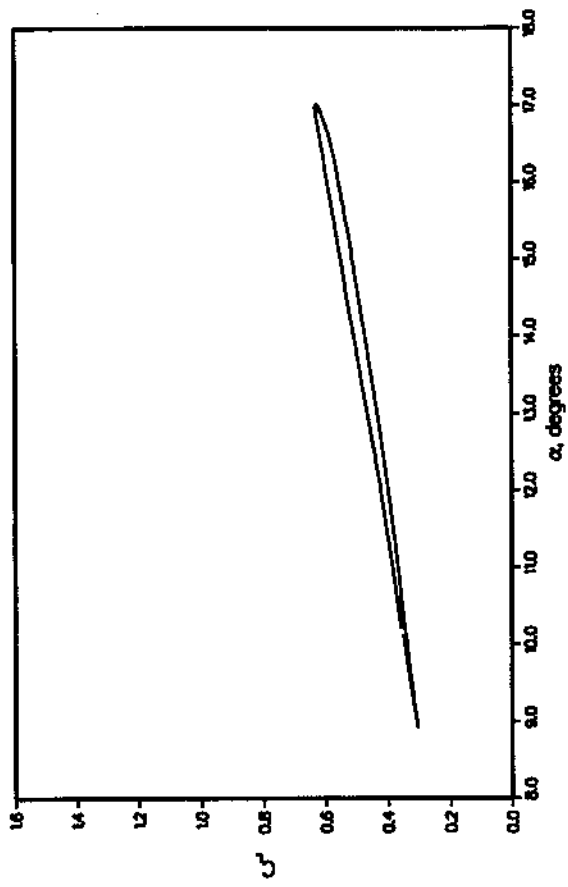


Figure 5(c). Lift and pitching-moment coefficients as a function of angle of attack, for 3-D wing experiencing dynamic stall at $M = 0.3$, $\alpha = 13^\circ + 4^\circ \sin \omega t$, $k = 0.04$ (from ref. 3).

99.5% SPAN

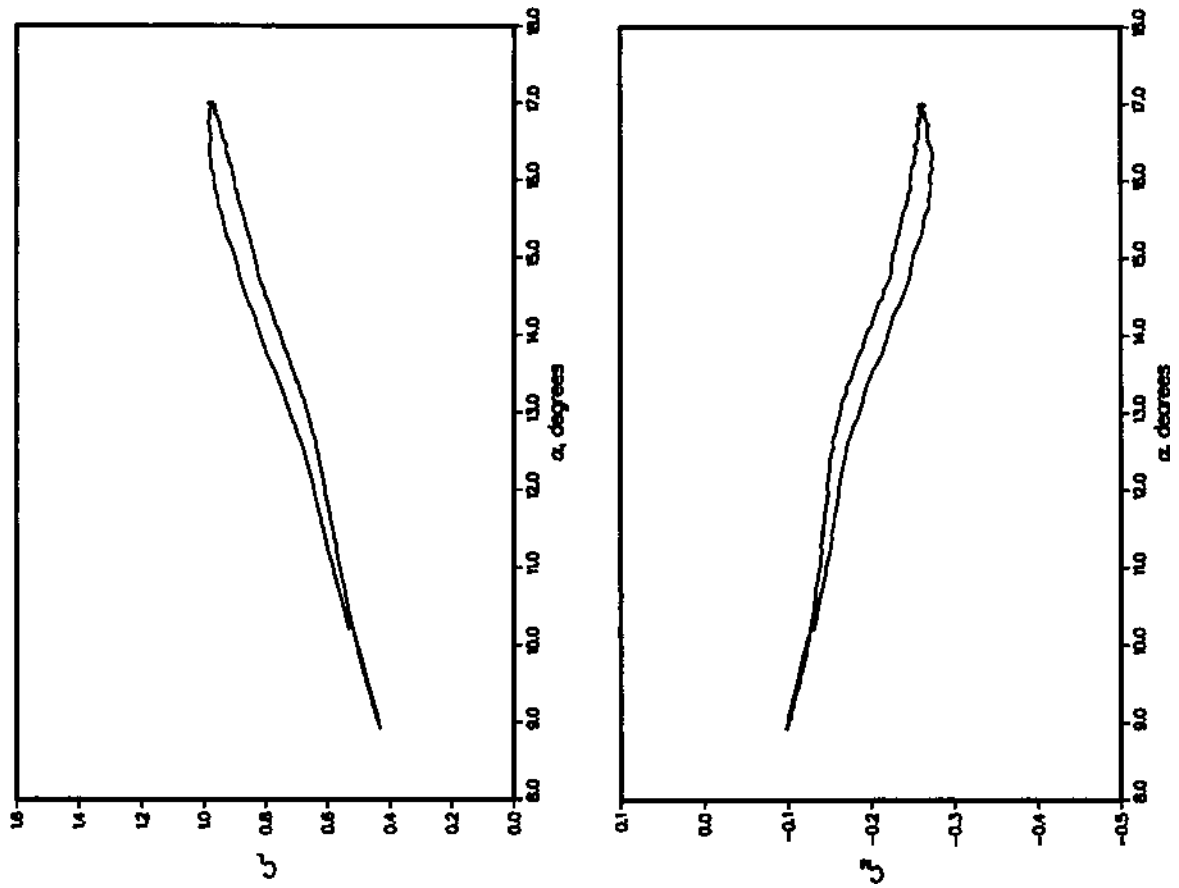
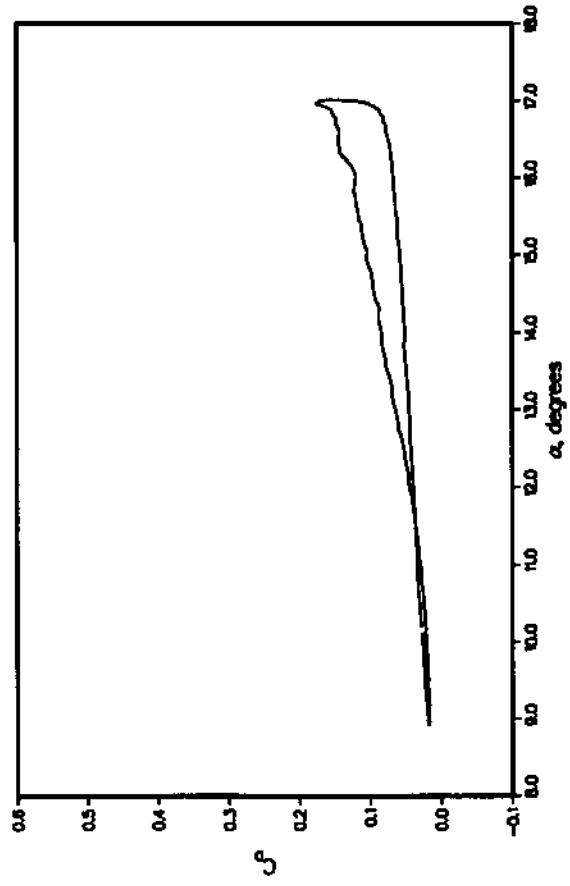
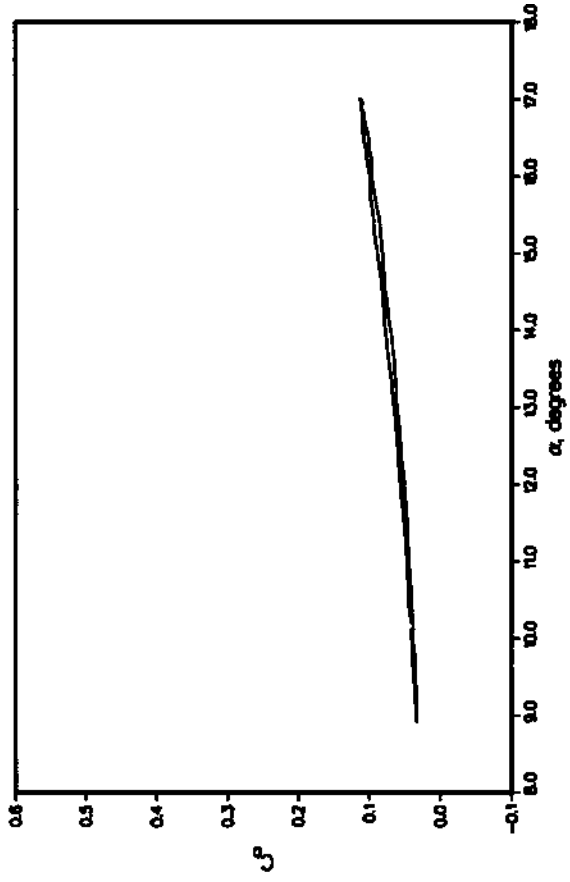


Figure 5(d). Lift and pitching-moment coefficients as a function of angle of attack, for 3-D wing experiencing dynamic stall at $M = 0.3$, $\alpha = 13^\circ + 4^\circ \sin \omega t$, $k = 0.04$ (from ref. 3).

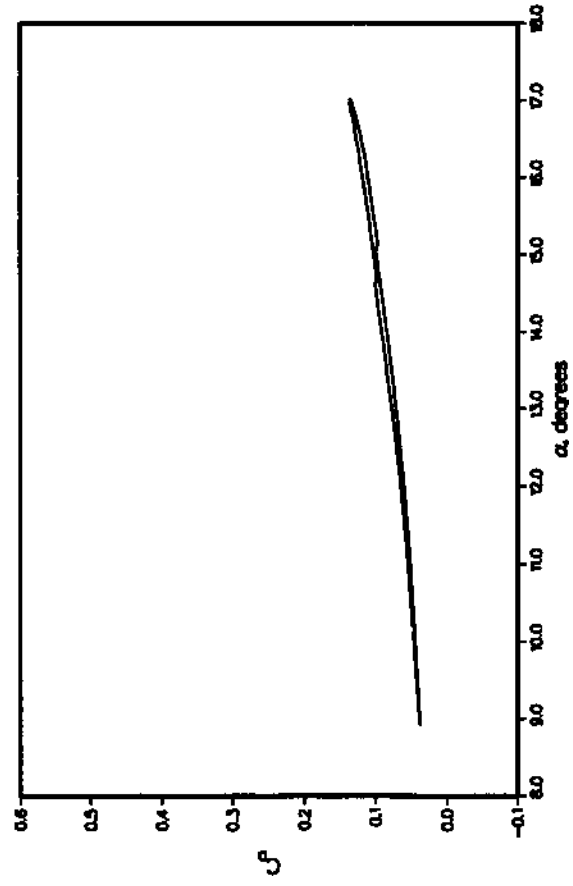
47.5% SPAN



96.6% SPAN



98.6% SPAN



99.5% SPAN

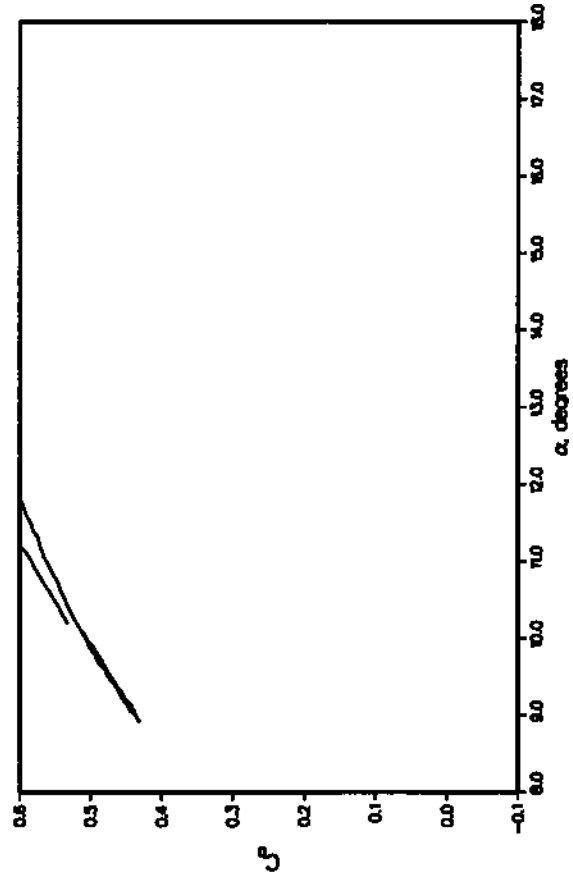
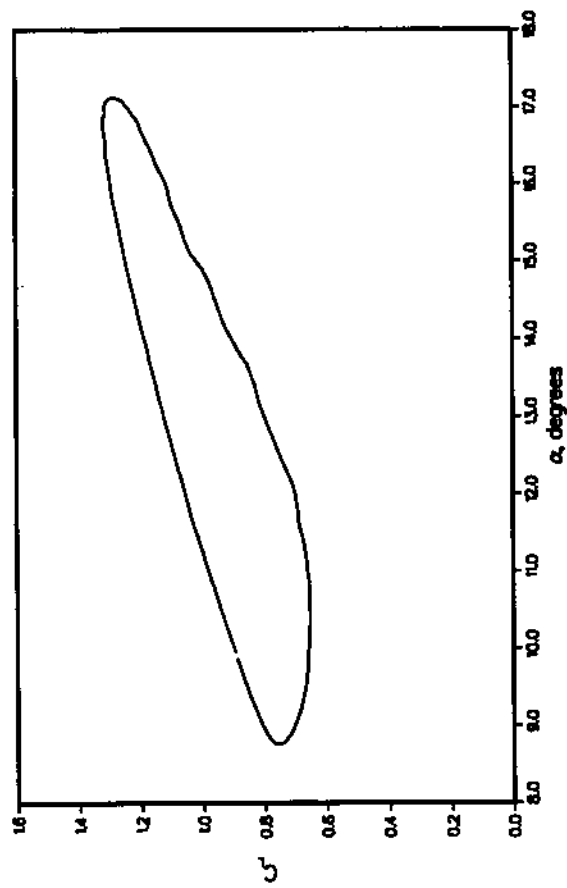


Figure 5(e). Drag coefficients as a function of angle of attack, for 3-D wing experiencing dynamic stall at $M = 0.3$, $\alpha = 13^\circ + 4^\circ \sin \omega t$, $k = 0.04$; drag at four spanwise stations (from ref. 3).

25% SPAN



47.5% SPAN

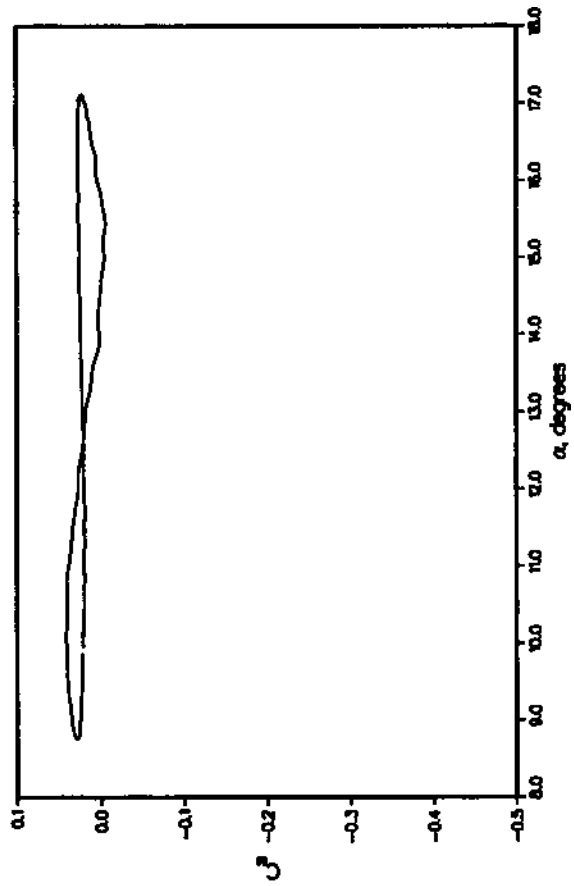
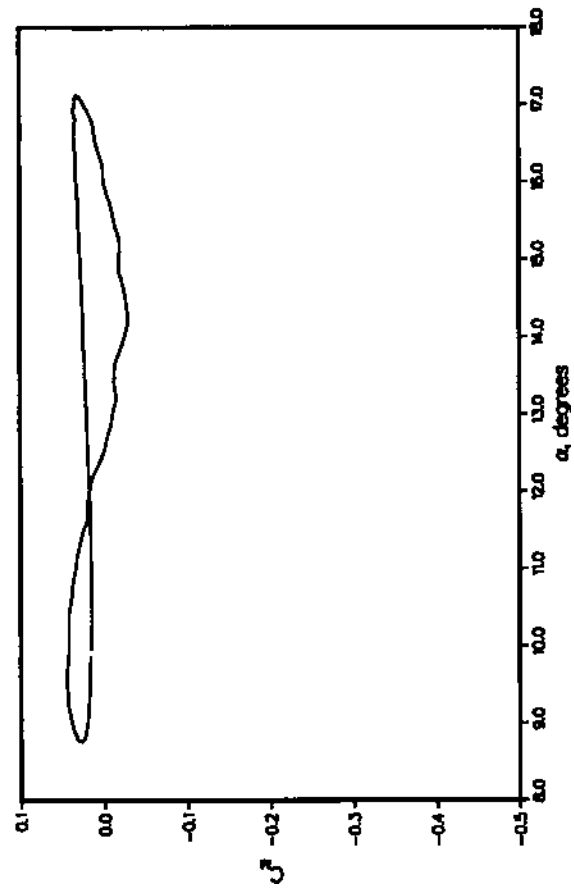
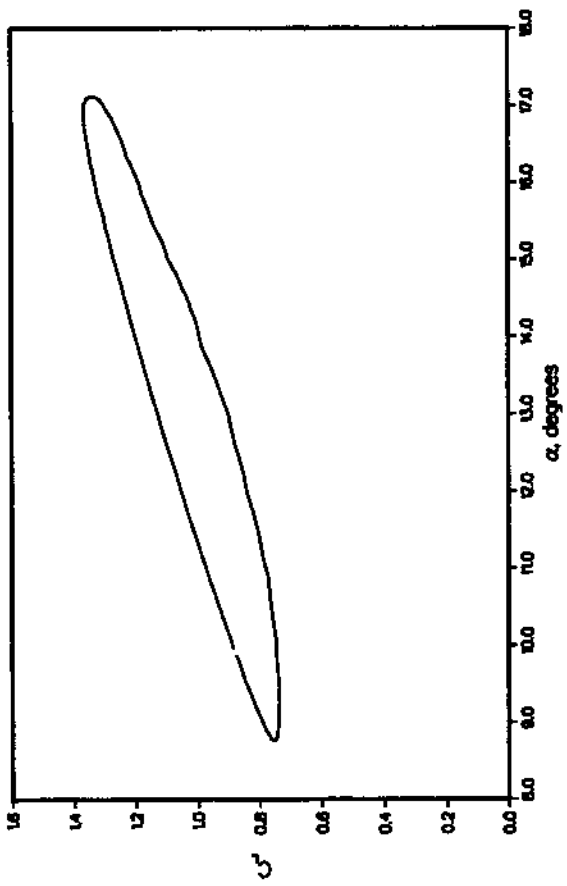
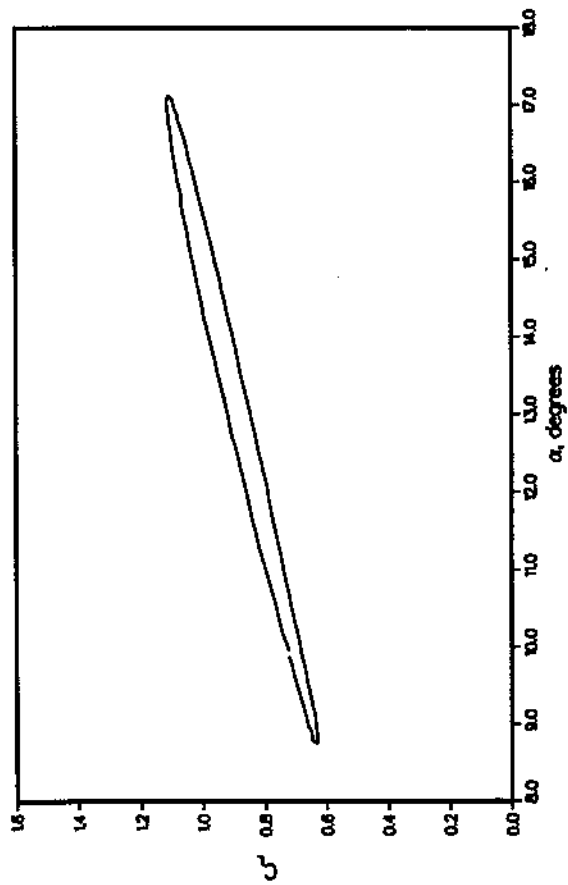


Figure 6(a). Lift and pitching-moment coefficients as a function of angle of attack, for 3-D wing experiencing dynamic stall at $M = 0.3$, $\alpha = 13^\circ + 4^\circ \sin \omega t$, $k = 0.10$ (from ref. 3).

80% SPAN



90% SPAN

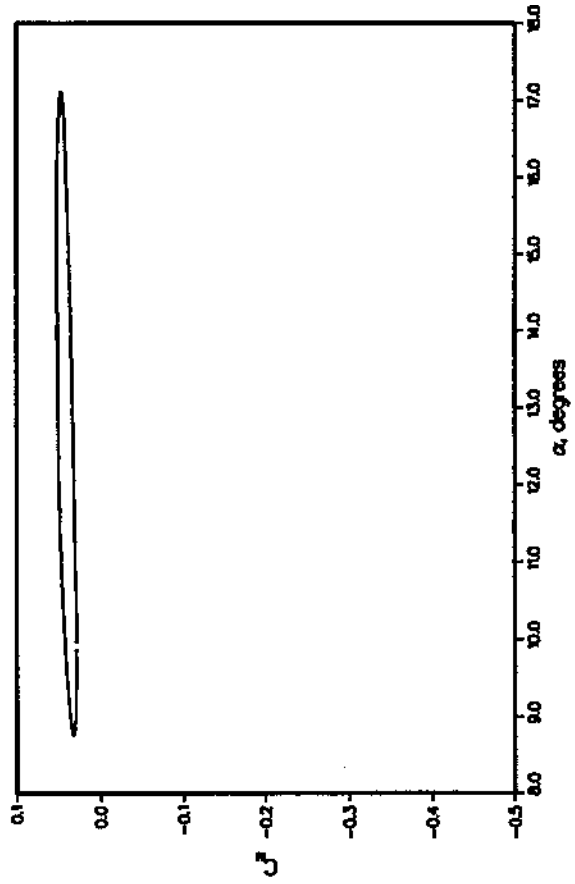
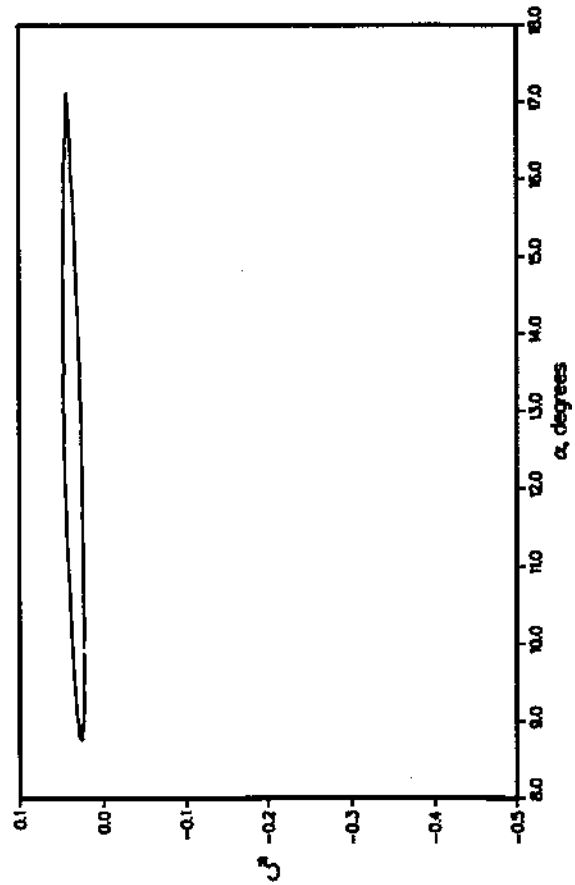
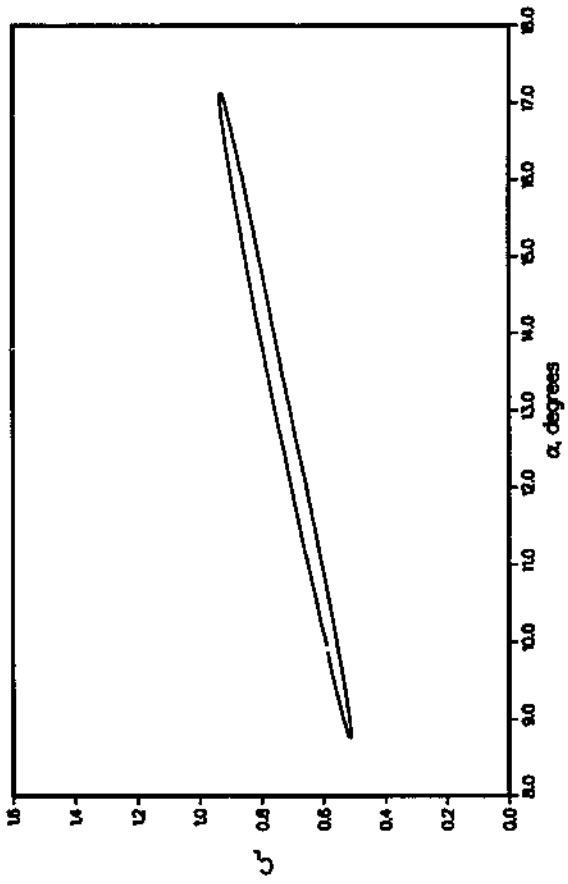
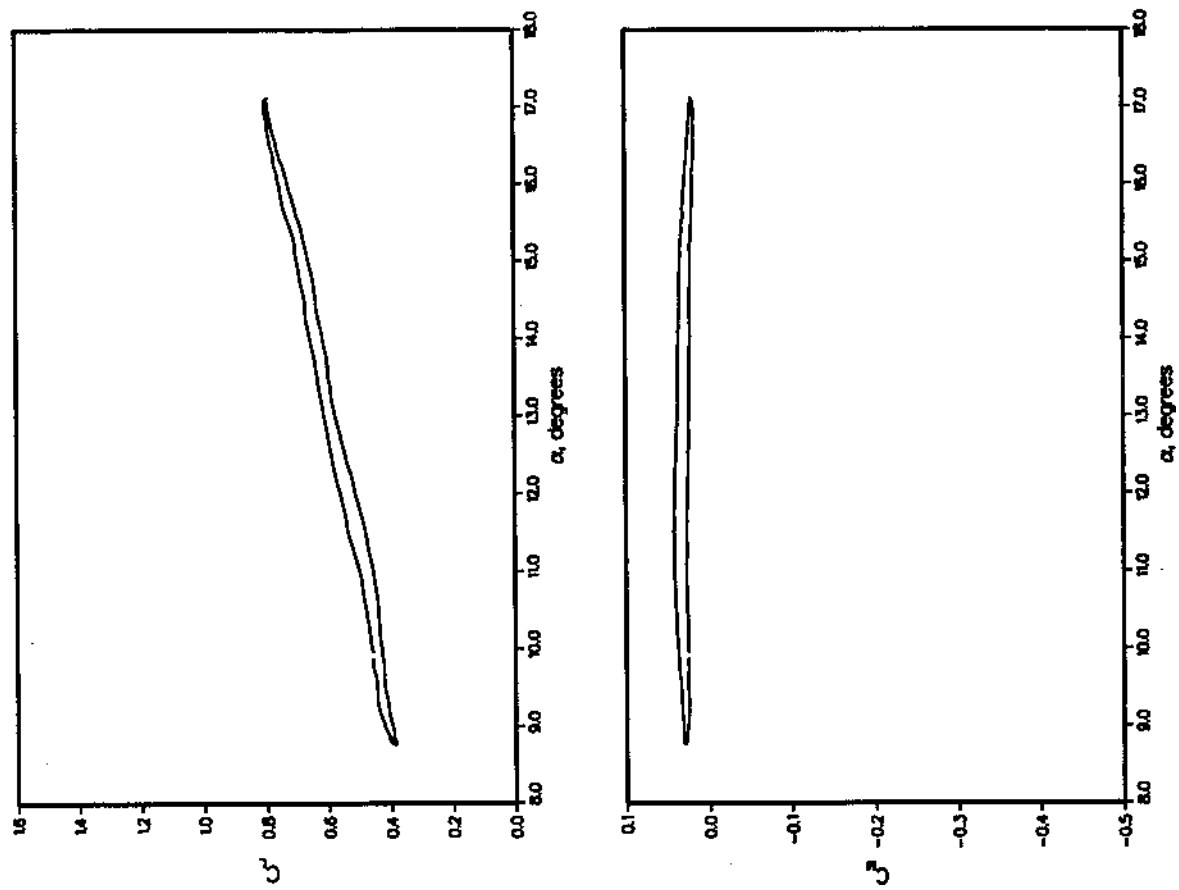


Figure 6(b). Lift and pitching-moment coefficients as a function of angle of attack, for 3-D wing experiencing dynamic stall at $M = 0.3$, $\alpha = 13^\circ + 4^\circ \sin \omega t$, $k = 0.10$ (from ref. 3).

96.6% SPAN



98.6% SPAN

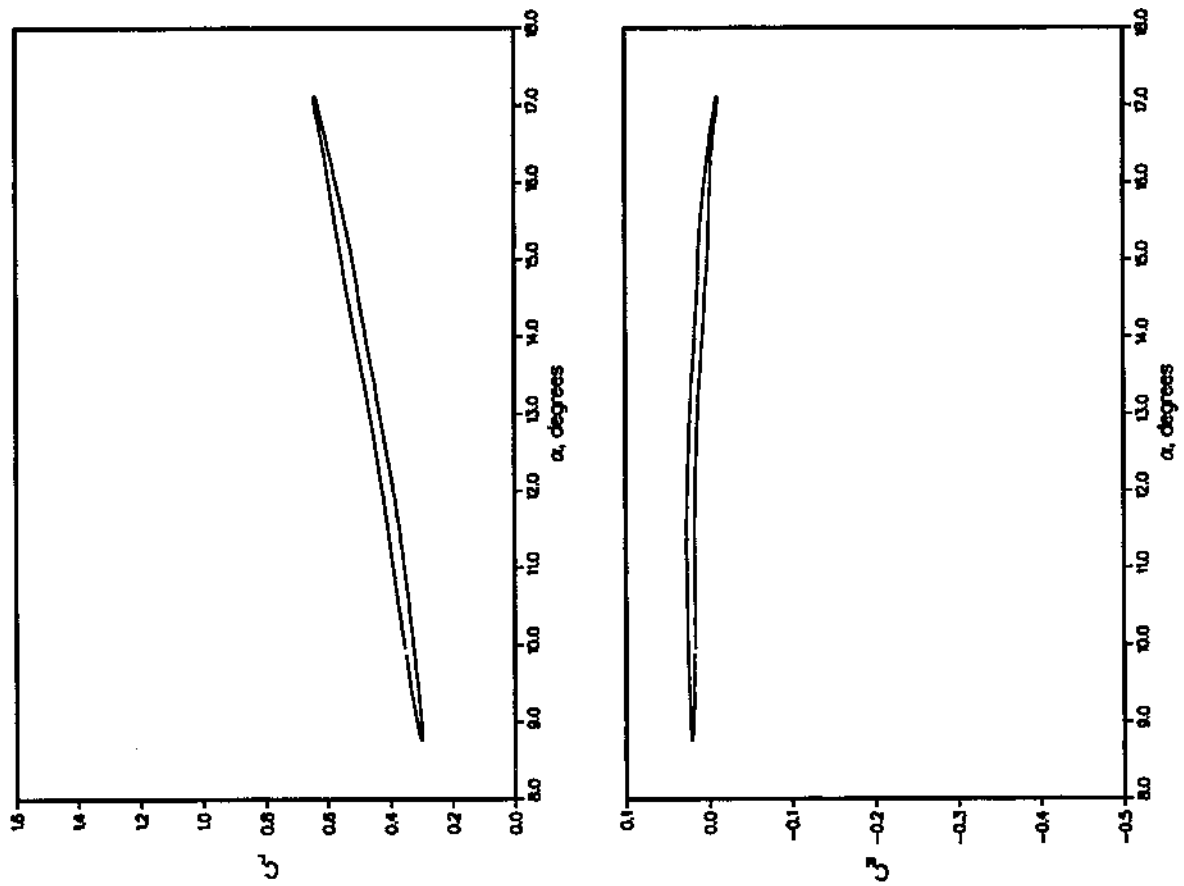


Figure 6(c). Lift and pitching-moment coefficients as a function of angle of attack, for 3-D wing experiencing dynamic stall at $M = 0.3$, $\alpha = 13^\circ + 4^\circ \sin \omega t$, $k = 0.10$ (from ref. 3).

99.5% SPAN

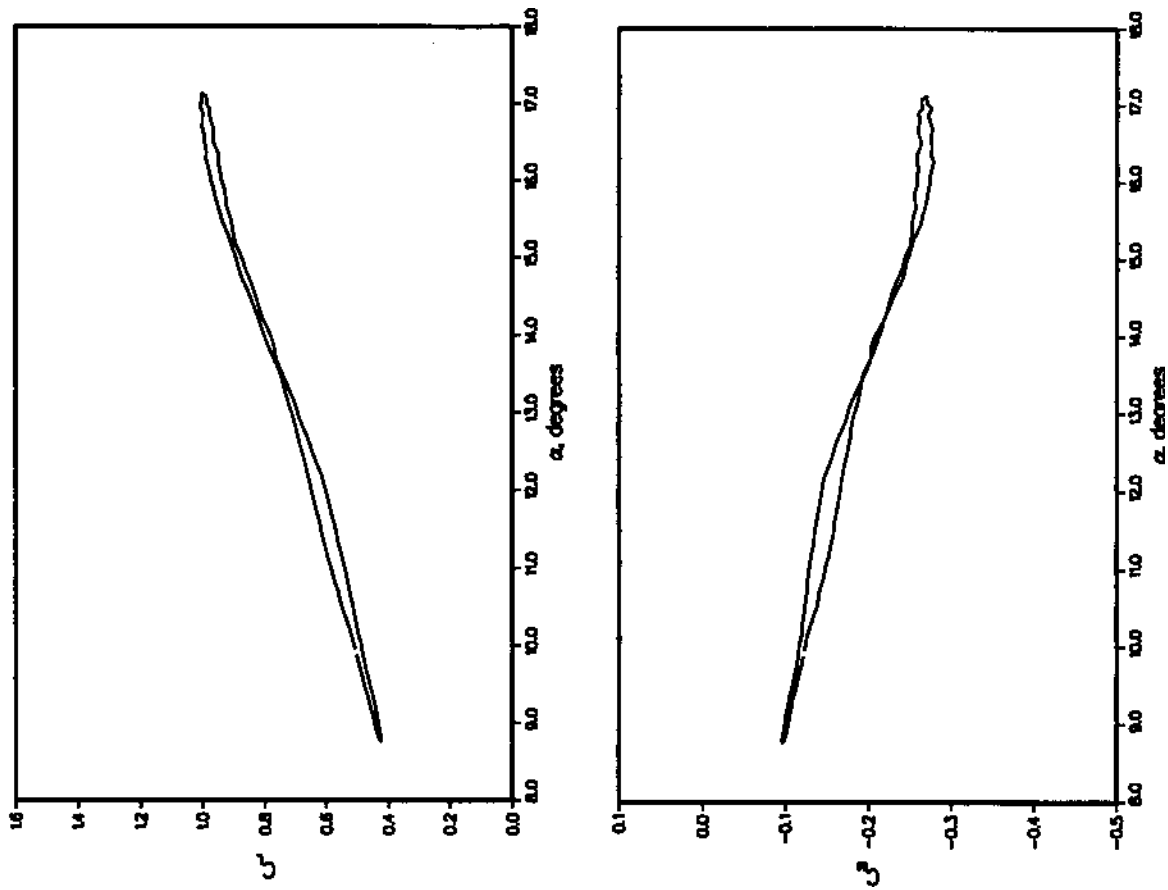
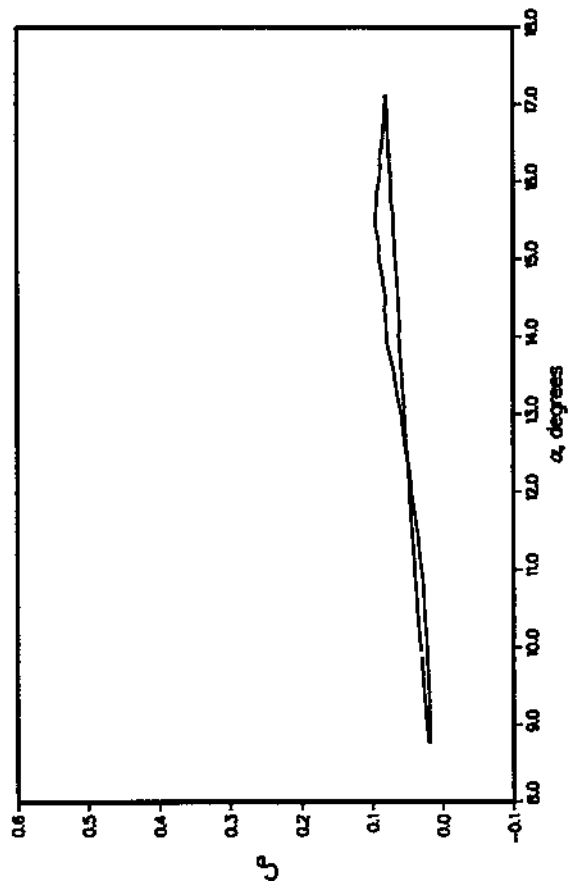
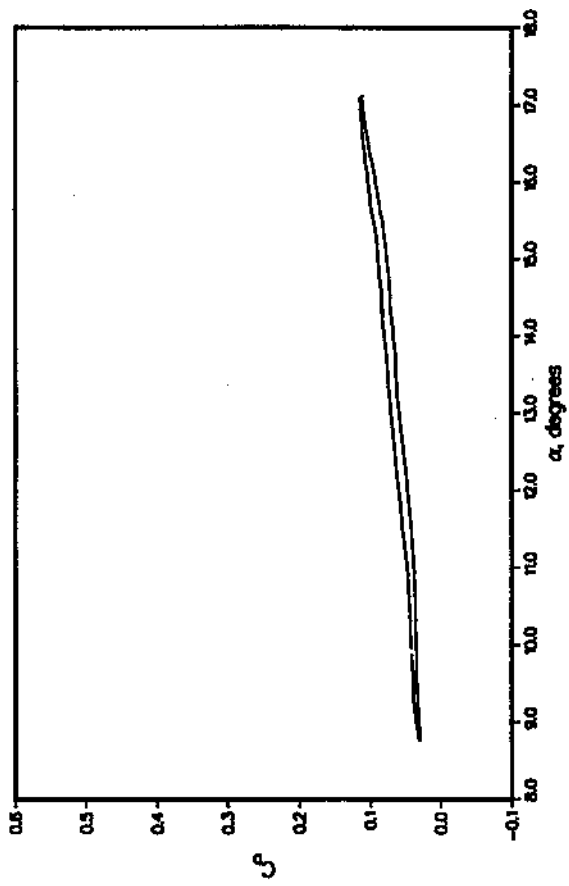


Figure 6(d). Lift and pitching-moment coefficients as a function of angle of attack, for 3-D wing experiencing dynamic stall at $M = 0.3$, $\alpha = 13^\circ + 4^\circ \sin \omega t$, $k = 0.10$ (from ref. 3).

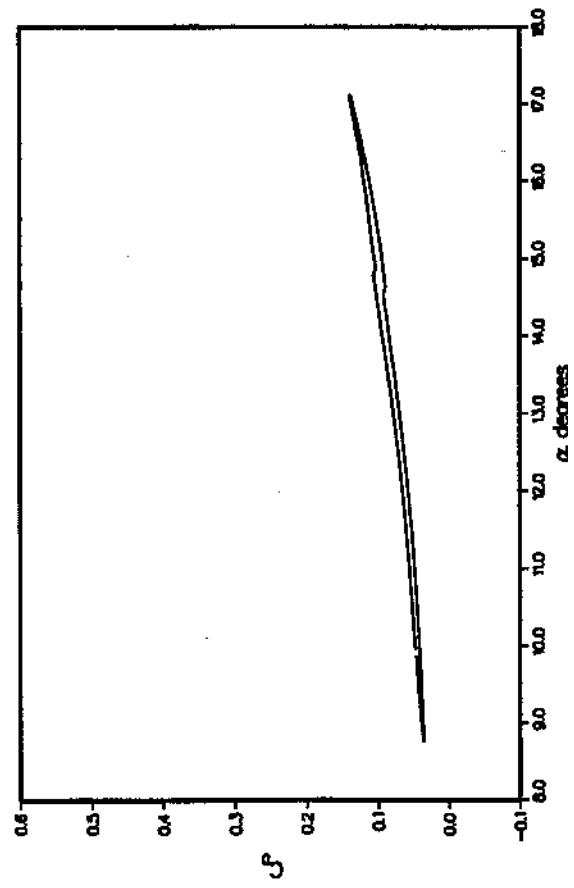
47.5% SPAN



96.6% SPAN



98.6% SPAN



99.5% SPAN

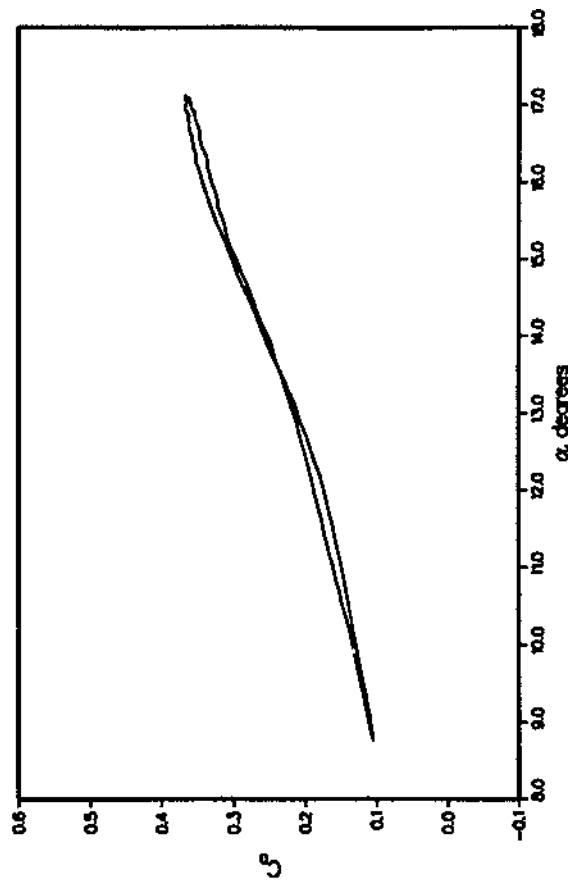
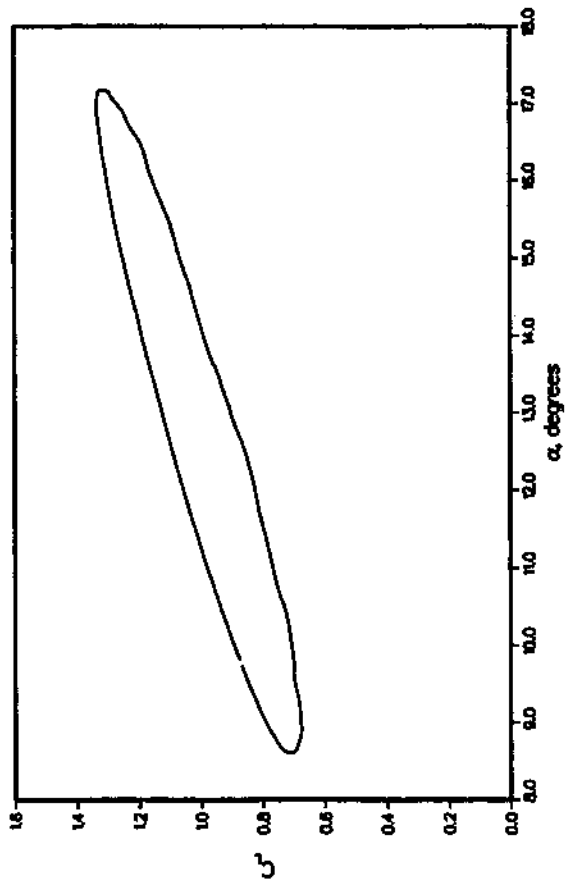


Figure 6(e). Drag coefficients as a function of angle of attack, for 3-D wing experiencing dynamic stall at $M = 0.3$, $\alpha = 13^\circ + 4^\circ \sin \omega t$, $k = 0.10$; drag at four spanwise stations (from ref. 3).

25% SPAN



47.5% SPAN

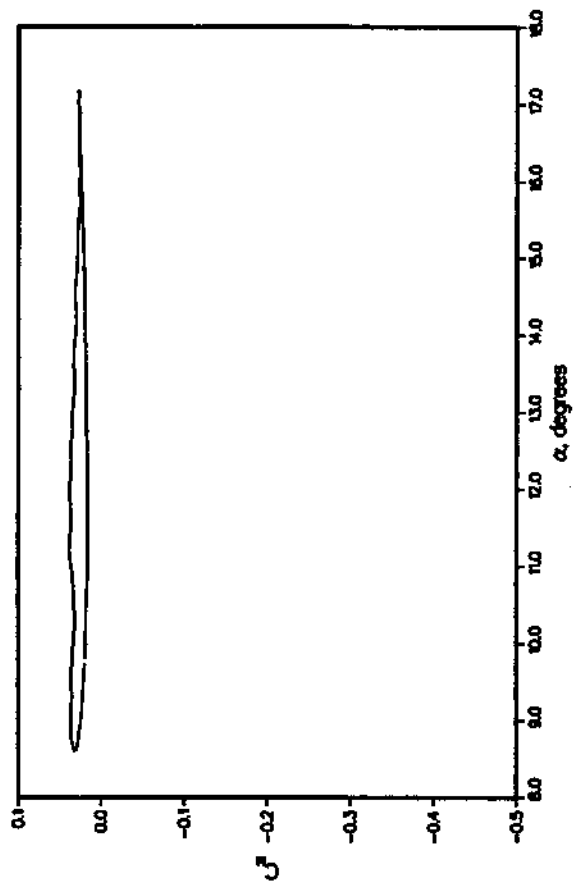
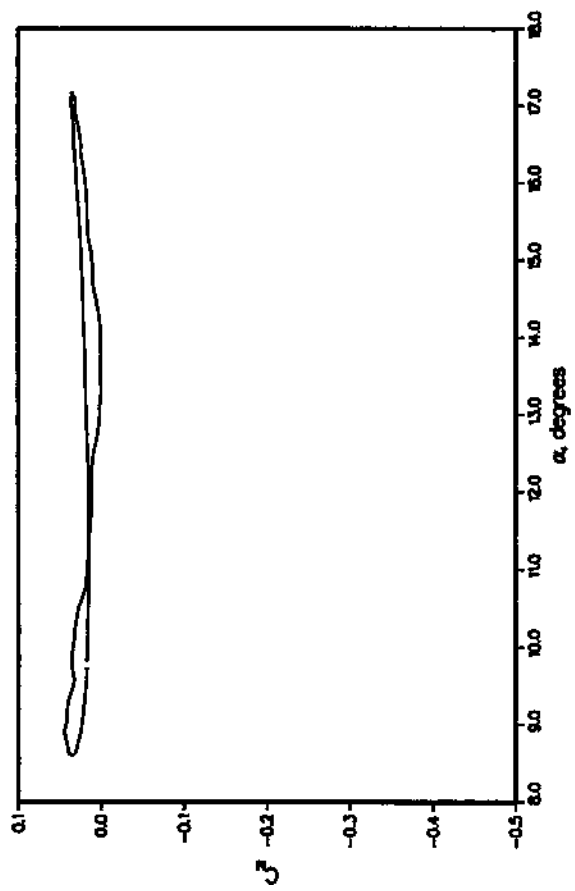
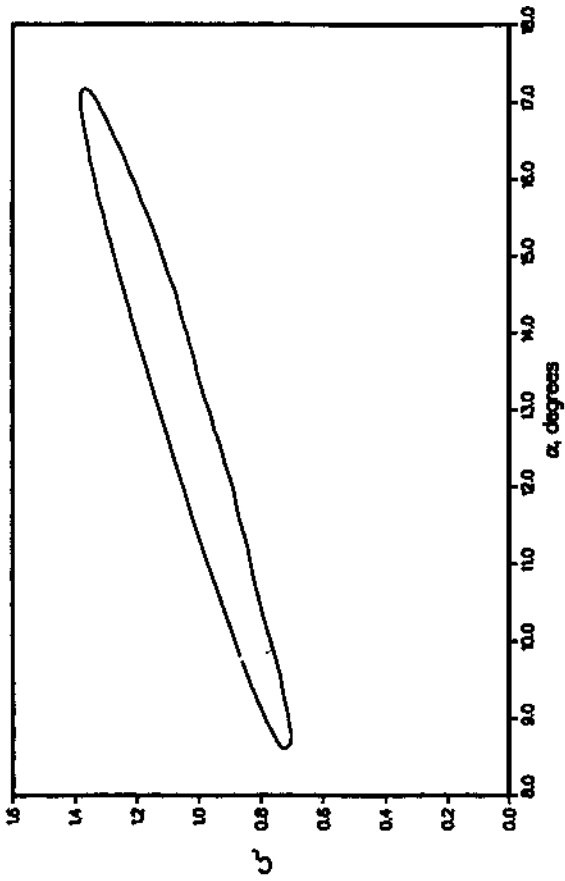
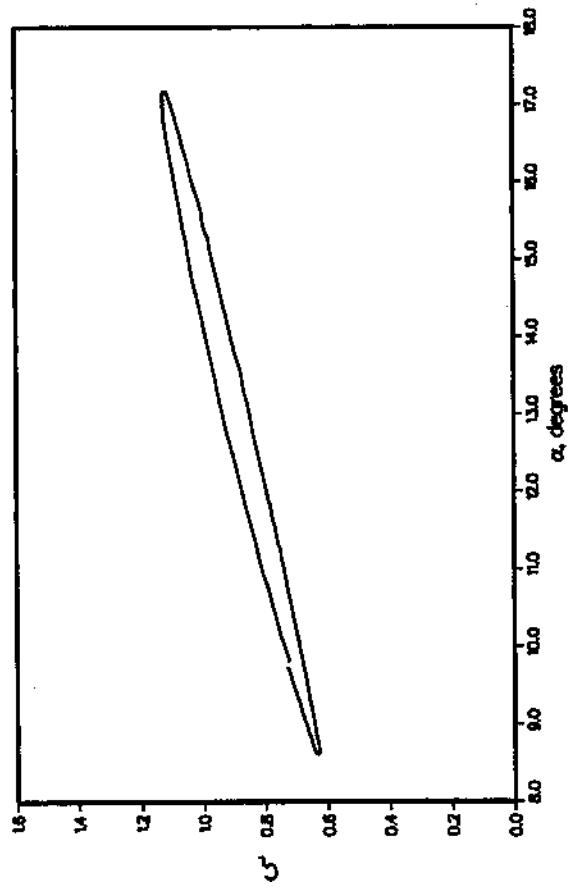


Figure 7(a). Lift and pitching-moment coefficients as a function of angle of attack, for 3-D wing experiencing dynamic stall at $M = 0.3$, $\alpha = 13^\circ + 4^\circ \sin \omega t$, $k = 0.14$ (from ref. 3).

80% SPAN



90% SPAN

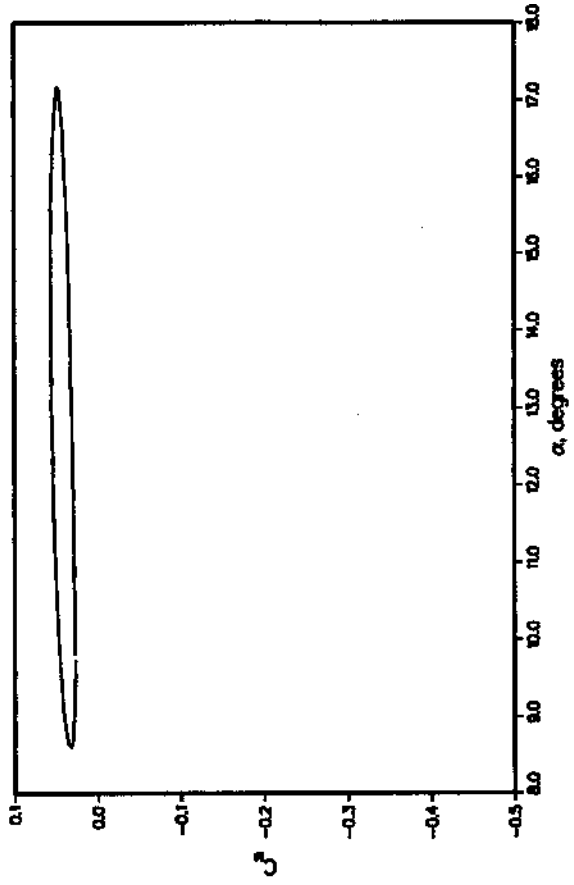
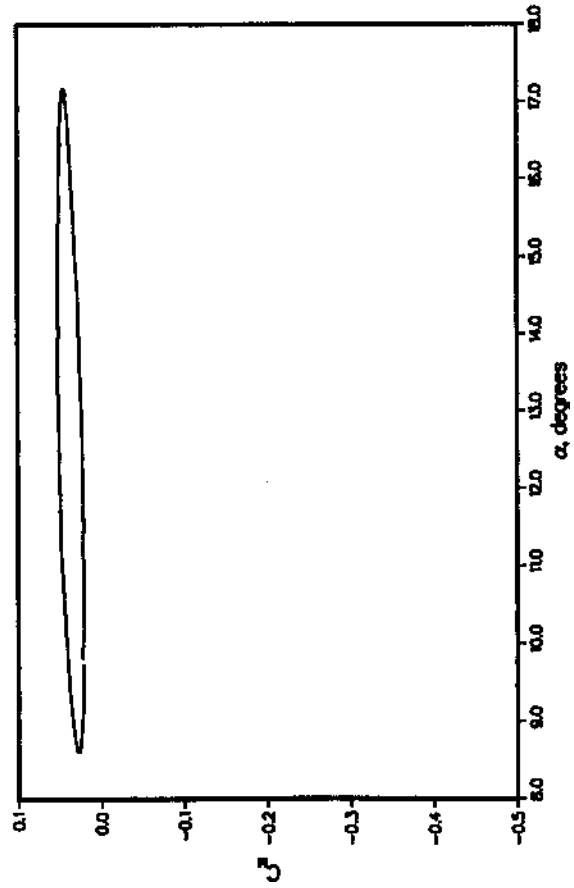
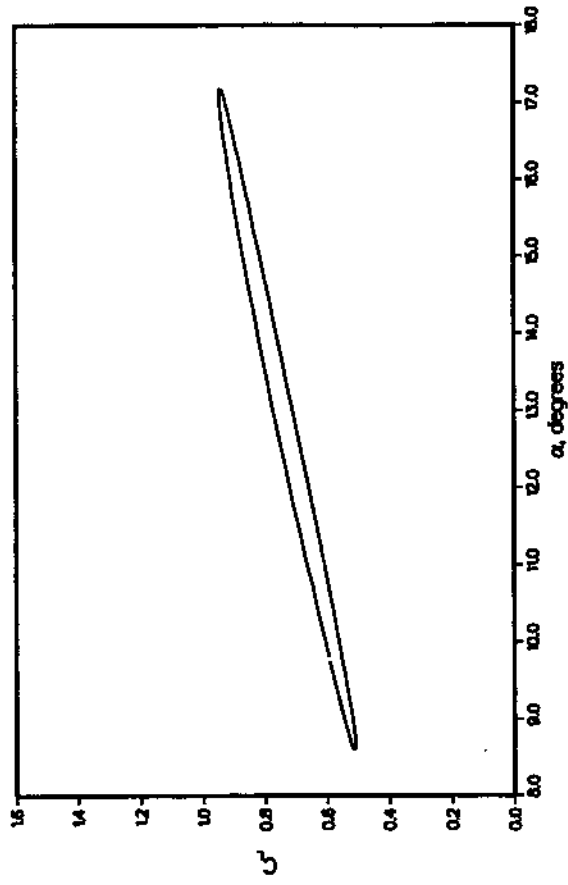
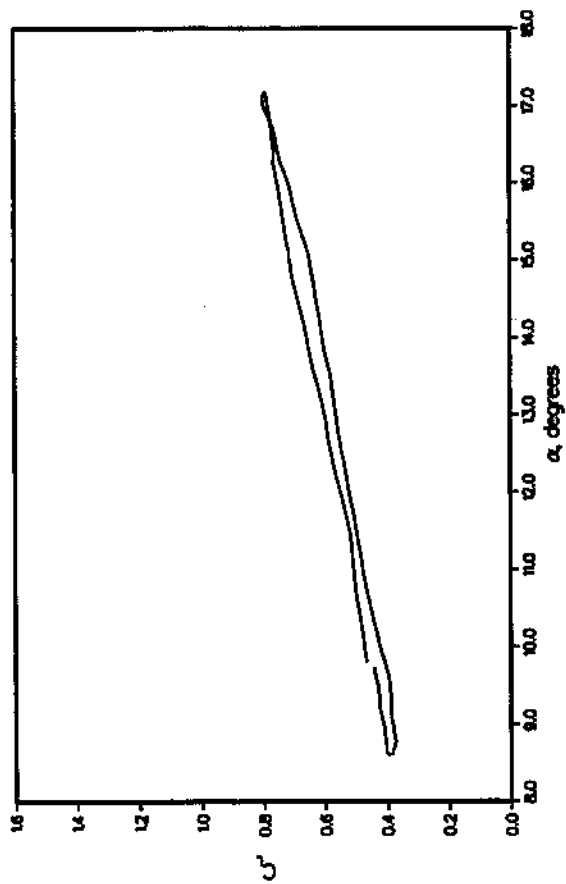


Figure 7(b). Lift and pitching-moment coefficients as a function of angle of attack, for 3-D wing experiencing dynamic stall at $M = 0.3$, $\alpha = 13^\circ + 4^\circ \sin \omega t$, $k = 0.14$ (from ref. 3).

96.6% SPAN



98.6% SPAN

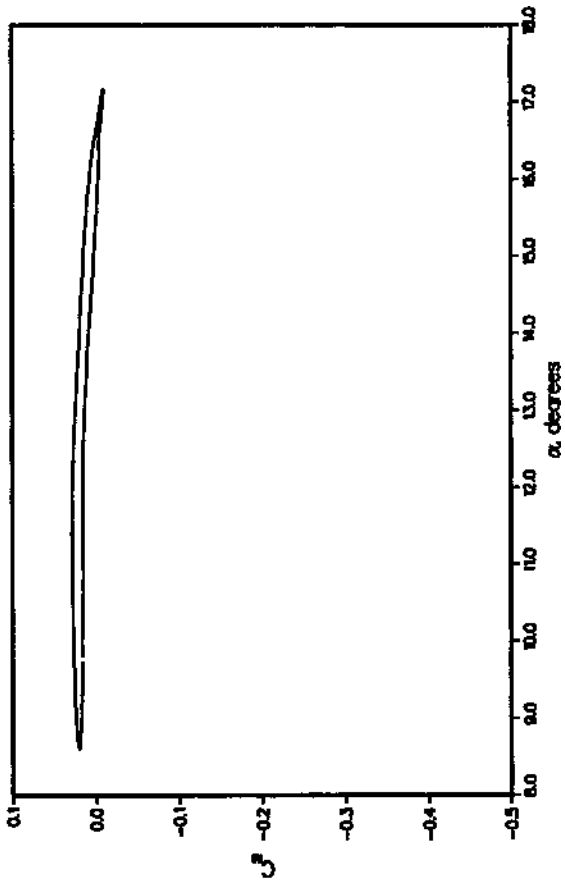
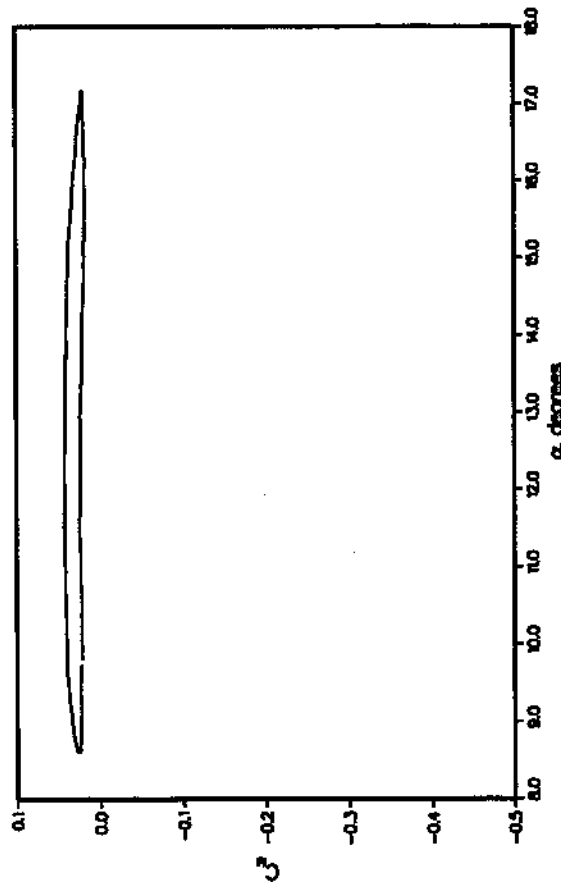
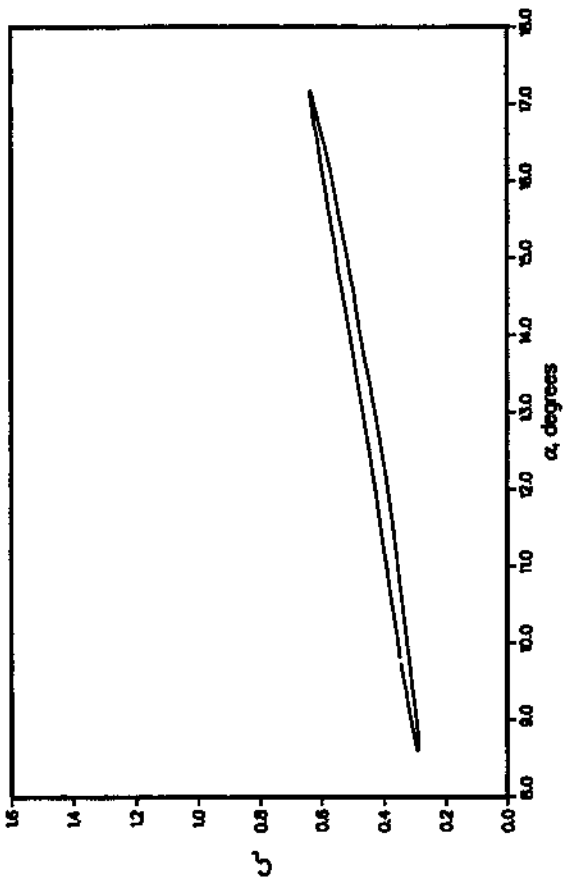


Figure 7(c). Lift and pitching-moment coefficients as a function of angle of attack, for 3-D wing experiencing dynamic stall at $M = 0.3$, $\alpha = 13^\circ + 4^\circ \sin \omega t$, $k = 0.14$ (from ref. 3).

99.5% SPAN

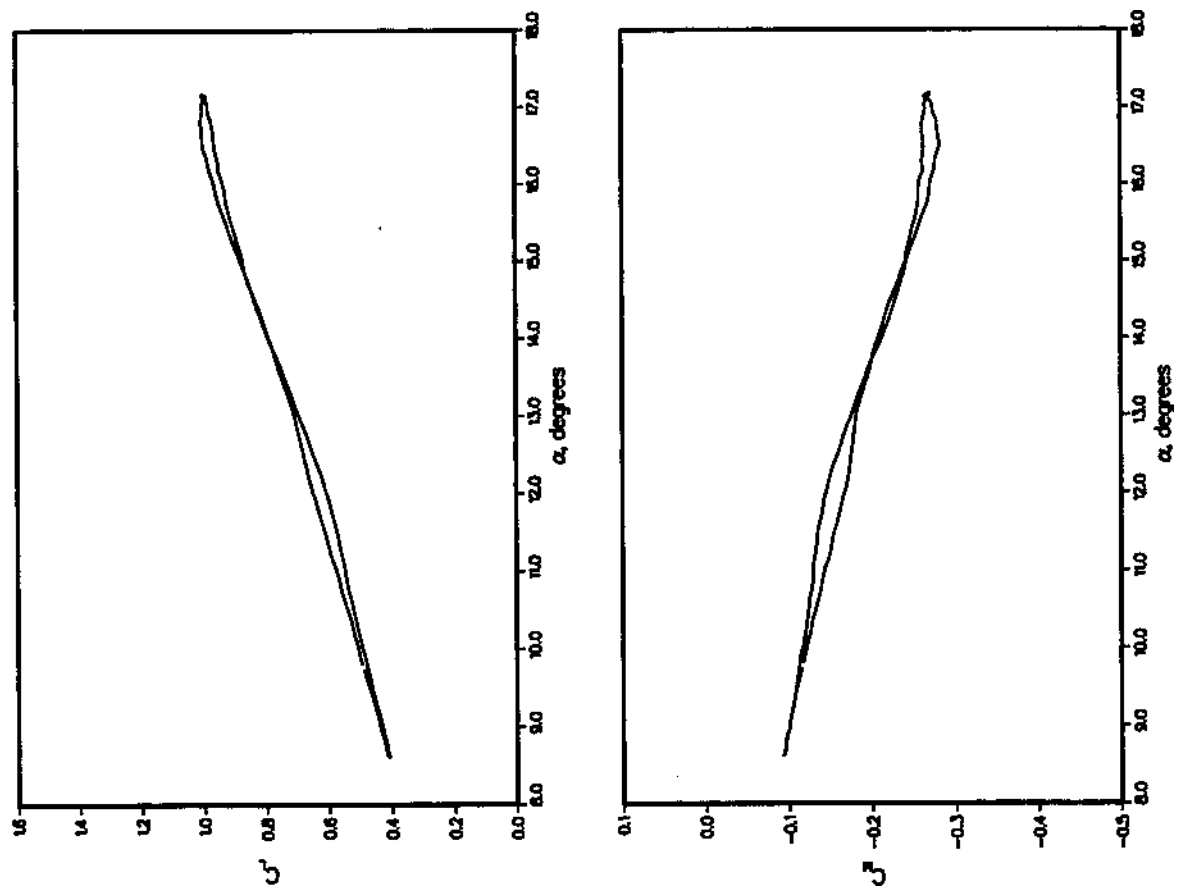
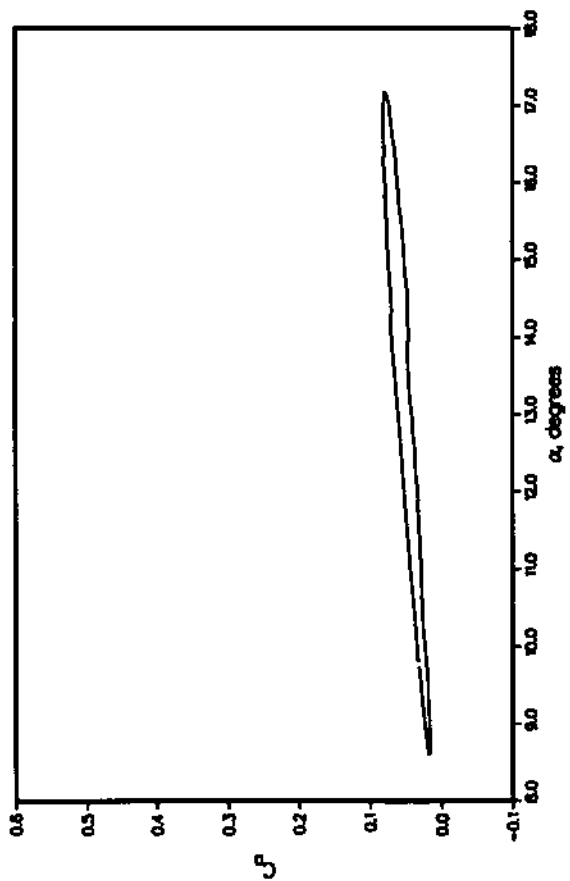
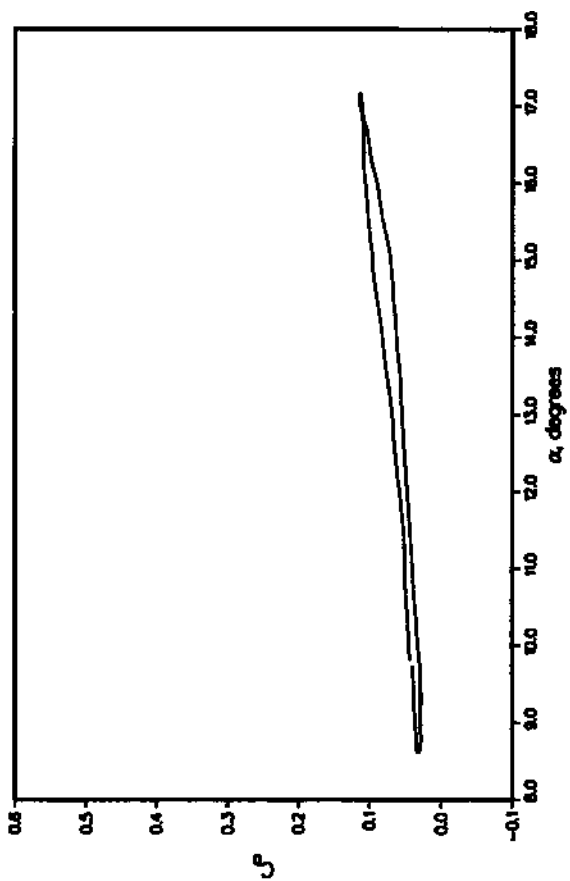


Figure 7(d). Lift and pitching-moment coefficients as a function of angle of attack, for 3-D wing experiencing dynamic stall at $M = 0.3$, $\alpha = 13^\circ + 4^\circ \sin \omega t$, $k = 0.14$ (from ref. 3).

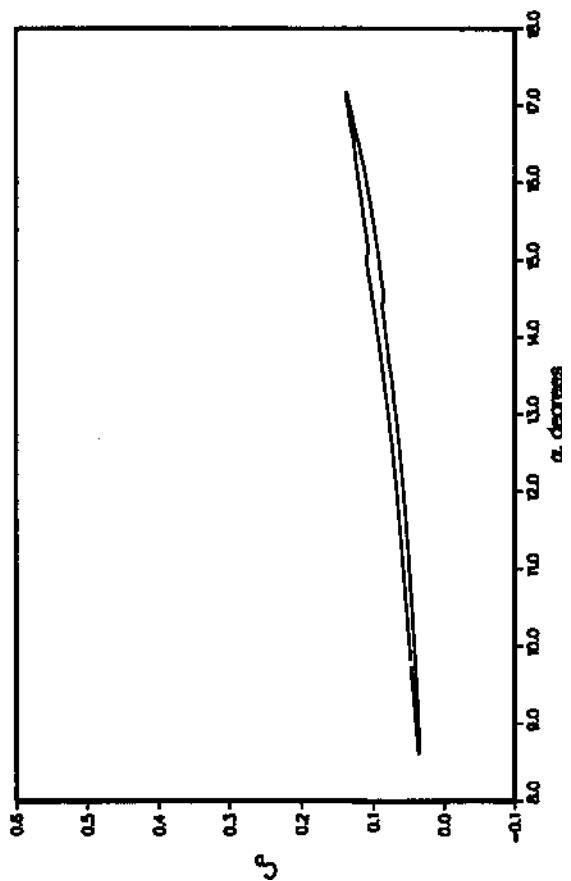
47.5% SPAN



96.6% SPAN



98.6% SPAN



99.5% SPAN

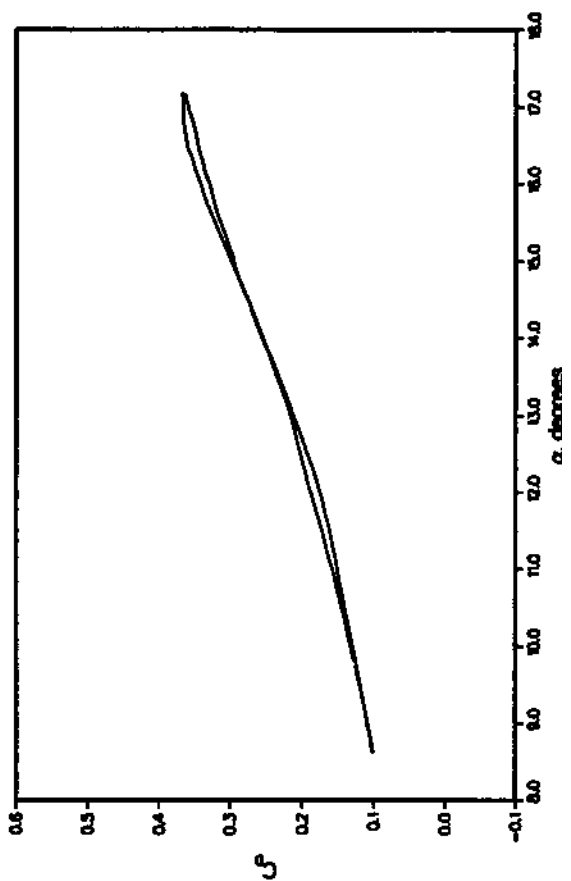
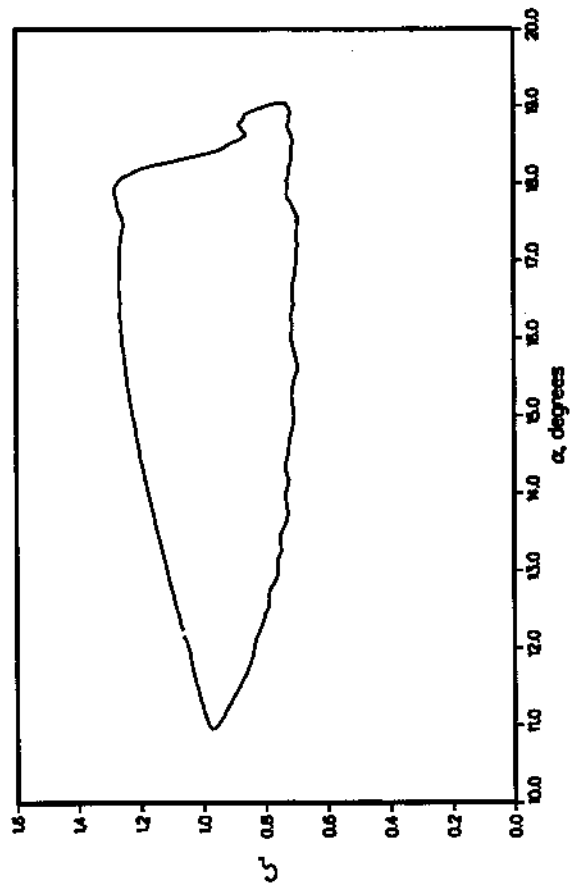


Figure 7(e). Drag coefficients as a function of angle of attack, for 3-D wing experiencing dynamic stall at $M = 0.3$, $\alpha = 13^\circ + 4^\circ \sin \omega t$, $k = 0.14$; drag at four spanwise stations (from ref. 3).

25% SPAN



47.5% SPAN

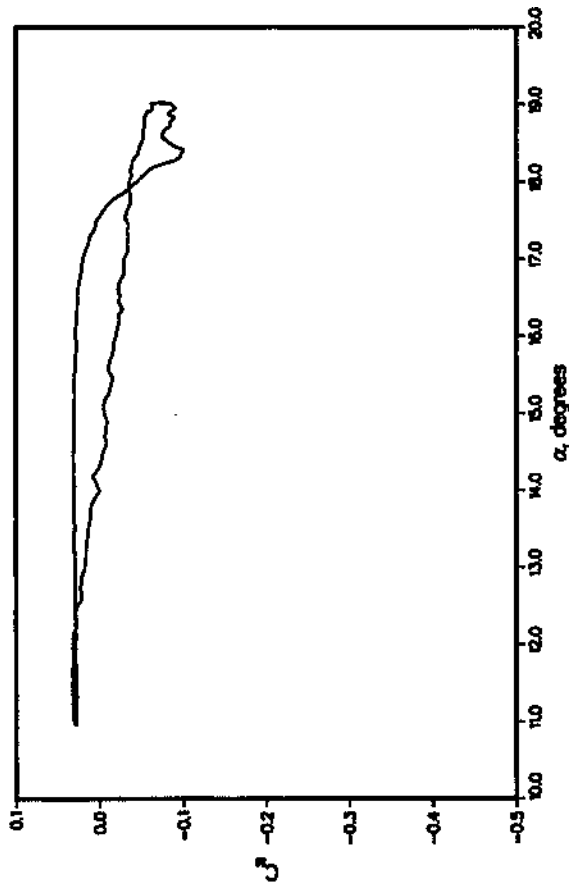
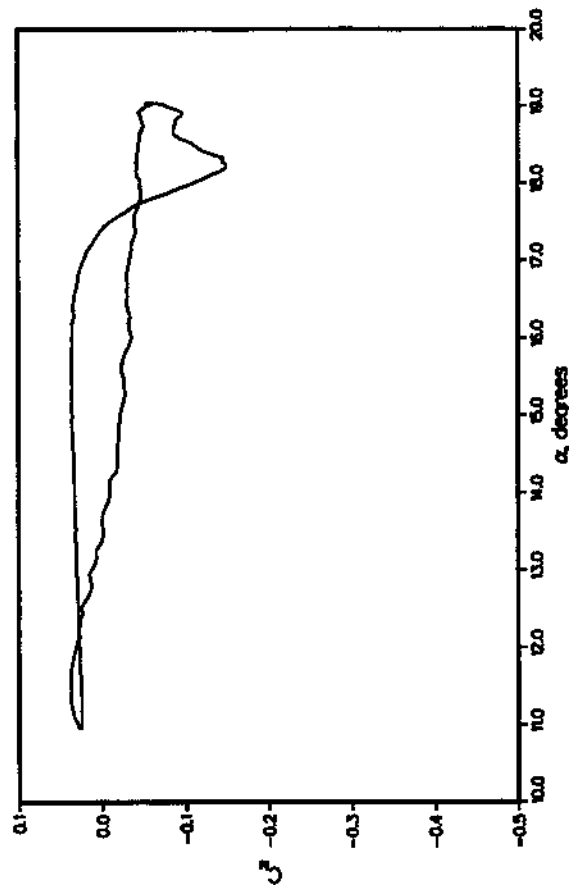
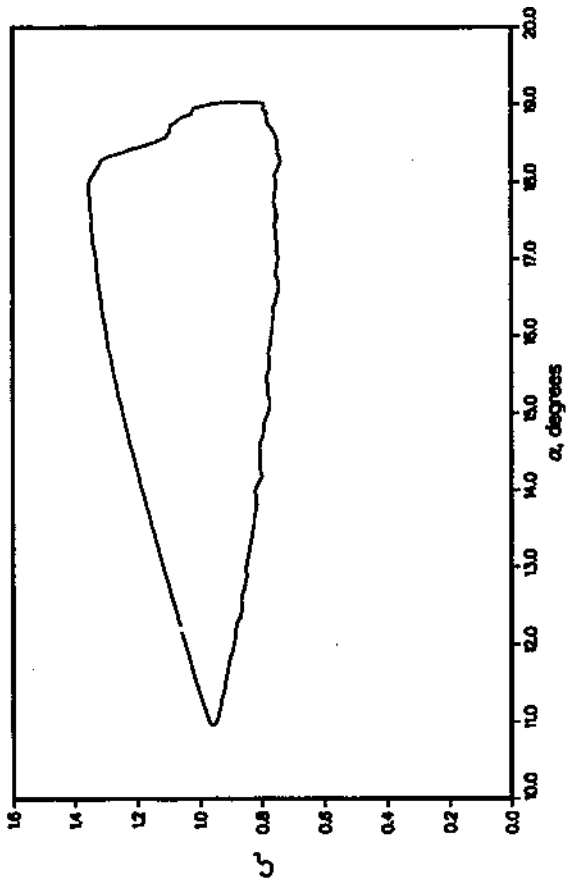
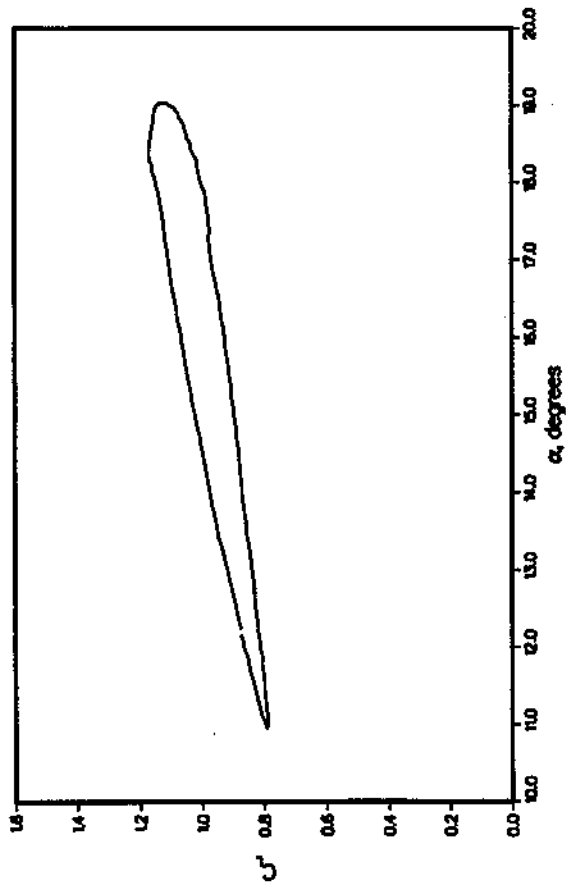


Figure 8(a). Lift and pitching-moment coefficients as a function of angle of attack, for 3-D wing experiencing dynamic stall at $M = 0.3$, $\alpha = 15^\circ + 4^\circ \sin \omega t$, $k = 0.04$ (from ref. 3).

80% SPAN



90% SPAN

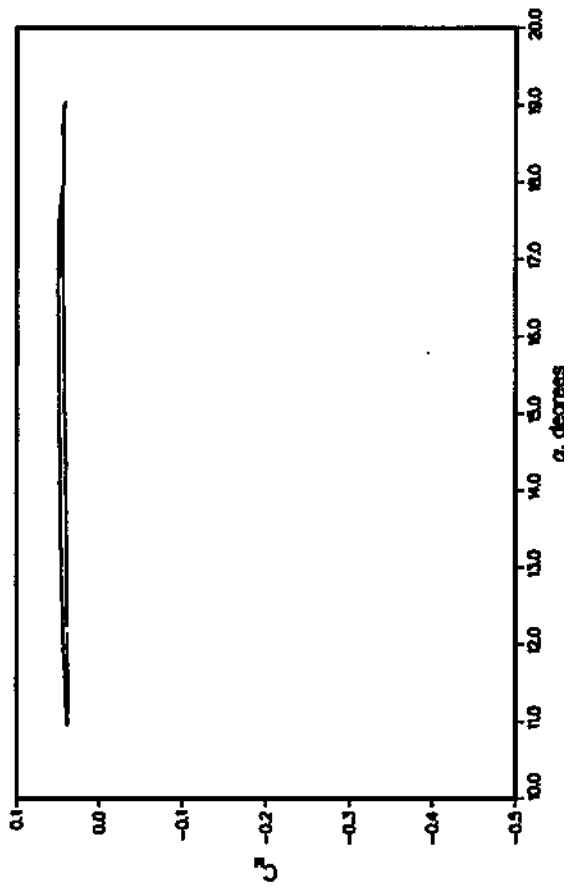
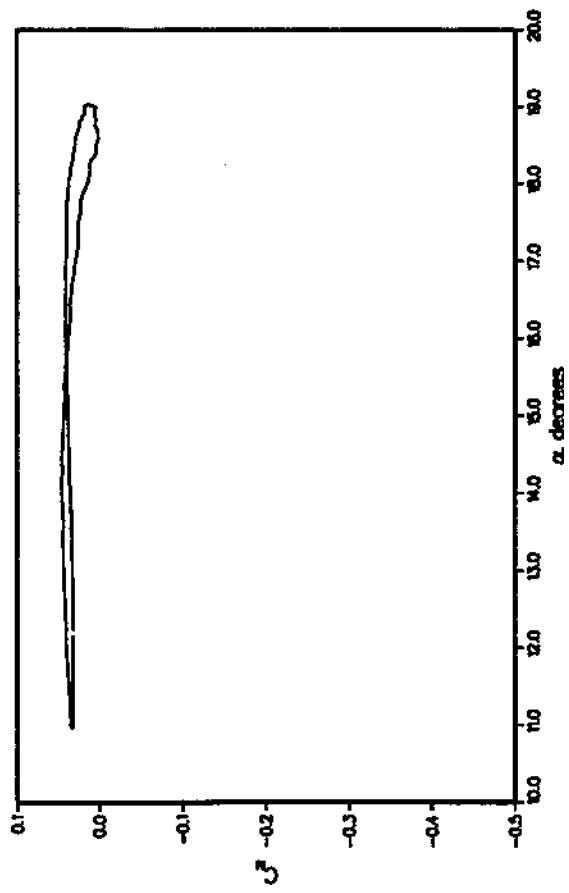
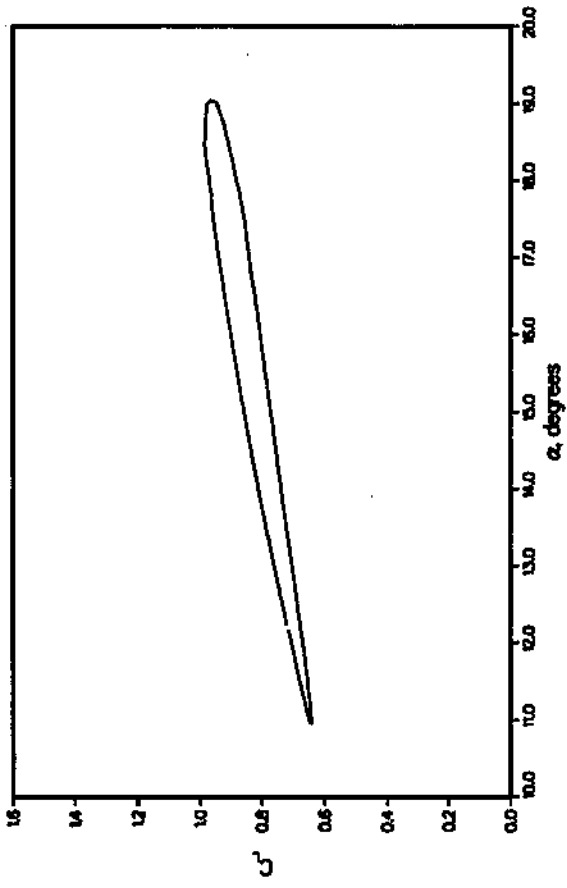
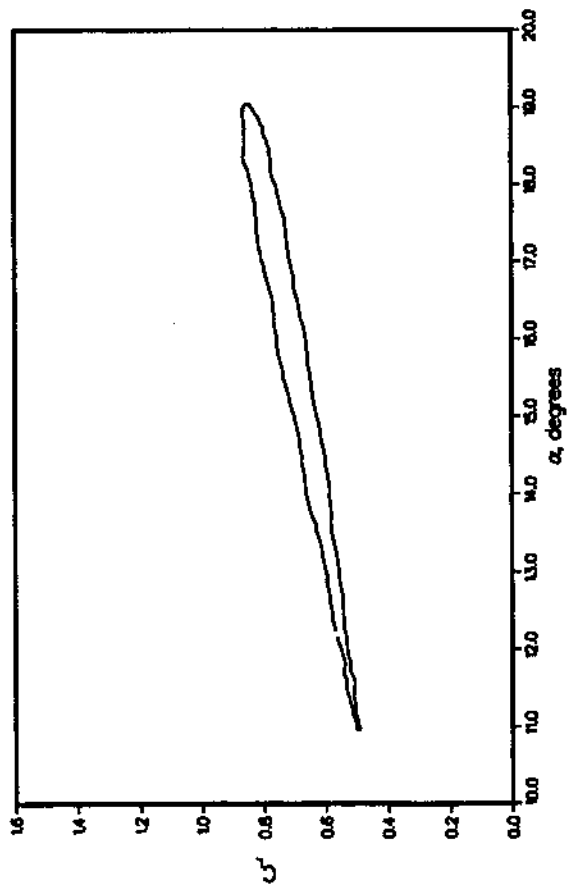


Figure 8(b). Lift and pitching-moment coefficients as a function of angle of attack, for 3-D wing experiencing dynamic stall at $M = 0.3$, $\alpha = 15^\circ + 4^\circ \sin \omega t$, $k = 0.04$ (from ref. 3).

96.6% SPAN



98.6% SPAN

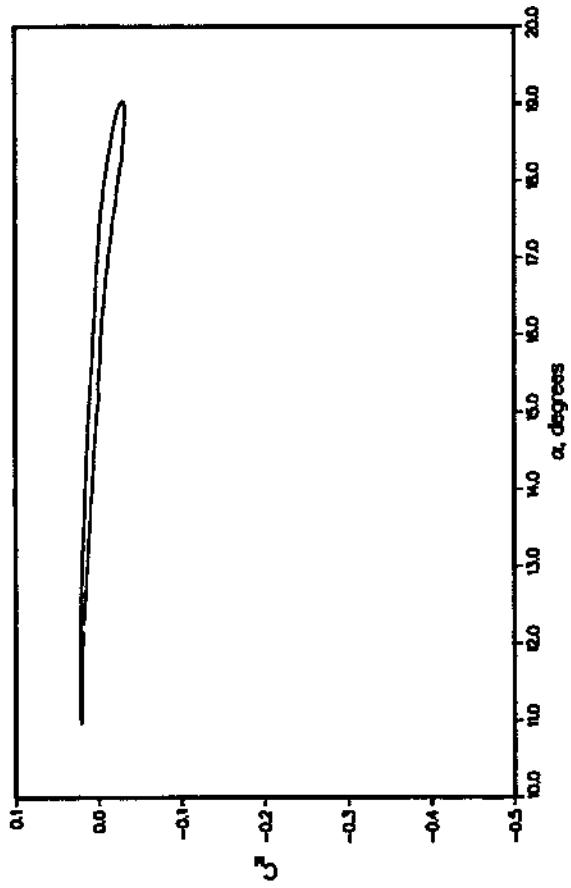
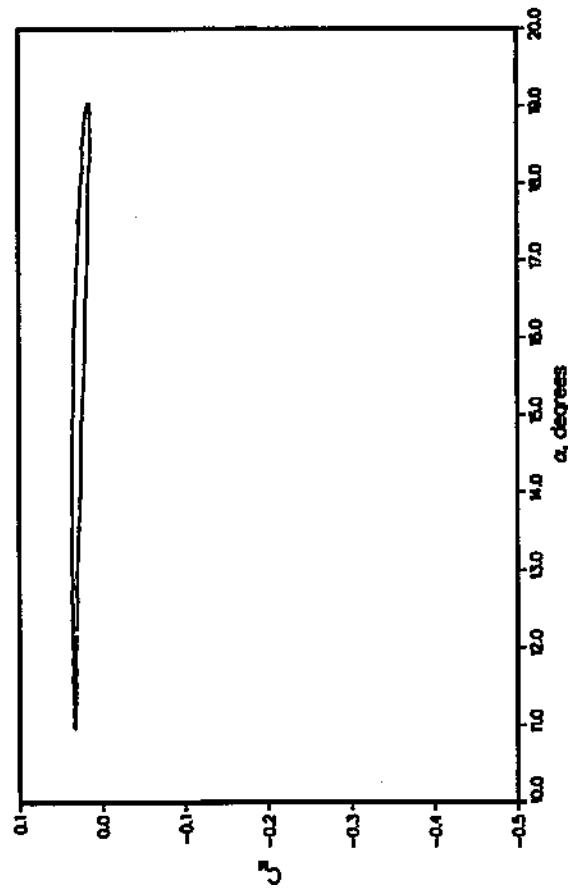
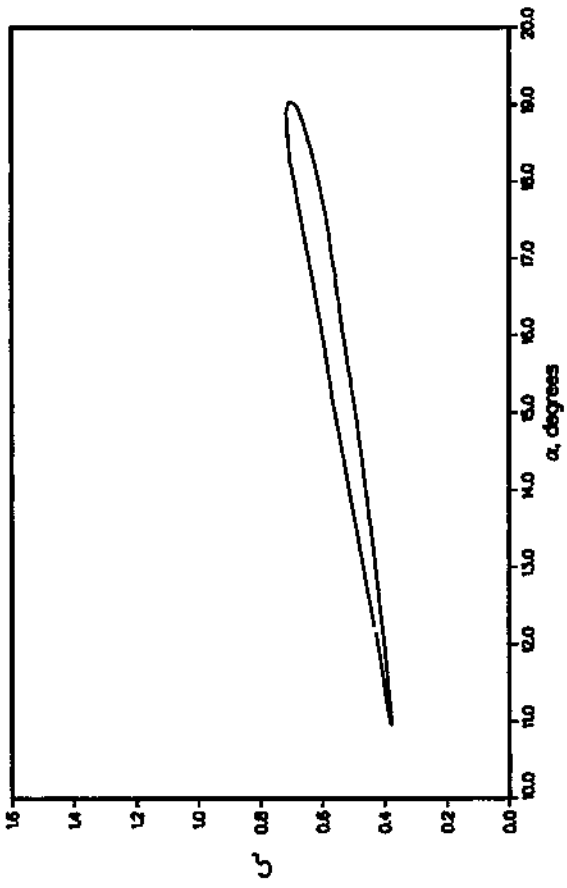


Figure 8(c). Lift and pitching-moment coefficients as a function of angle of attack, for 3-D wing experiencing dynamic stall at $M = 0.3$, $\alpha = 15^\circ + 4^\circ \sin \omega t$, $k = 0.04$ (from ref. 3).

99.5% SPAN

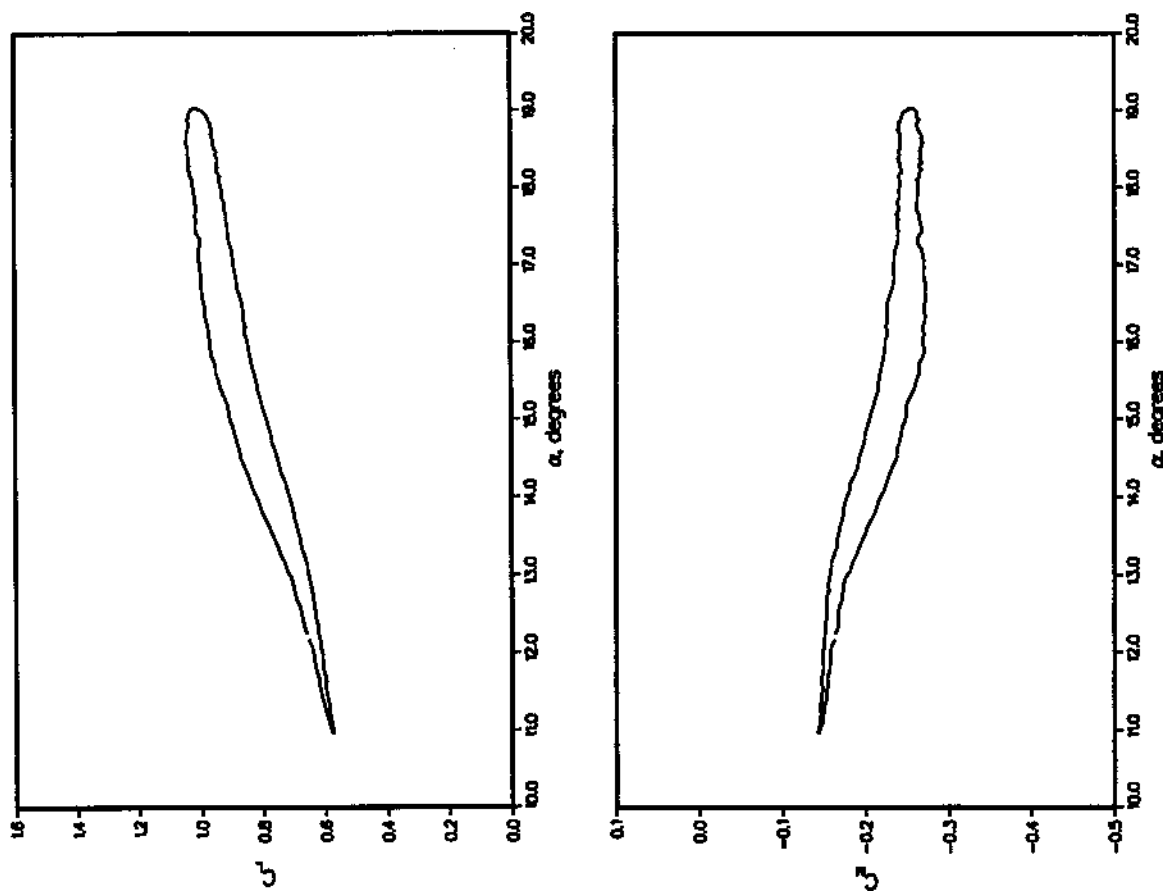
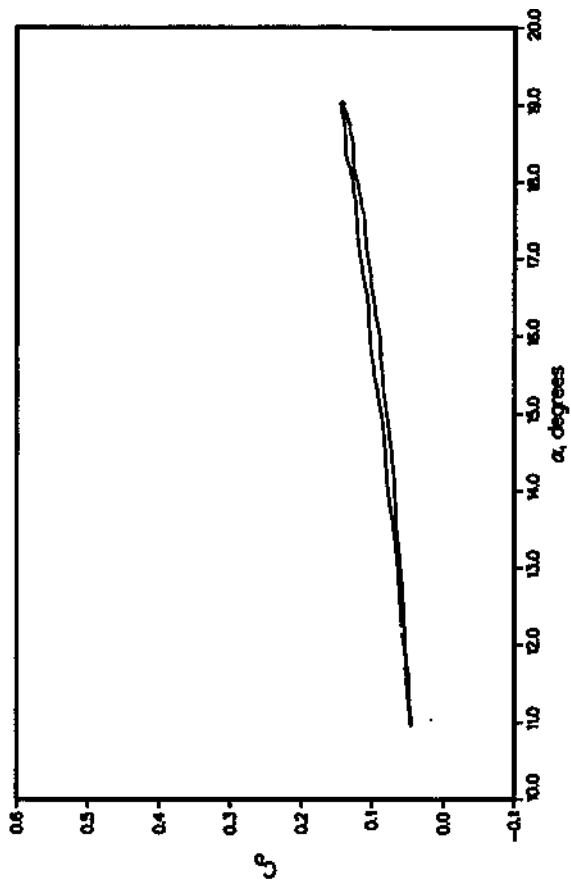
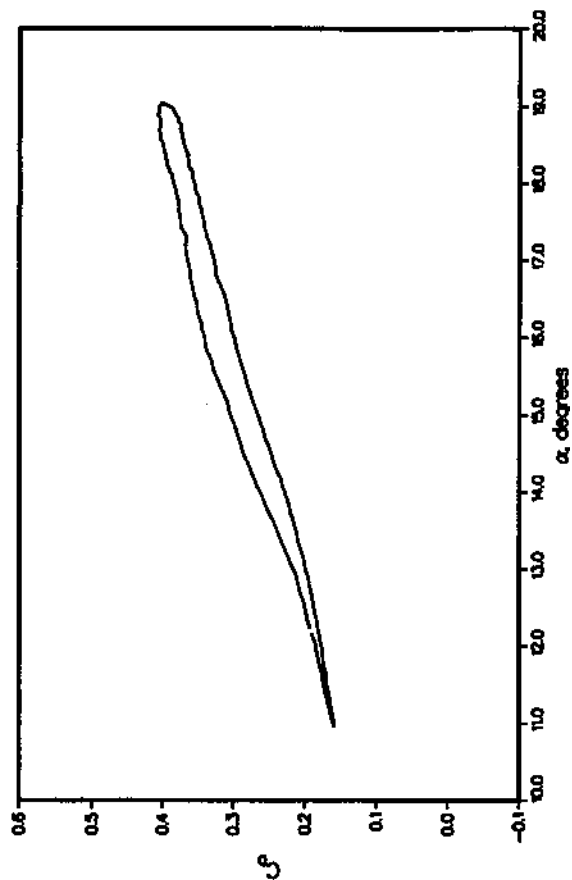


Figure 8(d). Lift and pitching-moment coefficients as a function of angle of attack, for 3-D wing experiencing dynamic stall at $M = 0.3$, $\alpha = 15^\circ + 4^\circ \sin \omega t$, $k = 0.04$ (from ref. 3).

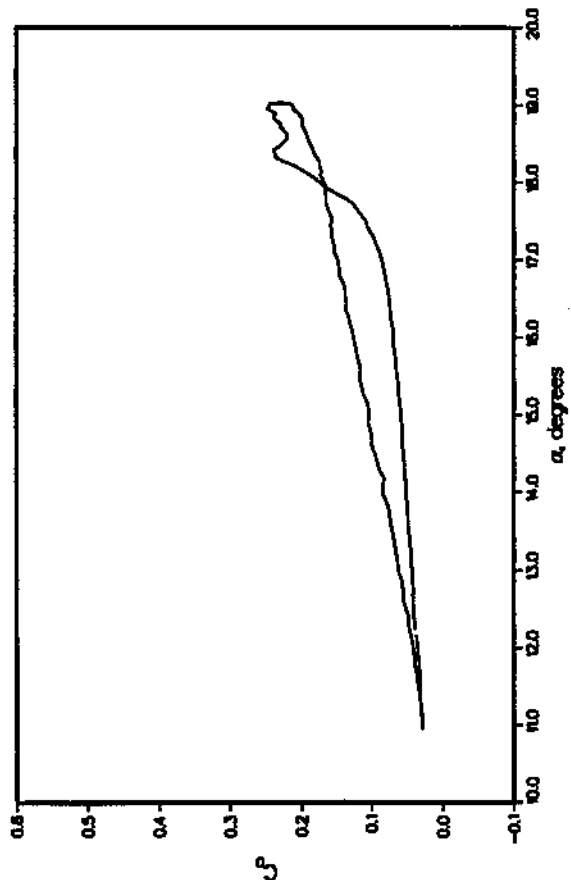
96.6% SPAN



99.5% SPAN



47.5% SPAN



98.6% SPAN

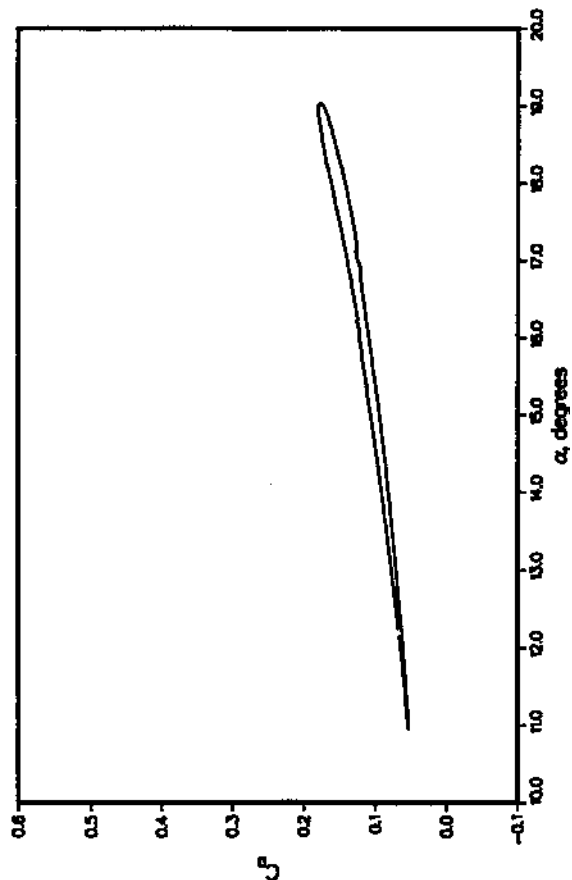
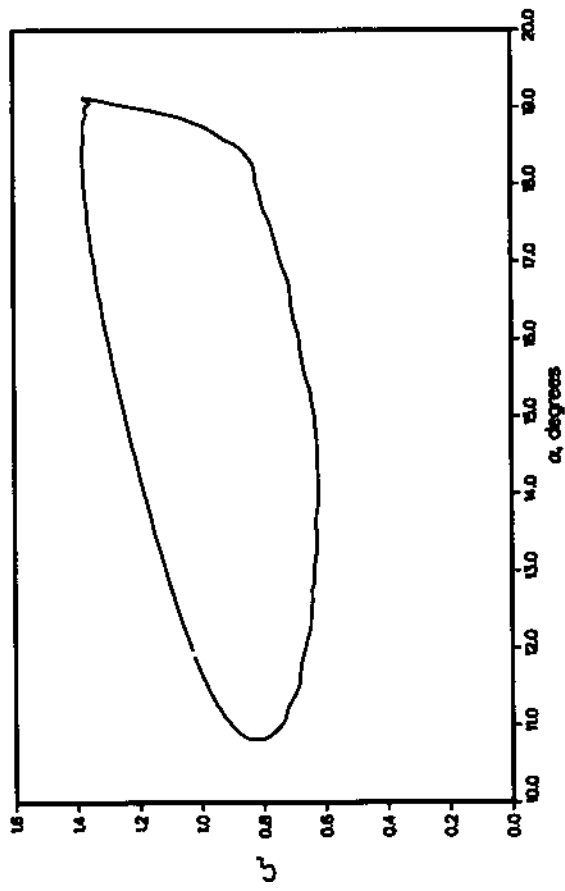


Figure 8(e). Drag coefficients as a function of angle of attack, for 3-D wing experiencing dynamic stall at $M = 0.3$, $\alpha = 15^\circ + 4^\circ \sin \omega t$, $k = 0.04$; drag at four spanwise stations (from ref. 3).

25% SPAN



47.5% SPAN

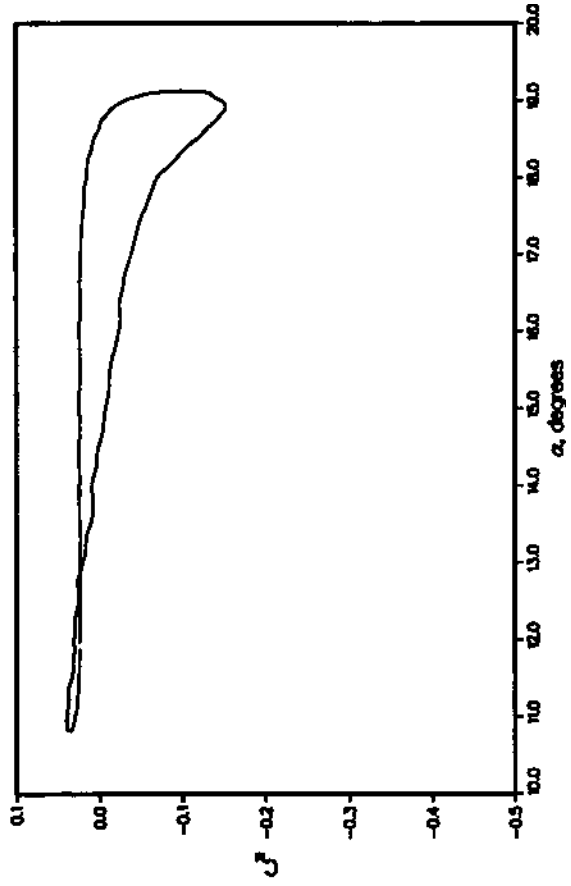
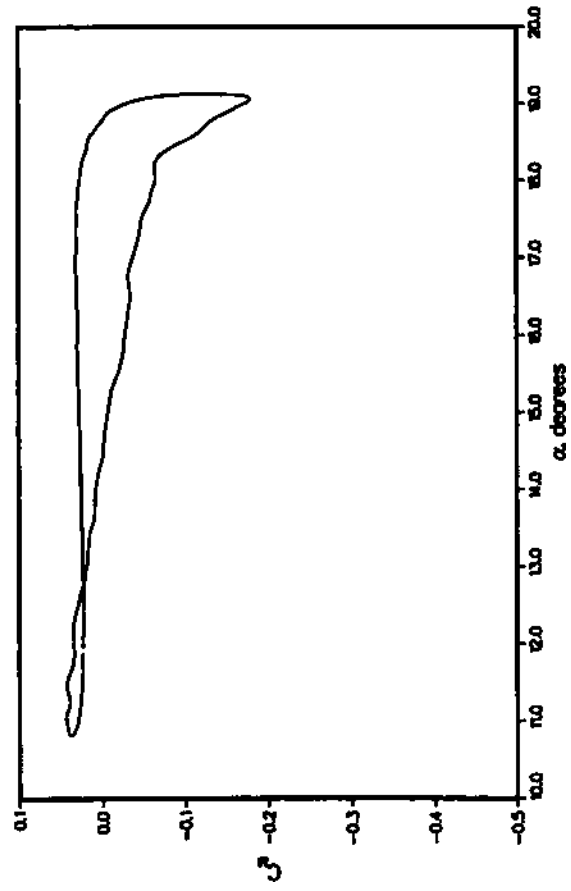
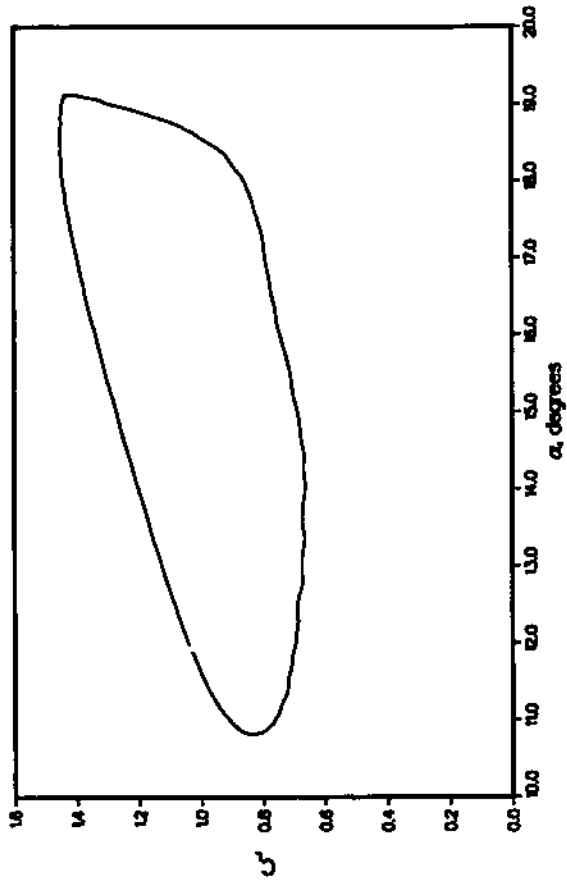
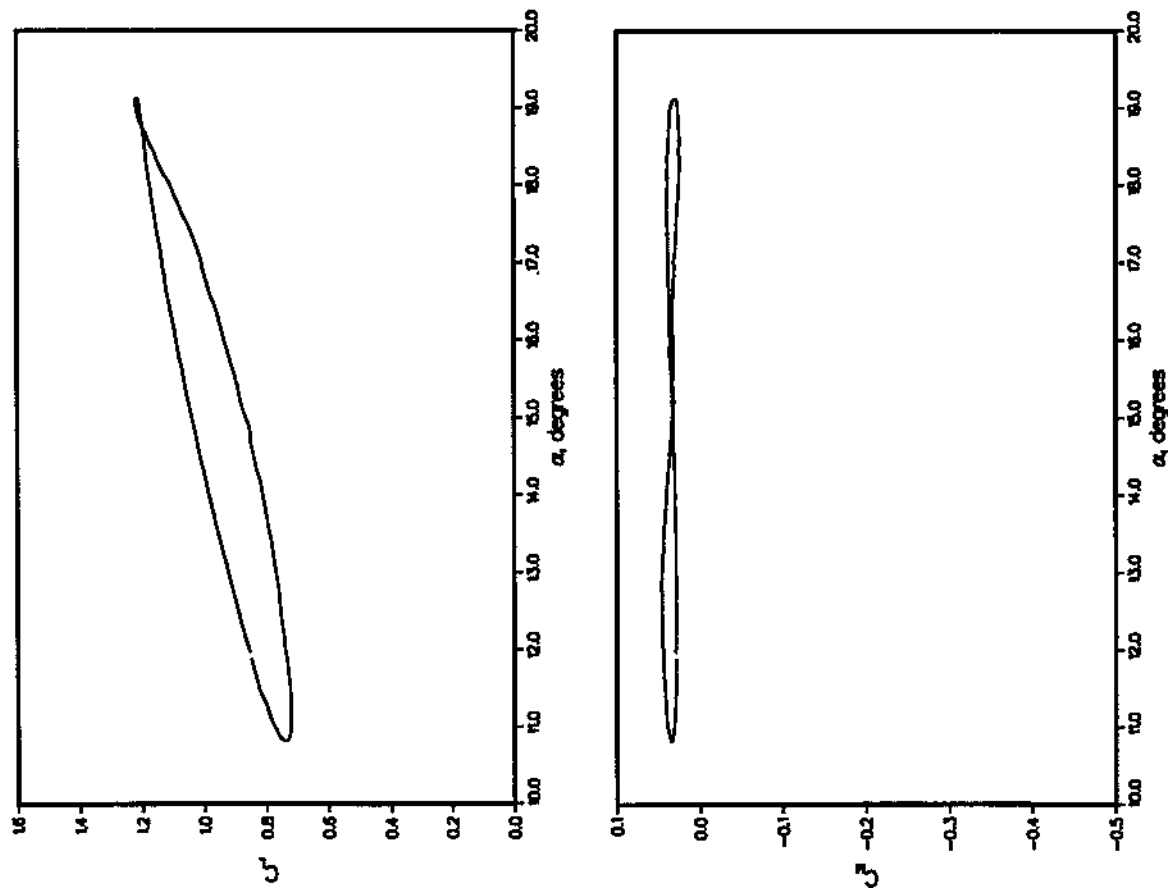


Figure 9(a). Lift and pitching-moment coefficients as a function of angle of attack, for 3-D wing experiencing dynamic stall at $M = 0.3$, $\alpha = 15^\circ + 4^\circ \sin \omega t$, $k = 0.10$ (from ref. 3).

80% SPAN



90% SPAN

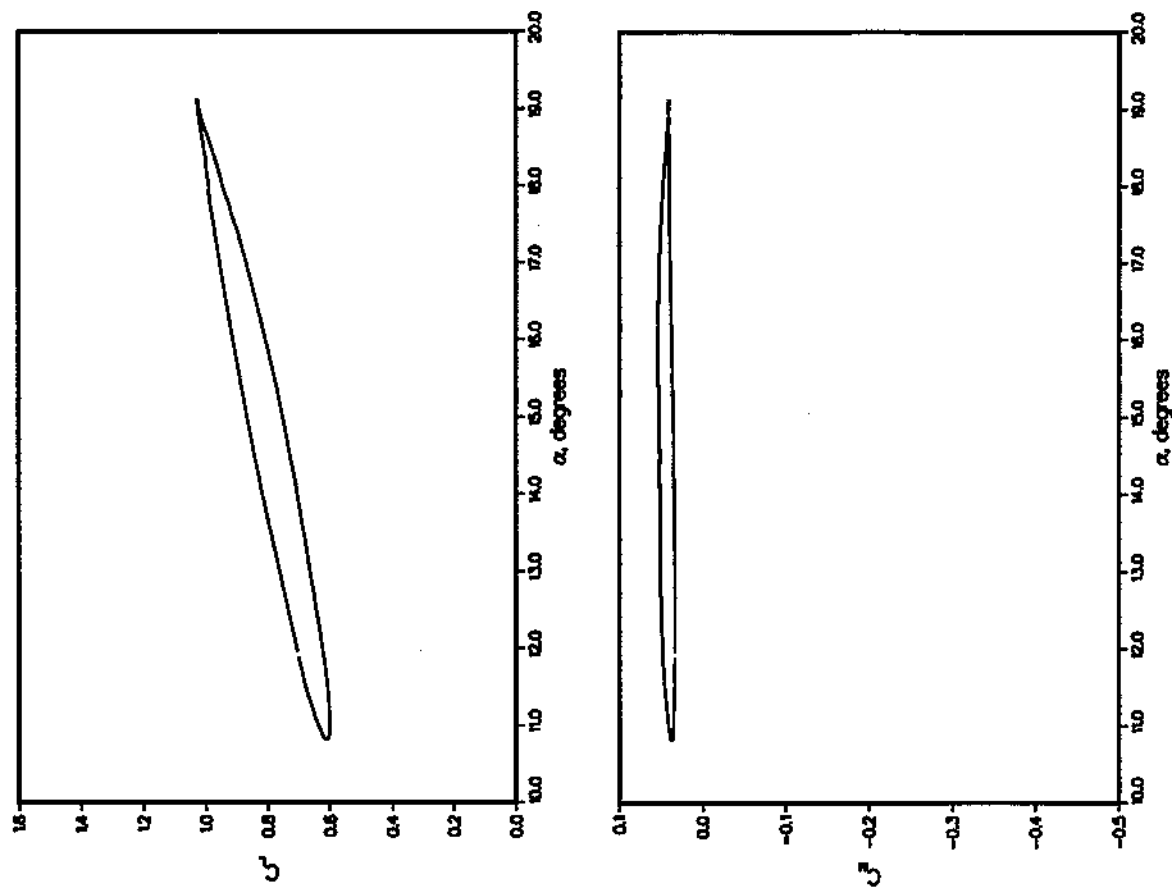
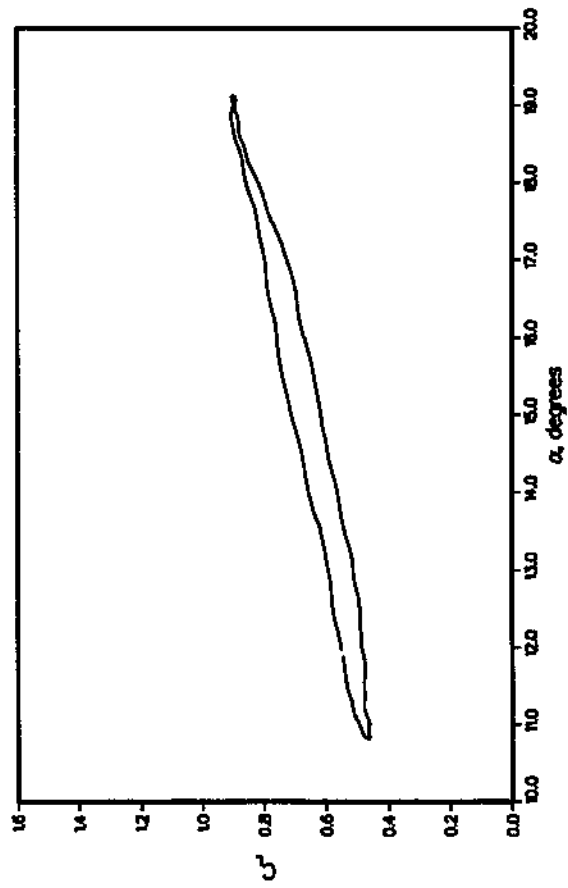


Figure 9(b). Lift and pitching-moment coefficients as a function of angle of attack, for 3-D wing experiencing dynamic stall at $M = 0.3$, $\alpha = 15^\circ + 4^\circ \sin \omega t$, $k = 0.10$ (from ref. 3).

96.6% SPAN



98.6% SPAN

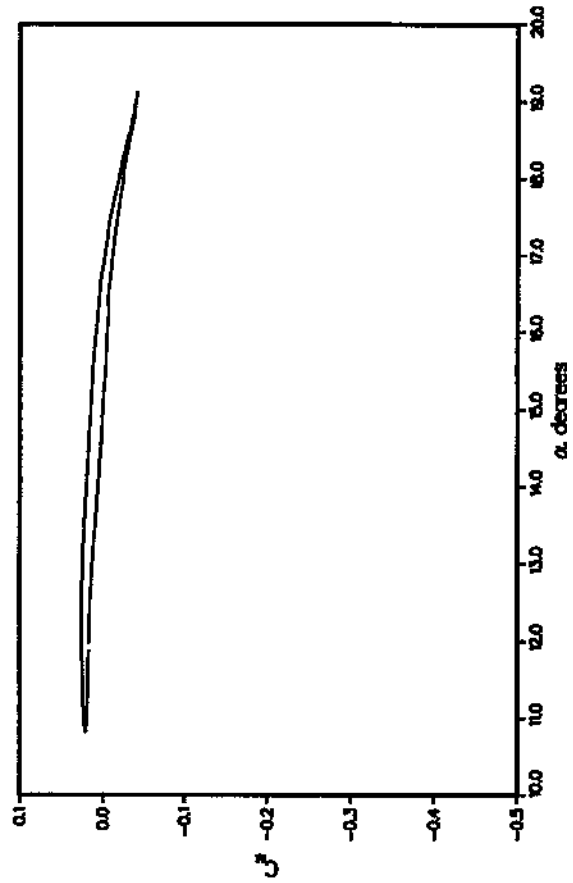
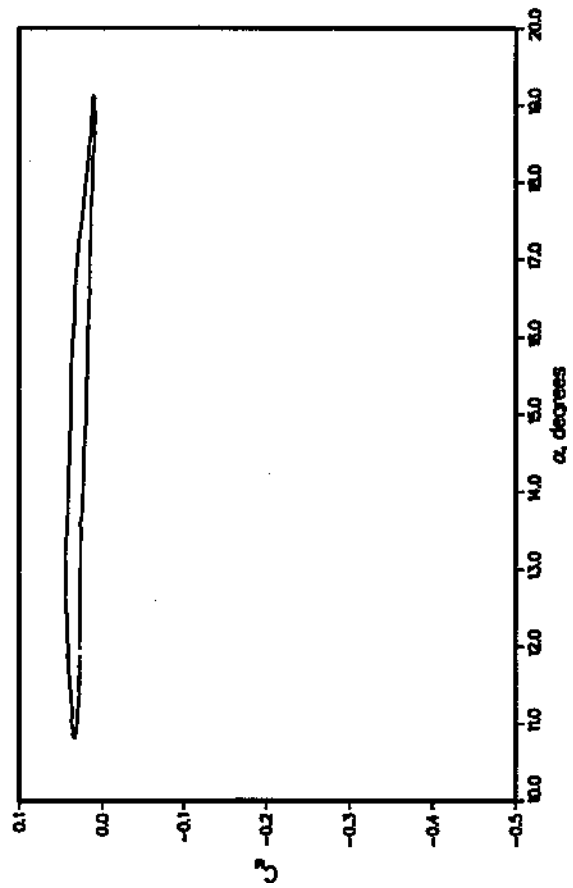
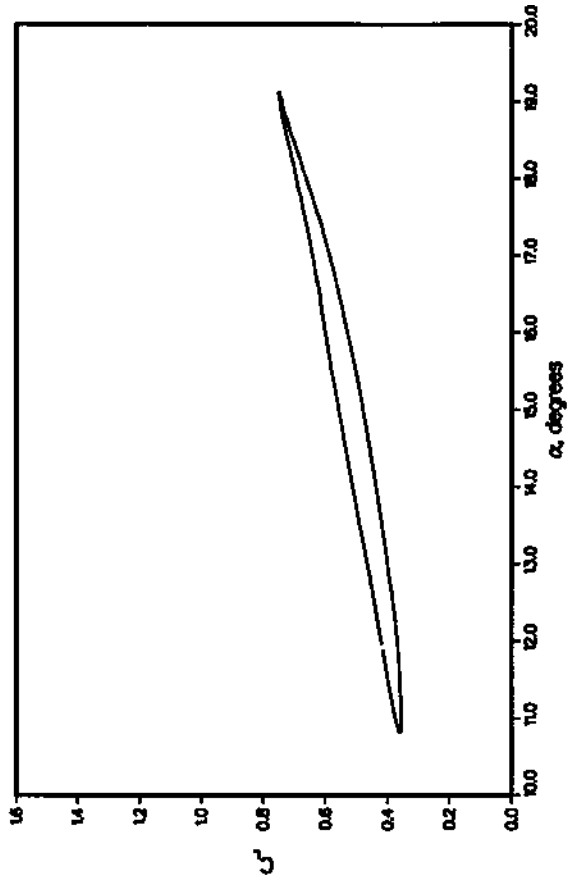


Figure 9(c). Lift and pitching-moment coefficients as a function of angle of attack, for 3-D wing experiencing dynamic stall at $M = 0.3$, $\alpha = 15^\circ + 4^\circ \sin \omega t$, $k = 0.10$ (from ref. 3).

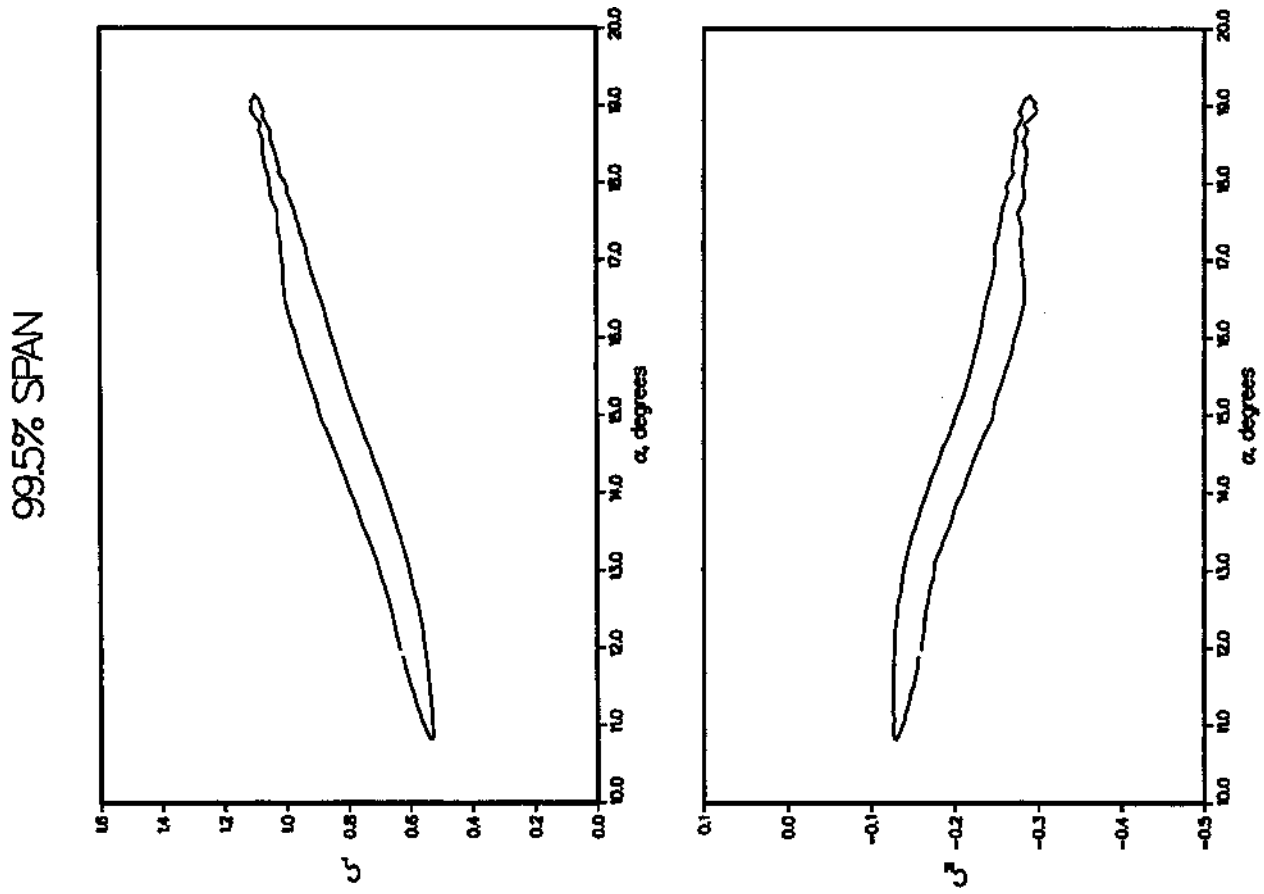
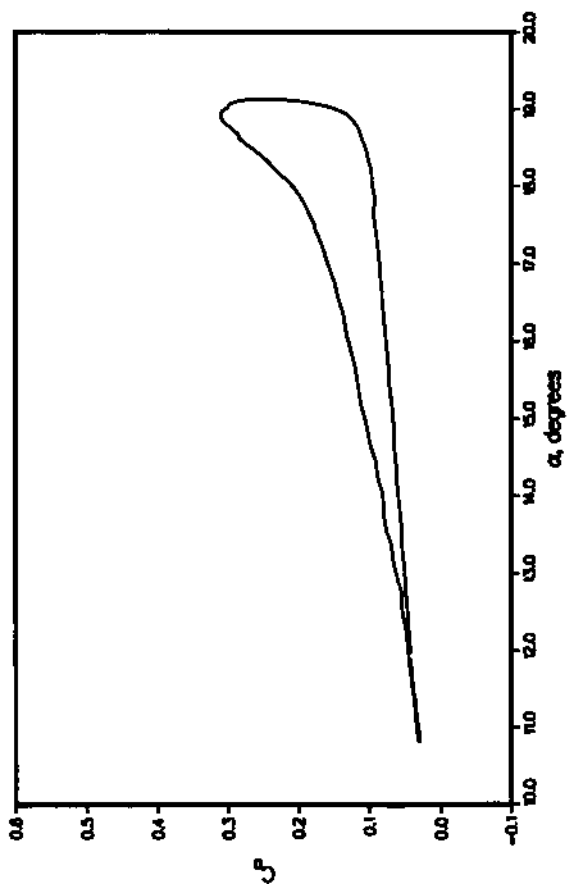
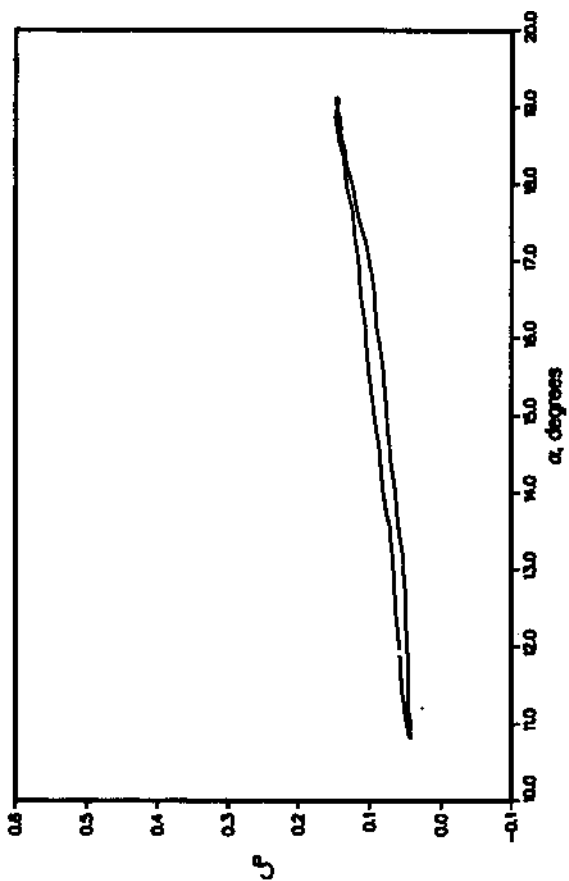


Figure 9(d). Lift and pitching-moment coefficients as a function of angle of attack, for 3-D wing experiencing dynamic stall at $M = 0.3$, $\alpha = 15^\circ + 4^\circ \sin \omega t$, $k = 0.10$ (from ref. 3).

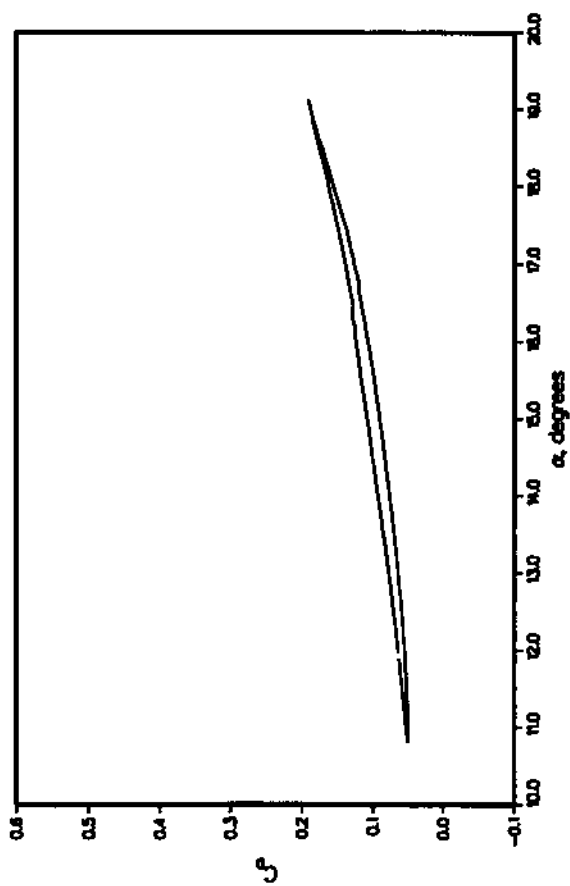
47.5% SPAN



96.6% SPAN



98.6% SPAN



99.5% SPAN

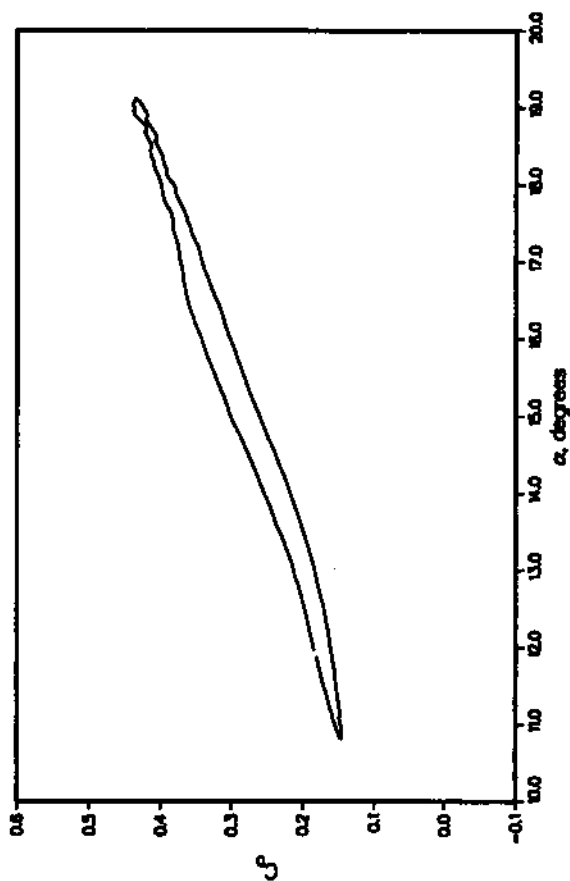
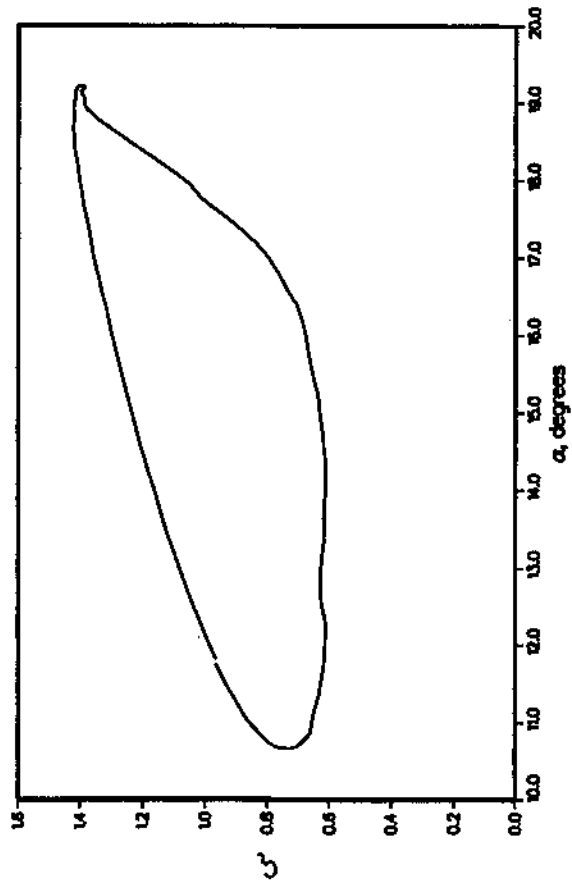


Figure 9(e). Drag coefficients as a function of angle of attack, for 3-D wing experiencing dynamic stall at $M = 0.3$, $\alpha = 15^\circ + 4^\circ \sin \omega t$, $k = 0.10$; drag at four spanwise stations (from ref. 3).

25% SPAN



47.5% SPAN

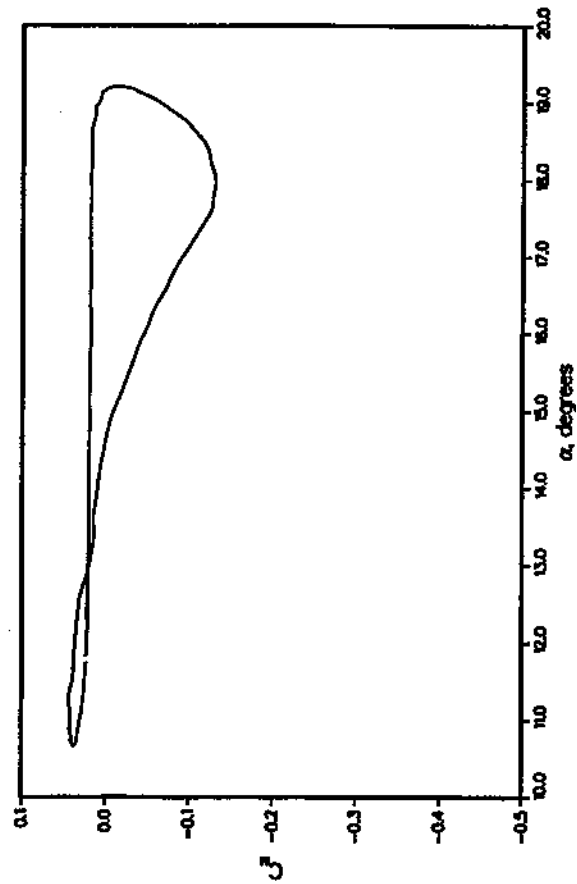
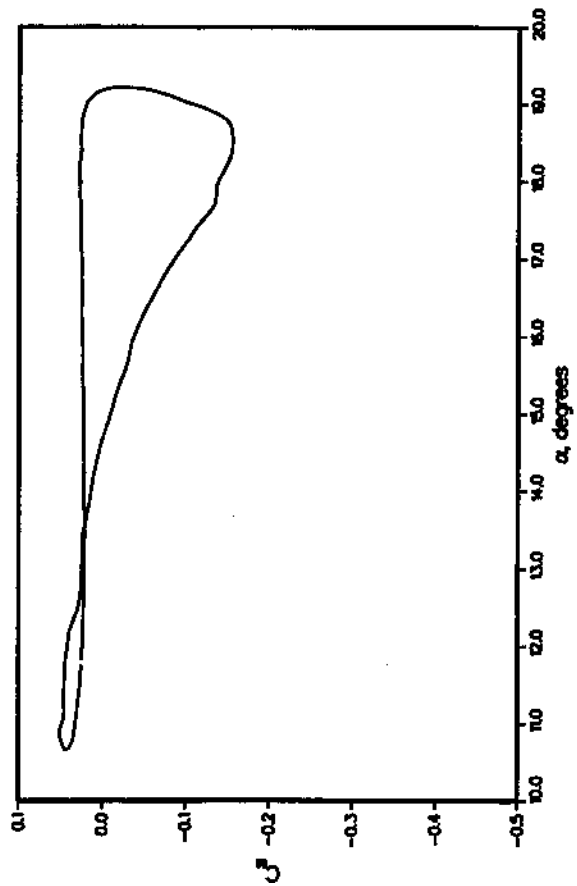
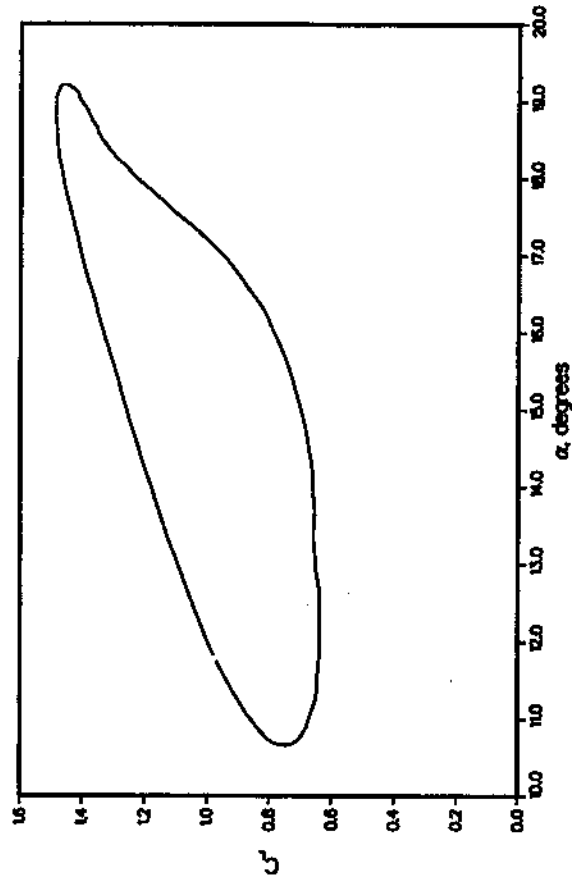
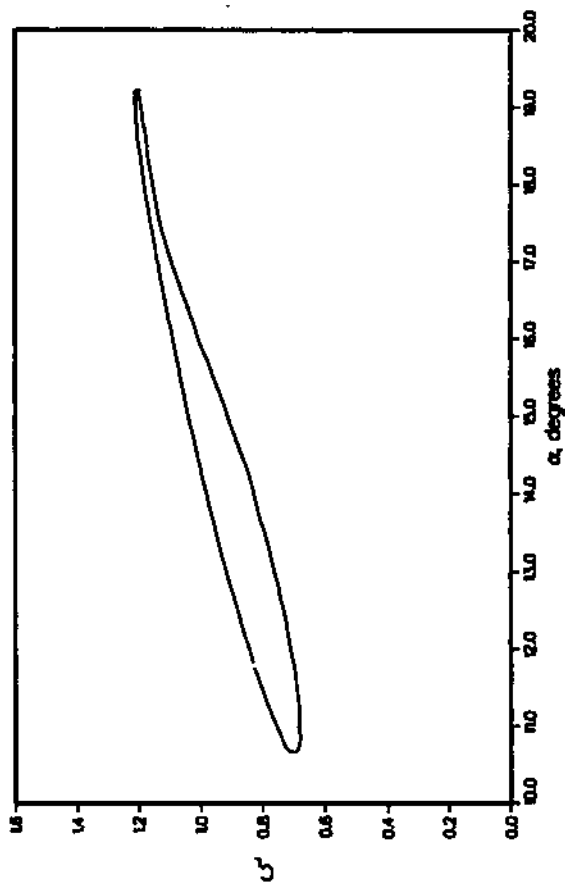


Figure 10(a). Lift and pitching-moment coefficients as a function of angle of attack, for 3-D wing experiencing dynamic stall at $M = 0.3$, $\alpha = 15^\circ + 4^\circ \sin \omega t$, $k = 0.14$ (from ref. 3).

80% SPAN



90% SPAN

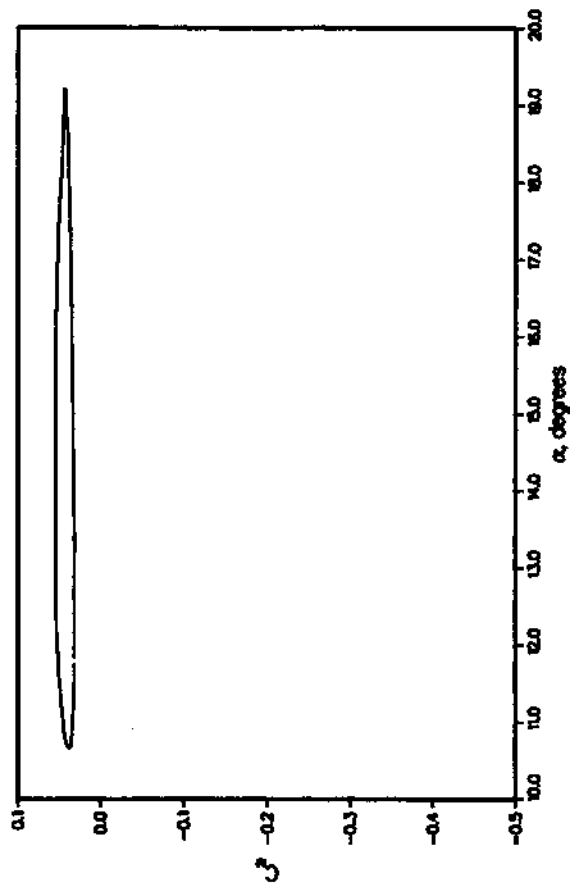
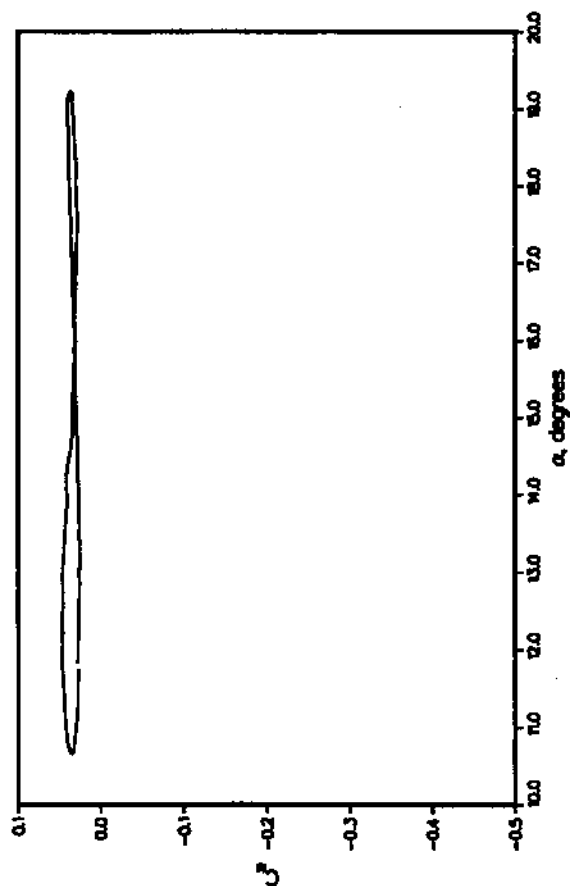
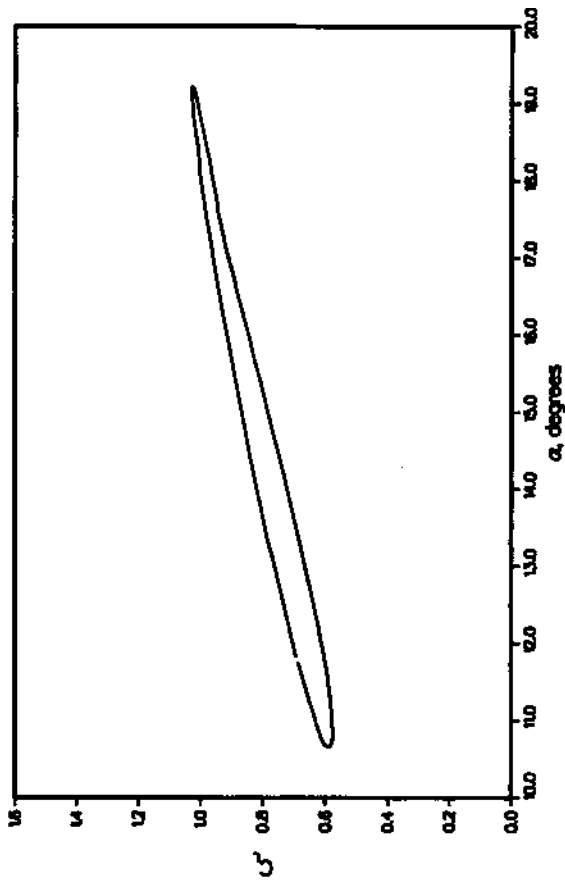
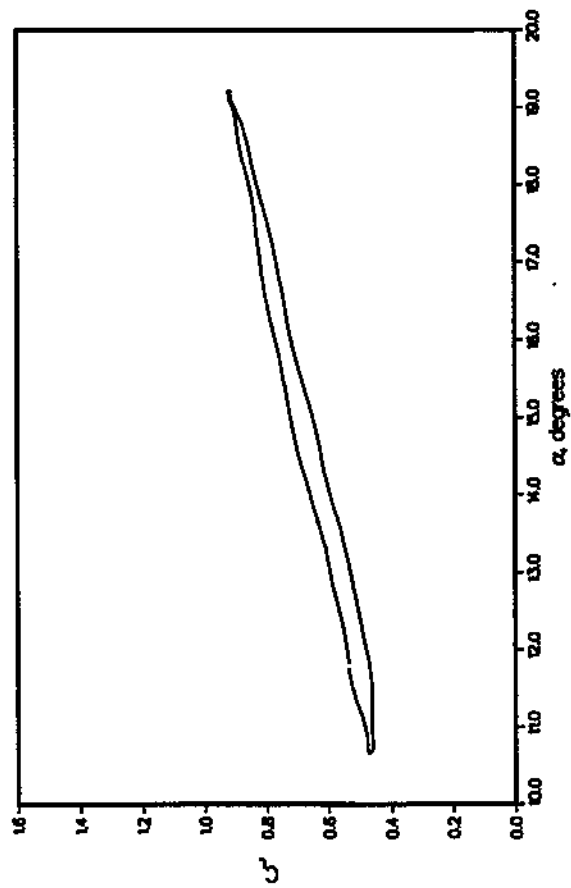


Figure 10(b). Lift and pitching-moment coefficients as a function of angle of attack, for 3-D wing experiencing dynamic stall at $M = 0.3$, $\alpha = 15^\circ + 4^\circ \sin \omega t$, $k = 0.14$ (from ref. 3).

96.6% SPAN



98.6% SPAN

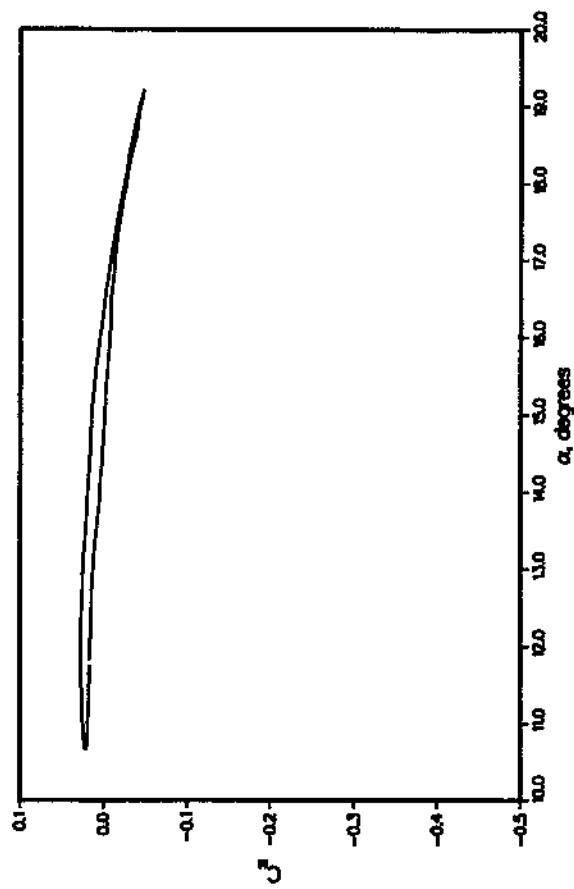
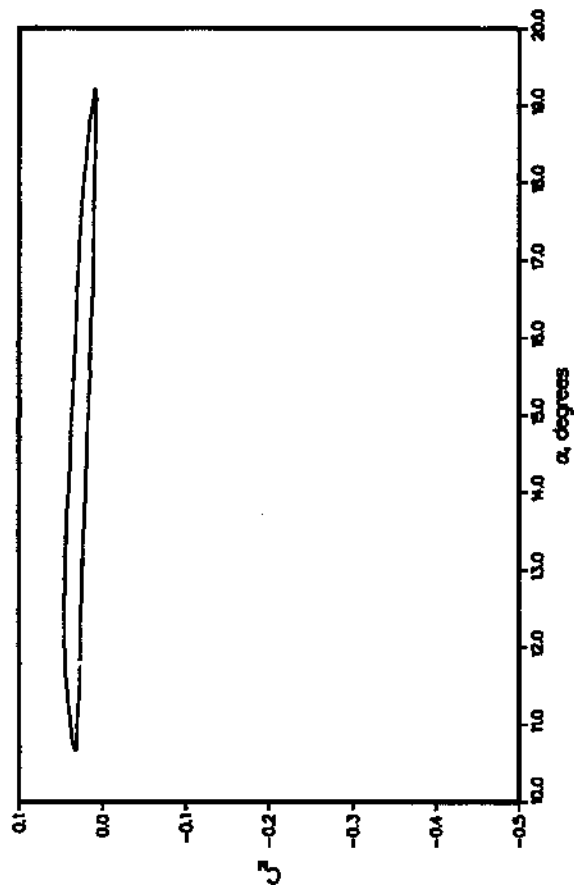
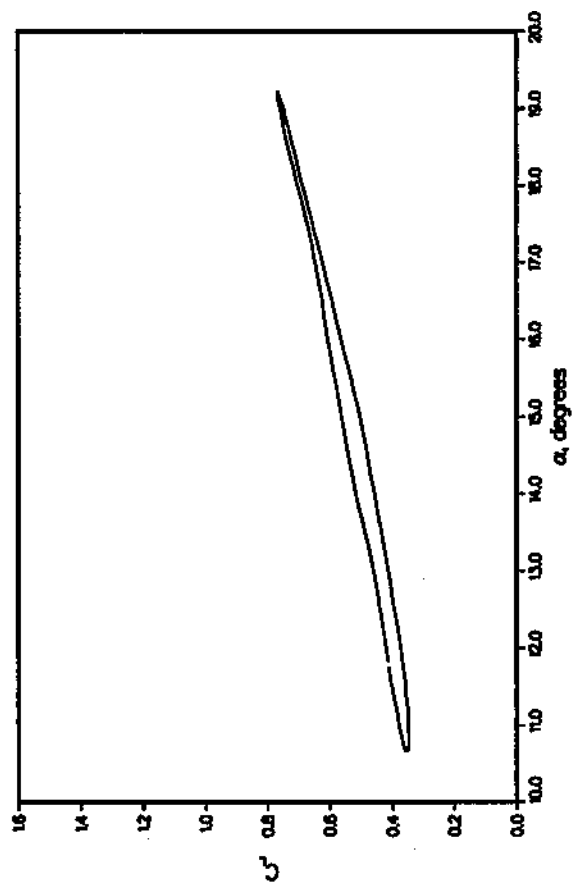


Figure 10(c). Lift and pitching-moment coefficients as a function of angle of attack, for 3-D wing experiencing dynamic stall at $M = 0.3$, $\alpha = 15^\circ + 4^\circ \sin \omega t$, $k = 0.14$ (from ref. 3).

99.5% SPAN

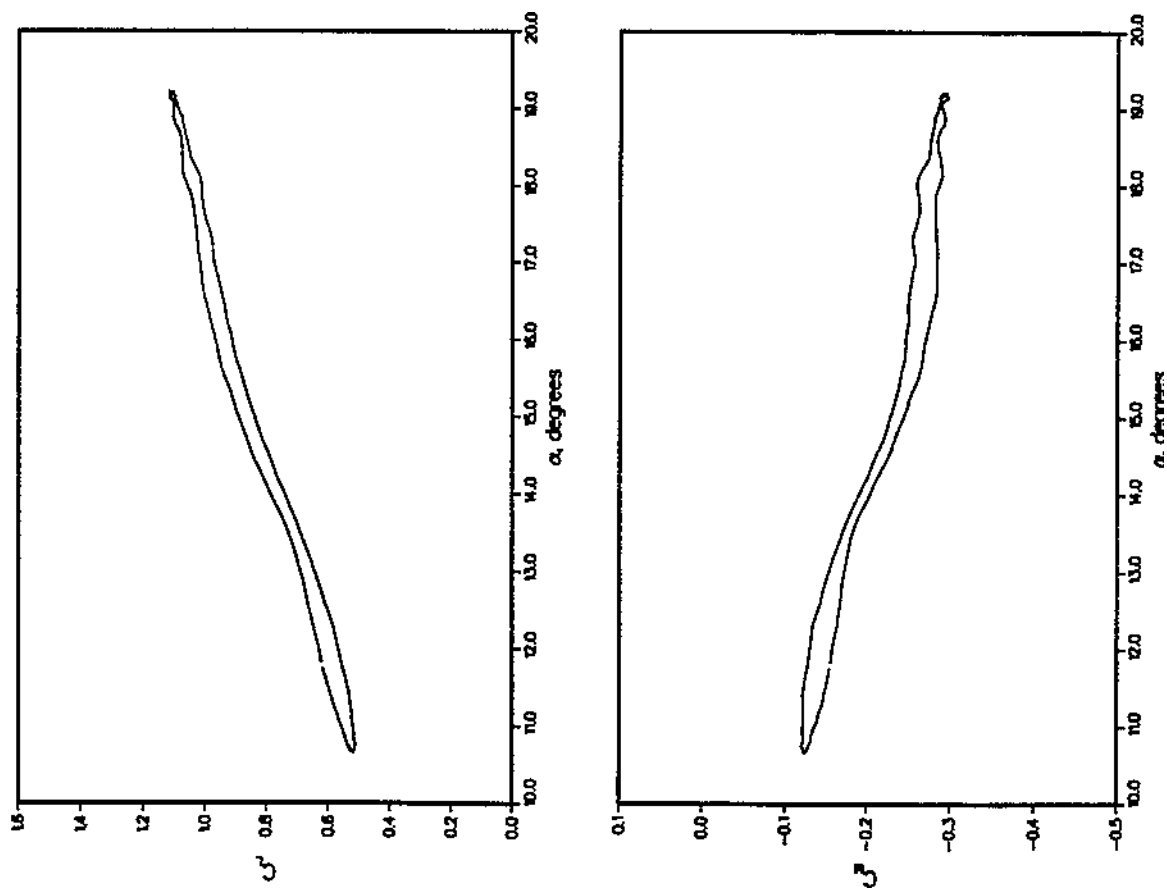
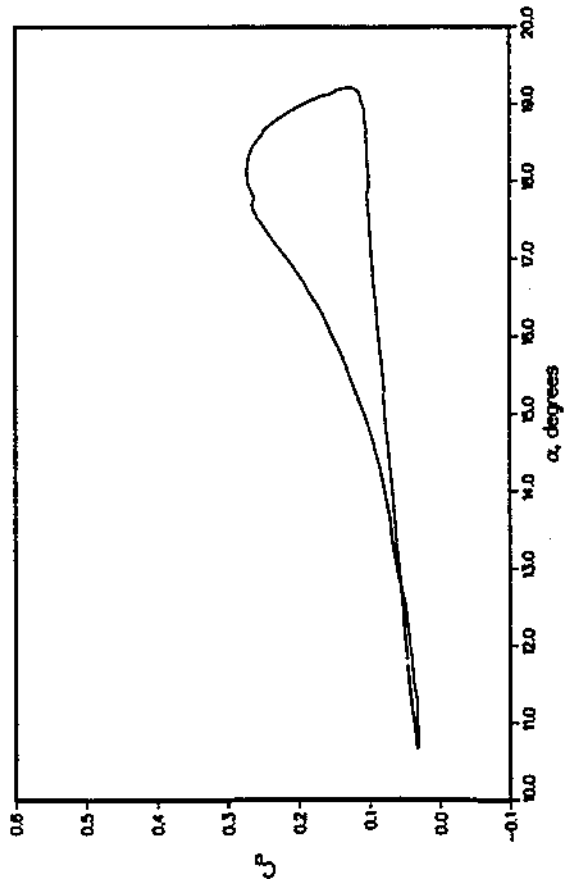
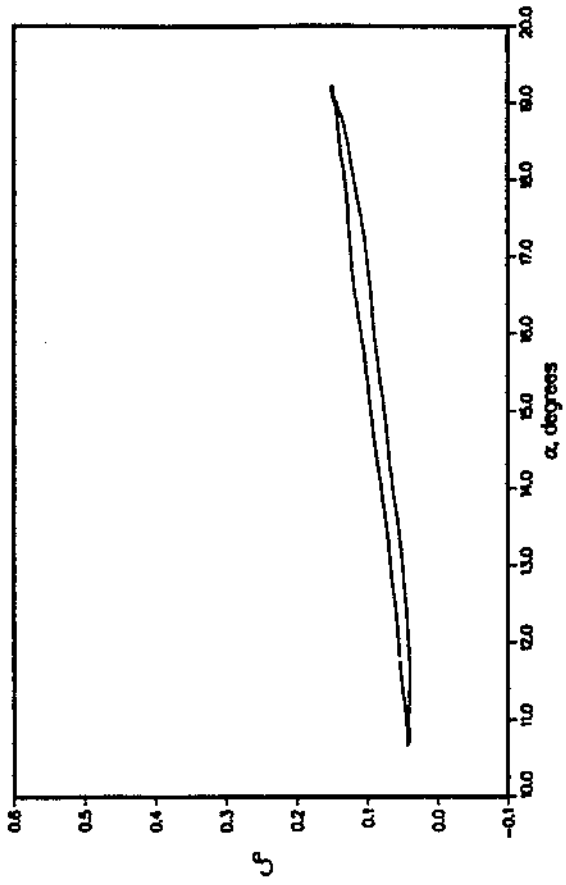


Figure 10(d). Lift and pitching-moment coefficients as a function of angle of attack, for 3-D wing experiencing dynamic stall at $M = 0.3$, $\alpha = 15^\circ + 4^\circ \sin \omega t$, $k = 0.14$ (from ref. 3).

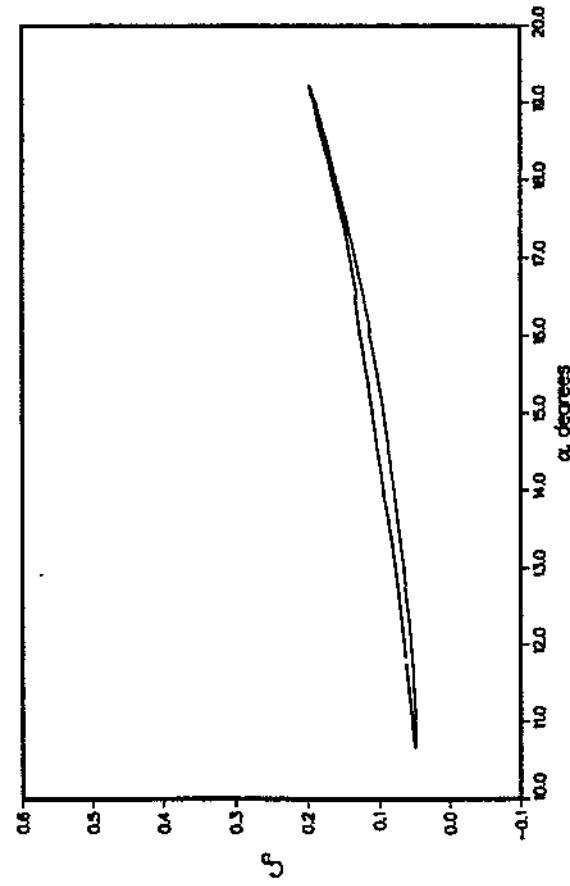
47.5% SPAN



96.6% SPAN



98.6% SPAN



99.5% SPAN

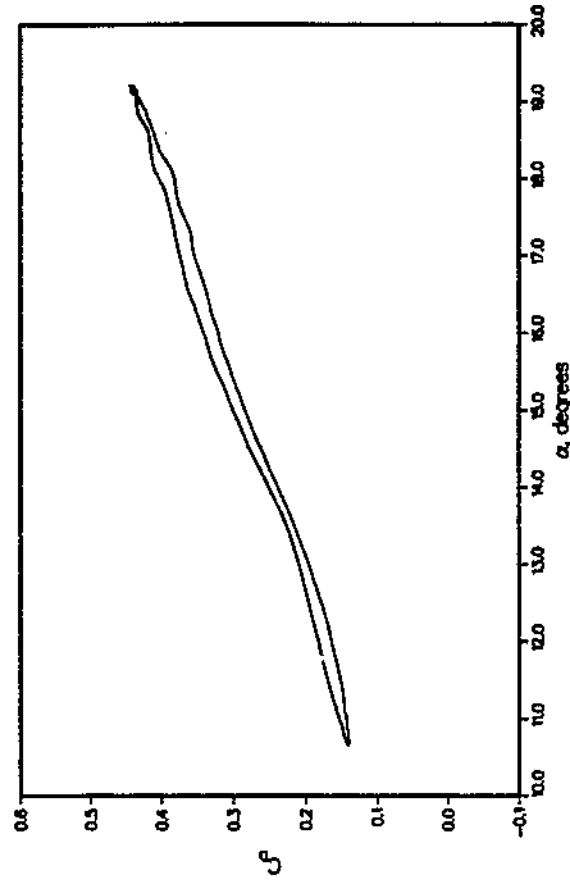
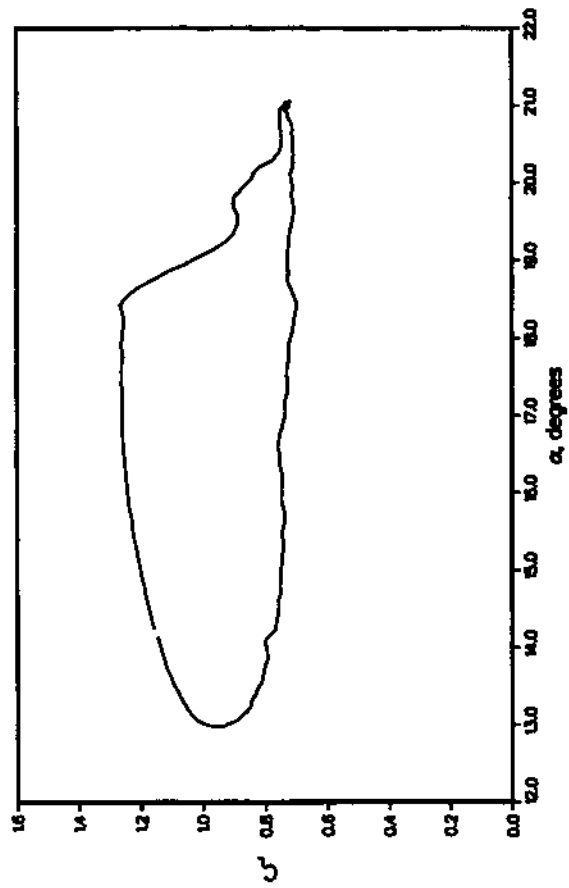


Figure 10(e). Drag coefficients as a function of angle of attack, for 3-D wing experiencing dynamic stall at $M = 0.3$, $\alpha = 15^\circ + 4^\circ \sin \omega t$, $k = 0.14$; drag at four spanwise stations (from ref. 3).

25% SPAN



47.5% SPAN

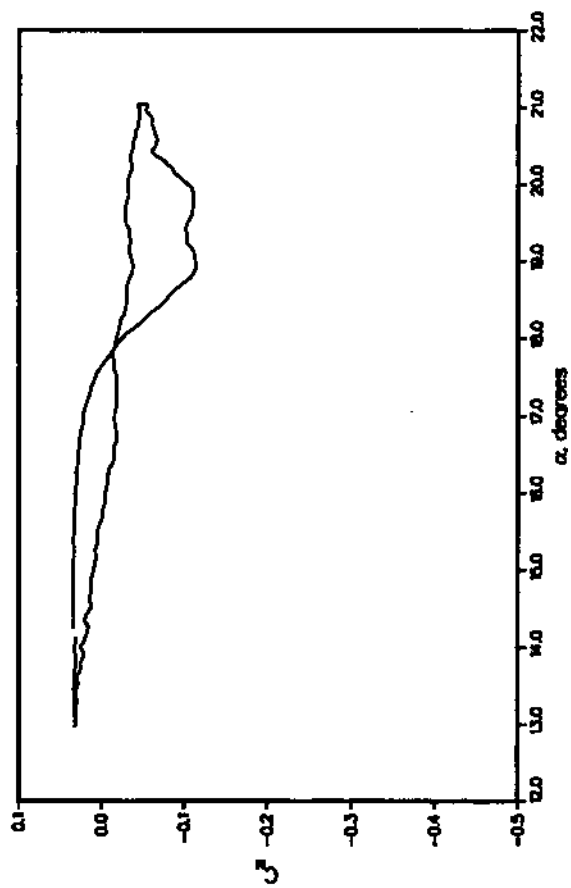
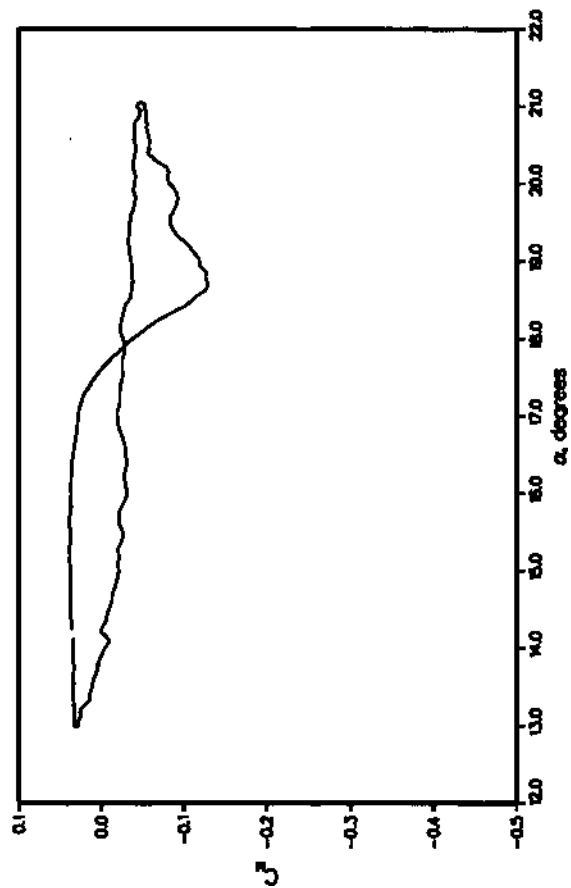
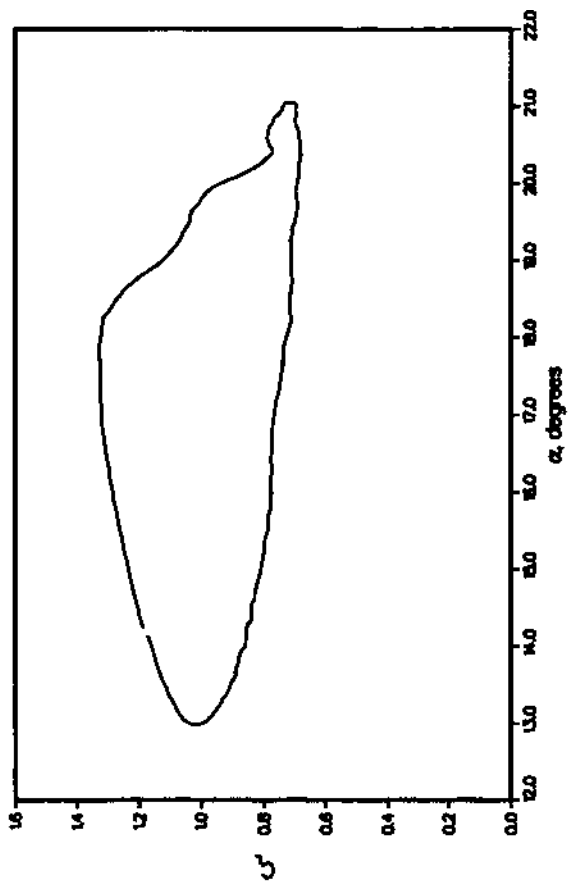
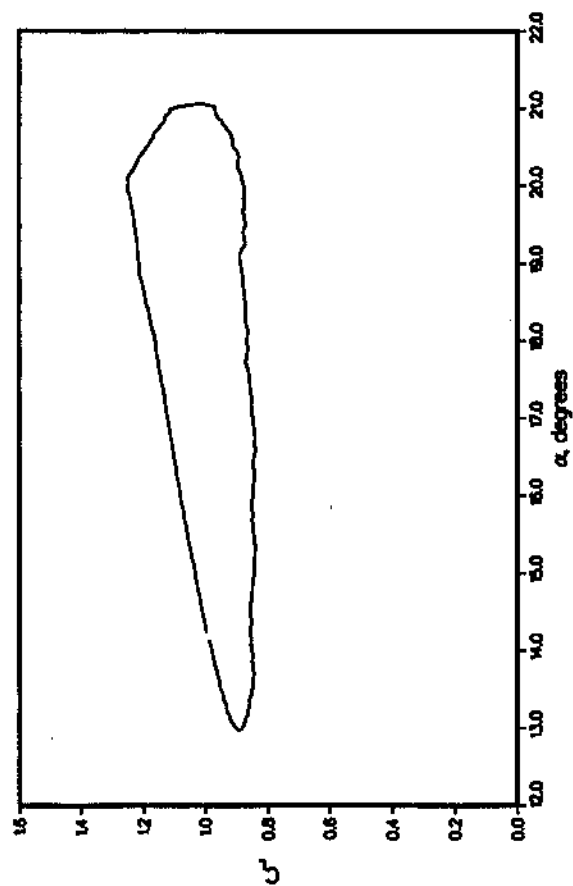


Figure 11(a). Lift and pitching-moment coefficients as a function of angle of attack, for 3-D wing experiencing dynamic stall at $M = 0.3$, $\alpha = 17^\circ + 4^\circ \sin \omega t$, $k = 0.04$ (from ref. 3).

80% SPAN



90% SPAN

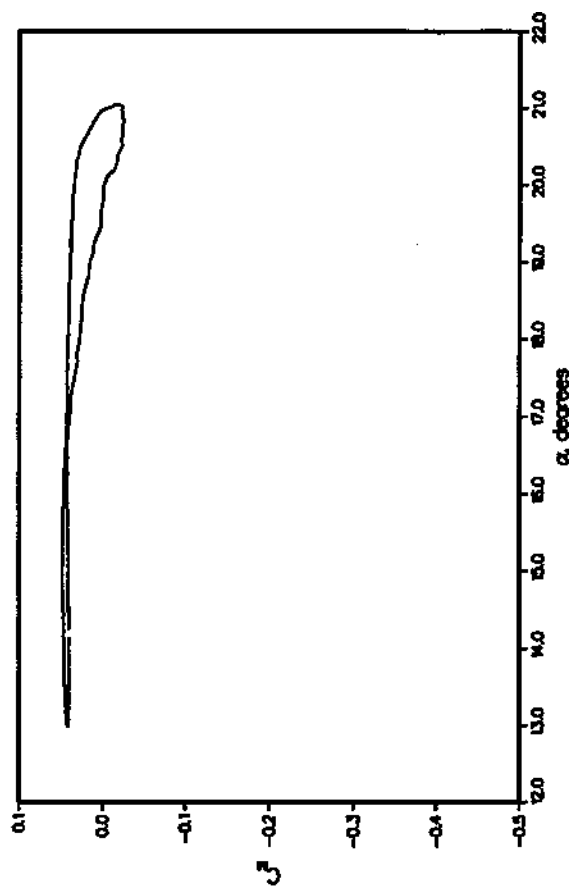
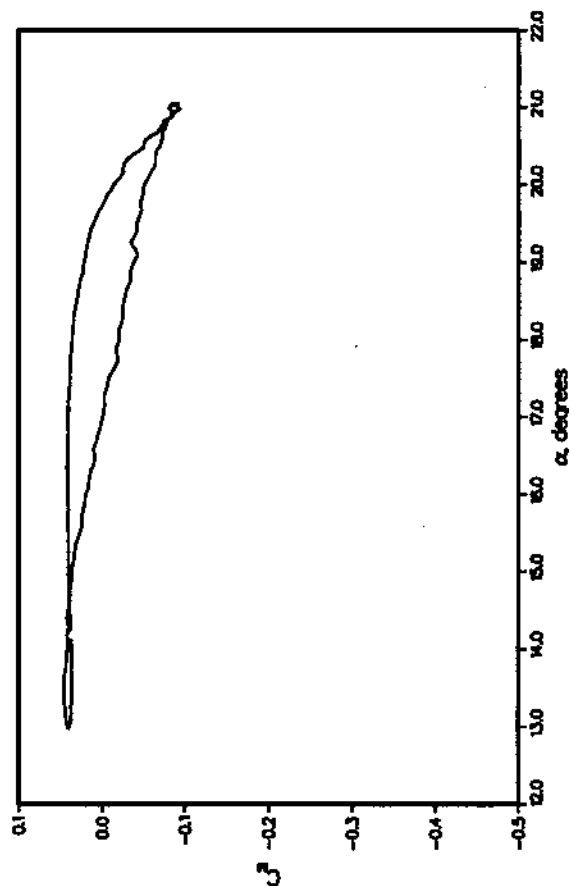
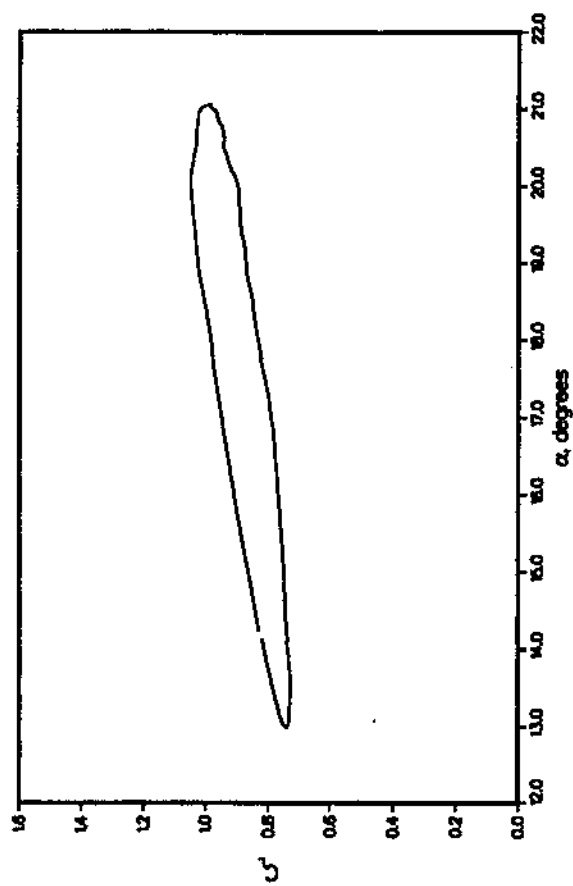
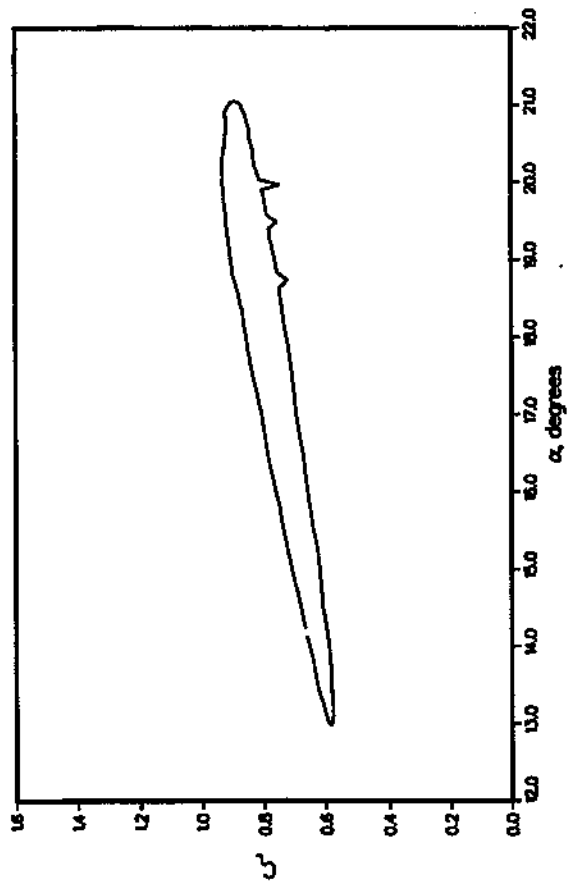


Figure 11(b). Lift and pitching-moment coefficients as a function of angle of attack, for 3-D wing experiencing dynamic stall at $M = 0.3$, $\alpha = 17^\circ + 4^\circ \sin \omega t$, $k = 0.04$ (from ref. 3).

96.6% SPAN



98.6% SPAN

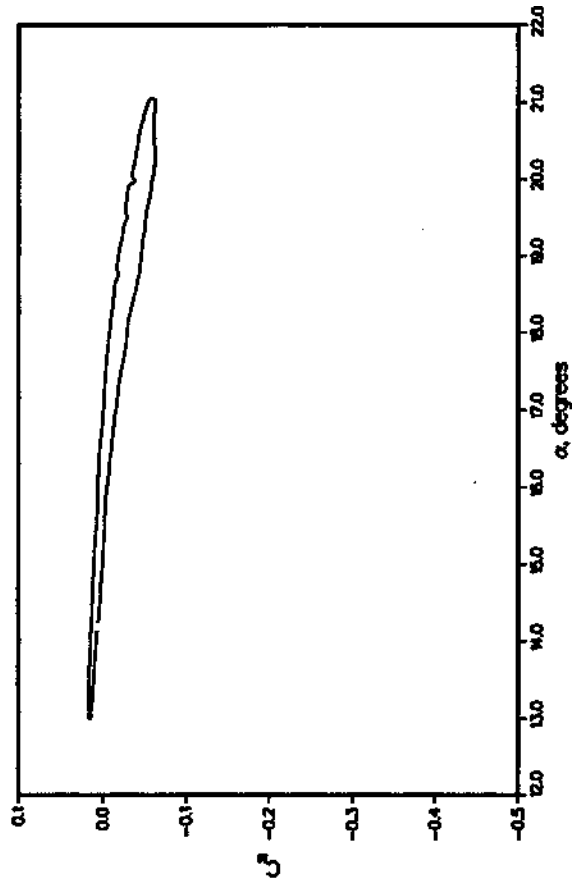
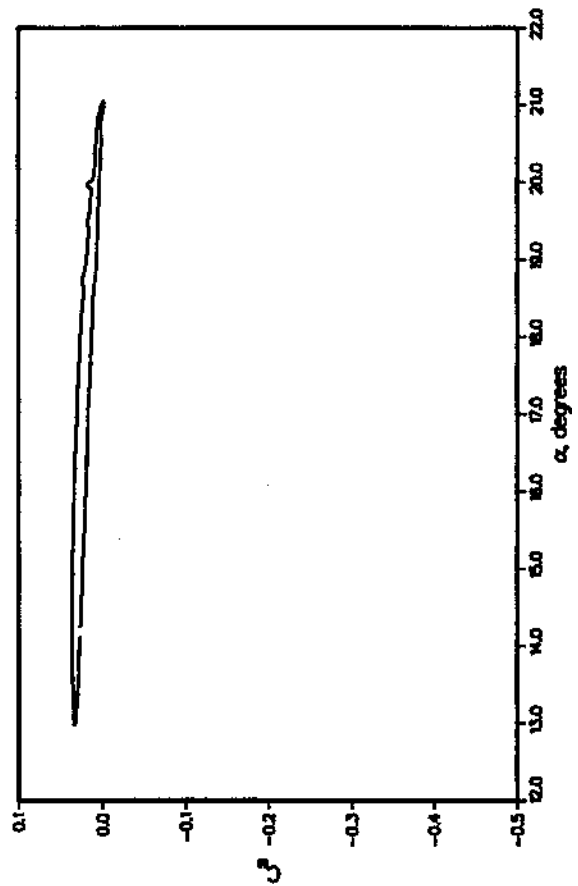
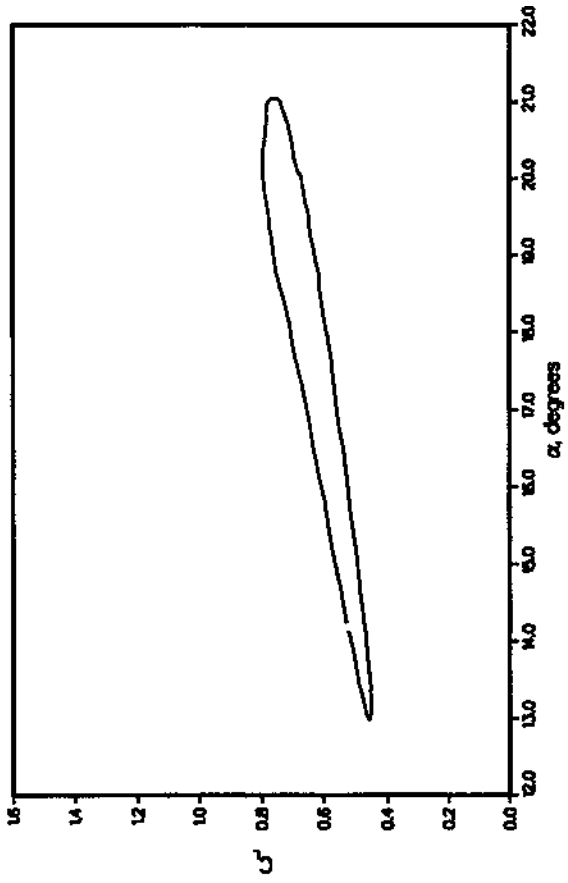


Figure 11(c). Lift and pitching-moment coefficients as a function of angle of attack, for 3-D wing experiencing dynamic stall at $M = 0.3$, $\alpha = 17^\circ + 4^\circ \sin \omega t$, $k = 0.04$ (from ref. 3).

99.5% SPAN

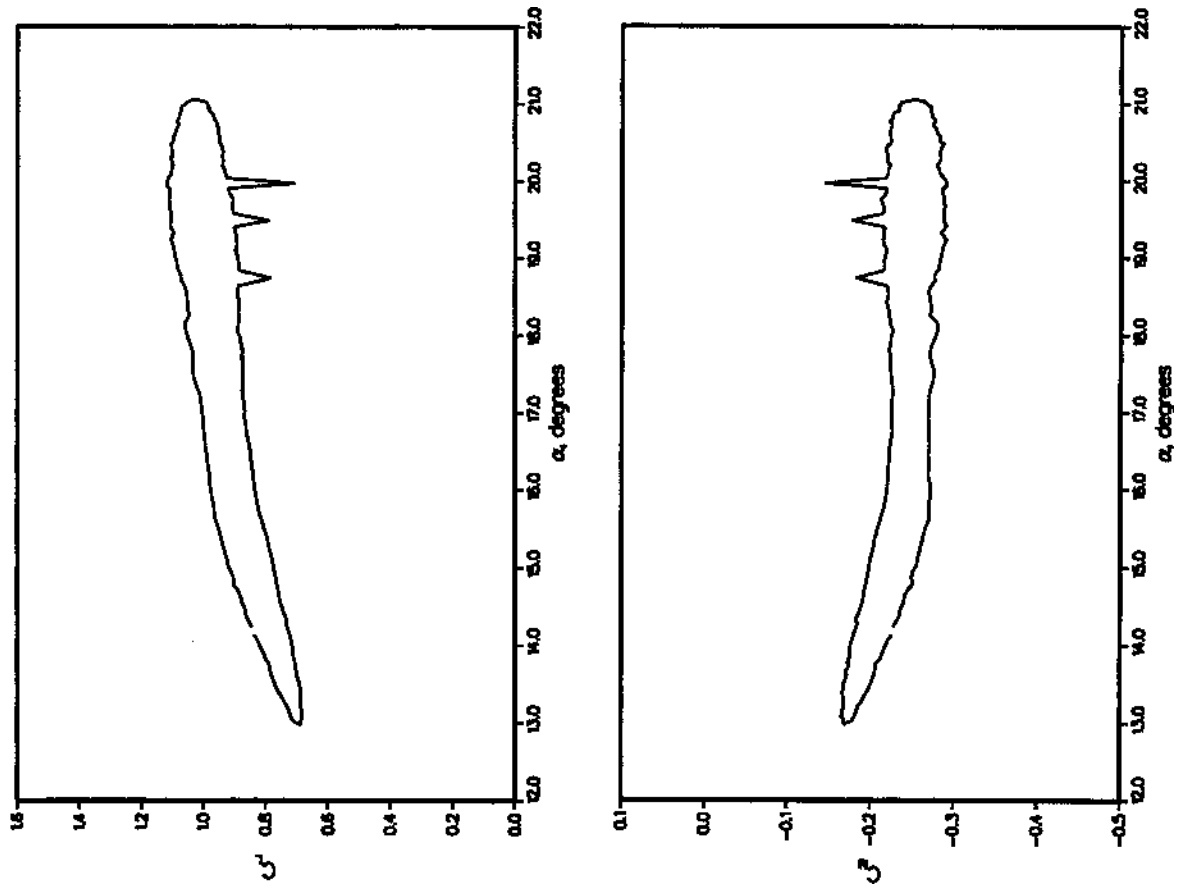
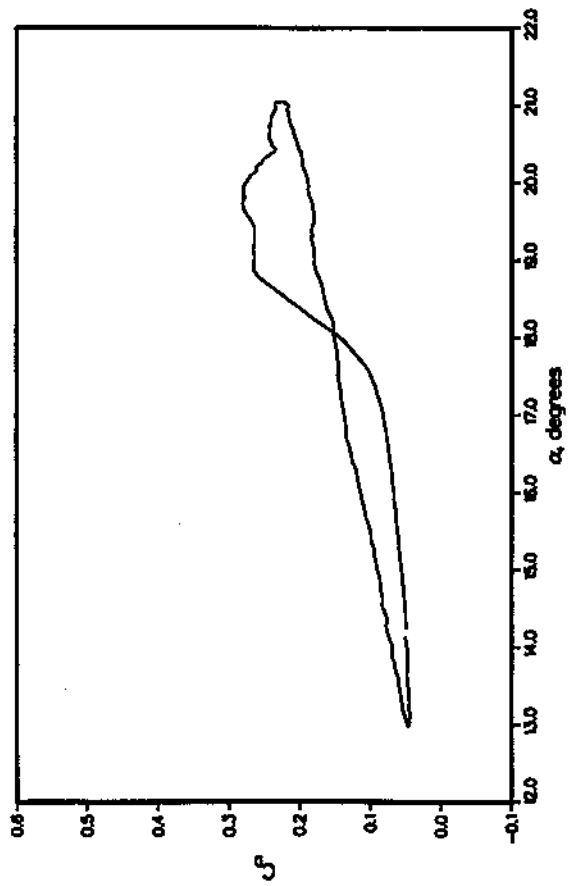
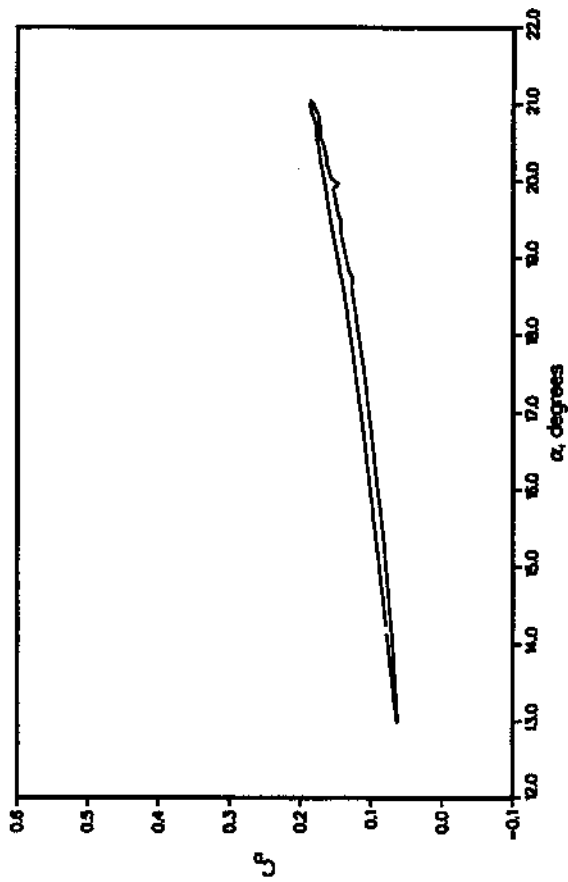


Figure 11(d). Lift and pitching-moment coefficients as a function of angle of attack, for 3-D wing experiencing dynamic stall at $M = 0.3$, $\alpha = 17^\circ + 4^\circ \sin \omega t$, $k = 0.04$ (from ref. 3).

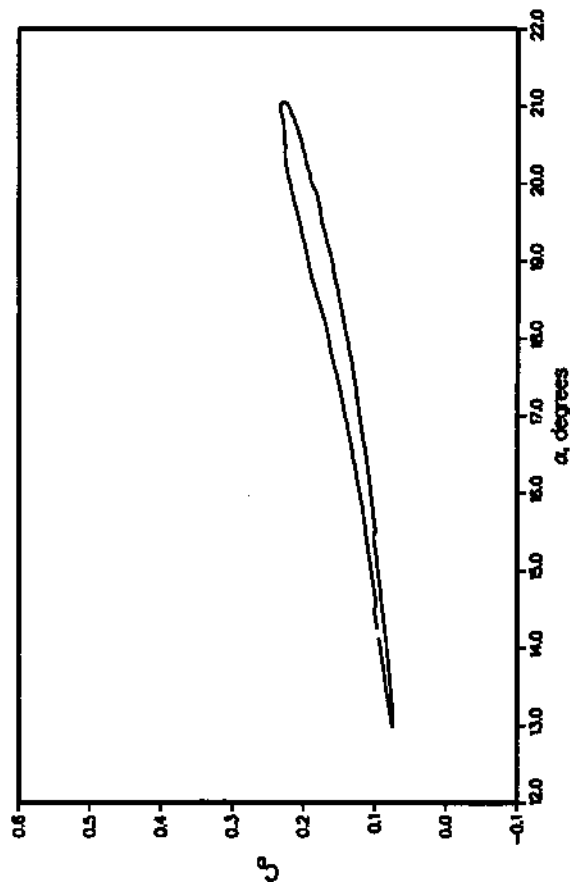
47.5% SPAN



96.6% SPAN



98.6% SPAN



99.5% SPAN

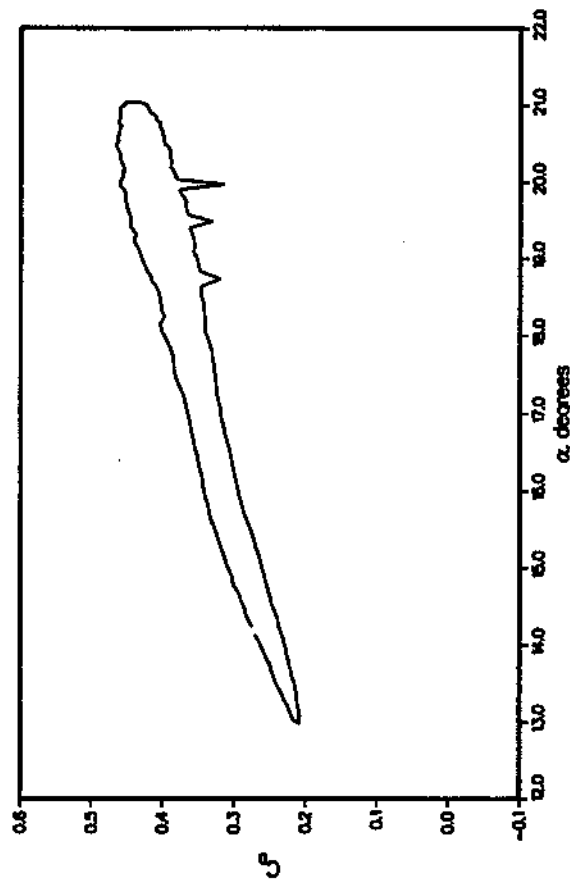
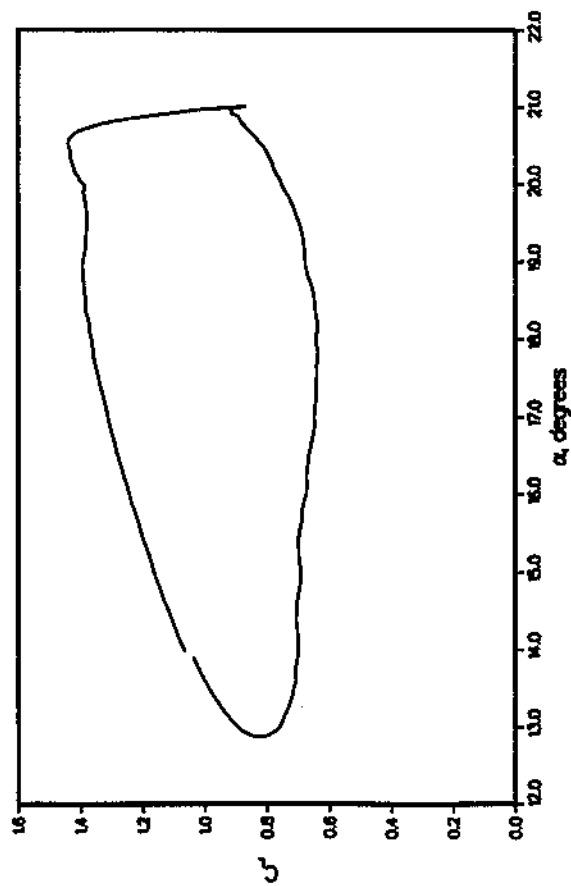


Figure 11(e). Drag coefficients as a function of angle of attack, for 3-D wing experiencing dynamic stall at $M = 0.3$, $\alpha = 17^\circ + 4^\circ \sin \omega t$, $k = 0.04$; drag at four spanwise stations (from ref. 3).

25% SPAN



47.5% SPAN

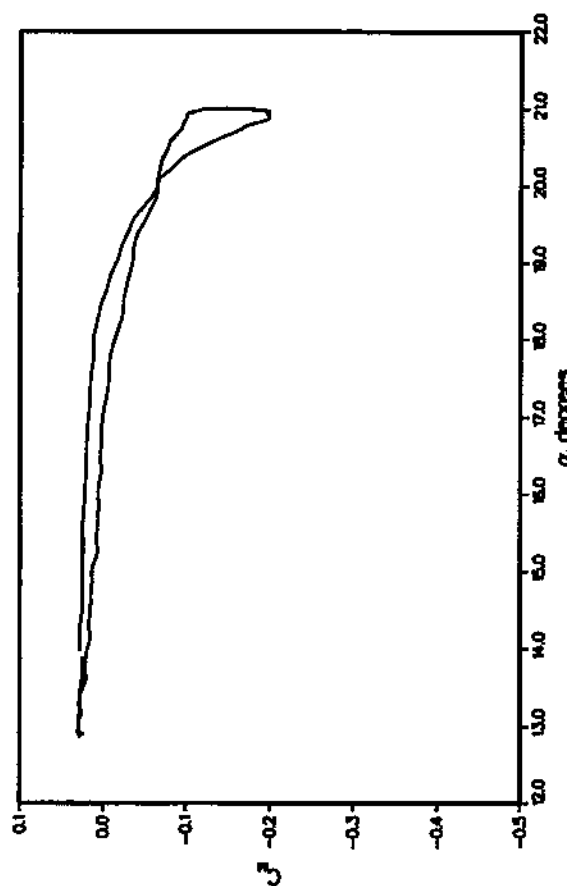
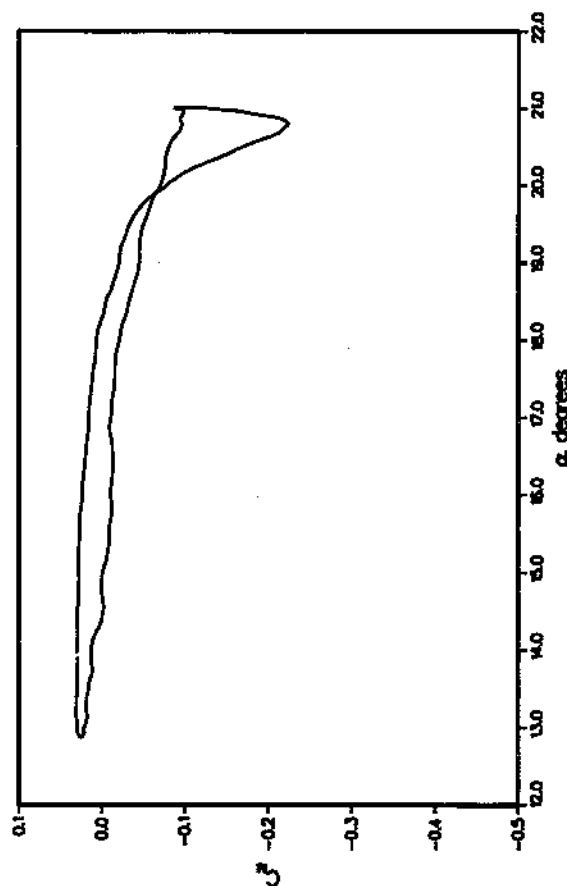
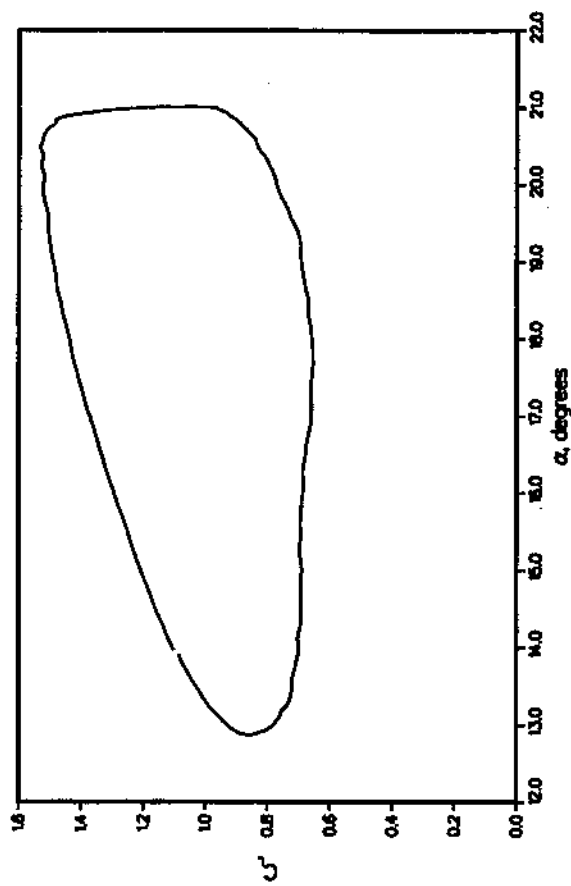


Figure 12(a). Lift and pitching-moment coefficients as a function of angle of attack, for 3-D wing experiencing dynamic stall at $M = 0.3$, $\alpha = 17^\circ + 4^\circ \sin \omega t$, $k = 0.10$ (from ref. 3).

90% SPAN

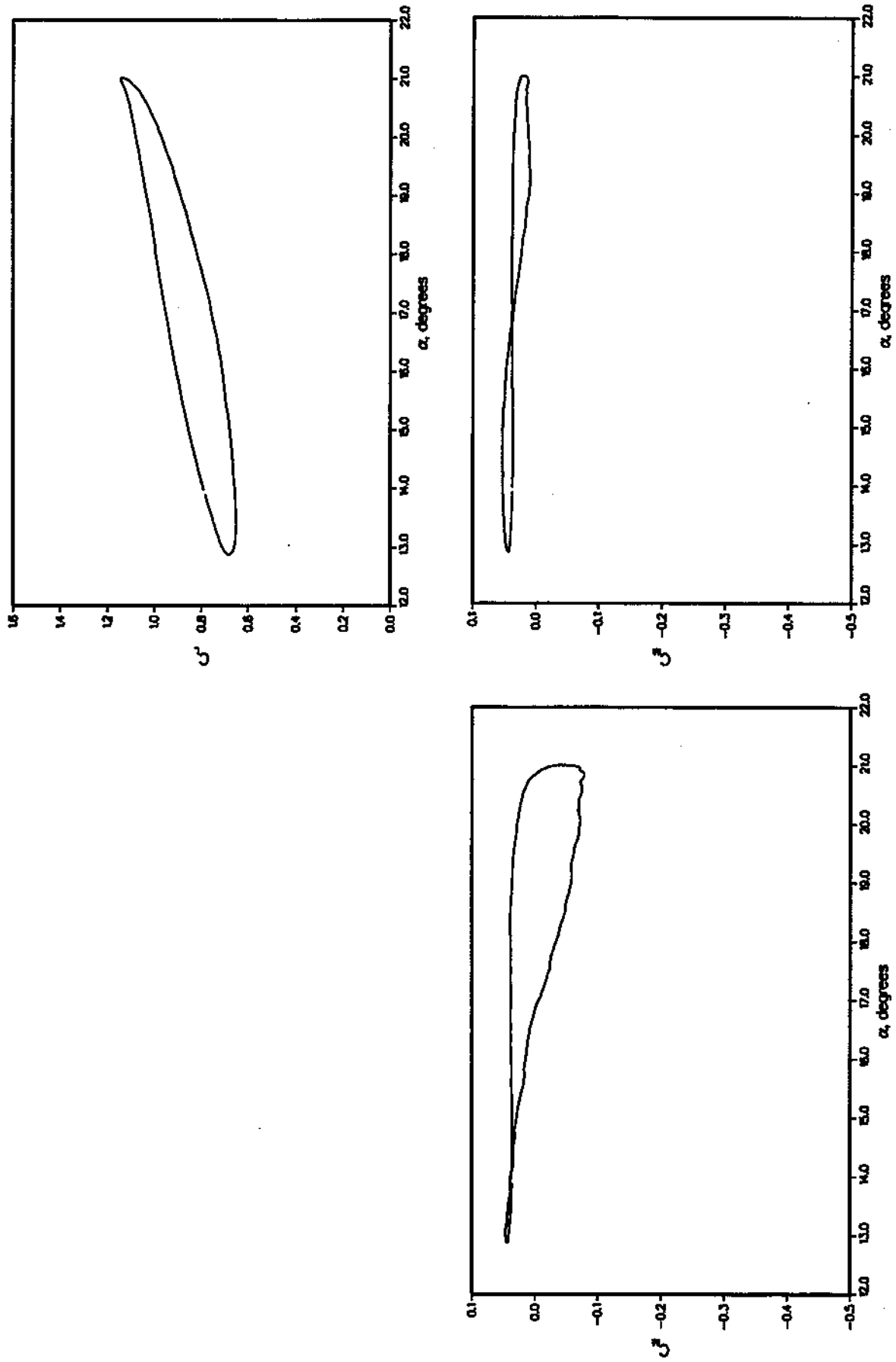
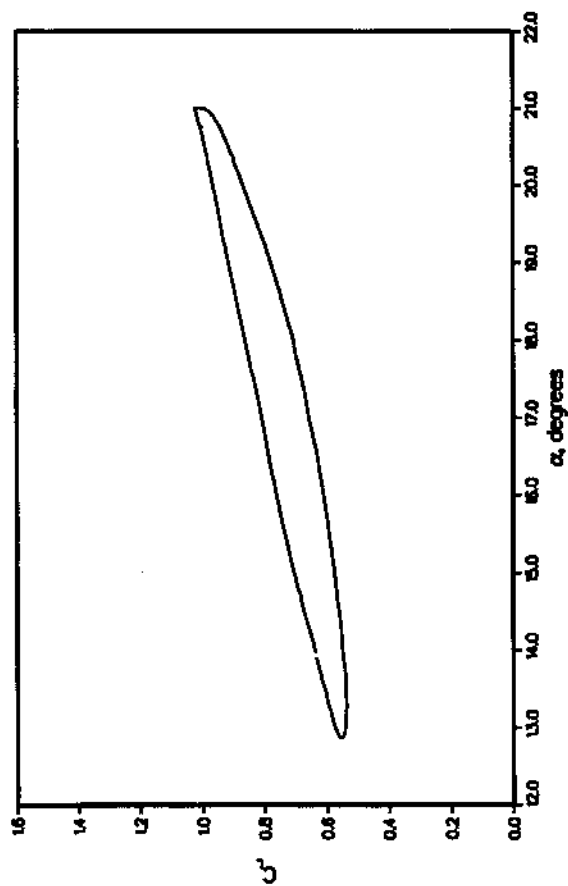


Figure 12(b). Lift and pitching-moment coefficients as a function of angle of attack, for 3-D wing experiencing dynamic stall at $M = 0.3$, $\alpha = 17^\circ + 4^\circ \sin \omega t$, $k = 0.10$ (from ref. 3).

96.6% SPAN



98.6% SPAN

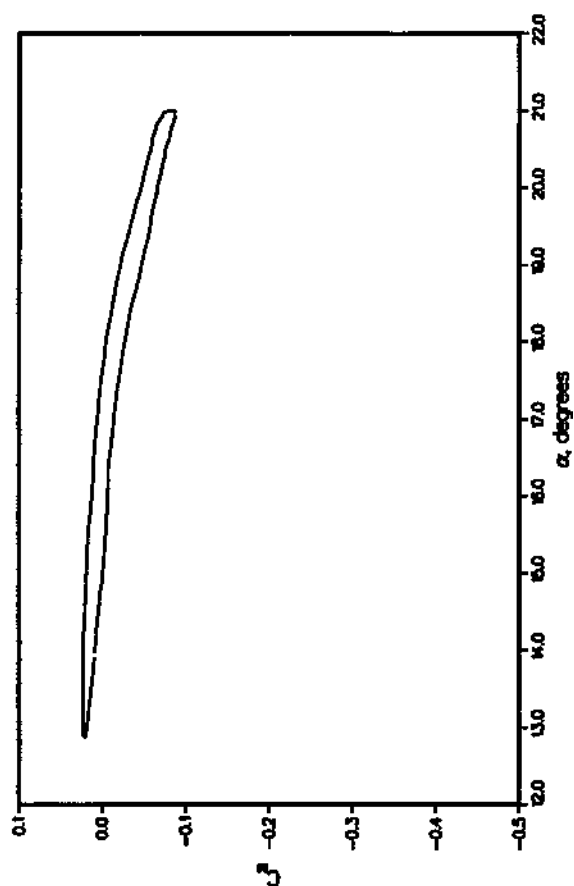
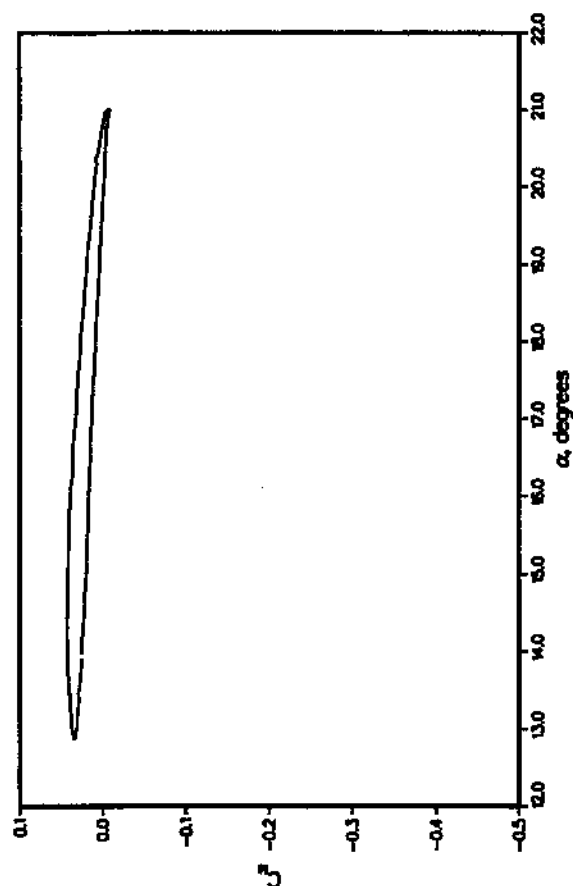
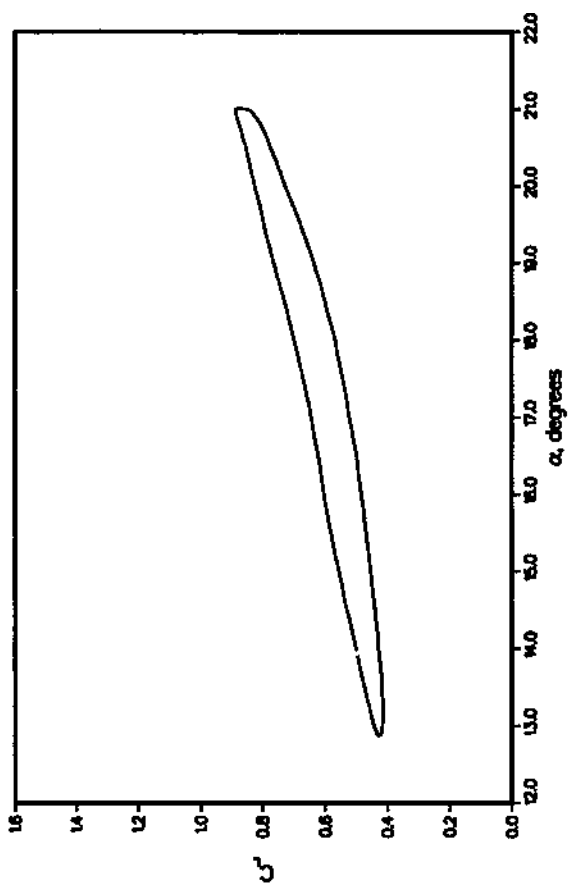


Figure 12(c). Lift and pitching-moment coefficients as a function of angle of attack, for 3-D wing experiencing dynamic stall at $M = 0.3$, $\alpha = 17^\circ + 4^\circ \sin \omega t$, $k = 0.10$ (from ref. 3).

99.5% SPAN

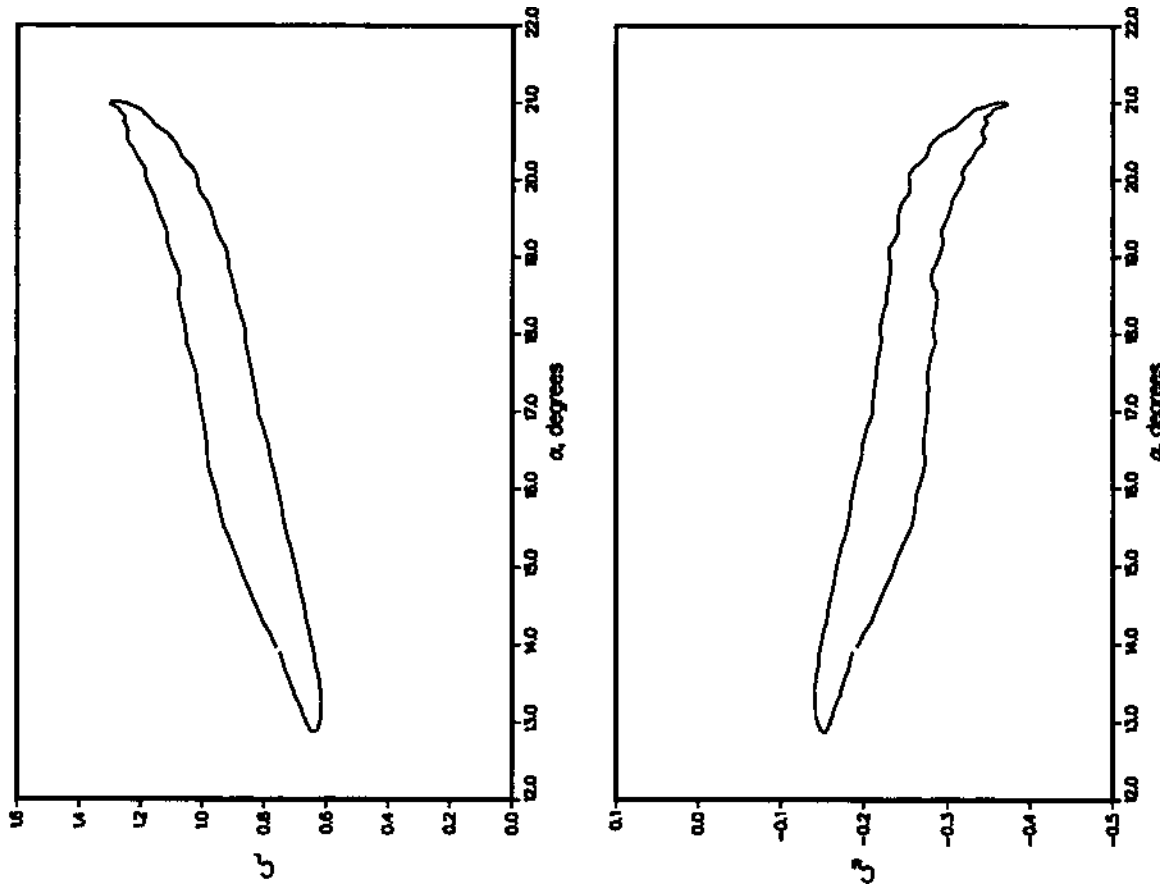
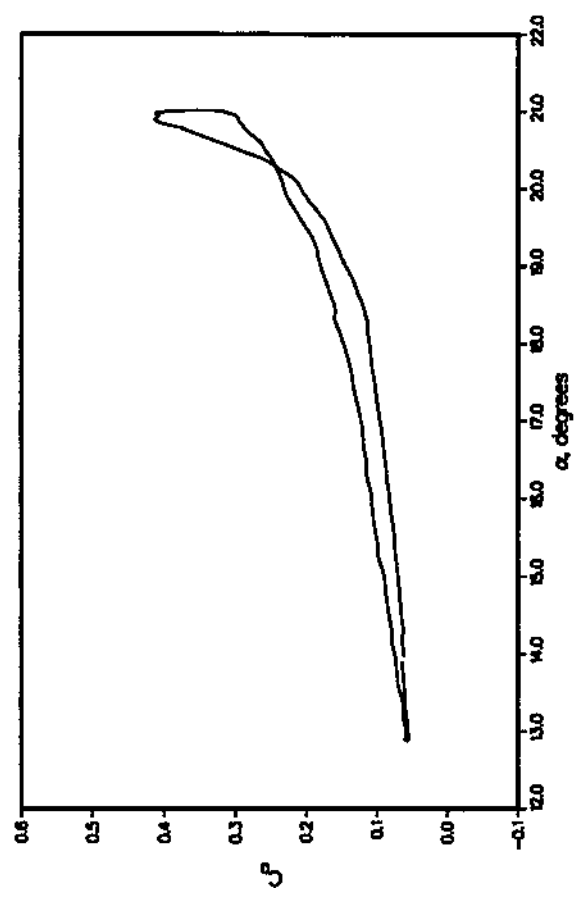
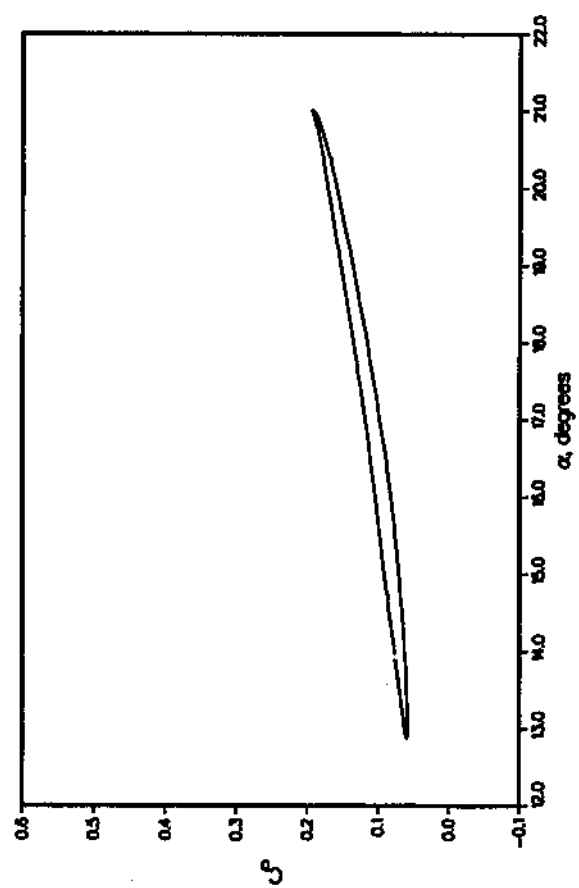


Figure 12(d). Lift and pitching-moment coefficients as a function of angle of attack, for 3-D wing experiencing dynamic stall at $M = 0.3$, $\alpha = 17^\circ + 4^\circ \sin \omega t$, $k = 0.10$ (from ref. 3).

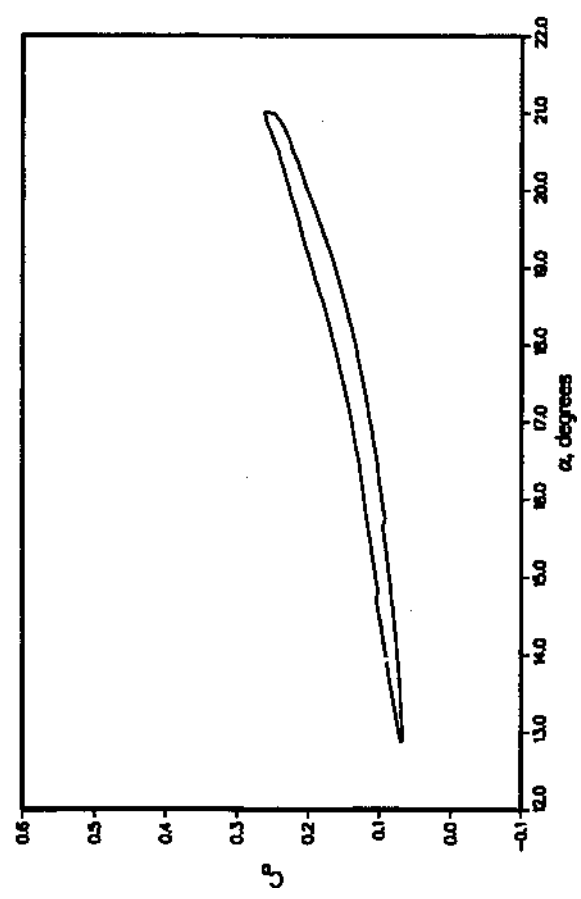
47.5% SPAN



96.6% SPAN



98.6% SPAN



99.5% SPAN

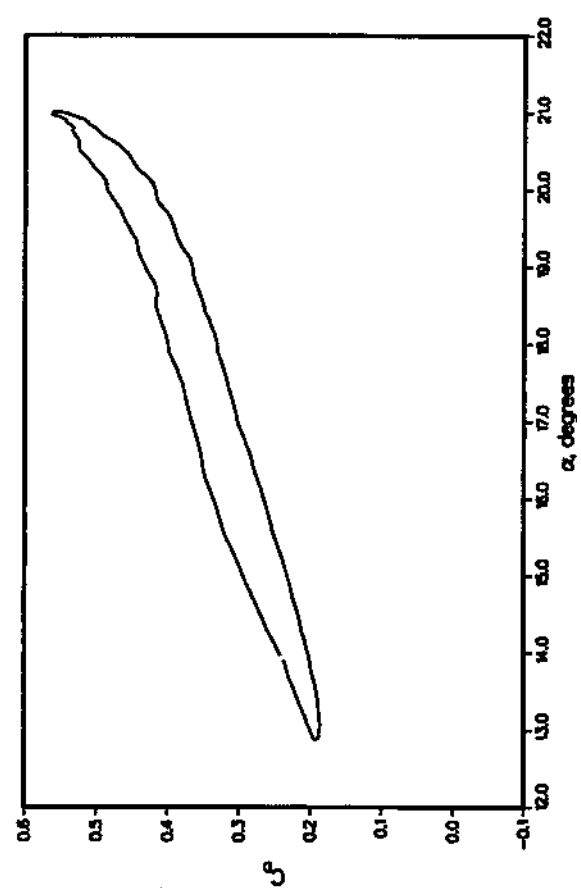
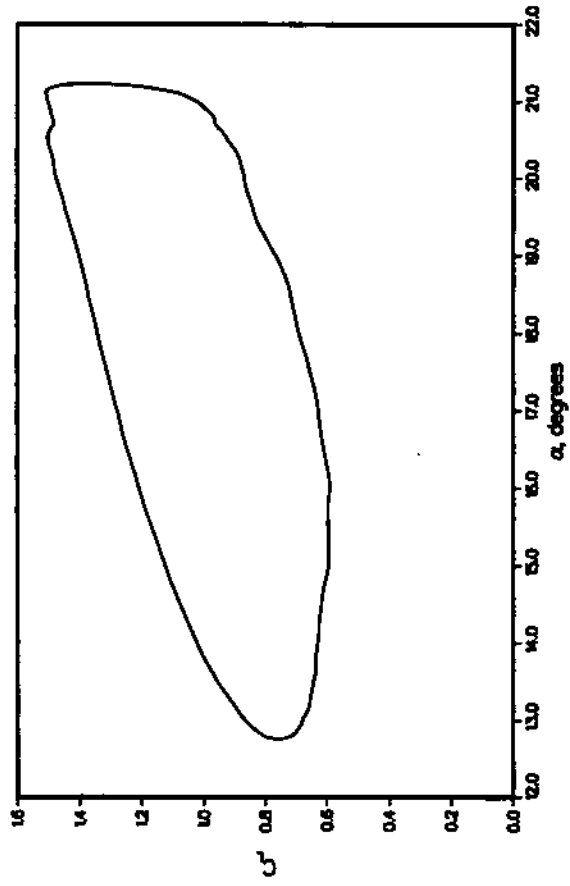


Figure 12(e). Drag coefficients as a function of angle of attack, for 3-D wing experiencing dynamic stall at $M = 0.3$, $\alpha = 17^\circ + 4^\circ \sin \omega t$, $k = 0.10$; drag at four spanwise stations (from ref. 3).

25% SPAN



47.5% SPAN

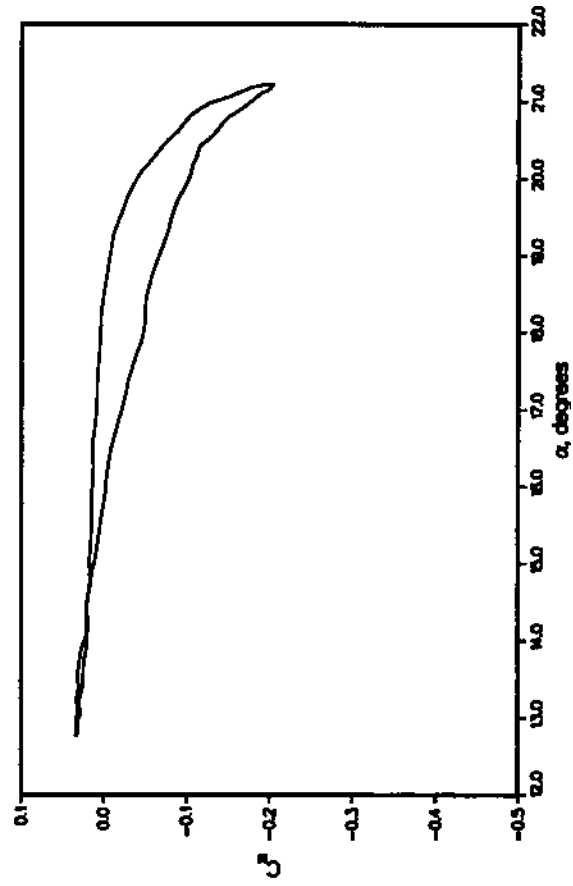
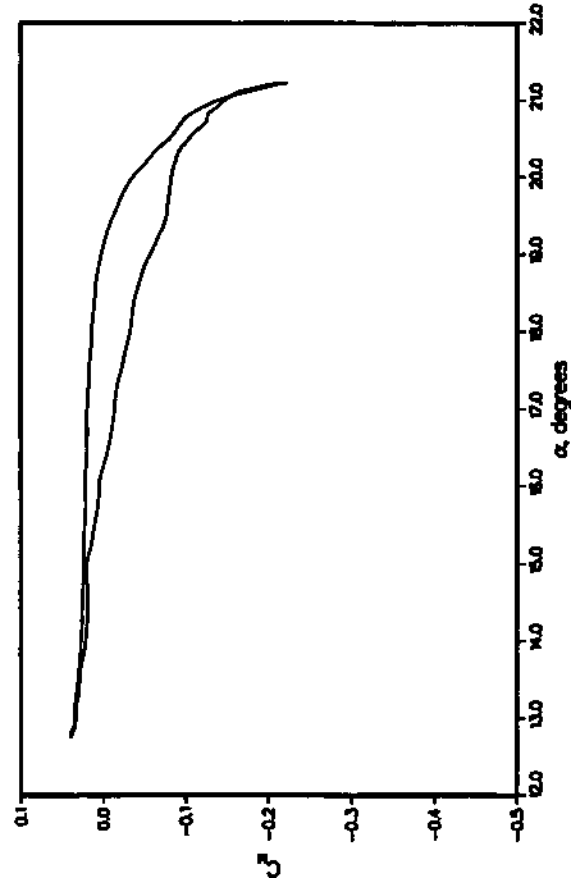
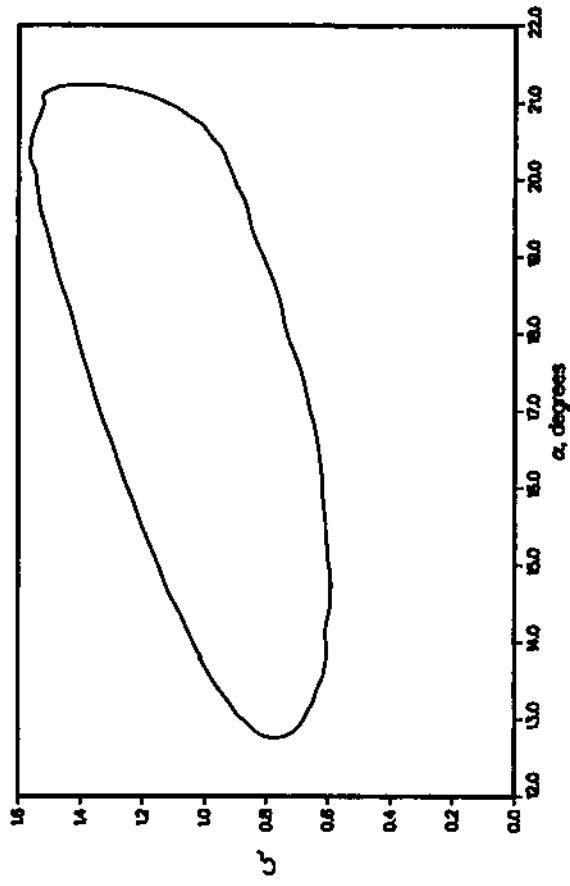
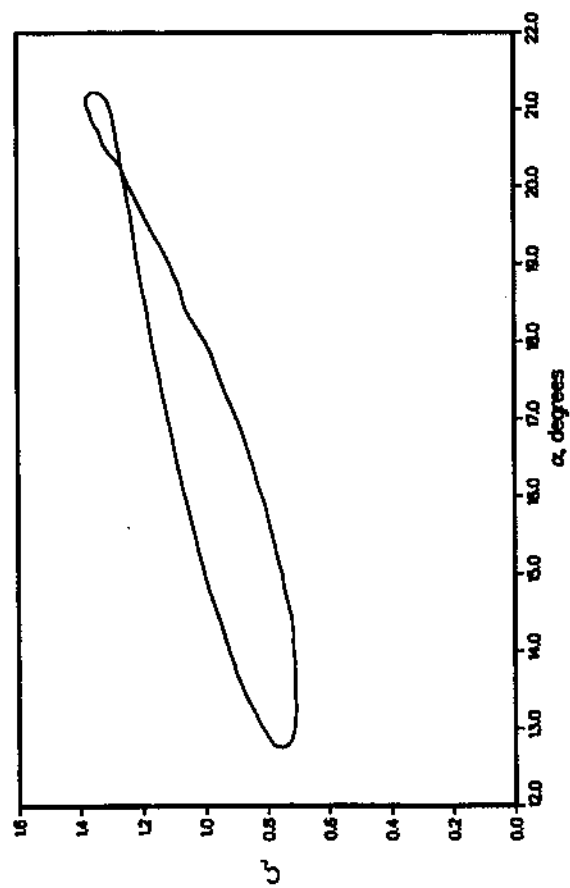


Figure 13(a). Lift and pitching-moment coefficients as a function of angle of attack, for 3-D wing experiencing dynamic stall at $M = 0.3$, $\alpha = 17^\circ + 4^\circ \sin \omega t$, $k = 0.14$ (from ref. 3).

80% SPAN



90% SPAN

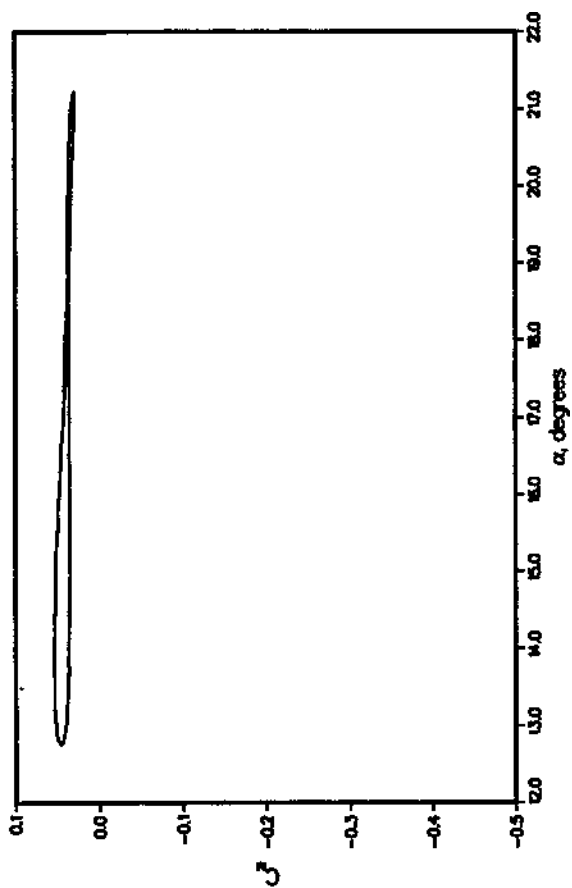
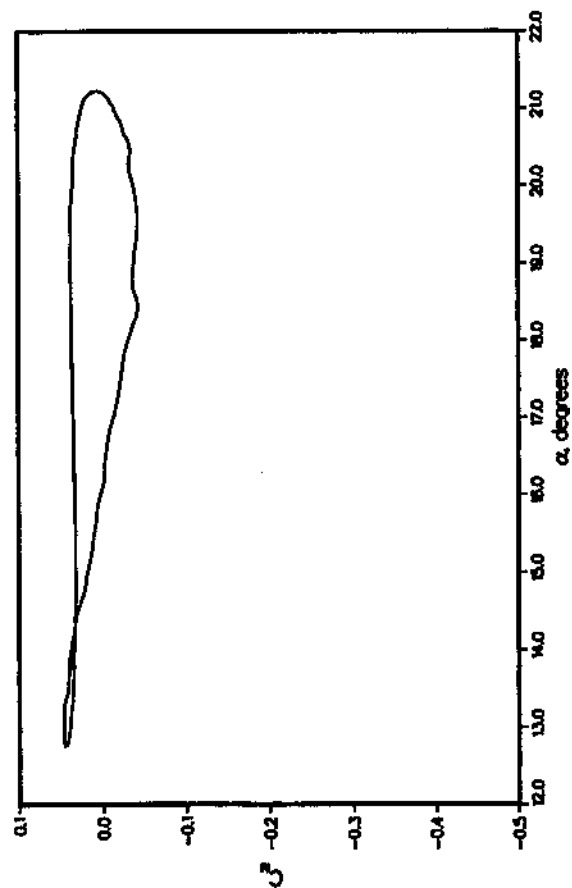
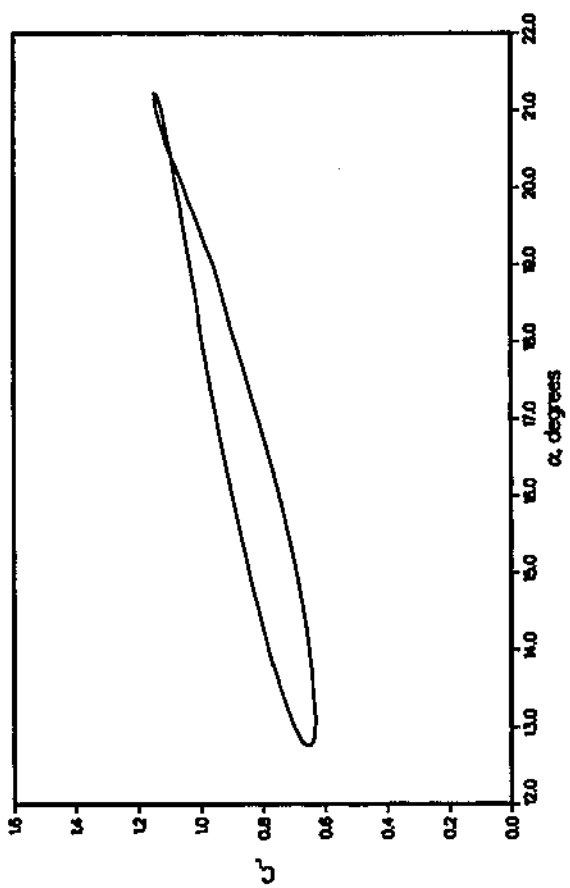
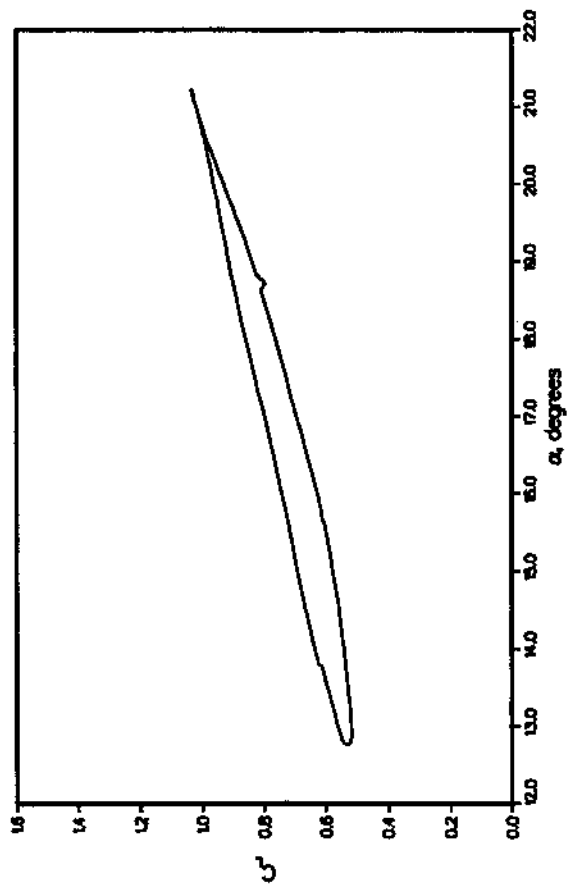


Figure 13(b). Lift and pitching-moment coefficients as a function of angle of attack, for 3-D wing experiencing dynamic stall at $M = 0.3$, $\alpha = 17^\circ + 4^\circ \sin \omega t$, $k = 0.14$ (from ref. 3).

96.6% SPAN



98.6% SPAN

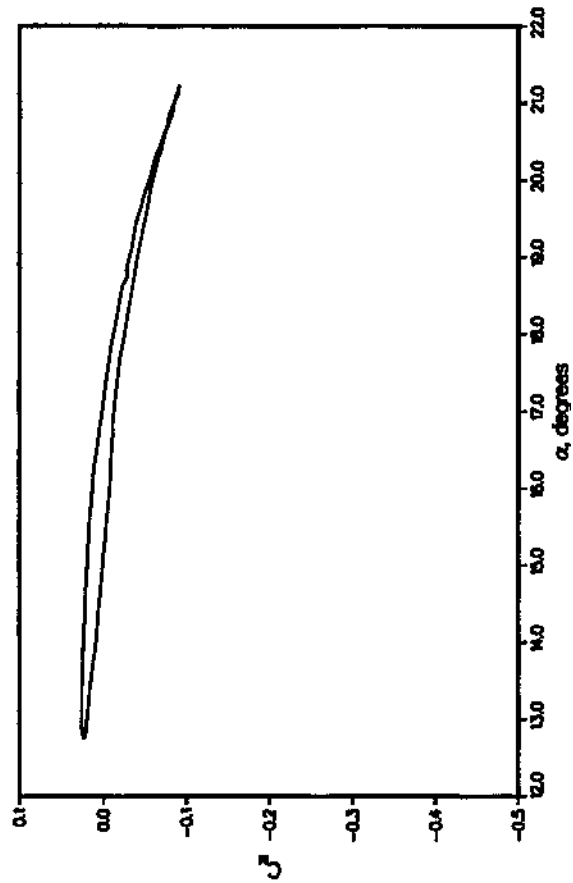
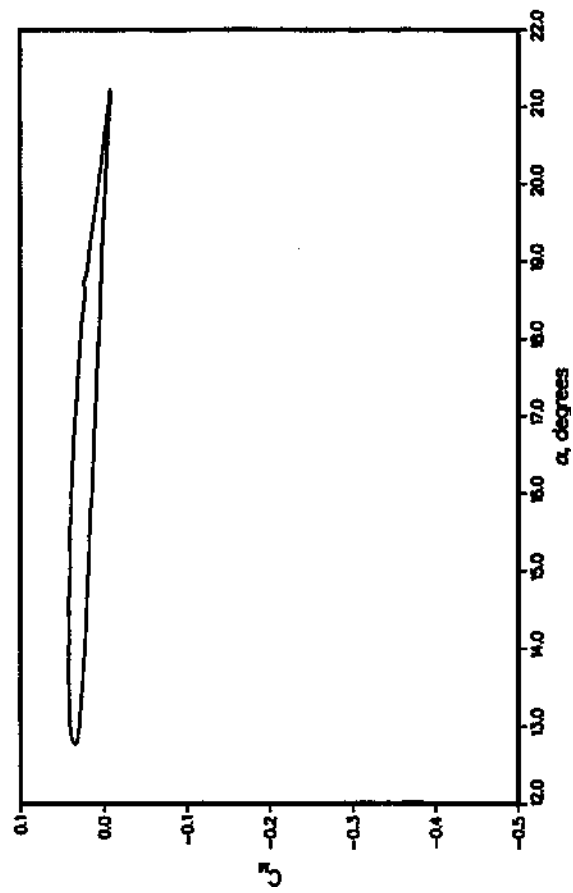
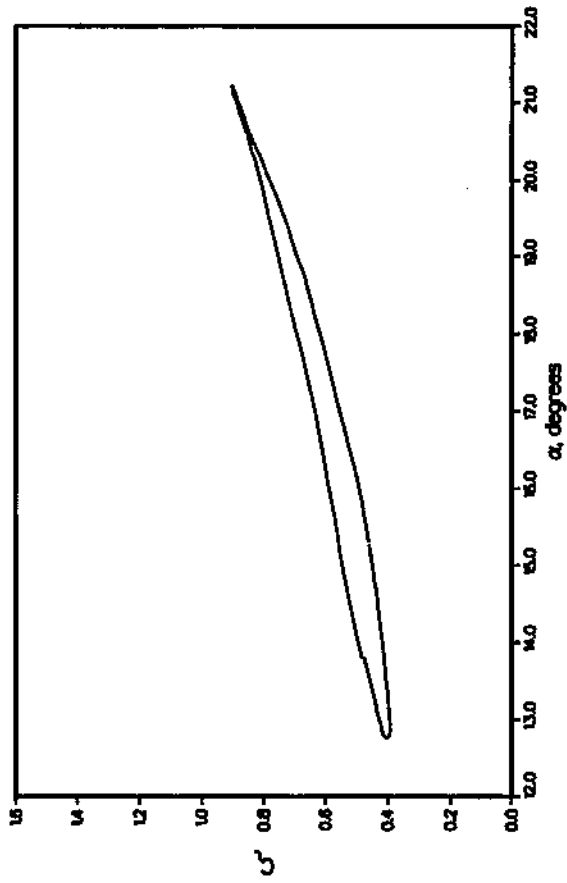


Figure 13(c). Lift and pitching-moment coefficients as a function of angle of attack, for 3-D wing experiencing dynamic stall at $M = 0.3$, $\alpha = 17^\circ + 4^\circ \sin \omega t$, $k = 0.14$ (from ref. 3).

99.5% SPAN

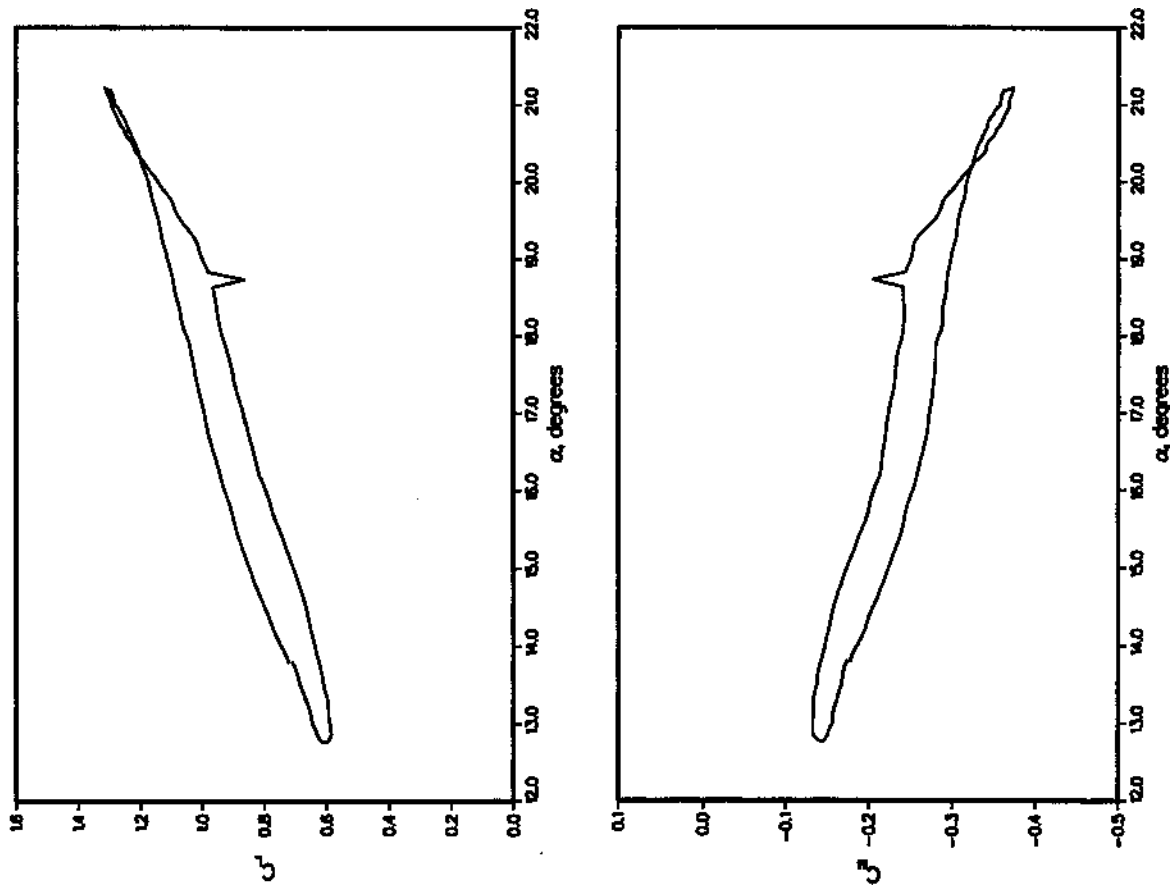
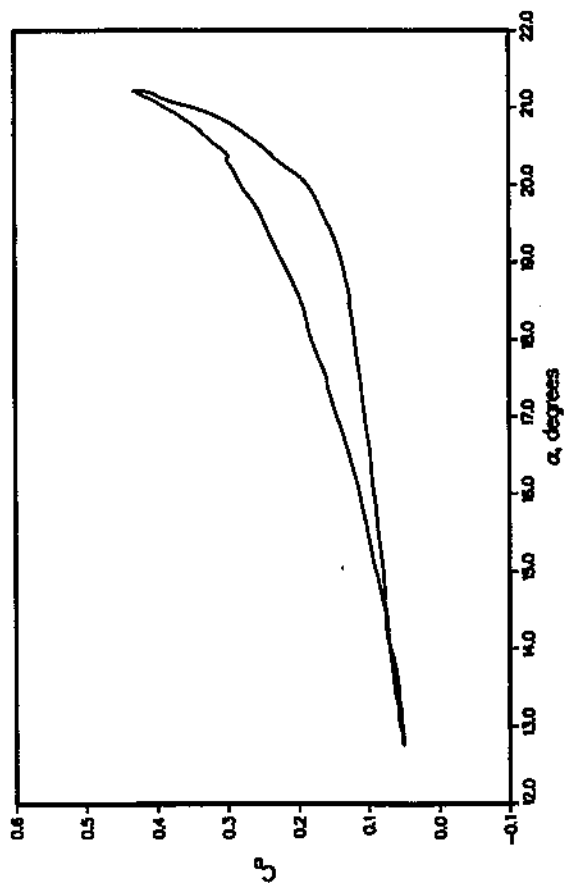
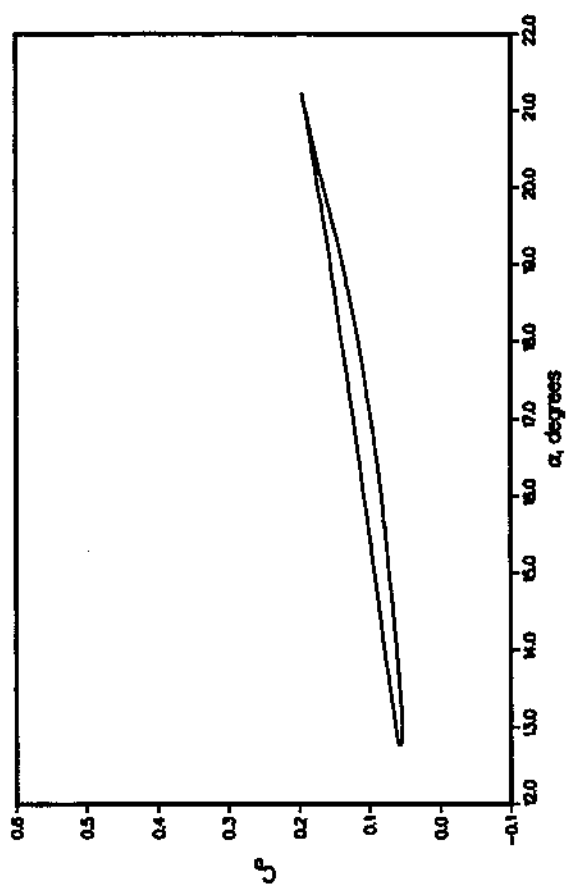


Figure 13(d). Lift and pitching-moment coefficients as a function of angle of attack, for 3-D wing experiencing dynamic stall at $M = 0.3$, $\alpha = 17^\circ + 4^\circ \sin \omega t$, $k = 0.14$ (from ref. 3).

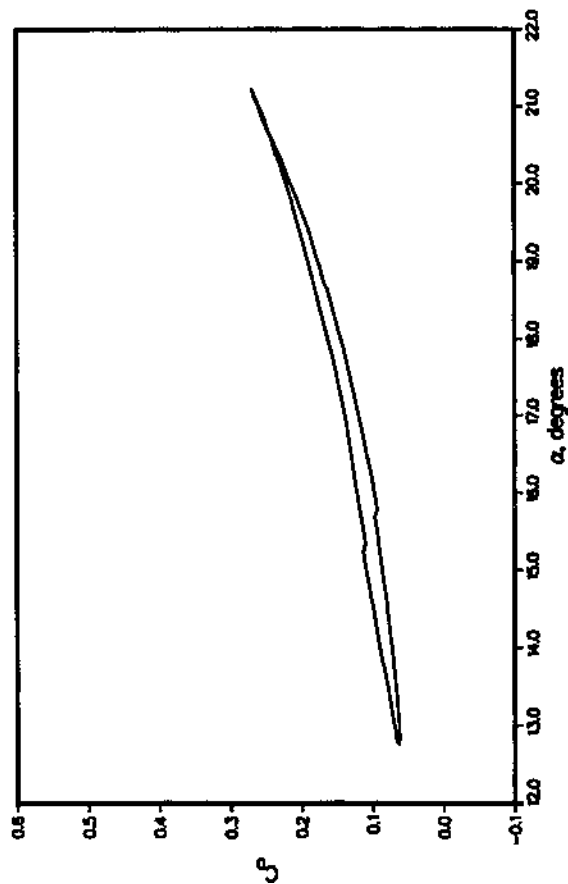
47.5% SPAN



96.6% SPAN



98.6% SPAN



99.5% SPAN

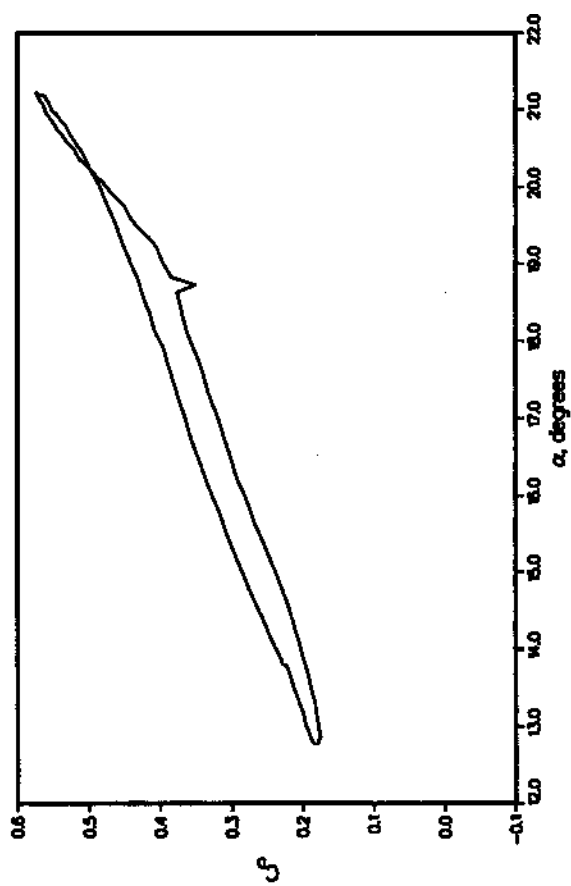


Figure 13(e). Drag coefficients as a function of angle of attack, for 3-D wing experiencing dynamic stall at $M = 0.3$, $\alpha = 17^\circ + 4^\circ \sin \omega t$, $k = 0.14$; drag at four spanwise stations (from ref. 3).

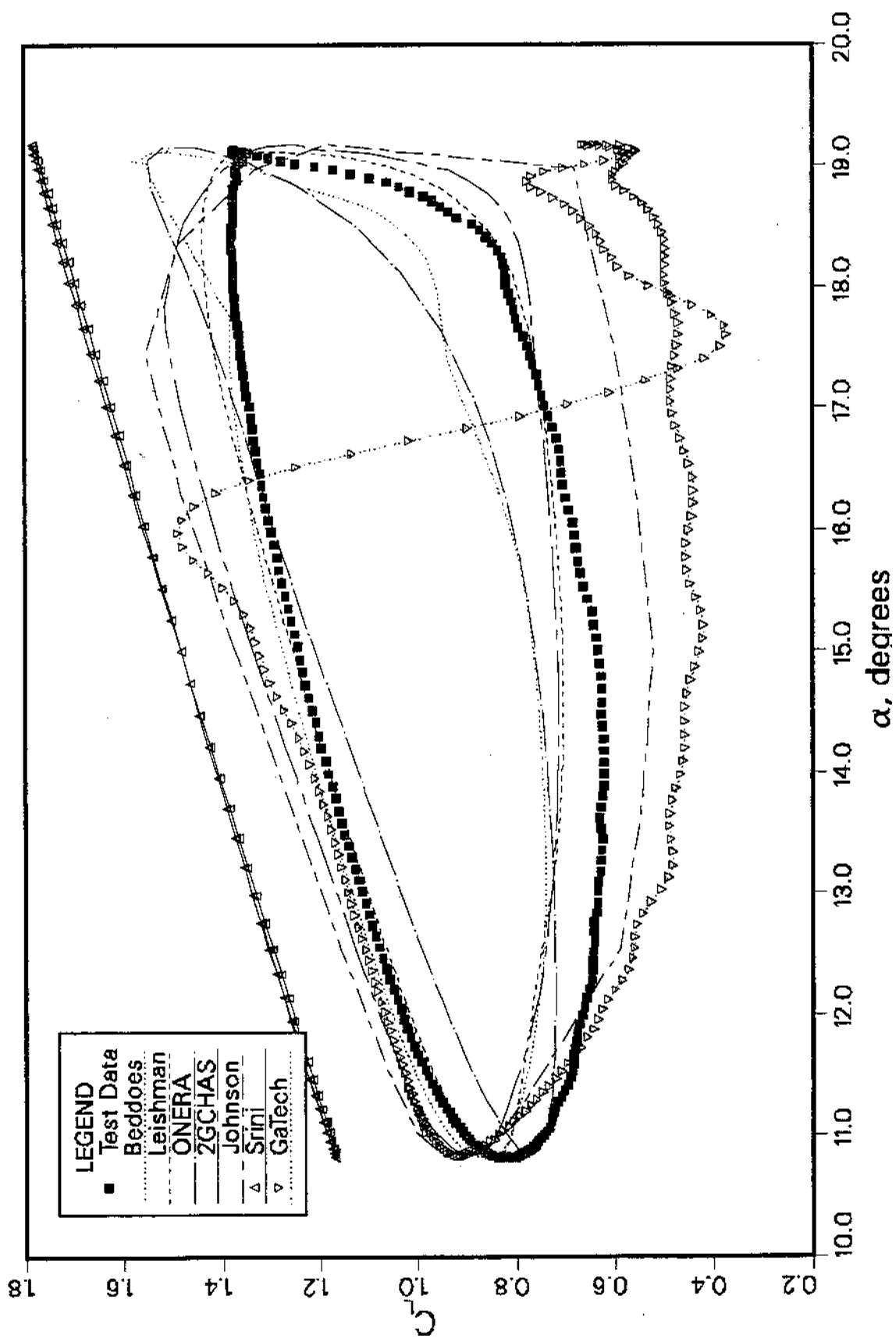


Figure 14(a). Comparison of calculation, modeling, and experimental results as a function of angle of attack, for $M = 0.3$, $k = 0.10$, $\alpha = 15^\circ + 4^\circ \sin \omega t$; lift at Station 1, 25.0 percent span.

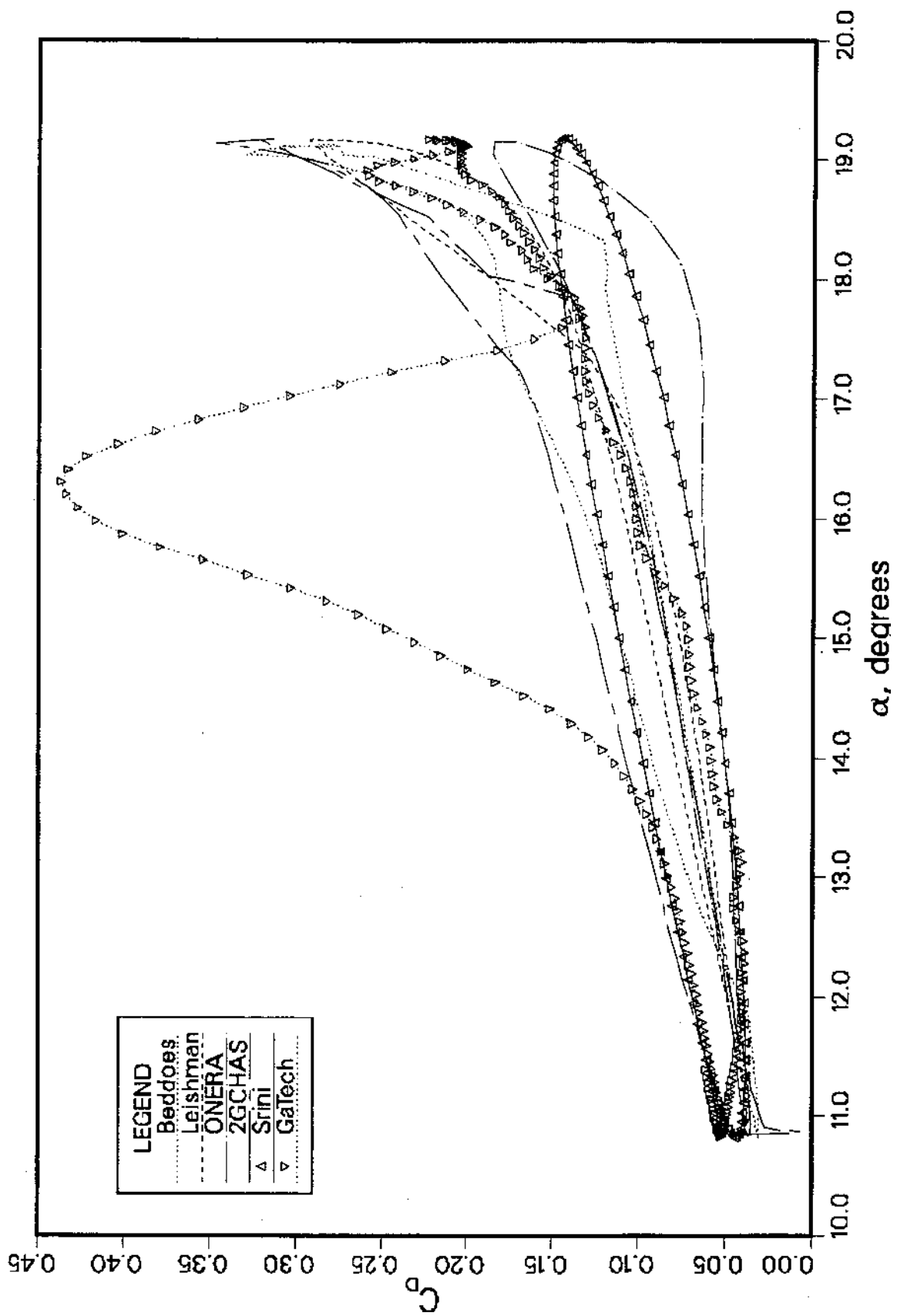


Figure 14(b). Comparison of calculation, modeling, and experimental results as a function of angle of attack, for $M = 0.3$, $k = 0.10$, $\alpha = 15^\circ + 4^\circ \sin \omega t$; drag at Station 1, 25.0 percent span.

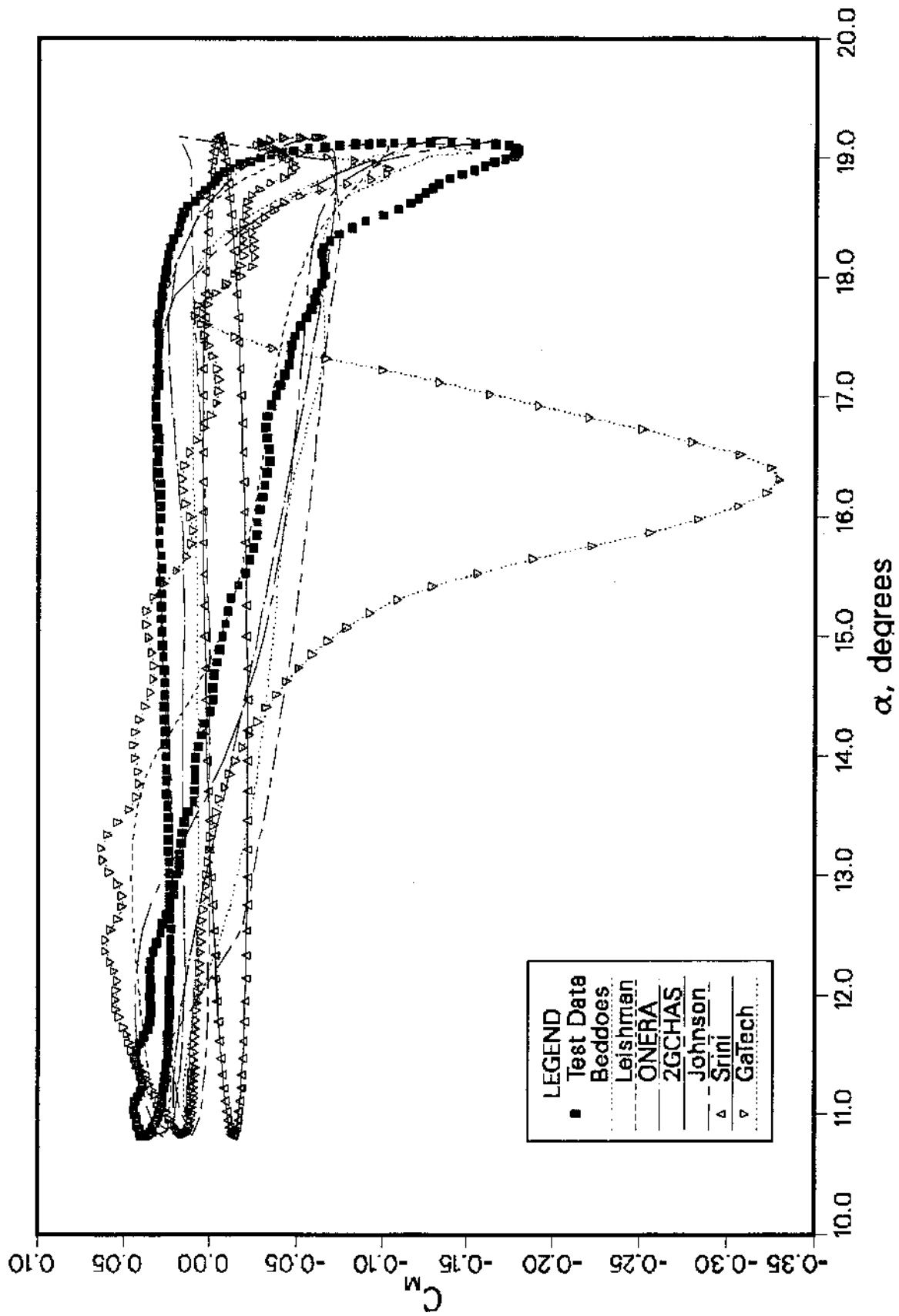


Figure 14(c). Comparison of calculation, modeling, and experimental results as a function of angle of attack, for $M = 0.3$, $k = 0.10$, $\alpha = 15^\circ + 4^\circ \sin \omega t$; pitching moment at Station 1, 25.0 percent span.

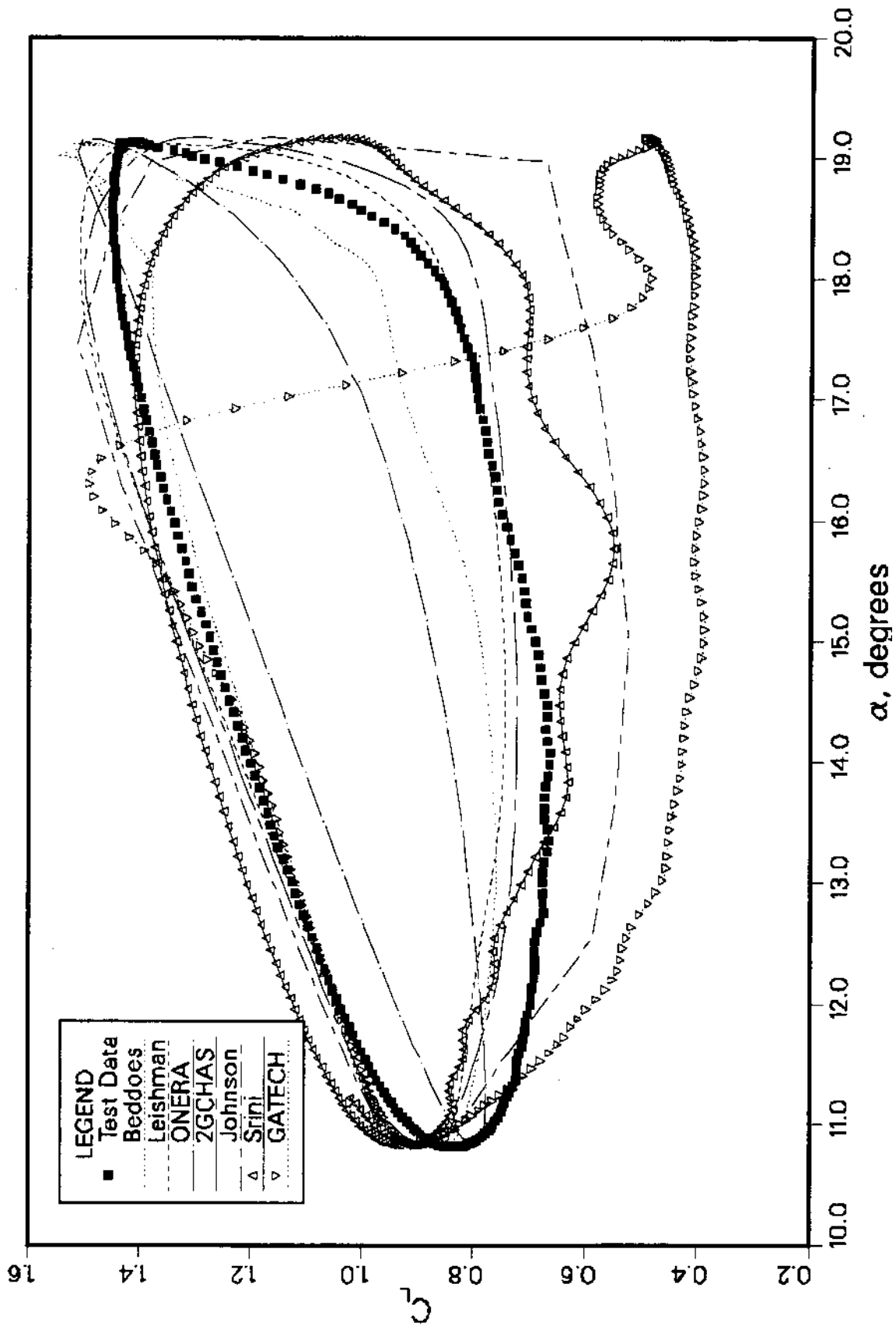


Figure 15(a). Comparison of calculation, modeling, and experimental results as a function of angle of attack, for $M = 0.3$, $k = 0.10$, $\alpha = 15^\circ + 4^\circ \sin \omega t$; lift at Station 2, 47.5 percent span.

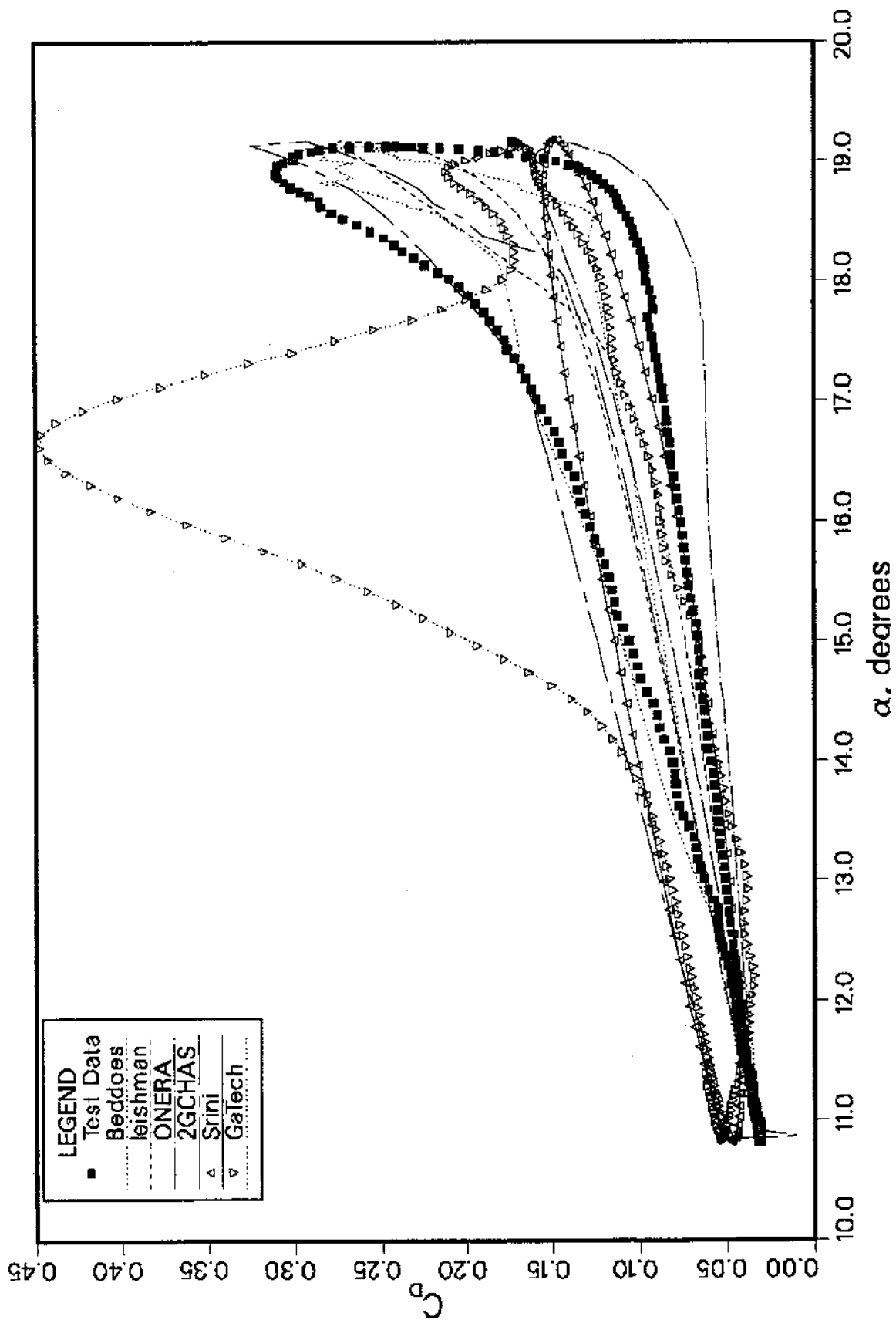


Figure 15(b). Comparison of calculation, modeling, and experimental results as a function of angle of attack, for $M = 0.3$, $k = 0.10$, $\alpha = 15^\circ + 4^\circ \sin \omega t$; drag at Station 2, 47.5 percent span.

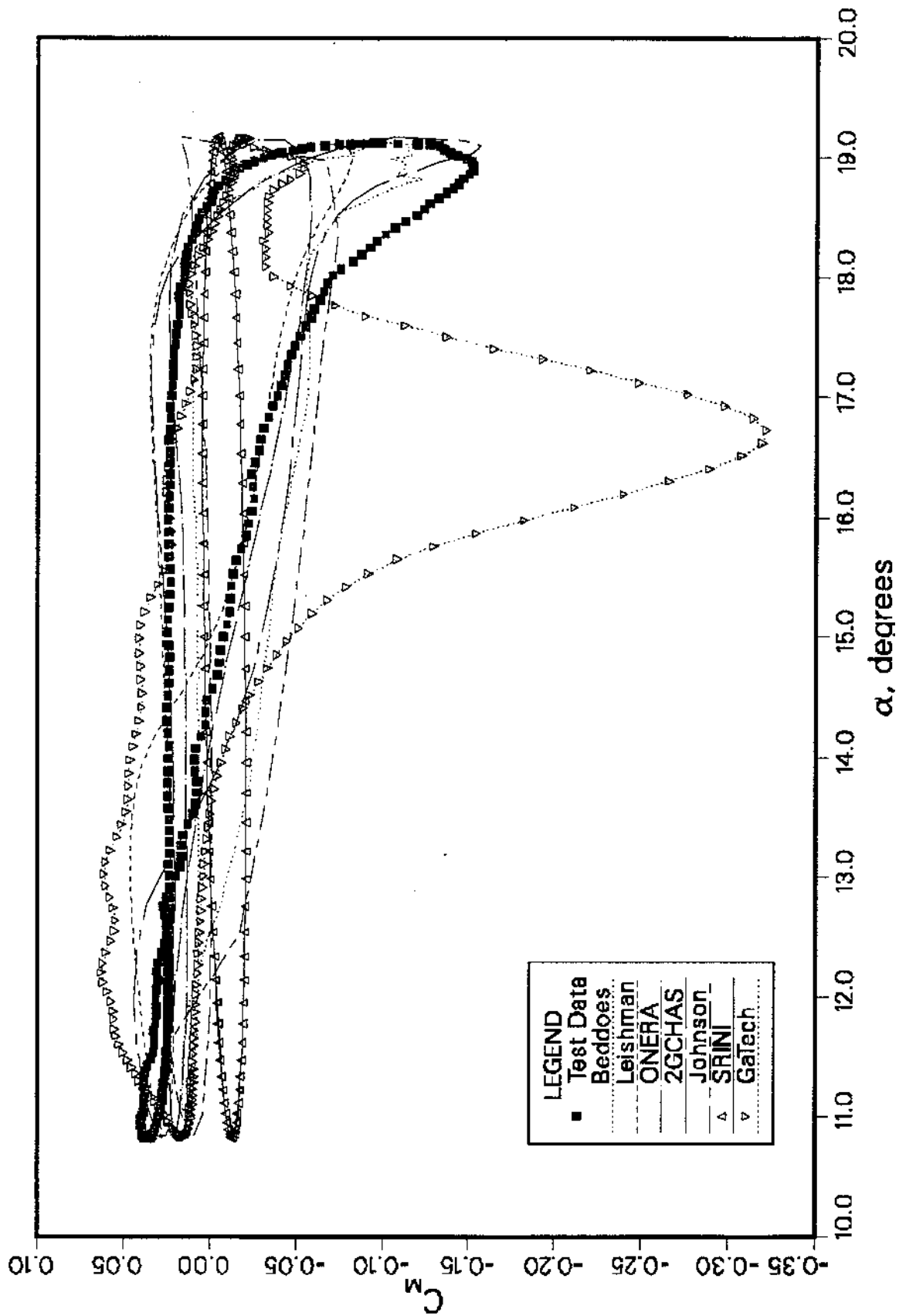


Figure 15(c). Comparison of calculation, modeling, and experimental results as a function of angle of attack, for $M = 0.3$, $k = 0.10$, $\alpha = 15^\circ + 4^\circ \sin \omega t$; pitching moment at Station 2, 47.5 percent span.

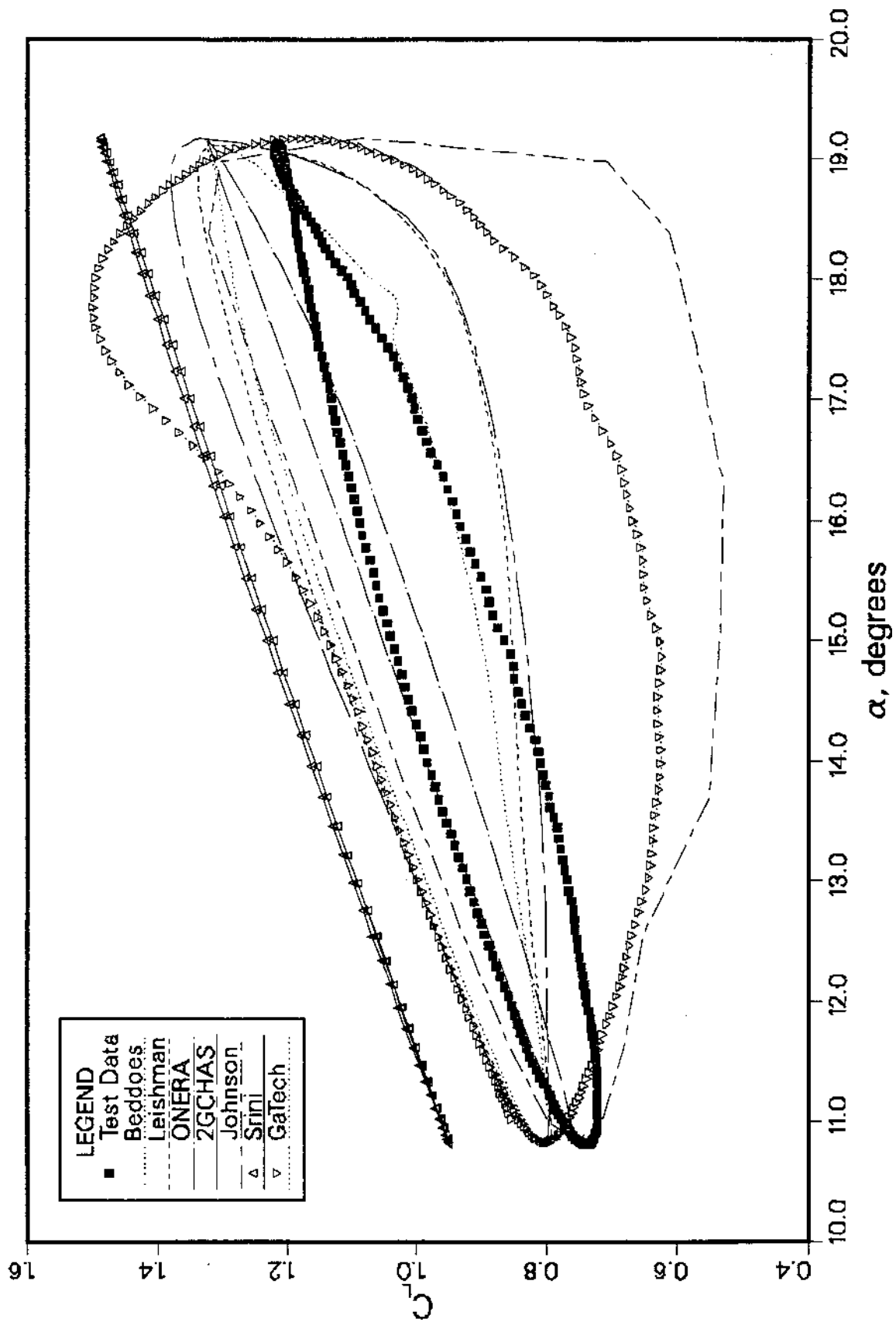


Figure 16(a). Comparison of calculation, modeling, and experimental results as a function of angle of attack, for $M = 0.3$, $k = 0.10$, $\alpha = 15^\circ + 4^\circ \sin \omega t$; lift at Station 3, 80.0 percent span.

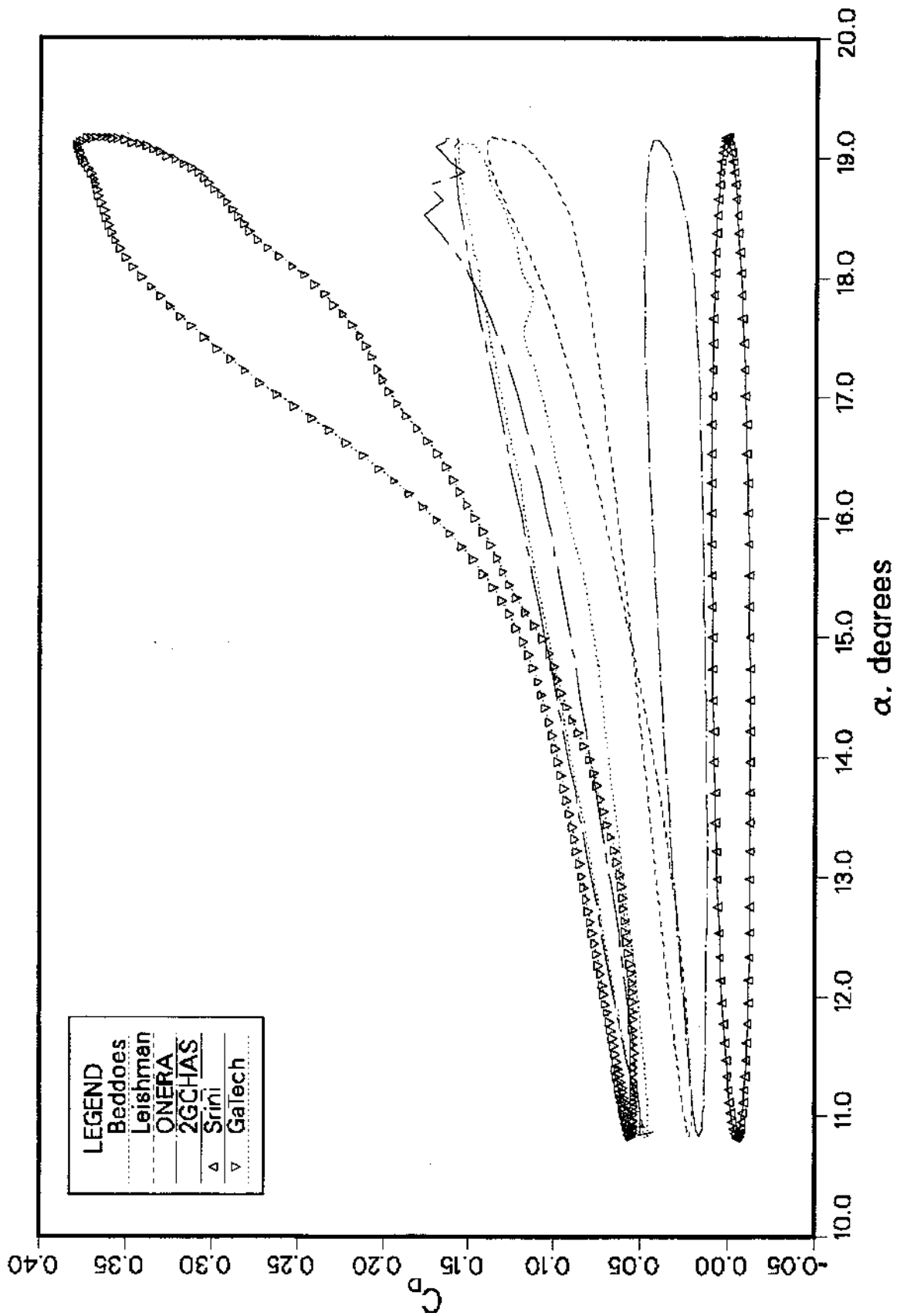


Figure 16(b). Comparison of calculation, modeling, and experimental results as a function of angle of attack, for $M = 0.3$, $k = 0.10$, $\alpha = 15^\circ + 4^\circ \sin \omega t$; drag at Station 3, 80.0 percent span.

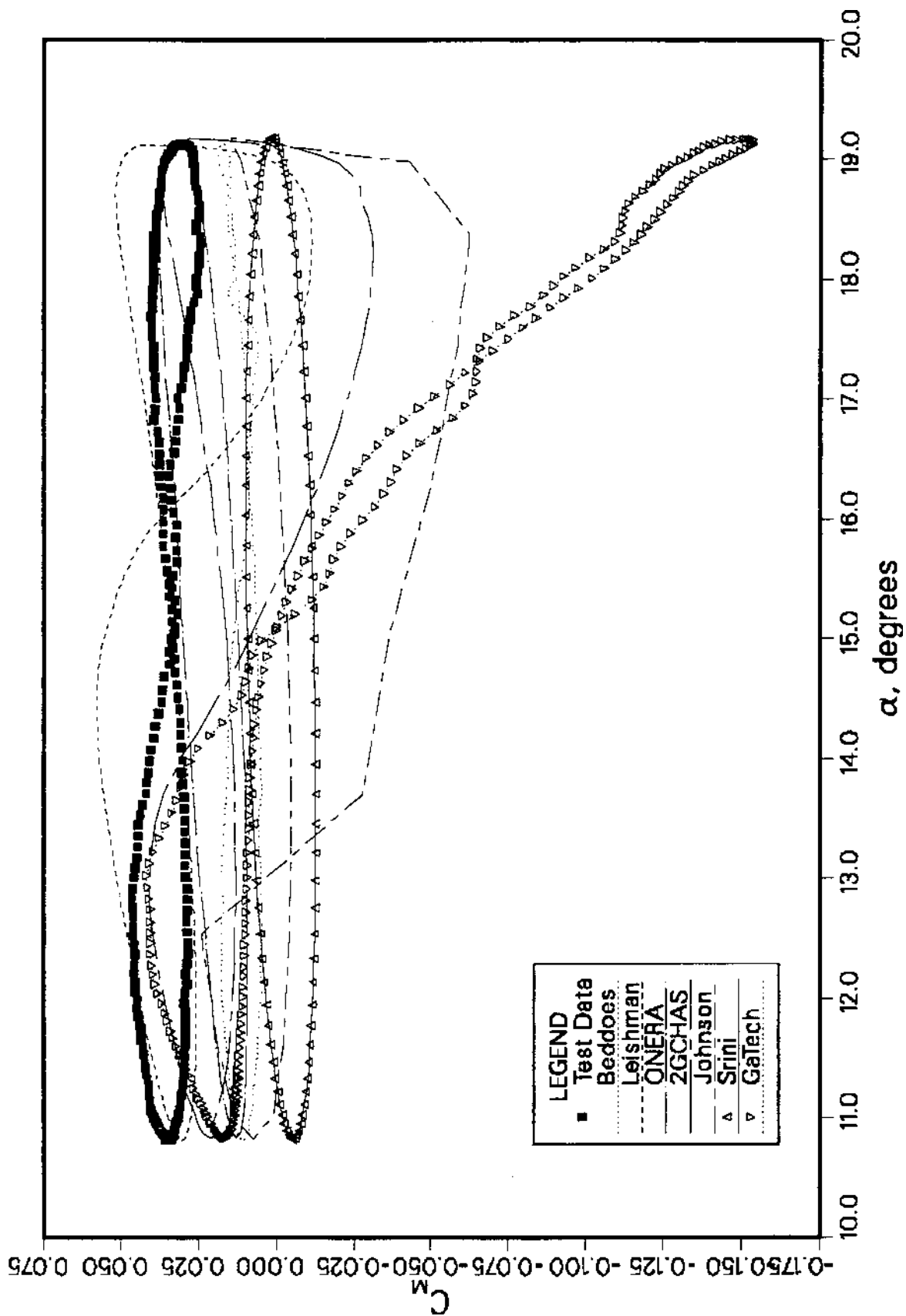


Figure 16(c). Comparison of calculation, modeling, and experimental results as a function of angle of attack, for $M = 0.3$, $k = 0.10$, $\alpha = 15^\circ + 4^\circ \sin \omega t$; pitching moment at Station 3, 80.0 percent span.

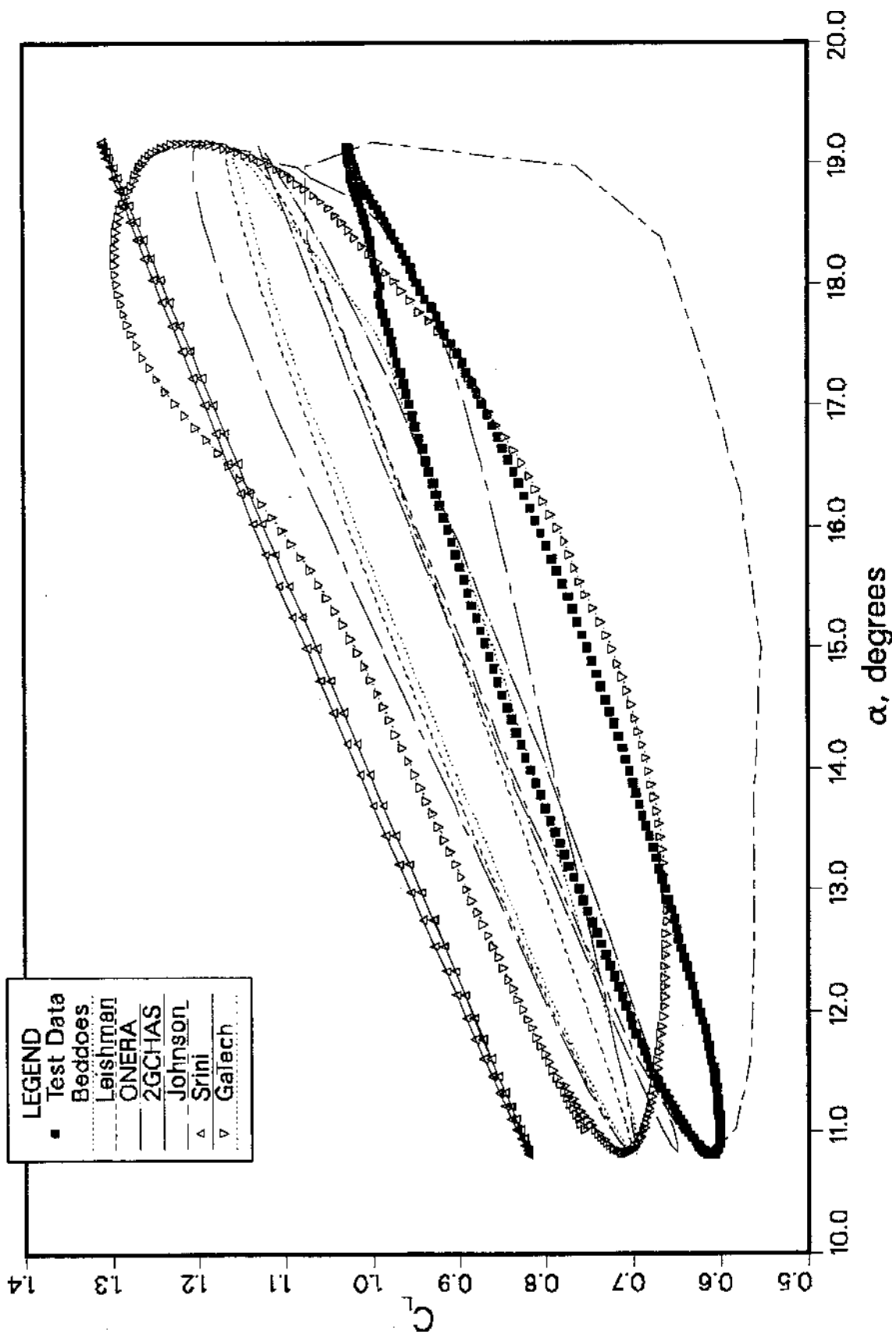


Figure 17(a). Comparison of calculation, modeling, and experimental results as a function of angle of attack, for $M = 0.3$, $k = 0.10$, $\alpha = 15^\circ + 4^\circ \sin \omega t$; lift at Station 4, 90.0 percent span.

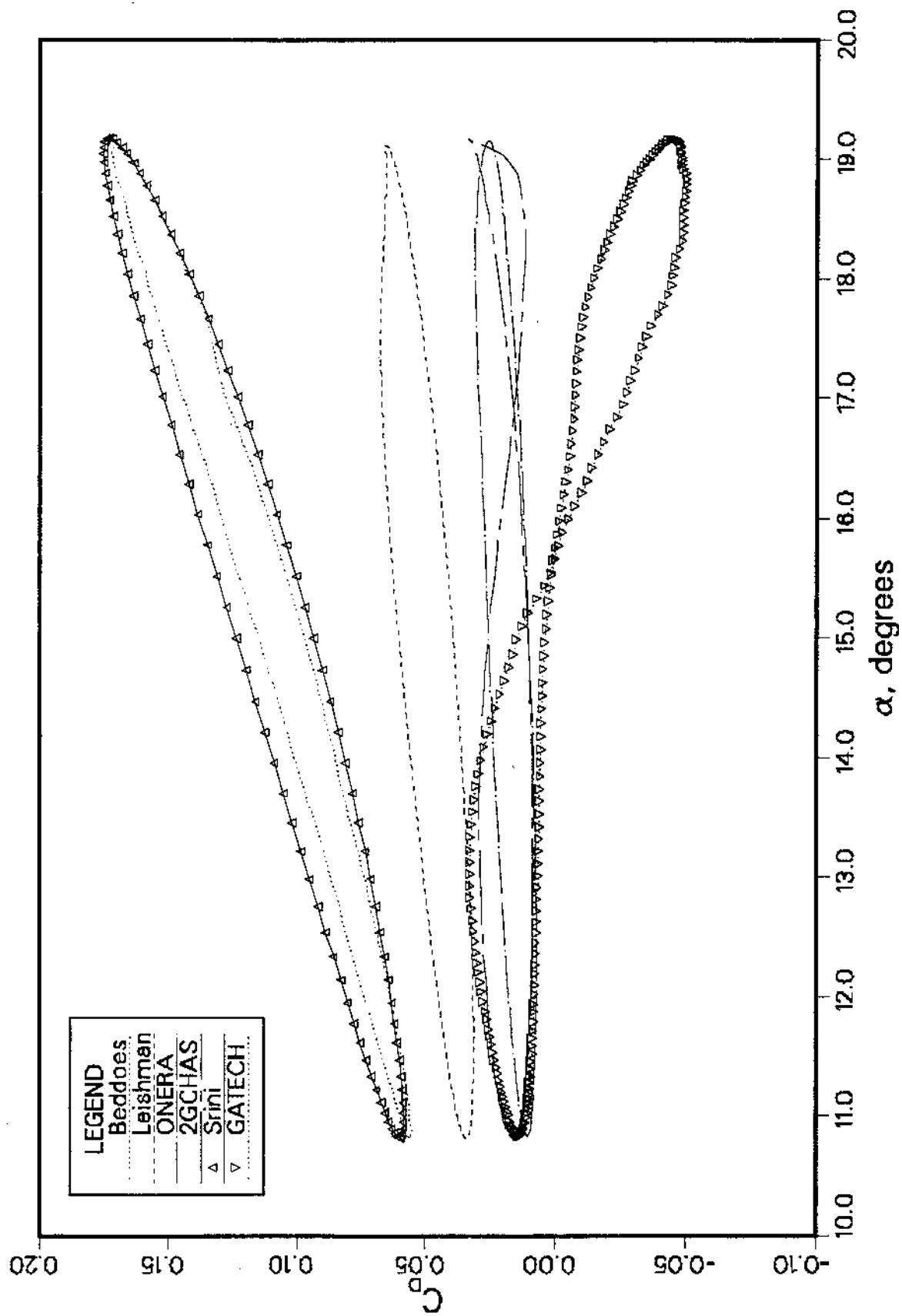


Figure 17(b). Comparison of calculation, modeling, and experimental results as a function of angle of attack, for $M = 0.3$, $k = 0.10$, $\alpha = 15^\circ + 4^\circ \sin \omega t$; drag at Station 4, 90.0 percent span.

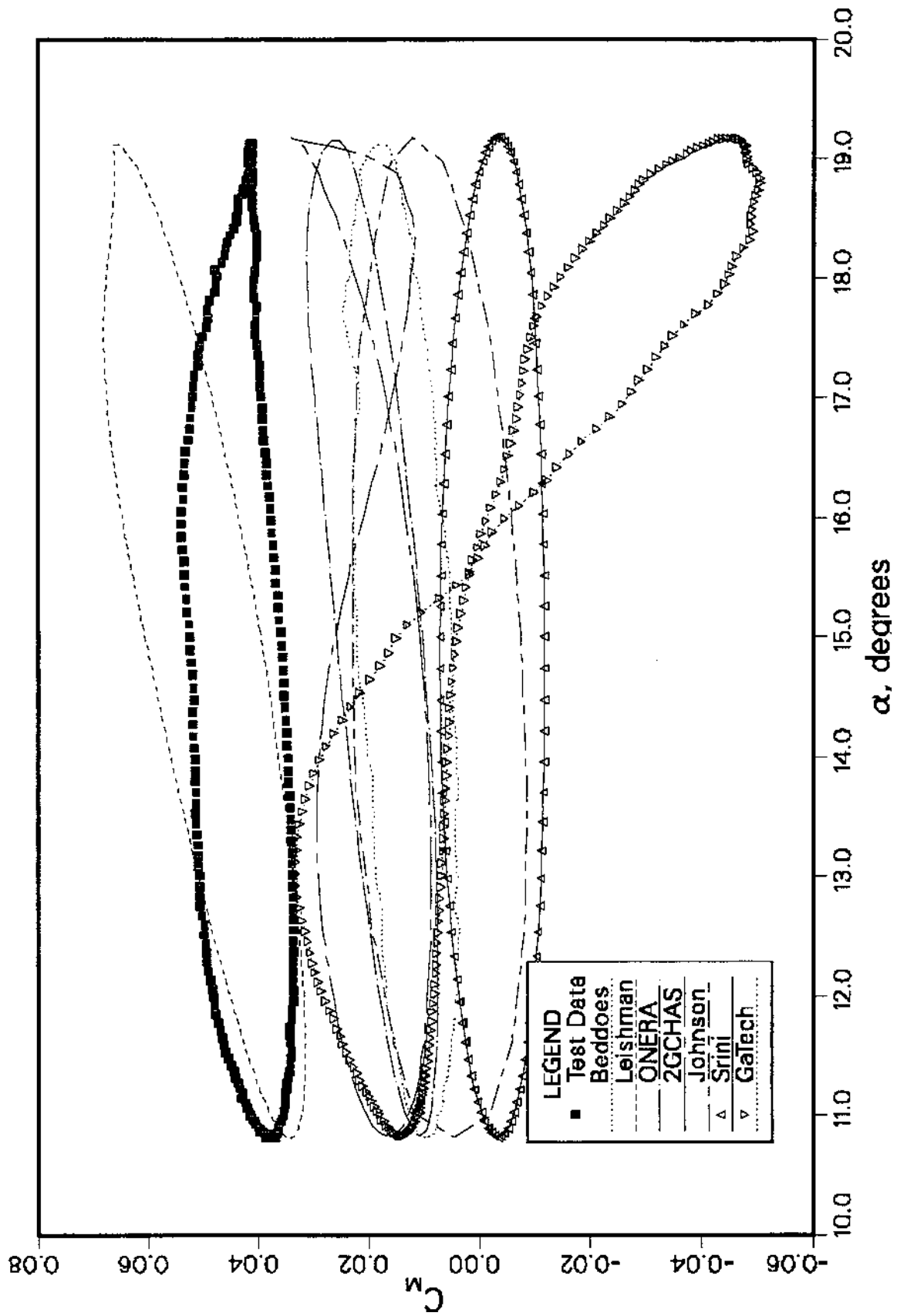


Figure 17(c). Comparison of calculation, modeling, and experimental results as a function of angle of attack, for $M = 0.3$, $k = 0.10$, $\alpha = 15^\circ + 4^\circ \sin \omega t$; pitching moment at Station 4, 90.0 percent span.

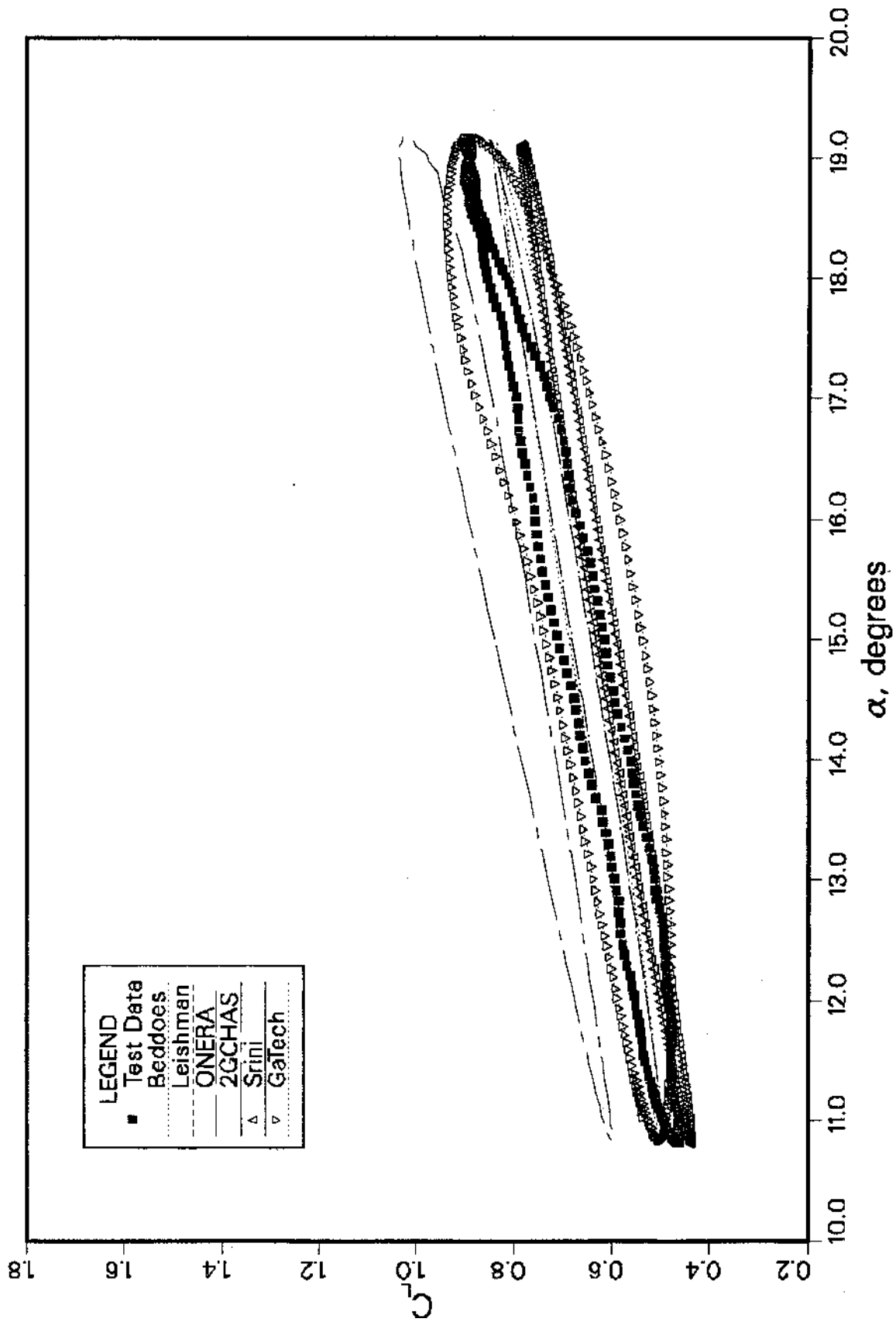


Figure 18(a). Comparison of calculation, modeling, and experimental results as a function of angle of attack, for $M = 0.3$, $k = 0.10$, $\alpha = 15^\circ + 4^\circ \sin \omega t$; lift at Station 5, 96.6 percent span.

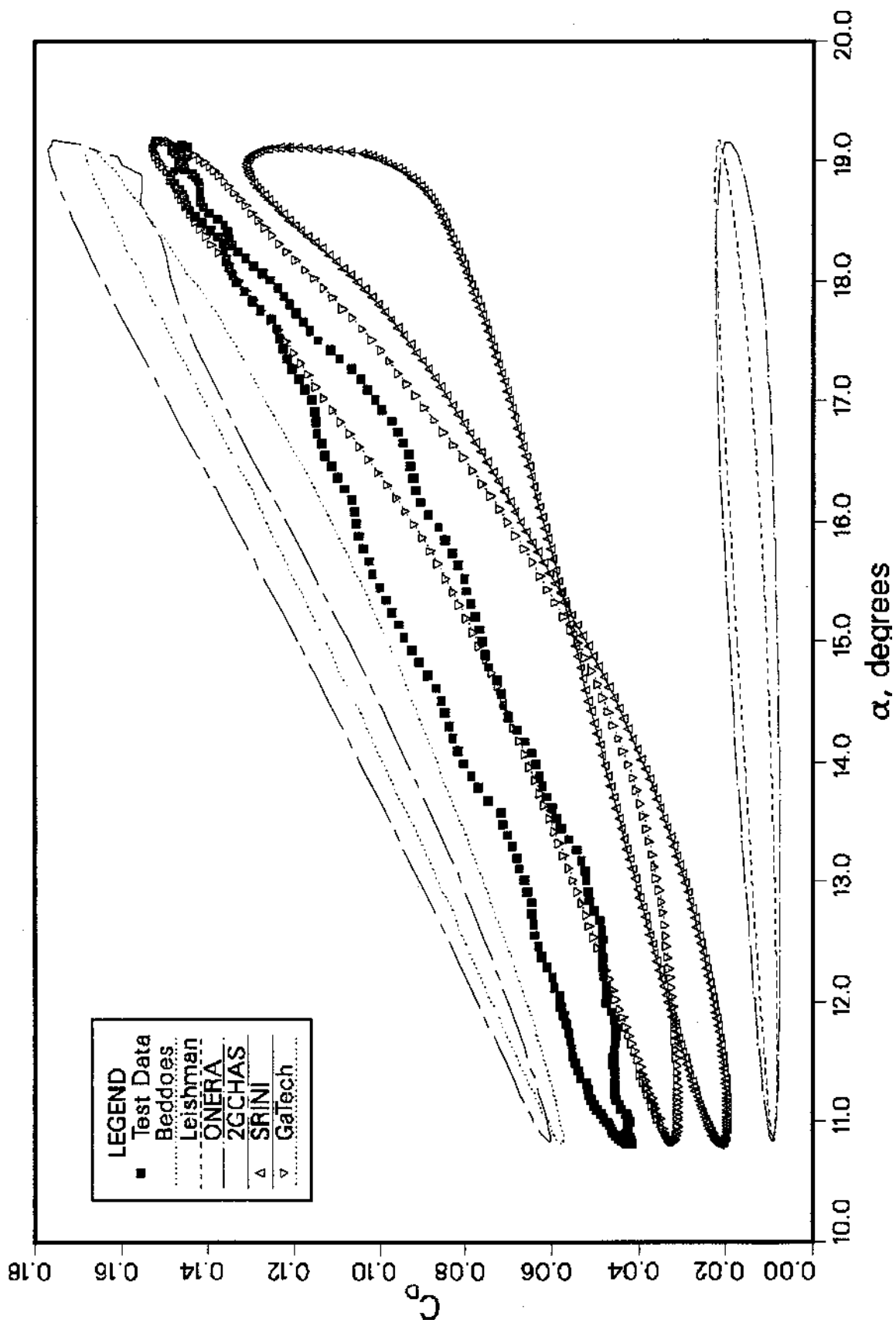


Figure 18(b). Comparison of calculation, modeling, and experimental results as a function of angle of attack, for $M = 0.3$, $k = 0.10$, $\alpha = 15^\circ + 4^\circ \sin \omega t$; drag at Station 5, 96.6 percent span.

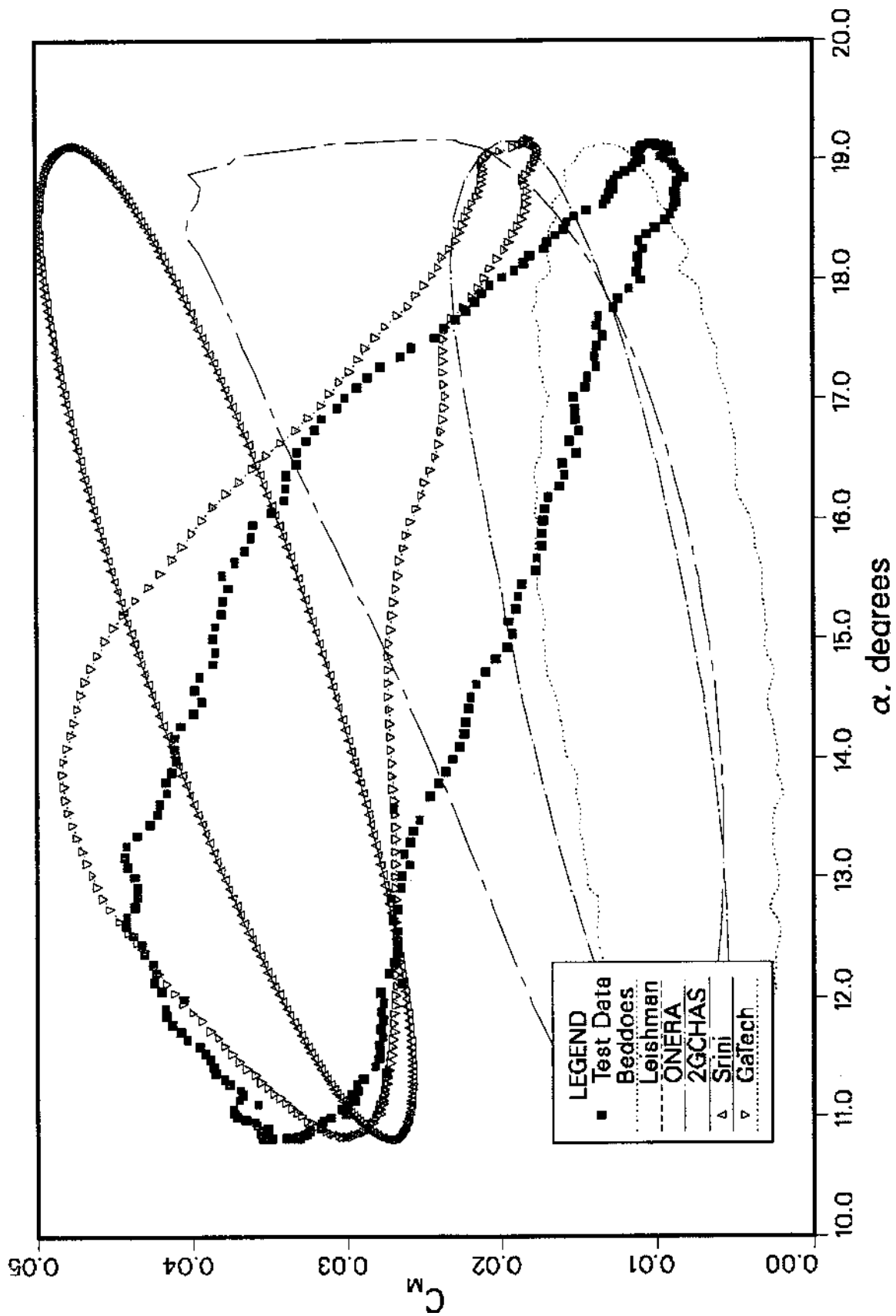


Figure 18(c). Comparison of calculation, modeling, and experimental results as a function of angle of attack, for $M = 0.3$, $k = 0.10$, $\alpha = 15^\circ + 4^\circ \sin \omega t$; pitching moment at Station 5, 96.6 percent span.

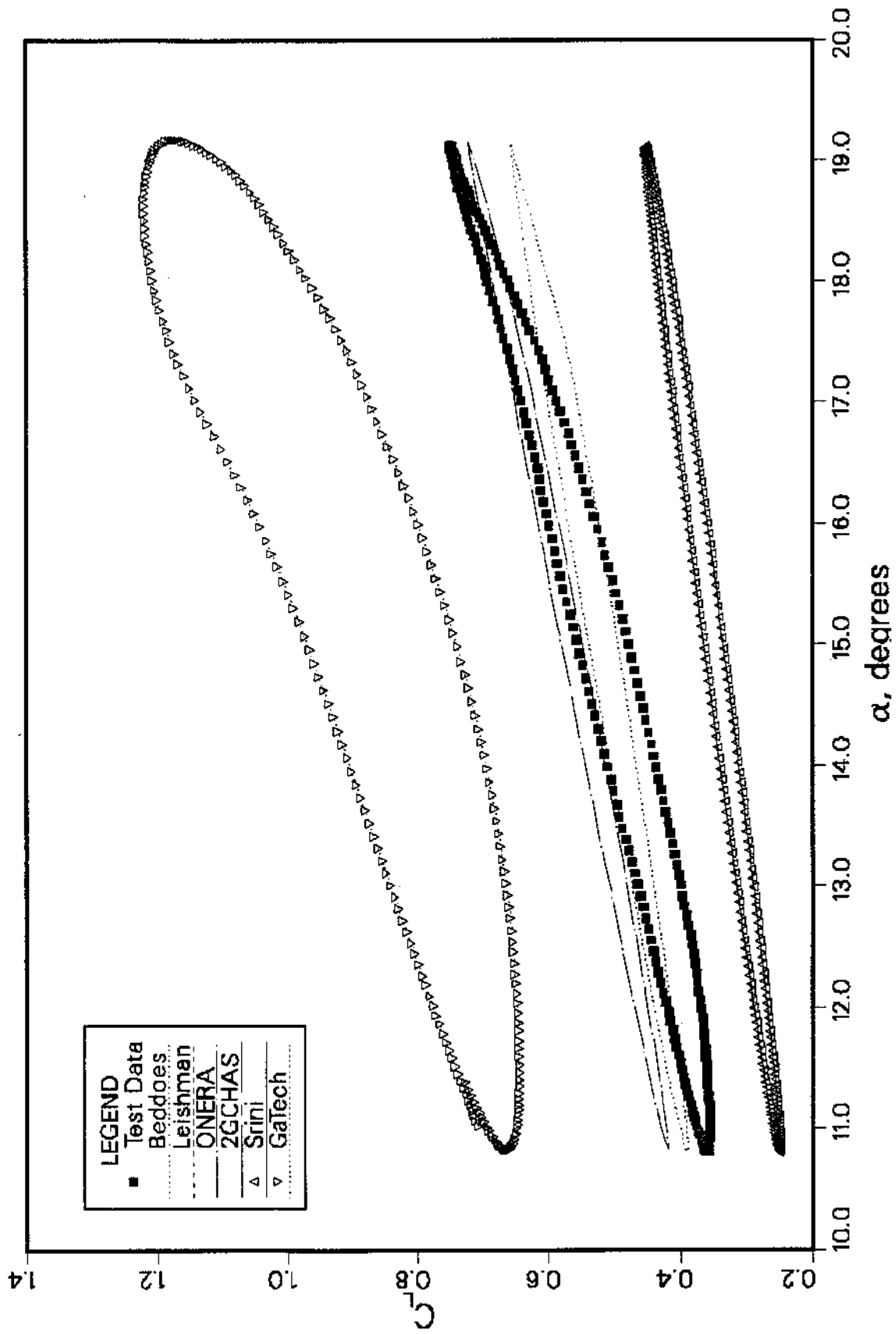


Figure 19(a). Comparison of calculation, modeling, and experimental results as a function of angle of attack, for $M = 0.3$, $k = 0.10$, $\alpha = 15^\circ + 4^\circ \sin \omega t$; lift at Station 6, 98.6 percent span.

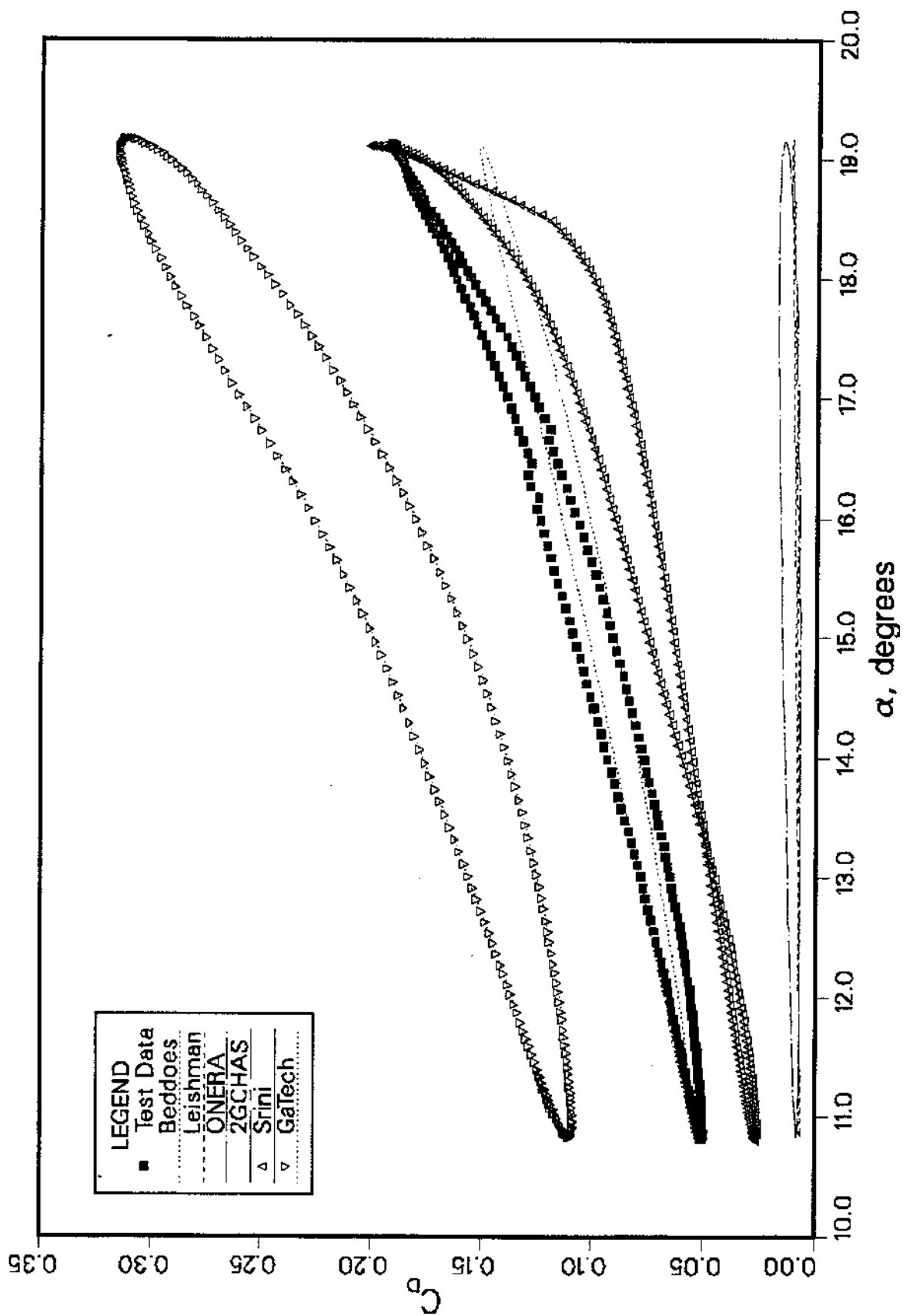


Figure 19(b). Comparison of calculation, modeling, and experimental results as a function of angle of attack, for $M = 0.3$, $k = 0.10$, $\alpha = 15^\circ + 4^\circ \sin \omega t$; drag at Station 6, 98.6 percent span.

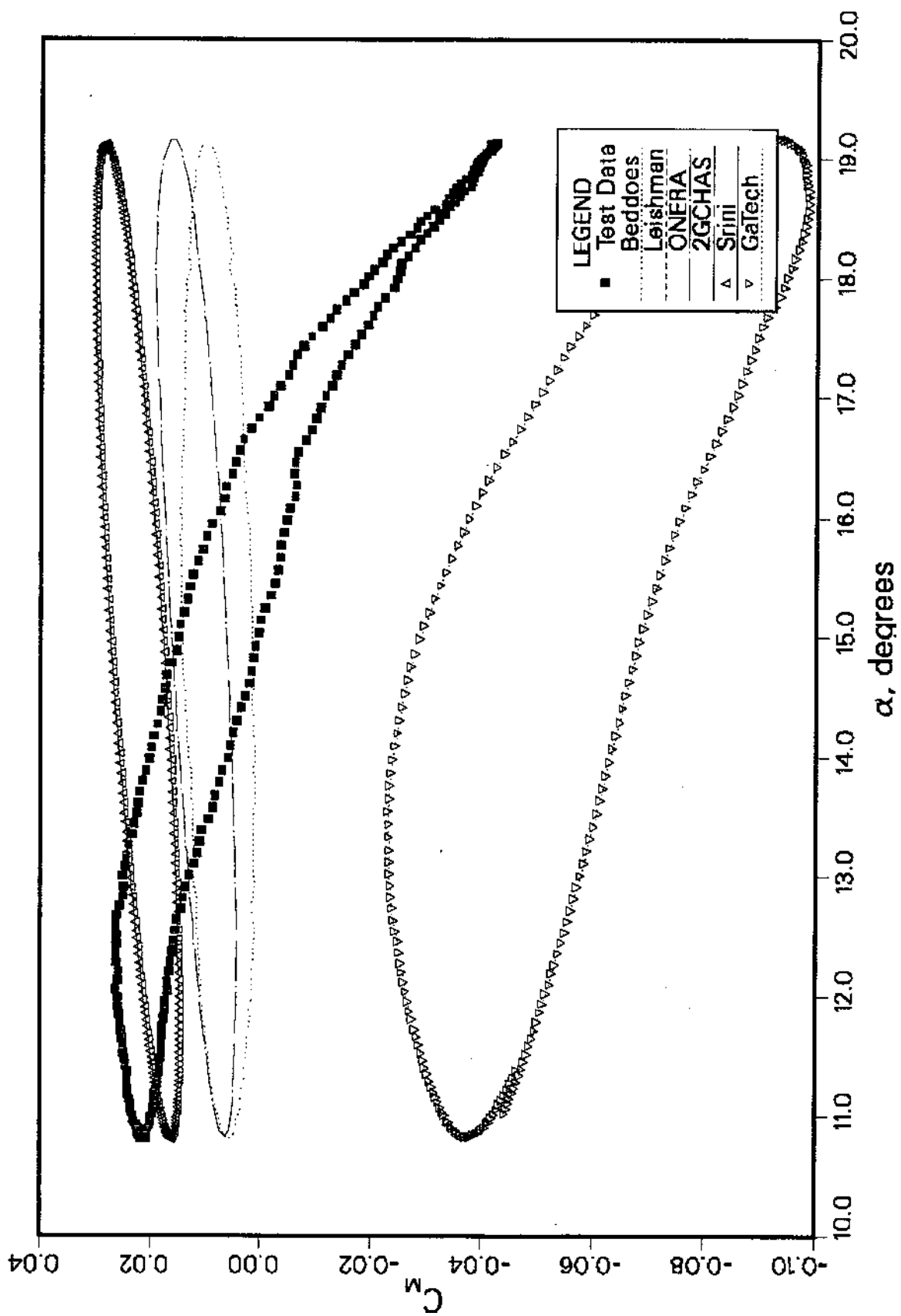


Figure 19(c). Comparison of calculation, modeling, and experimental results as a function of angle of attack, for $M = 0.3$, $k = 0.10$, $\alpha = 15^\circ + 4^\circ \sin \omega t$; pitching moment at Station 6, 98.6 percent span.

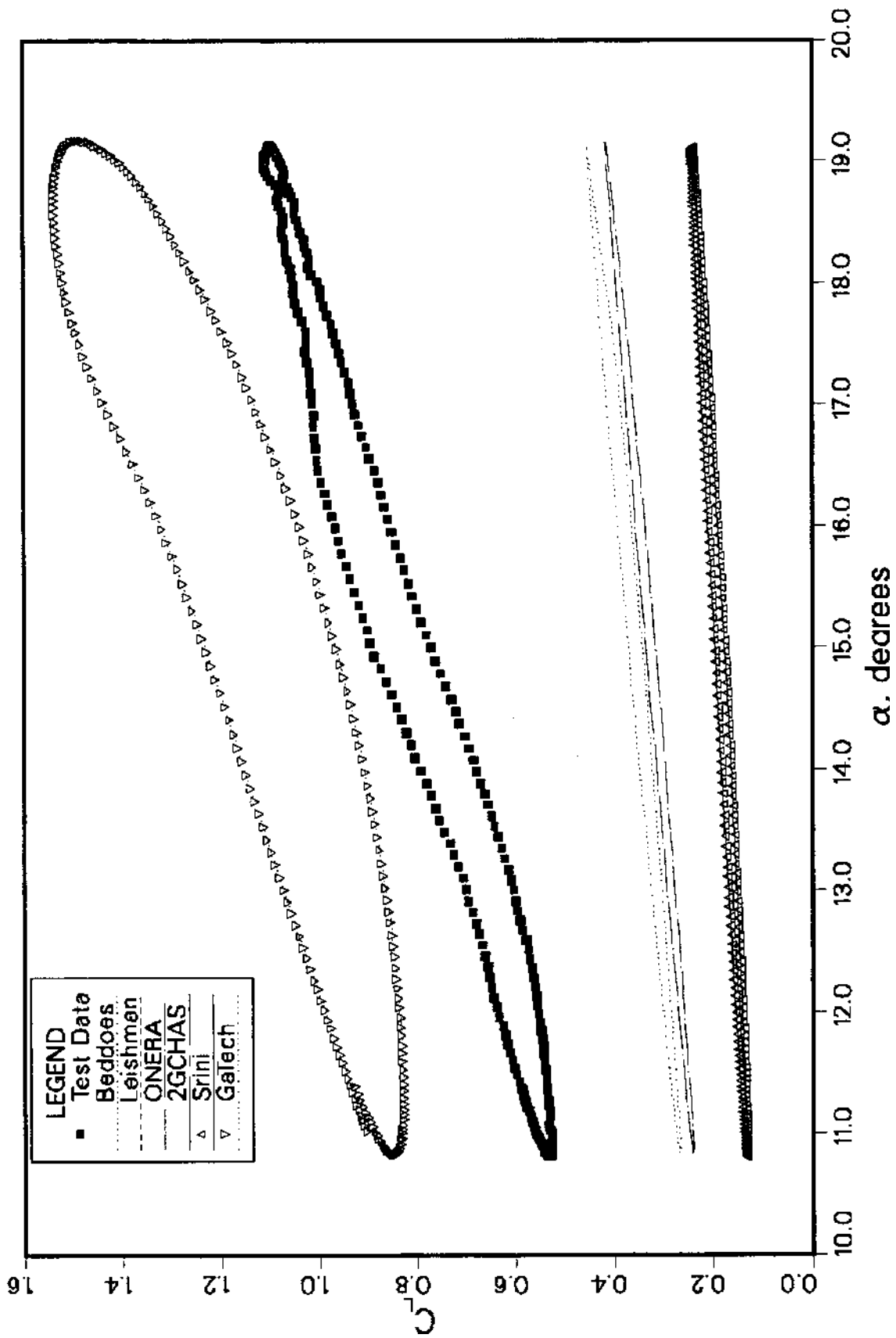


Figure 20(a). Comparison of calculation, modeling, and experimental results as a function of angle of attack, for $M = 0.3$, $k = 0.10$, $\alpha = 15^\circ + 4^\circ \sin \omega t$; lift at Station 7, 99.5 percent span.

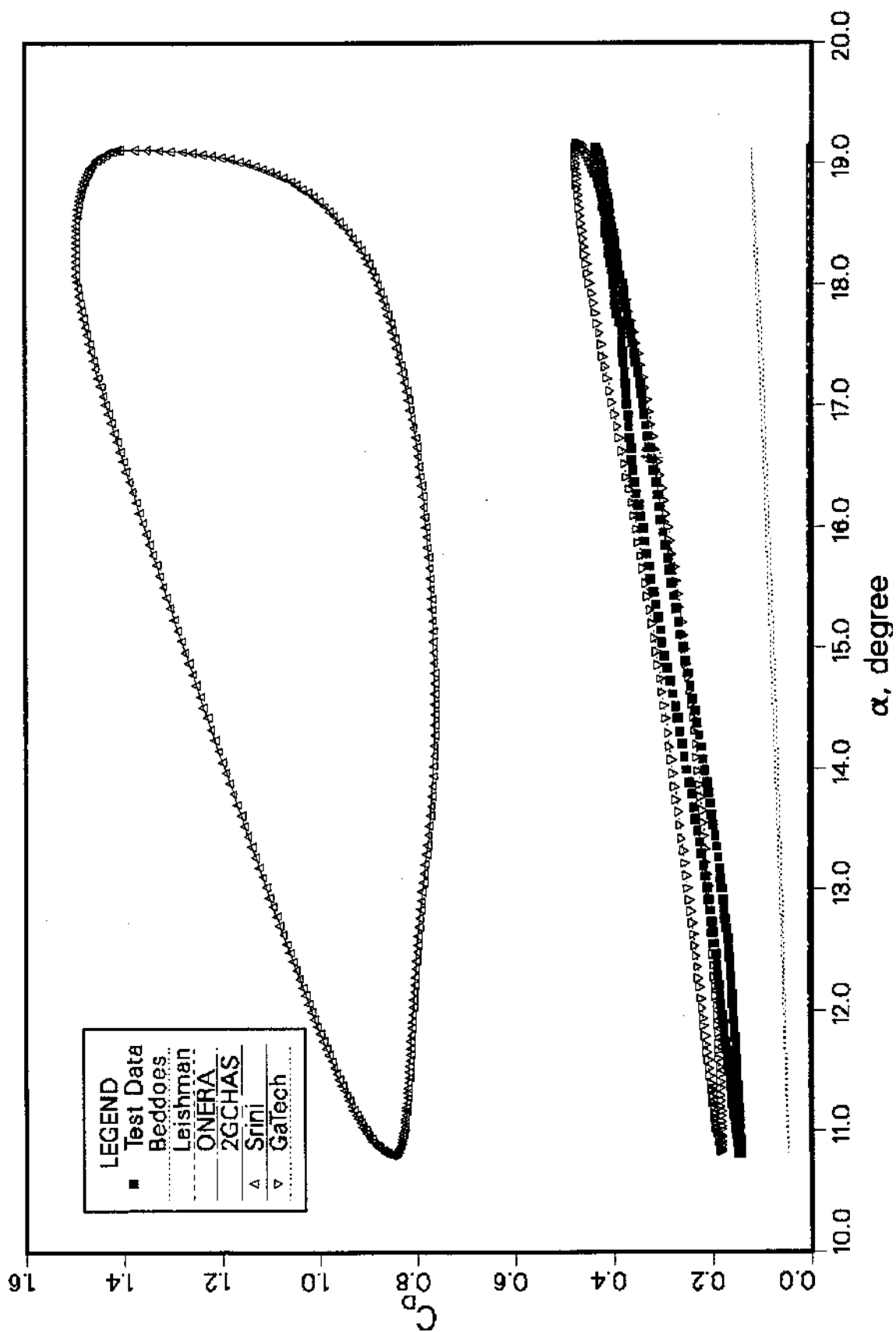


Figure 20(b). Comparison of calculation, modeling, and experimental results as a function of angle of attack, for $M = 0.3$, $k = 0.10$, $\alpha = 15^\circ + 4^\circ \sin \omega t$; drag at Station 7, 99.5 percent span.

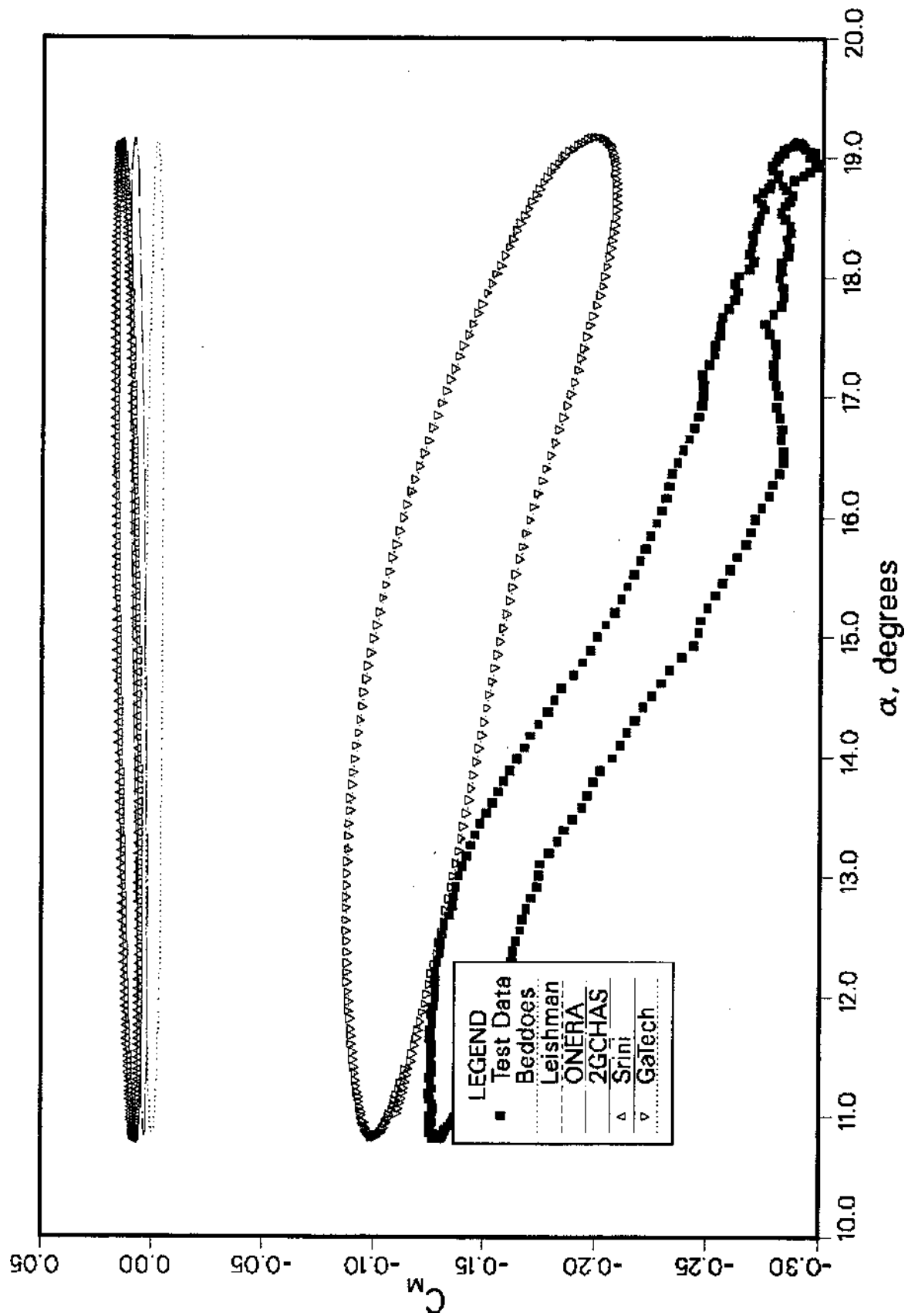


Figure 20(c). Comparison of calculation, modeling, and experimental results as a function of angle of attack, for $M = 0.3$, $k = 0.10$, $\alpha = 15^\circ + 4^\circ \sin \omega t$; pitching moment at Station 7, 99.5 percent span.

REPORT DOCUMENTATION PAGE			Form Approved OMB No. 0704-0188	
Public reporting burden for this collection of information is estimated to average 1 hour per response, including the time for reviewing instructions, searching existing data sources, gathering and maintaining the data needed, and completing and reviewing the collection of information. Send comments regarding this burden estimate or any other aspect of this collection of information, including suggestions for reducing this burden, to Washington Headquarters Services, Directorate for Information Operations and Reports, 1215 Jefferson Davis Highway, Suite 1204, Arlington, VA 22202-4302, and to the Office of Management and Budget, Paperwork Reduction Project (0704-0188), Washington, DC 20503.				
1. AGENCY USE ONLY (Leave blank)		2. REPORT DATE July 1996		3. REPORT TYPE AND DATES COVERED Technical Memorandum
4. TITLE AND SUBTITLE The AFDD International Dynamic Stall Workshop on Correlation of Dynamic Stall Models with 3-D Dynamic Stall Data			5. FUNDING NUMBERS 505-59-52	
6. AUTHOR(S) C. M. Tan and L. W. Carr				
7. PERFORMING ORGANIZATION NAME(S) AND ADDRESS(ES) Aeroflightdynamics Directorate, U.S. Army Aviation and Troop Command, Ames Research Center, Moffett Field, CA 94035-1000			8. PERFORMING ORGANIZATION REPORT NUMBER A-960632	
9. SPONSORING/MONITORING AGENCY NAME(S) AND ADDRESS(ES) National Aeronautics and Space Administration Washington, DC 20546-0001 and U.S. Army Aviation and Troop Command, St. Louis, MO 63120-1798			10. SPONSORING/MONITORING AGENCY REPORT NUMBER NASA TM-110375 USAATCOM TR-96-A-009	
11. SUPPLEMENTARY NOTES Point of Contact: L. W. Carr, Ames Research Center, MS 260-1, Moffett Field, CA 94035-1000 (415) 604-4143				
12a. DISTRIBUTION/AVAILABILITY STATEMENT Unclassified — Unlimited Subject Category 02			12b. DISTRIBUTION CODE	
13. ABSTRACT (Maximum 200 words) A variety of empirical and computational fluid dynamics two-dimensional (2-D) dynamic stall models were compared to recently obtained three-dimensional (3-D) dynamic stall data in a workshop on modeling of 3-D dynamic stall of an unswept, rectangular wing of aspect ratio 10. Dynamic stall test data both below and above the static stall angle of attack were supplied to the participants, along with a "blind" case where only the test conditions were supplied in advance, with results being compared to experimental data at the workshop itself. Detailed graphical comparisons are presented in the report, which also includes discussion of the methods and the results. The primary conclusion of the workshop was that the 3-D effects of dynamic stall on the oscillating wing studied in the workshop can be reasonably reproduced by existing semi-empirical models once 2-D dynamic stall data have been obtained. The participants also emphasized the need for improved quantification of 2-D dynamic stall.				
14. SUBJECT TERMS Dynamic stall, Aerodynamic stalling, Wing oscillations, Helicopter design			15. NUMBER OF PAGES 93	
			16. PRICE CODE A05	
17. SECURITY CLASSIFICATION OF REPORT Unclassified	18. SECURITY CLASSIFICATION OF THIS PAGE Unclassified	19. SECURITY CLASSIFICATION OF ABSTRACT	20. LIMITATION OF ABSTRACT	